MRAM based neuromorphic cell for Artificial Intelligence

Louis Farcis

THÈSE

Pour obtenir le grade de

DOCTEUR DE L'UNIVERSITÉ GRENOBLE ALPES

École doctorale : EEATS - Electronique, Electrotechnique, Automatique, Traitement du Signal (EEATS)
Spécialité : Nano électronique et Nano technologies
Unité de recherche : Spintronique et Technologie des Composants

Cellule MRAM neuromorphique pour l'Intelligence Artificielle

MRAM based neuromorphic cell for Artificial Intelligence

Présentée par :

Louis FARCIS

Direction de thèse :

Ricardo SOUSA Directeur de Recherche, CEA	Directeur de thèse
Liliana BUDA-PREJBEANU PROFESSEURE DES UNIVERSITES, GRENOBLE INP	Co-directrice de thèse

Rapporteurs :

Damien QUERLIOZ
DIRECTEUR DE RECHERCHE, CNRS DELEGATION ILE-DE-FRANCE SUD
Michel HEHN
PROFESSEUR DES UNIVERSITES, Université de Lorraine

Thèse soutenue publiquement le **16 février 2024**, devant le jury composé de :

Lorena ANGHEL, PROFESSEURE DES UNIVERSITES, GRENOBLE INP	Présidente
Ricardo SOUSA, DIRECTEUR DE RECHERCHE, CEA CENTRE DE GRENOBLE	Directeur de thèse
Liliana BUDA-PREJBEANU, PROFESSEURE DES UNIVERSITES, GRENOBLE INP	Co-directrice de thèse
Damien QUERLIOZ, DIRECTEUR DE RECHERCHE, CNRS DELEGATION ILE-DE-FRANCE SUD	Rapporteur
Michel HEHN, PROFESSEUR DES UNIVERSITES, Université de Lorraine	Rapporteur
Alina DEAC, SENIOR SCIENTIST, Helmholtz-Zentrum Dresden-Rossendorf	Examinatrice
Julie GROLLIER, DIRECTRICE DE RECHERCHE, CNRS DELEGATION ILE-DE-FRANCE SUD	Examinatrice

Abstract

The rapid evolution of the society terms of computational needs tends to target applications that were once human exclusive. Development of deep learning algorithms made possible overpassing some capabilities in the task the human brain was performing the best as for instance image and speech recognition, decision making and optimization problems. However, the Artificial Neural Networks (ANNs) capable of solving these tasks use intensively massive amount of data and require multiple operations at the same time. When running ANN algorithms in a classical Von Neumann architecture where the computing unit is separated by the memory, latency and high energy consumption start to rise exponentially with the size of the emulated neural network. From this observation, the scientific community starts looking at brain-inspired computing schemes to overcome the current limitation. In particular, spiking neural networks (SNNs) were early predicted by W. Maass in 1997 to be a suitable candidate to leverage the sparsity of the network while showing egal if not better results than the first generations of ANN. Up until now, some Application Specific Integrated Circuits (ASICs) were proposed by companies such as Intel and IBM to emulate SNN with CMOS-based technology. The number of transistors needed to accomplish some critical functionality like spiking neurons in these solutions is still very large and not suitable for downscaling strategies. In this context, new hardware solutions were proposed to emulate the synaptic and neuronal features while reducing the footprint and the energy consumption. In particular, various types of nano-synapses based on emerging non-volatile memory (NVM) explored multi-level synaptic weights and short-term/long-term memory. Among them, the spintronic solutions are the most advanced in maturity compared to the other technology because magnetic-random-access-memory technology, which represents a binary synapse, has already reached the market for ten years. However, a spiking neuron compatible with spintronic-based synapse is still missing in the literature. The thesis takes place in this context of developing new solutions with spintronics in order to emulate spiking neurons. Magnetic tunnel Junctions (MTJs) have been widely used in spintronics as memory unit because of their high endurance while demonstrating relatively small energy for writing and reading operation and are BEOL CMOS compatible. The solution elaborate along the manuscript takes all the benefits of the MTJs to design a spiking neuron based on the windmill dynamics. The dual-free layer MTJ concept is modelled, designed, nano-patterned and electrically characterized to give a constructive outlook on how viable this structure is for emulating spiking neurons.

Résumé

La constante évolution de la société en termes de besoin computationnel tend vers les applications d'intelligence artificielle qui étaient autrefois réservées exclusivement à l'Homme. Le développement d'algorithmes reposant sur l'apprentissage profond a rendu possible le dépassement des capacités du cerveau humain dans ces domaines de prédilections comme la reconnaissance d'images et de paroles, la prise de décision et les problèmes d'optimisation. Pourtant, les réseaux de neurones artificiels capables de résoudre ces problèmes repose de manière intensive sur d'énorme quantité de données et requiert de nombreuses opérations en parallèle. Quand ces algorithmes tournent sur des architectures classiques de type Von Neumann où l'unité de calcul est séparée de l'unité mémoire, la latence du réseau et son énergie consommée augmente exponentiellement avec sa taille. De ce constat, la communauté scientifique commença à développer des schémas informatiques inspirés du cerveau afin de surpasser les limitations observées. En particulier, les réseaux de neurones impulsionnels ont été prédit par W. Maass en 1997 comme étant un candidat adapté à la maximisation du dispersement des opérations dans le réseau tout en démontrant des performances égales, sinon meilleures, aux premières générations de réseaux de neurones. Jusqu'à maintenant, des circuits intégrés orientés vers une application donnée (ASICs) ont été développés par des industriels tels que Intel ou IBM pour émuler des réseaux de neurones impulsionnels, se basant sur des technologies courantes CMOS. Le nombre de transistors nécessaire pour accomplir certaines fonctionnalités critique propre aux réseaux de neurones, comme les neurones impulsionnels, est toujours très important, ce qui n'est pas souhaitable dans une stratégie de réduction de miniaturisation poussées. Dans ce contexte, de nouvelles solutions ont été proposées pour reproduire les caractéristiques synaptiques et neuronales tout en essayant de réduire un maximum l'empreinte physique et la consommation énergétique. En outre, différents types de nano-synapses reposant sur des mémoires émergentes non-volatiles ont exploré des poids synaptiques multi-niveaux ainsi que la reproduction des fonctions mémoires court-terme et long-terme. Parmi elles, les solutions basées sur une technologie spintronique sont celles les plus matures d'un point de vue industriel puisque les mémoires à accès direct magnétique (MRAM), pouvant servir de synapses binaires, ont déjà atteint le marché international depuis une dizaine d'années. Pourtant, l'existence d'un neurone impulsionnel compatible avec une synapses spintronique est toujours manquant dans la littérature actuelle. Cette thèse prend donc sa place dans ce contexte de développement de nouvelles solutions spintroniques afin d'émuler un neurone impulsionnel. Les jonctions tunnels magnétiques (JTMs) largement utilisées en spintronique pour leur endurance en tant que mémoire tout en démontrant des énergies d'écriture et de lecture très faible ainsi qu'une compatibilité "back-end of line" et CMOS. La solution élaborée dans ce présent manuscrit prend l'avantage des JTMs pour concevoir un neurone impulsionnel basé sur la dynamique "windmill". Le concept de JTM à double couche libre est modélisé, nano fabriqué et caractérisé électriquement pour donner une perspective constructive sur son potentiel utilisation en tant que neurone impulsionnel.

Acknowledgement

Completing this PhD journey has been a challenging yet rewarding experience, and I am profoundly grateful to those who have supported me along the way.

First and foremost, I extend my heartfelt gratitude to my supervisor, Ricardo Sousa, whose expertise and unwavering support have been instrumental throughout this research work. Ricardo's insightful feedback, encouragement, and mentorship have shaped not only the outcome of this thesis in terms of experimental results but also my growth as a researcher.

I would like to express my sincere appreciation to Liliana Buda-Prejbeanu for her invaluable assistance and support throughout the three years of my doctoral studies. Liliana's expertise in modeling and simulations, dedication, and encouragement have been invaluable assets.

This PhD work grew in a conducive environment enabled by the precious support of the technical staff led by Isabelle Joumard for experimental set-up, with valuable help from Nicolas Mollard for the realization of mechanical parts and Eyub Yildiz for expertise in electrical circuitry. Almost all the technical skills that I acquired in the cleanroom can be attributed to invaluable assistance from Alvaro Palomina, Daniel S. Hasen, Marco Mansueto, and Nuno Caçoilo, all members of the MRAM team; and cleanroom staff represented by Thomas Charvolin (etching tools), Christophe Lemonias (lithography and imaging), Florian Disdier (process flow), Aurelien Olivier (etching and process flow), Laurent Vila (Electron-beam lithography), Stephan Auffret, and Jérôme Faure-Vincent for the deposition of stacks.

I personally enjoyed scientific discussions with Philippe Talatchian, Ursula Ebels, Bernard Dieny, and Kevin Garello, who pushed me towards intellectual growth and discovery.

Daily interactions with David Salomoni, Bruno Teixeira, and Sergi Martin Rio were precious for me to gain interesting insights about my work and how to overcome some issues. During this PhD, I met people who, beyond their scientific thinking, demonstrate incredible human values and became naturally very good friends such as Hasan, David, Libor, and Ilaria.

Additionally, I would like to acknowledge the support of my friend and office mate, whose companionship, encouragement, and understanding have been a source of strength and inspiration during both the triumphs and challenges of this journey: Nuno, Marco, Javier, Hanna, Pedro, Capucine, Joseba, Subham, Matteo, Aurélie, Anda, Maxime, Théo, Leandro, Andrea, Miina, Michael, Tan, Lucile, Ajay, Abderrazak, and Kamal.

Furthermore, I extend my gratitude to my parents, Alain and Pascale, and my brother, Clément, for their unfailing love, encouragement, and belief in my abilities. Their constant support and understanding have been a source of motivation and strength throughout this endeavor. I am grateful to my uncle Olivier, my cousin Hugues, and Catherine, from whom I received precious encouragement on the day of my defense.

Lastly, to my partner Valentine, your unwavering love, patience, and understanding have been the base frame of my journey. Your support and encouragement, even during the most challenging times, have sustained me and inspired me to push forward. Your belief in my abilities and your sacrifices have been invaluable, and I am deeply grateful to have you by my side throughout this adventure.

I am deeply grateful to everyone who has contributed to this journey, and I look forward to continuing to build upon the foundation laid during my doctoral studies.

List of Figures

List of Tables

List of Abbreviations

AC	alternating current
AI	artificial intelligence
ANN	artificial neural network
AP	anti-parallel
ASICs	application specific integrated circuits
BCC	body-centered cubic
CDF	cumulative distribution function
CMOS	complementary metal–oxide–semiconductor
CPU	central processing unit
DC	direct current
DFL-MTJ	dual free layer magnetic tunnel junction
DMM	digital multimeter
DW	domain-wall
E-beam	electron-beam
FCC	face-centered cubic
FL	free layer
FM	ferromagnet
FMR	ferromagnetic resonance
GMR	giant magnetoresistance
IBE	ion beam etching
IEC	interlayer exchange coupling
IPA	isopropanol
iPMA	interfacial perpendicular magnetic anisotropy
LIF	leaky integrate-and-fire

LLG	Landau Lifshitz Gilbert
LTD	long-term depression
LTP	long-term potentiation
MIBK	methyl isobutyl ketone
MNIST	Modified National Institute of Standards and Technology
MOKE	magneto-optical Kerr effect
MOSFETs	metal-oxide-semiconductor field effect transistors
MRAM	magnetic random-access memory
MTJ	magnetic tunnel junction
NB	Néel-Brown
NM	non-magnetic
NN	neural network
P	parallel
p-MTJ	perpendicular magnetic tunnel junction
PG	pulse generator
PMMA	poly(methyl methacrylate)
PVD	physical vapor deposition
QCM	quartz crystal microbalance
RF	radio-frequency
RIE	reactive ion etching
RL	reference layer
SAF	synthetic anti-ferromagnet
SNN	spiking neural network
SOT	spin-orbit torque
STDP	spike-timing dependent plasticity
STT	spin-transfer torque
TMR	tunnel magnetoresistance
VSM	vibrating sample magnetometer

Introduction

Since the mid-20th century, we have witnessed an unprecedented technological revolution known as the information age. This era introduced the emergence of digital electronics, accompanied by the advancement of metal-oxide-semiconductor field effect transistors (MOSFETs), marking the beginning of an intensive pursuit of technology miniaturization. In 1965, Moore's law prophesied the doubling of transistors within an integrated circuit every two years [1]. At the same time, the transformation of knowledge into a digital form, especially with the introduction of the Internet, has caused the amount of available data to skyrocket. However, the foundation of modern computing to process data, known as Von Neumann architecture, today faces limitations which affect its performances [2].

The miniaturization of the building block in a classical Von Neumann architecture (i.e. transistor) is not enough to compensate the need in terms of computational speed. For the past 70 years, the amount of calculations has not only increased, but the type of tasks has also shifted from algorithmic and logical operations to more complex computational tasks due to the advancement of artificial intelligence (AI) applications. Many deep learning algorithms employed for AI tasks rely on artificial neural networks (ANNs) to accurately solve optimization problems [3], pattern recognition [4, 5], speech recognition [6] and medical diagnostics [7]. Throughout the years, ANNs have revolutionized computing in many different areas, demonstrating their ability to perform tasks that were once considered too complex for machines and exclusive to humans. From image and speech recognition to medical diagnostics and gaming, ANNs have reshaped the technological landscape.

However, ANNs require frequent access and manipulation of data. In the classical Von Neumann architecture, the continuous transfer of data between the memory and the processor leads to high energy consumption and latency, which is commonly referred to as the Von Neumann bottleneck or memory wall [2, 8]. Overall, the inherent limitations of this architecture, particularly its sequential and separate memory processor design, hinder the efficient execution of neuromorphic algorithms that are inspired by highly parallel, low-latency and asynchronous processing. Transitioning to specialized architectures capable of accommodating these unique requirements is crucial to maximize the performance of neuromorphic computing. Integrating ANNs into hardware is a fundamental challenge in contemporary technology. The solution appears to reside in the integration of AI algorithms directly into edge devices. Integration of this kind could lead to a decrease in energy use, shorter waiting times, less reliance on internet access, and improved security and privacy by reducing the amount of data sent between personal devices and cloud servers.

In this context, spiking neural networks (SNNs) have emerged as potentially energy-efficient alternatives to ANNs [9, 10]. Inspired by brain neural operations, SNNs encode information through sparse temporal events known as spikes, as opposed to the dense and high-precision activation of ANNs. These SNNs operate by integrating input spikes over time in neurons' membrane potentials, simulating the leaky integrate-and-

fire (LIF) dynamics observed in neural systems [11]. Their ability to harness spatio-temporal information makes them particularly appealing for processing real time data.

To run efficiently SNNs on hardware platforms, architectures resort to application specific integrated circuits (ASICs). The main realizations developed to date are TrueNorth from IBM [12], Loihi from Intel [13], SpiNNaker from the University of Manchester [14], and Neurogrid from Standford University [15]. These computing platforms contain many cores on-chip and multichip configurations, taking advantage of running many computations in parallel. However, these CMOS-based platforms employ a large number of transistors for neuronal and synaptic operations, which would be impractical for modern embedded applications due to their energy requirements and circuit footprint [16]. Moreover, a trade-off seems to remain in place between the versatility of the tasks solved by these platforms (SpiNNaker) and the more high-density energy-efficient hardware demonstrator (TrueNorth, Loihi). For the past decade, the progress of SNN hardware has been groundbreaking, yet a significant breakthrough is hindered by the parallel progress of the CMOS industry and ever-changing computing requirements. It is then difficult to state at this stage what the best architectures would be to adopt, since none fulfills all the potential benefits at the same time.

Most traditional neural network accelerators are based on fully digital architectures. However, analog implementations, which are closer to the brain-inspired vision of neuromorphic computing, have gained more interest recently. By implementing basic operation within the physics of the building blocks of networks [10], it is possible to significantly reduce the amount of area and energy used. For example, the organization of the crossbar matrix of memristive elements allows one to simply cascade information from one layer of neurons to the next using the Kirchoff law. The capacitor element is also a device that allows one to easily mimic leaky and integration functionality at the base of the LIF neuron model. The development of phase-change transition materials to emulate long- and short-term memory has also been proposed.

Closer to commercially available technology, spintronics-based devices have already demonstrated suitable characteristics [17, 18] to build multi-level synapses and brain-inspired hardware platforms. Promising results were shown recently by Julie Grollier's group [19–21] on how spin-torque nano-oscillator and spin-diode effect can be used to emulate neural networks capable of solving vowel recognition task. In addition to showing an energy-efficient dynamical mechanism, spintronics-based devices have already reached the commercial market in embedded memory technology. However, there is still a gap between the large spectrum of SNN algorithms showing promising results and the limited hardware development of the neuromorphic chip. This thesis investigates the potential of spintronics to construct physical spiking neurons in hardware. In particular, dual-free layer magnetic tunnel junctions (MTJs) are at the heart of this study due to their potential spiking dynamics predicted in the simulation by Matsumoto *et al.* [22].

Objective The aim of this thesis is to explore solutions based on MTJ that generate spiking output when exposed to an excitatory input. The relation between the input and the output of the device should be a nonlinear function, which is a crucial requirement to emulate the activation function of the neuron in NN. The device should ideally work without the need of an external magnetic field and be highly scalable in order to target dense hardware spiking neural network application. The integration with existing spintronic-based devices should guide the approach to design this spiking neurons. Exploring the possibility of creating a spiking neuron that is compatible with the spike-timing dependent plasticity (STDP) local learning rule to modify the weights of adjacent synapses would be of great interest.

Outline The thesis is organized as follows :

Chapter 1 : Background This chapter gives the necessary background in terms of physics and applications related to the thesis. In particular, nanomagnetism and spintronic phenomena essential to the working principle of magnetic tunnel junction (MTJ) are addressed, as well as a brief description of spiking neural networks (SNNs) and the existing hardware development at the device level.

Chapter 2 : Experimental techniques This chapter compiles the practical methods encountered in the thesis. Characterization techniques and the nanofabrication process are described.

Chapter 3 : Modeling dual free layer MTJ for spiking neuron This chapter properly describes the concept of the dual free layer system used to emulate hardware spiking neuron. In particular, the macrospin model and simulations present the expected behavior as a function of material parameters, applied current, and external magnetic field.

Chapter 4 : Material developments for the dual free layer MTJ This chapter designs the dual free layer structure according to the requirements identified in the modeling chapter. In particular, optimization of the MTJ stacks is carried by magneto-optical Kerr effect (MOKE) and vibrating sample magnetometer (VSM) characterizations.

Chapter 5 : Nanodevice characterizations This chapter presents the electrical results of nanopatterned devices and demonstrates windmill dynamics with a time-resolved measurement technique. Comparisons with expected behavior from the macrospin model and simulations are also developed.

Chapter 6 : Perspectives In order to connect the present work to the development of hardware SNN platform, we envision in this chapter some applications of the dual free layer MTJ. We explore the possibility to use MTJ-based devices as input neurons, LIF neurons and synapses with local learning rules.

Chapter 7 : Conclusion Finally, the last chapter summaries the main achievements of this thesis in term of modeling and macrospin simulations correlated with nano-device electrical characterizations.

Contents

Chapter 1

Background

Contents

1.1 Introduction

This first chapter provides some background to this thesis in terms of the physics involved (spintronics) and the targeted application (neural networks). After a short overview of the origin of nanomagnetism, at the base of spintronics, the main interactions taking place in our system will be defined. Second, the concept of neural networks and particularly SNNs will present the main motivation of this work, although the concept developed in this thesis is not limited to SNN applications. Finally, the last part reviews the previous studies on concepts similar to the one at the core of this work.

1.2 Spintronics

In order to explain the magnetization dynamics that were explored in this work, a reasonable understanding of magnetization is required first.

1.2.1 Nanomagnetism

Magnetism has a rich history dating back to ancient times, when the Greeks first noticed interaction forces between lodestones and iron. In China, navigation was improved with a compass made of iron and lodestones. Scientific understanding has advanced over centuries through the contributions of individuals like H. C. Oersted, A.-M. Ampere, M. Faraday, and J. C. Maxwell, who laid the groundwork for electromagnetic theory. The famous Maxwell equations [23] , although essential in the macro-scale world, failed to explain the origin of magnetism in matter at the micro- and nanoscale. It was only one century after the famous experience of H. C. Oersted in 1820 [24] that a significant breakthrough to explain the origin of magnetism was proposed by Wolfgang Pauli in February 1925[25].

The emerging quantum physics in the early twentieth century was decisive for Pauli, who introduced the spin state of the electron. This spin corresponds to an intrinsic angular momentum that depends on the nature of the particle and is noted $\vec{S}$. The observable quantity of the spin angular momenta s^z is associated with a *spin quantum number* m_s that can take a value of 1/2 or -1/2 for an electron ($s^z = m_s\ \hbar$). The magnetic moment generated by a single electron spin is equal to one Bohr magneton, expressed as $\mu_S^z = -g_S\ \mu_B\ m_s = \mu_B$, with g_S the spin g-factor (≈ 2). In addition to this intrinsic property, the electron acquires an additional orbital angular momentum because of its motion around the nucleus as a consequence of the Biot-Savart law. The projection of this orbital angular momentum is $\mu_L^z = -g_L\ \mu_B\ m_l$ with a g-factor g_L equal to 1 and m_l the (secondary) angular momentum quantum number which depends on the orbital in which the electron is located. Finally, the observable total magnetic moment associated with the spin and orbital angular momenta is expressed by $\mu_J^z = -g_J\ \mu_B\ m_j$ with g_J the Landé g factor (≈ 2) and m_j the secondary total angular momentum quantum number. The Hund rules and the Pauli exclusion principle establish the method for calculating the total angular momentum J from the electronic configuration of any atom in the periodic table. From these rules we note that some atoms have their last electron shell completely filled and exhibit only diamagnetism. Diamagnetic materials show a repulsive force with respect to the external magnetic field as a consequence of the opposite induction field created by the current loop of an electron around the external magnetic field (Lenz law).

The rest of the elements are expected to have a non-zero magnetic moment because of their partially filled electron shell. Indeed, electrons with the same spin tend to fill different orbitals to reduce their electrostatic repulsion. Meanwhile, the spins of the electrons on different orbitals are maintained parallel to maximize the total spin ($\sum \mu_S$) according to the Hund rules. This case of a partially filled electron shell is found for 79 elements in the periodic table. However, a material made of a magnetic compound is not necessarily magnetic. When considering a sufficiently large number of atoms (solid state), the only materials showing ferromagnetic behavior at room temperature are 3d transition metals [26]: iron (Fe), cobalt (Co), and nickel (Ni).

In transition metals, such as Co, Fe and Ni, 3d electrons occupy the outermost shell. When considering a large number of atoms, the overlapping 3d orbitals extend into a wider 3d band. The itinerant nature of these 3d electrons in this band amplifies the interatomic coupling, while their spins remain conserved over

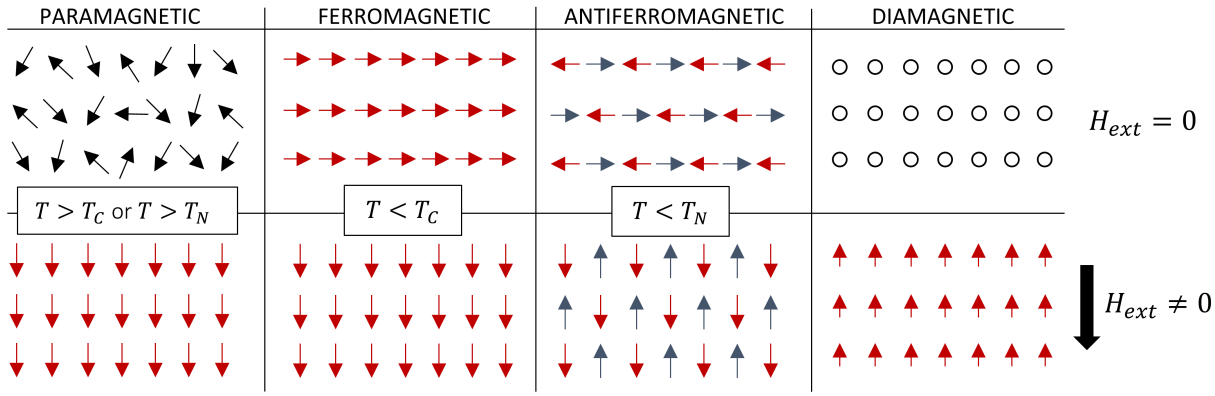

Figure 1.1: Schematic of different types of magnetic materials and their behavior with applied magnetic field. Black arrows refer to disordered magnetic moments, red arrows to ordered magnetic moments and blue arrow to antiferromagnetic coupled magnetic moment with respect to the blue arrows.

a specific characteristic length. This length is substantial for Ni and Co, resulting in ferromagnetic coupling, whereas it is shorter than the interatomic distance in Mg, leading to antiferromagnetic coupling. In the case of Fe, its magnetic behavior, whether ferromagnetic (in the α phase with a body-centered cubic structure) or non-magnetic (in the γ phase with a face-centered cubic structure), is determined by its crystalline arrangement.

The global magnetic behavior of a material is then strongly dependent on the coupling between atom sites, which was formulated by Werner Heisenberg [27] and Paul Dirac [28] in the 1920s as the exchange interaction. As long as the exchange interaction between the atom sites prevails over thermal excitation, the material exhibits ferromagnetic or antiferromagnetic behavior for negative or positive exchange constant values, respectively ($E_{\text{ex}} = J_{\text{ex}}\ \vec{S}_i \cdot \vec{S}_j$). The total magnetic moments in the volume of a magnetic body constitute the saturation magnetization, denoted M_s and measured in $\mathrm{A/m}$. This saturation magnetization decreases with increasing temperature until it reaches the critical Curie temperature ($\mathrm{T_C}$), beyond which the ferromagnetic phase vanishes into a paramagnetic phase, with magnetic moments pointing randomly in all directions.

Another class of interesting magnetic material is composed of 4f rare earth metals. These materials exhibit significantly weaker interatomic coupling due to the localization of the inner 4f shell around the nucleus, thereby limiting interactions with neighboring atoms. Consequently, the Curie temperature ($\mathrm{T_C}$) of these materials falls below room temperature. The alignment of moments in 4f rare-earth metals hinges on significant spin-orbit coupling, resulting in a parallel orientation of the large spin and orbital moments. This phenomenon is the driving force behind magnetocrystalline anisotropy.

Finally, in paramagnetic materials, the magnetic moments of individual atoms are predominantly influenced by thermal energy, leading to a net magnetic moment of zero. However, upon the application of an external magnetic field to a paramagnetic material, the magnetic moments align themselves along this field, resulting in a non-zero saturation magnetization.

Other types of interaction, listed in the next section, take place in ferromagnetic materials modifying the orientation of the magnetic moments.

1.2.2 Energy terms

In spintronics, various energy terms play crucial roles in understanding and manipulating the behavior of magnetization processing for information processing and storage. Here are some of the key energy terms involved in spintronics.

Zeeman energy

The Zeeman energy is associated with the interaction of a magnetic moment with an external magnetic field, causing the spin to align with or against the direction of the magnetic field. The Zeeman energy per unit of volume is expressed by the following equation, where $\overrightarrow{M} = M_s\,\vec{m}$ with $\vec{m}$ a unit vector, $\overrightarrow{H_{ext}}$ refers to the external magnetic field applied and μ_0 is the vacuum permeability :

$$E_{Zeeman} = -\mu_0 \int_V \overrightarrow{M} \cdot \overrightarrow{H_{ext}}\, dV \tag{1.1}$$

Magnetostatic interaction

A magnetic body is subjected to its own magnetic field, which counteracts its magnetization. This internal field is consistently called the demagnetization field. A practical way to calculate this demagnetization field is to use a magnetic pole model, by analogy to electric charges. The opposite magnetic charges at the surface of the magnet will tend to repeal each other. The closer those opposite charges are, the higher the repealing forces. The demagnetizing field varies with the geometry of the magnetic body and increases with saturation magnetization.

$$E_{demag} = -\frac{1}{2}\mu_0 \int_V \overrightarrow{M}.\overrightarrow{H}_{dem}\, dV \tag{1.2}$$

In an approximation of uniform magnetized ellipsoids, the demagnetization field is expressed by $\overrightarrow{H}_{dem} = -\overline{\overline{N}} \cdot \overrightarrow{M}$ where $\overline{\overline{N}}$ is the demagnetizing tensor (diagonal). By varying the shape of this ellipsoid, one can calculate the diagonal terms of the demagnetizing tensor of the basic geometries. For a sphere, this leads to $N_{xx} = N_{yy} = N_{zz} = 1/3$ and for an infinite thin film $N_{xx} = N_{yy} = 0$ and $N_{zz} = 1$ where z is the direction perpendicular to the film. The demagnetizing energy in the ferromagnetic material is the origin of the creation of domains in the material. The opposite direction of magnetic domains close to each other helps to close the magnetic flux and reduces the total energy of the system. In contrast, the exchange interaction forces the neighboring spins to align with each other. The competition between these two interactions defines the minimal domain size and the domain-wall (DW) width observed in the material. For example, in the case of the Bloch-type DW, the width of the DW is $\delta_W = \pi\sqrt{A_{ex}/K}$ with A_{ex} the exchange constant and K the magnetocrystalline anisotropy.

Magnetocrystalline anisotropy

This term of energy represents the dependence of the magnetic properties on the crystallographic orientation of the material. It determines the preferred direction of magnetization in a system, known as its magnetic anisotropy. The magnetocrystalline anisotropy takes its origin in the spin-orbit coupling in matter. The total magnetization results from orbital and spin angular momenta. As the orbitals follow the crystal symmetries

of the material, a strong spin-orbit coupling affects the spin angular momentum as well. The total magnetic moment would then prefer to point towards some *easy-axis* directions, which depend on the crystal symmetries. The anisotropy energy per unit of volume is derived in a cubic structure (eq. 1.3) and in the most common case of uniaxial anisotropy observed in a tetragonal and hexagonal crystal (eq. 1.4) where K_1, K_2 and K_u are anisotropy constants (in $\mathrm{J/m^3}$). The second-order approximation of the uniaxial anisotropy gives a rather simple and accurate equation with θ the angle between the easy axis and the magnetization direction.

$$E_{cubic} = \int_V \left(K_1 \left(m_x^2 m_y^2 + m_y^2 m_z^2 + m_z^2 m_x^2 \right) + K_2 \, m_x^2 m_y^2 m_z^2 \right) dV \tag{1.3}$$

$$E_{uni} = \int_V K_u \left(1 - (\vec{u} \cdot \vec{m})^2 \right) dV \approx \left(K_u \, \sin^2 \theta \right) V \tag{1.4}$$

Interfacial anisotropy

The discovery of interfacial anisotropy in coupled ferromagnet (FM)/non-magnetic (NM) materials and FM/Oxide materials provides a new degree of freedom in manipulating magnetization and opens a downscaling path for spintronics devices. The origin of this anisotropy comes mainly from the inversion symmetry breaking at the interface and orbital hybridization, anticipated by L. Néel in 1954 [29]. A fairly recent example is the hybridization of the Fe-3d and O-2p orbitals, which gives rise to a strong interfacial perpendicular magnetic anisotropy (iPMA) in FeCo/MgO interface [30–33]. Before that, the interfaces between non-magnetic heavy metals and magnetic transition metals such as Pt/Co [34] and Pd/Co [35] showed a strong iPMA by the hybridization of the 3d orbitals of the transition metal and the 5d orbitals of the heavy metal. By analogy to magnetocrystalline anisotropy, it is common to represent the iPMA as an easy axis direction perpendicular to the interface, where S is the interface area:

$$E_{interfaces} = \left(K_S \, \sin^2 \theta \right) S \tag{1.5}$$

Magnetocrystalline anisotropy, interfacial anisotropy, and demagnetization energy are often grouped into an effective anisotropy per unit of volume, noted K_{eff} ($\mathrm{J/m^3}$), in the case where all contributions point in the same direction. Note that the demagnetizing energy can be seen as a negative easy axis in the perpendicular direction of the film.

$$K_{\mathrm{eff}} = \left(K_u - \frac{1}{2} \mu_0 M_s^2 \right) + \frac{K_S}{t} \tag{1.6}$$

Interlayer exchange coupling

Two ferromagnetic materials separated by a non-magnetic spacer can be coupled by exchange coupling if the spacer layer is sufficiently thin. The main feature of this exchange coupling is its dependence on sign and amplitude with the thickness of the spacer layer. The interlayer exchange coupling (IEC) energy is expressed as function of the relative orientation between the two magnetic moments $\overrightarrow{m_i}$ and $\overrightarrow{m_j}$:

$$E_{IEC} = -J_{IEC} \left(\overrightarrow{m_i} \cdot \overrightarrow{m_j} \right) S \tag{1.7}$$

where J_{IEC} is the coupling constant ($\mathrm{J/m^2}$). This effect is attributed to the indirect exchange coupling between localized d- or f-shell electrons and the conduction electrons. The coupling derives from spin-dependent reflection of the electron wave function at the interface between the non-magnetic metal and

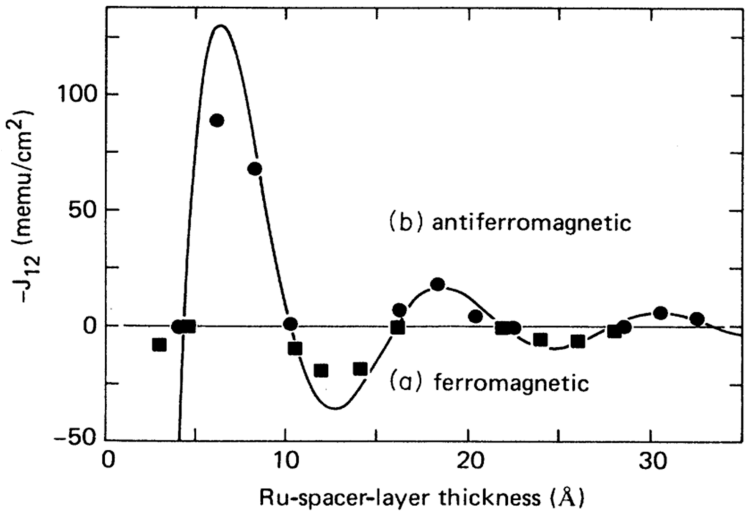

Figure 1.2: Interlayer exchange coupling strength J_{IEC} for coupling of $Ni_{80}Co_{20}$ layers through a ruthenium (Ru) spacer layer. J_{12} is determined from magnetization curves of structures of the form (a) Si/Ru (85Å)/[Co (15Å)/Ru (6Å) / $Ni_{80}Co_{20}$(15Å)/Ru(t_s)/$Ni_{80}Co_{20}$ (15Å)]$_5$ for ferromagnetic coupling, and (b) Si/Ru (105Å) [$Ni_{80}Co_{20}$ (30Å)/Ru(t_{Ru})]$_{20}$/Ru (105Å) for antiferromagnetic coupling. Adapted from Parkin and Mauri [36].

magnetic metal. This leads to an oscillation of the coupling between the antiferromagnetic and ferromagnetic regions as a function of the thickness of the spacer layer. This oscillation is known to be damped with a decay length that depends on the nature of the spacer material.

Ruthenium (Ru) is a good spacer candidate to show the dependence of the coupling constant on the thickness. Figure 1.2 is extracted from the Parkin and Mauri paper [36], where the authors calculate the Ru interlayer exchange coupling in the NiCo/Ru/NiCo system. The Ru spacer layer is often used in synthetic anti-ferromagnet (SAF) structures based on Pt/Co multilayers in STT-MRAM technology. The first and second peak of the antiferromagnetic coupling are around 4 Å and 8 Å of Ru. Because the second peak is wider than the first, it is easier to observe in full-stack deposition.

1.2.3 Spin polarized current and transfer phenomena

Electrical transport in transition metals

In normal metals, electrical transport depends mainly on the density of states (DOS) of the electrons at the Fermi level. In ferromagnetic transition metal, the 4s and 3d bands overlap at the Fermi level. Due to the strong exchange interaction favoring the parallel alignment of spin, each of these bands splits into two sub-bands of opposite spins. The majority electrons are usually called "spin-up" and represent magnetic moments aligned with the total magnetic moment of the material. Oppositely, the minority electrons carry magnetic moment oriented anti-parallel to the total magnetization and are called "spin-down". As the 4s orbital is more delocalized than the 3d orbital, the conduction electrons are mainly composed of 4s electrons, and the exchange splitting of this band is too small to play an important role in the magnetization. On the contrary, the 3d electrons are localized around the nucleus, and the exchange splitting of this sub-band creates a significant difference of DOS for spin-up and spin-down electrons at the Fermi level. As proposed by Mott in 1964 [37] the overall conductivity of ferromagnetic materials can be described by a two-current model in which the

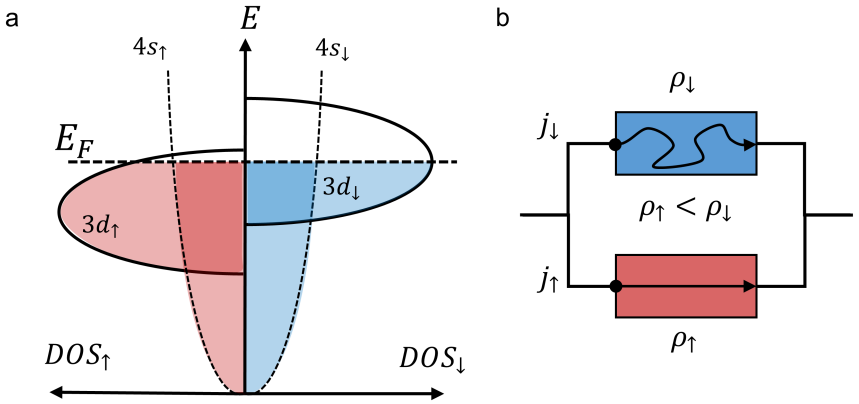

Figure 1.3: (a) Schematic representation of the density of states (DOS) for spin up and spin down electrons. (b) Mott's model of the conductivity in ferromagnetic material.

majority carrier and the minority carrier show a distinct conductivity value. However, the conductivity of the minority and majority carriers depends not only on the DOS at the Fermi level of the 4s electron but also on the scattering probability of the 4s electron with the localized 3d electrons. The minority spin-down channel has more available 3d↓ states in which 4s↓ electrons can be scattered than the majority carriers, making the resistivity of the spin-down electrons higher than that of the majority.

Tunnel magnetoresistance

In 1975, Michel Jullière first demonstrated the tunnel magnetoresistance effect at 4.2 K in Fe/Ge-O/Co [38]. Later, the effect has been observed in various systems, called magnetic tunnel junctions (MTJs), composed of two ferromagnetic materials separated by an insulator. Under the application of a bias voltage, the electrons in the first ferromagnet (FM1) can tunnel through the insulator (if thin enough) and are collected in the second ferromagnet (FM2). The probability that the electrons originating from FM1 tunnels through the barrier depends on the height and width of the insulator barrier. However, it is also spin dependent because it also depends on the density of spin-up and spin-down electron states at the Fermi level on both sides of the barrier, which are not the same in ferromagnetic material (see Figure 1.3.a). In the 3d transition metals, the density of states of spin-up and spin-down electrons at the Fermi level is shifted. If the magnetic moment of both FM electrodes is oriented parallel to each other, the majority (minority) electrons in FM1 are also majority (minority) in FM2. On the contrary, majority electrons in FM1 become minority in FM2, and vice versa if the two magnetic moments are antiparallel. In the AP state, the majority of electrons that come from FM1 have a lower probability of transmission to FM2 because the minority electrons in FM2 have fewer states available at the Fermi level. Taking into account the density of state of each spin channel (↑ and ↓) in each ferromagnet (1 and 2), noted $D^{1,2}_{\uparrow,\downarrow}$, the conductance of the MTJ is expressed in the parallel (P) and anti-parallel (AP) states as :

$$G_P \propto D^1_\uparrow \times D^2_\uparrow + D^1_\downarrow \times D^2_\downarrow \tag{1.8}$$

$$G_{AP} \propto D^1_\uparrow \times D^2_\downarrow + D^1_\downarrow \times D^2_\uparrow \tag{1.9}$$

The tunnel magnetoresistance (TMR) is defined by Julliere as the difference between the AP and P conductance divided by the AP conductance in its optimistic definition. Using Eq. 1.8 and 1.9, the TMR can

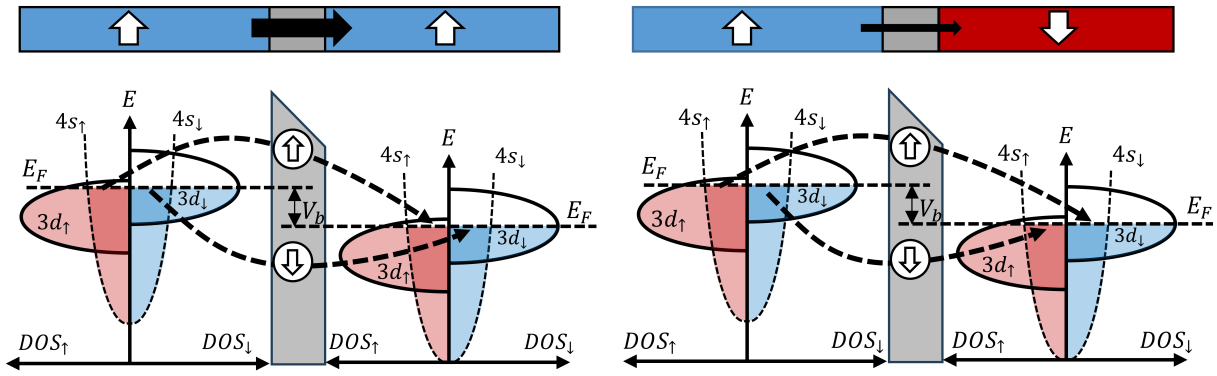

Figure 1.4: Schematic representation of the DOS of spin up and spin down electrons from which the TMR arises in the parallel (left) and anti-parallel (right) alignment of the ferromagnetic layer.

be calculated by :

$$TMR = \frac{G_P - G_{AP}}{G_{AP}} = \frac{R_{AP} - R_P}{R_P} \tag{1.10}$$

$$TMR = \frac{(D^1_\uparrow - D^1_\downarrow)(D^2_\uparrow - D^2_\downarrow)}{D^1_\uparrow \times D^2_\downarrow + D^1_\downarrow \times D^2_\uparrow} \tag{1.11}$$

Introducing the spin polarization of the ferromagnetic layer as $P_{1,2} = \frac{D^{1,2}_\uparrow - D^{1,2}_\downarrow}{D^{1,2}_\uparrow + D^{1,2}_\downarrow}$, the TMR is also expressed as :

$$TMR = \frac{P_1\, P_2}{1 - 2\, P_1\, P_2} \tag{1.12}$$

According to this formula, TMR depends only on the spin polarization of each electrode. Taking the example of FeCoB material with a maximum spin polarization of around 0.6, the TMR value calculated from Eq. 1.12 leads to 50%. The phenomenological approach developed by Jullière estimates the expected TMR values only from the spin polarization of both FM, which make it more appropriate for amorphous Al_2-O_2 based MTJ as observed by Moodera et al. [39] and Myazaki et al. [40] in 1995.

However, MTJ based on FeCo(100)/MgO(100)/FeCo(100) demonstrates to 600% of TMR at room temperature [41]. In a crystalline barrier (MgO, for instance), tunneling becomes a symmetry dependent tunneling process that provides an additional filtering effect. The crystalline structure of Fe(100) makes the electron wave functions modified by the periodic arrangement of ions. Wavefunctions (called Bloch states) showing similar properties (propagation in the direction perpendicular to the plane) are grouped according to their symmetries, mainly Δ_1 (for s, p, $d_{3Z^2-r^2}$ orbitals), Δ_5 (for p_x, p_y, d_{xz} and d_{yz} orbitals), and $\Delta_2^{'}$ (for $d_{x^2-y^2}s$ orbitals). In MTJ, the Bloch states originating from the FM propagate in the tunnel barrier through evanescent states. The transverse k-vector of those wave functions inside the MgO contains a decay rate κ that depends on the Bloch symmetry groups tunneling from the electrodes [42]. The different decay rates of the Δ_1, $\Delta_2^{'}$ and Δ_5 symmetries can be seen in Figure 1.5 for the P states (majority-majority and minority-minority) and the AP states (majority-minority and minority-majority). For all configurations, the $\Delta_2^{'}$ symmetry never participates in conduction, due to its strong decay within the first four monolayers of MgO. The fully spin-polarized Δ_1 symmetry is responsible for the high conductance of the P state, whereas the Δ_5 symmetry carries most

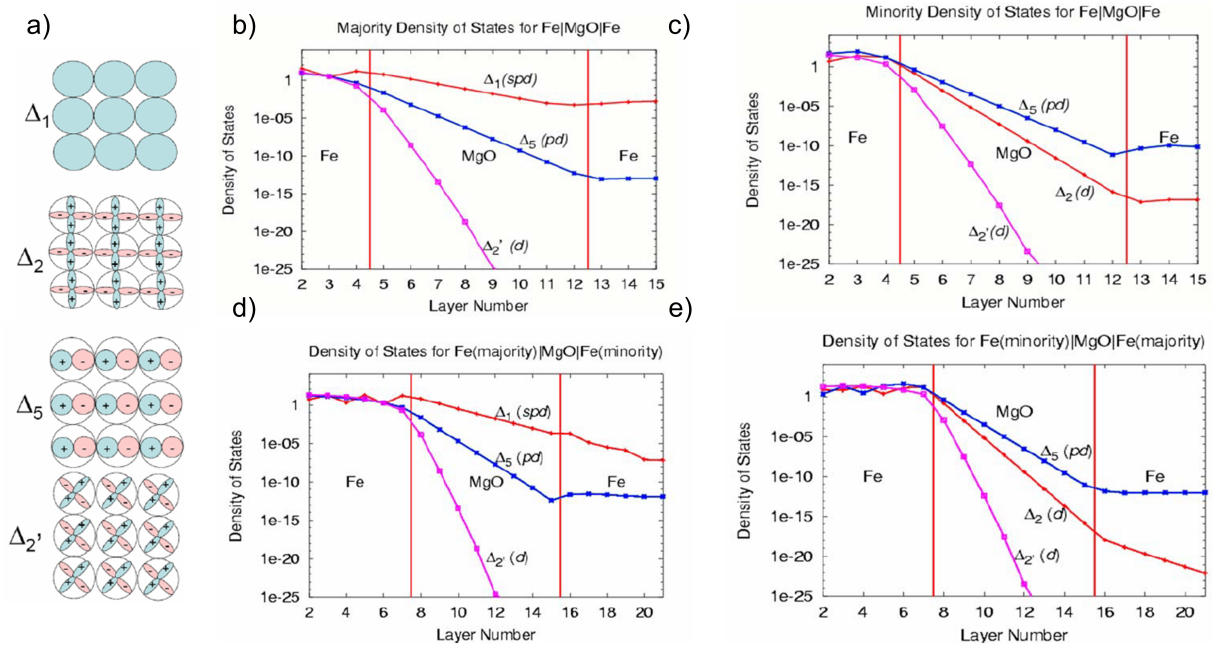

Figure 1.5: a) Δ_1, Δ_2, Δ_5 and $\Delta_2^{'}$ orbital symmetries involved in the coherent tunneling process. DOS of the electrons in the MgO barrier with respect to the symmetries considering parallel (b and c) and anti-parallel (d and e) alignment of the FM layers. The illustrations are adapted from Butler *et al.*[42].

of the conductance of the AP state. Note that the Δ_1 symmetry in the majority-minority case does not contribute to the current because it cannot propagate to the minority spin channel. The wave function decays exponentially in the minority Fe electrode on the right-hand side of the barrier.

Spin-transfer torque

In ferromagnetic materials, the exchange interaction favors the parallel alignment of spins. This interaction leads to a torque being exerted on the local magnetic moment when electrons with a different spin orientation compared to the local magnetic moment flow inside the material. If the collective torque produced by a set of spin-polarized electrons is sufficiently strong, it can modify the magnetization direction of a thin ferromagnetic material. This phenomenon, proposed by Slonczewski [43] and Berger [44] in 1996, is called spin-transfer torque (STT). In 1998, current-induced excitations in magnetic multilayers were observed in Co/Cu multilayers by Tsoi et al. [45]. Two years later, Katine et al. demonstrated spin-torque switching of the magnetization of Co layers in a Co/Cu/Co system [46]. Finally, STT in MTJs was reported in 2004 with MTJ based on the AlOx barrier [47] and one year later in MTJs based on MgO [48–50]. Independently of the nature of the spacer (NM, amorphous, or crystalline oxide) between the two FMs, the spin transfer torque can be applied reciprocally on both FMs. With a non-magnetic metallic spacer, the spin-polarized electrons are extracted from a first magnetic body by spin accumulation at the interface with the spacer. If the spacer is smaller than the spin diffusion length, it reaches the interface of the other FM. At the NM/FM2 interface, the spin current ($\vec{Q}$) decomposed into longitudinal and transverse spin currents. Although the longitudinal spin current is conserved, the transverse spin current shows a discontinuity. By conservation of the spin-angular momentum, the missing transverse spin current must be transferred to the lattice of the ferromagnet. In fact,

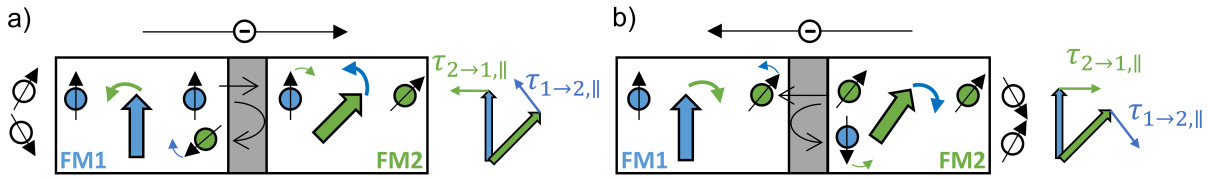

Figure 1.6: Schematic illustration the mutual STT between FM1 and FM2 for electrons flowing from FM1 to FM2 (a) and FM2 to FM1 (b).

the spin momentum carried mainly by the s-electrons ($\vec{s}$) transfers to the localized moment of the d-electrons ($\vec{S_d}$). The spin transfer torque is then related to this s-d coupling (J_{sd}) by the following relation.

$$\vec{T} = \vec{\nabla} Q = \frac{J_{sd}}{\hbar} \vec{S}_d \times \vec{s} \tag{1.13}$$

By analogy to classical mechanics, the torque on the magnetization can be expressed as a sum of an adiabatic (damping-like) $\tau_{\parallel}$ and a non-adiabatic (field-like) torque $\tau_{\perp}$. The term $\tau_{\parallel}$ is in the plane defined by the vector of the polarized current ($\vec{p} = \vec{m}_1$) and the magnetization ($\vec{m}_2$) while $\tau_{\perp}$ is perpendicular to this plane :

$$\tau_{STT,1\to2} = \gamma \vec{T} = \frac{\partial \vec{m}_2}{\partial t} = \tau_{\parallel} + \tau_{\perp} = -\gamma a_{\parallel} \vec{m}_2 \times (\vec{m}_2 \times \vec{p}) + \gamma a_{\perp} \vec{m}_2 \times \vec{p} \tag{1.14}$$

where $a_{\parallel}$ and $a_{\perp}$ are derived in case of MTJs as:

$$a_{\parallel} = \frac{\hbar \eta}{2e} \frac{1}{M_s t} \frac{1}{RA} V \tag{1.15}$$

$$a_{\perp} = c_1 V + c_2 V^2 \tag{1.16}$$

As reported in [51–53], the field-like torque can exhibit a symmetric (c_2 in Oe/V^2) and anti-symmetric (c_1 in Oe/V) component with respect to the bias voltage. In the case of p-MTJ, the field-like torque is most often neglected because it is much smaller than the adiabatic damping-like term [51, 53–55]. Note that the non-magnetic spacer is necessary to eliminate the direct coupling between the FM layers.

1.2.4 Magnetization dynamics

The minimization of the energies listed in Section 1.2.2 indicates the equilibrium state of the system, without describing how the system converges towards this equilibrium. The magnetization of the system follows the dynamics dictated by the Larmor equation (eq. 1.17), which describes the precession of the magnetic moment around the total effective field $\vec{H}_{\text{eff}}$. This effective field is derived from the total energy of the system in a macrospin approximation (Eq. 1.18).

$$\frac{\partial \vec{m}}{\partial t} = -\gamma \vec{m} \times \mu_0 \vec{H}_{\text{eff}} \tag{1.17}$$

$$\vec{H}_{\text{eff}} = -\frac{1}{\mu_0 M_s V} \frac{\partial E_{\text{tot}}}{\partial \vec{m}} \tag{1.18}$$

The Larmor equation is conservative, so the magnetization indefinitely undergoes a precessional motion around the effective field without reaching equilibrium. To account for dissipative phenomena such as magnon-magnon scattering, magnon-photon scattering, or eddy currents, Gilbert and Kelly [56] introduced a viscous term proportional to the derivative of the magnetization. The constant α is a dimensionless phenomenological constant, typically ranging from 0.001 to 0.1, known as Gilbert damping or magnetic damping. The complete set of phenomena that contribute to the origin of α remains a topic of ongoing debate within the scientific community. It is possible to transform the Gilbert equation (Eq. 1.19) in the form previously established by Landau and Lifshitz [57] (Eq. 1.20).

$$\frac{\partial \vec{m}}{\partial t} = -\gamma \vec{m} \times \mu_0 \vec{H}_{\text{eff}} + \alpha \vec{m} \times \frac{\partial \vec{m}}{\partial t} \tag{1.19}$$

$$\frac{\partial \vec{m}}{\partial t} = -\frac{\mu_0 \gamma}{1+\alpha^2} \left(\vec{m} \times \vec{H}_{\text{eff}} + \alpha \vec{m} \times (\vec{m} \times \vec{H}_{\text{eff}}) \right) \tag{1.20}$$

The STT adds a field-like and a damping-like contribution to the Landau Lifshitz Gilbert (LLG) equation to form the LLG-Slonczewski (LLG-S) equation. As mentioned previously, the field-like torque in the pMTJ structure is negligible compared to the damping-like torque. Thus, the LLG-S can be expressed in the LLG formalism (Eq. 1.21) and the LL formalism (Eq. 1.22) as:

$$\frac{\partial \vec{m}}{\partial t} = -\gamma \vec{m} \times \mu_0 \vec{H}_{\text{eff}} + \alpha \vec{m} \times \frac{\partial \vec{m}}{\partial t} - \gamma a_{\parallel} V \vec{m} \times (\vec{m} \times \vec{p}) \tag{1.21}$$

$$\frac{\partial \vec{m}}{\partial t} = -\frac{\mu_0 \gamma}{1+\alpha^2} \left(\vec{m} \times \vec{H}^*_{\text{eff}} + \alpha \vec{m} \times (\vec{m} \times \vec{H}^*_{\text{eff}}) \right) \text{ with : } \vec{H}^*_{\text{eff}} = \vec{H}_{\text{eff}} + \frac{a_{\parallel}}{\mu_0} V (\vec{m} \times \vec{p}) \tag{1.22}$$

Macrospin approximation

In ferromagnetic body, the demagnetization energy favors continuous reorientation of the magnetization according to its shape to minimize the self-magnetostatic energy. In contrast, the exchange energy promotes uniform magnetization of the magnetic body. The competition between the exchange energy of the ferromagnet and the demagnetization energy is characterized by the exchange length, which represents the smallest scale under which the magnetization cannot be twisted:

$$l_{\text{ex}} = \sqrt{\frac{2A_{ex}}{\mu_0 M_{\text{s}}^2}} \tag{1.23}$$

where A_{ex} is the exchange constant in J/m. The exchange length is close to 3 nm in CoFe and NiFe [58].

Two domains with opposite magnetization direction would lead to a reduction of the magnetostatic energy by closing the field lines, but also to an increase of the exchange and anisotropy energy by introducing a domain-wall (DW). If the anisotropy (K) is negligible, the magnetization can be non-uniform throughout the sample (curling, vortex state). If the anisotropy is dominant, as is the case in thin film with perpendicular magnetic anisotropy, the DW size is expressed as:

$$\lambda = \pi\sqrt{\frac{A_{ex}}{K}} \tag{1.24}$$

The size of the DW is typically 2 μm in NiFe, 64 nm in Fe and 24 nm in Co [58]. Magnetic domains can also result from an excess of energy introduced into the system when attempting to reverse magnetization. The DW is then nucleated and propagates until it is expelled. When the exchange constant (A_{ex}) is sufficiently strong such that the magnetostatic exchange length and DW size are large compared to the dimensions of the sample, the magnetization is approximately uniform over the volume (V) of the sample. Then it can be regarded as a single magnetic moment with fixed amplitude $\mu = M_s V$. This is referred to as the macrospin approximation if the magnetization dynamics is coherent.

1.2.5 Current-driven reversal mode in magnetic tunnel junction

Switching at 0 K

From the LLG-S equation, it is possible to derive the critical line for which the magnetization reverses, either by field or by spin transfer torque. Using the perturbation method, the critical limits at which magnetization becomes unstable are derived from the c-variable model [59]. The c variable is represented by the amplitude (p) and the phase (ϕ) of the oscillation of the magnetization precession around its effective field. The critical lines are defined by the stability equation of these oscillations ($\frac{dp}{dt} = 0$). It results in the following set of critical equations for out-of-plane magnetization dynamic with perpendicular uniaxial anisotropy :

$$\omega_H + \left(\frac{\omega_\parallel}{\alpha} - \omega_\perp\right) P_z - (\omega_M - \omega_A) = 0 \tag{1.25}$$

$$-\omega_H - \left(\frac{\omega_\parallel}{\alpha} - \omega_\perp\right) P_z - (\omega_M - \omega_A) = 0 \tag{1.26}$$

$$\omega_H - (\omega_M - \omega_A) P_z = 0 \tag{1.27}$$

$$-\omega_H - (\omega_M - \omega_A) P_z = 0 \tag{1.28}$$

$$\tag{1.29}$$

where $\omega_H = \frac{\mu_0\gamma}{1+\alpha^2} H_{app}$, $\omega_M = \frac{\mu_0\gamma}{1+\alpha^2} M_s$, $\omega_A = \frac{\mu_0\gamma}{1+\alpha^2}\frac{H_a}{2}$, $\omega_\parallel = \frac{\mu_0\gamma}{1+\alpha^2}\frac{a_\parallel}{\mu_0} V$, $\omega_\perp = \frac{\mu_0\gamma}{1+\alpha^2}\frac{a_\perp}{\mu_0} V^2$

The critical current density J_{c0} (or voltage V_{c0}) can then be extracted from this set of equation considering $H_{app} = 0$ and negligible field like torque :

$$J_{c0} = 2\frac{(-e)\alpha}{\hbar\eta}\mu_0 M_s\, t\, H_{\mathrm{K}} \tag{1.30}$$

$$V_{c0} = 2\frac{(-e)\alpha}{\hbar\eta}\mu_0 M_s\, t\, H_{\mathrm{K}}\, RA \tag{1.31}$$

$$\tag{1.32}$$

where $H_{\mathrm{K}} = \left(\frac{2K_i}{\mu_0 M_s . t} - M_s\right)$ and RA is the resistance area product of the system.

The approximation at zero temperature already highlights some quantities that play a role in the critical

switching current. A magnetic material with low damping and saturation magnetization is a way to reduce the critical switching current. Moreover, decreasing the effective anisotropy also reduces the critical current. In MRAM devices, this equation creates a trade-off between high stability and very low critical current. The thermal stability is directly proportional to the energy barrier E_b between the P and AP states, which also depend on the effective anisotropy: $E_b = \mu_0 M_s H_K V/2$.

Switching at T $\neq$ 0 K

When thermal excitation is considered, the transition between two states deviates from a deterministic process to a probabilistic one. Indeed, the energy ($k_B T$) provided by thermal agitation can be significant for a small magnetic volume. As the transition from one state to the other occurs below the critical current density defined by equation 1.30, the energy barrier (E_b) must be compared to the thermal energy to obtain the thermal stability (Δ) of the magnetic body: $\Delta = E_b/k_B T$. The distribution of the switching probability is derived by considering magnetic thermal noise as Brownian motion and is formulated by the Néel-Brown (NB) model [60]. This outcome is deduced from the transformation of the LLG equation with a stochastic (thermal) field to a Fokker-Planck equation. This model is valid for the cases where the energy barrier is significantly larger than the thermal agitation ($E_b \gg k_B T$).

The switching probability at time t in the thermally activated regime [60–62] is given by :

$$P(t) = 1 - \exp\left[\frac{t}{\tau_0}\exp\left(-\Delta\left(1-\frac{J}{J_{c0}}\right)\right)\right] \tag{1.33}$$

where τ_0 is the reciprocal attempt frequency, J_{c0} the critical current density, and J the applied current density.

For a current density greater than J_{c0}, the switching dynamics deviates from a purely stochastic process described by the Néel-Brown model. In that case, the main effect of temperature on the switching delay is through the initial angular position of the magnetization, noted θ_0. Considering a distribution of θ_0 around the direction of the easy axis, the mean switching time is recovered by averaging multiple trajectories [63, 64]. In this precessional switching regime, the switching probability as function of the current density applied is given by [65]:

$$P(t) = \exp\left[-4\Delta\exp\left(-2\frac{t}{\tau_D}\left(\frac{J}{J_{c0}}-1\right)\right)\right] \tag{1.34}$$

where the attempt frequency in the precessional regime is expressed as : $1/\tau_D = \alpha\gamma\mu_0 H_K$.

A gap still remains between these two regimes to explain the dynamics in the intermediate regime. Previous researches have attempted to link the various regimes into a single, unified model [66–69]. Lim *et al.* proposed a continuous expression to merge the precessional and thermal regime by introducing a new threshold current depending only on the material parameters. Vincent *et al.* [68] first defined the validity range for the thermal activated regime ($J < J_{\mathrm{NB}}$), when the effective energy barrier remains below a well-chosen value of 7.25 $k_B T$, and for the Sun model ($J < J_{\mathrm{Sun}}$)[63] when the switching time is below the stochastic Brownian time scale. Then, the expression in the intermediate model is approached by a polynomial function with a continuous and derivable transition towards the Sun's and Néel-Brown's model. Although the total expression fits the mean lifetime and the probability distribution of the macrospin model quite accurately, the use of additional arbitrary values (J_{NB}, ε) makes this model less attractive compared to others. Finally, as far as I know, this model has not been compared with experimental data to confirm the

quality of the fit. Another work worth mentioning at this stage is the paper of Tomita *et al.* in 2013 [65], where the authors went beyond a constant approximation of the characteristic time τ_0 to give an expression related to material parameters.

$$\tau_0^{-1} = \Omega\sqrt{\frac{\Delta}{\pi}}(1-h)(1-h^2) \tag{1.35}$$

$$\Omega = \alpha(-\gamma_0)H_K \text{ and } h = \frac{H_{ext}}{H_K} + \frac{I}{I_{c0}} \tag{1.36}$$

where H_K is the anisotropy field. The unified model proposed by Tomita *et al.* uses the same physical parameters in the thermally activated and precessional regime, but still presents a discontinuity at the intermediate switching range. More recently, Yang *et al.* [69] combined the two regimes with a single expression by the mean of the spin-torque intensity k. The latter evaluates how much the precessional regime takes over the thermal mode in the intermediate regime. The unified model is given by the following equations:

$$\tau = \frac{k\,\Delta\,B + A\,\exp\left((1-k)\,\Delta\,j\right)}{\ln\left(1+\exp\left(-k\,\Delta\,j\right)\right)} \tag{1.37}$$

$$A = -\tau_0\,\ln(1-P) \tag{1.38}$$

$$B = \frac{1}{2}\,\tau_D\,\ln\left(-\frac{4\,\Delta}{\ln(P)}\right) \tag{1.39}$$

$$j = \left(1 - \frac{J}{J_{c0}}\right) \tag{1.40}$$

Yang *et al.* correlate their model with experimental data in the literature for spin-valves [65, 70] and MTJ structures [71]. Interestingly, the authors note that the value k is inversely proportional to the spin torque efficiency ($k \propto 1/(\Delta/I_{c0})$). Devices having higher spin-torque efficiency are prone to show more thermally driven dynamics in the intermediate regime compared to devices with poor efficiency. We choose to use the Yang *et al.* model for the characterization of MTJ devices in Chapter 5 because of its single expression to describe the entire switching time range.

1.3 Neural Networks

1.3.1 From Von Neuman architecture to neuromorphic computing

The field of artificial intelligence (AI) has been a rich and extensive area of study for more than four decades, encompassing the development of systems capable of emulating tasks typically associated with human intelligence. Within this wide domain (see Fig. 1.7), *machine learning* relies on extensive data sets to facilitate its learning process. *Deep learning* specifically targets algorithms structured around neural networks, where *deep* denotes a significant number of layers of neurons [72, 73]. These networks can be classified into two main classes: artificial neural networks (ANNs), which are traditional formal models, and spiking neural networks (SNNs), which operate in an event-driven manner. Although ANNs have served as foundational elements in machine learning since their inception, SNNs represent a more recent advancement, with initial reports emerging approximately two decades ago [9].

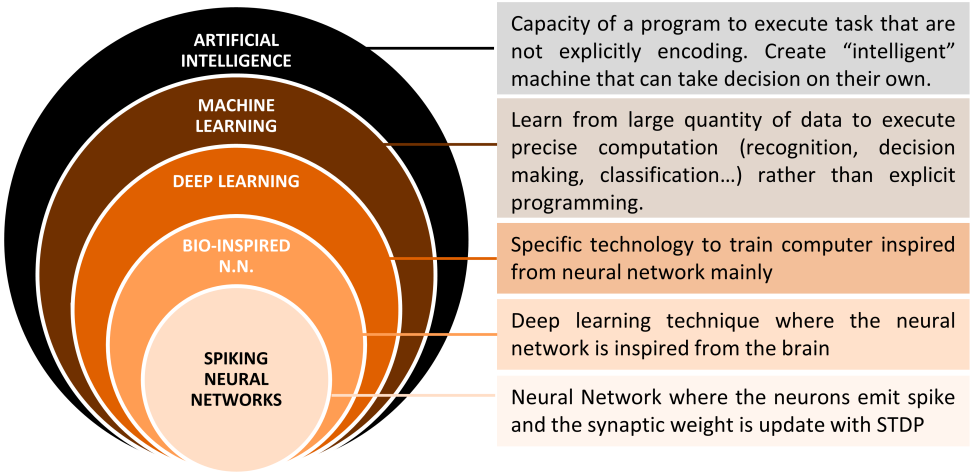

Figure 1.7: Schematic of the different concepts encompassed by the artificial intelligence realm.

Looking back to the twentieth century, neuroscientists have provided important information on how neurons and synapses behave in the brain and from which SNNs took inspiration. Pioneer works by Ramon y Cajal in 1909 [74] reported neuronal structures observed under the microscope, and Lapicque in 1907 [11] introduced a phenomenological model close to the leaky integrate and fire model commonly used nowadays as a simplification of membrane potential dynamic. Later, Hogkin and Huxley [75] successfully measured the currents resulting from an action potential passing through the ion channel of the cell membrane. In 1952, their experimental work was published along with an elegant mathematical description of the ions' dynamics through differential equations. This groundbreaking work was recognized by the community and led to a Nobel prize in 1963. Wolfgang Maass's paper grouped the recent advances of the neuroscientist community at that time, highlighting that many biological neural systems use the timing of single action potentials (*spikes*) to encode information. In particular, W. Maass evaluates the benefit of building SNNs showing that they exhibit computational capabilities at least equal to those of ANNs [9]. Beyond the curiosity of neuroscientists to understand how the brain works, or at least some regions, neural networks attracted strong interest from the computer science community to overcome some limitations of the current computer architecture. Indeed, the actors in the CMOS industry are facing difficulties in down-scaling the elementary build block (transistor) [76] of all processors, in addition to the bottleneck experienced between the memory

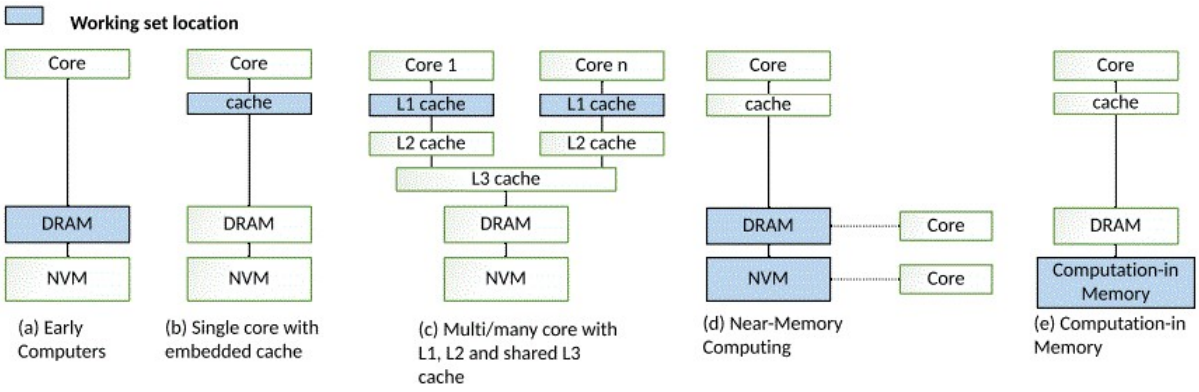

Figure 1.8: Prior systems were based on a CPU-centric approach where data is moved to the core for processing (a-c), whereas with near-memory processing (d) the processing cores are brought to the place where data resides. Computation-in-memory (e) further reduces data movement by using memories with compute capability. Illustration extracted from Singh *et al.* [77]

and the computing unit inherent to the Von Neumann architecture. In this architecture, both the data and the processing instructions are stored in the same memory system. This means that to perform tasks, the central processing unit (CPU) must constantly switch between processing data and retrieving instructions from the memory (Figure 1.8. ab). As CPU speeds and memory capacities have seen rapid growth compared to the throughput that connects them, the bottleneck issue has become more and more pronounced.

Architectures with computation in parallel and multicore processors (Figure 1.8.c) naturally arise from this problem, but do not solve it completely. The recent development of *near-memory computing* [77, 78] aims to bring the computing unit closer to memory and minimize expensive data transfer (Figure 1.8.d). Finally, the ultimate goal is certainly a *in-memory computing* approach [79–81] where data are calculated directly at its storage location (Figure 1.8.c). As neural networks need access almost constantly to memory, their evaluation in a traditional computer architecture requires an extreme amount of time and power. Subsequently, hardware engineers focused their effort on the creation of dedicated accelerators optimized for the execution of such algorithms. The hardware spiking neural network seems to be a good candidate at the cross-roads of artificial intelligence routes and the new area of in-memory computing.

Before describing the recent hardware development of SNNs, the next section explains their basic working principle, starting with the neuron, the synapse, and finally the overall neural network.

1.3.2 Building blocks of SNN : neurons and synapses

The elementary building blocks of a neural networks, regardless of its classification, rely on neurons, also called perceptrons, and synapses making connection between neurons. The brain comprises 86 billion neurons and synapses intricately interconnected in 3-dimensions. Different types of architecture co-exist in the brain dedicated to solve specific tasks. We propose here a basic description common to all types of spiking neurons [82] and their interconnection through synapses (Figure 1.9.a). Information transmission in our brain occurs in the form of discrete electrical events known as spikes, which are emitted by neurons when their chemical potential exceeds a given threshold [83]. Assuming that a presynaptic neuron emits a spike toward a second postsynaptic neuron, the synapse between them responds differently based on its type. Inhibitory synapses release glutamate neurotransmitters, inducing the influx of positively charged ions (Na^+,

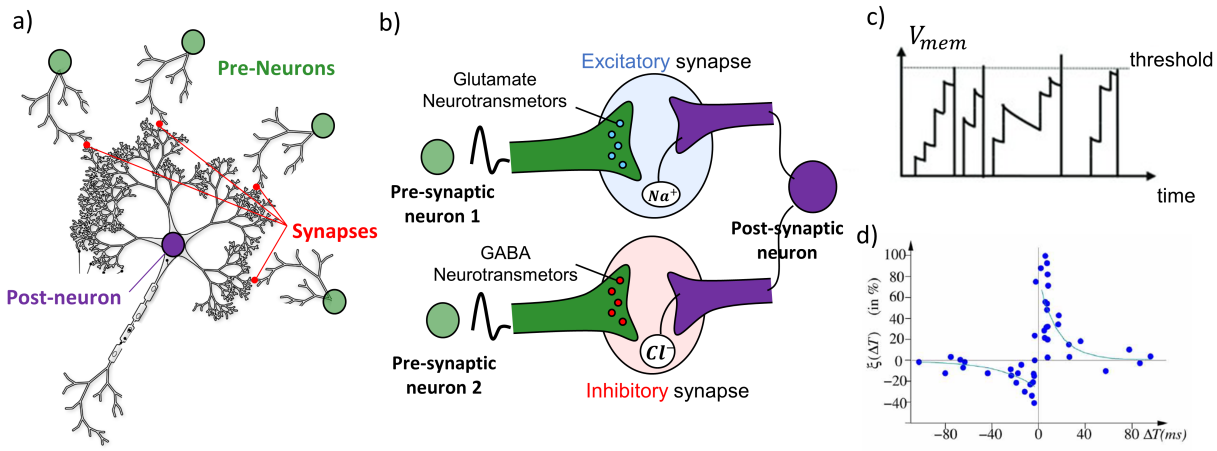

Figure 1.9: a) Neuron schematic representation, b) excitatory and inhibitory synapses, c) leaky integrate-and-fire model representation. (d) Experimentally measured spike-timing dependent plasticity function on biological synapses (data from [85, 86])

Ca^{2+}) into the dendrites of the post-synaptic neuron, thus increasing its membrane potential. On the contrary, excitatory synapses release GABA neurotransmitters, allowing only negatively charged ions (Cl^{-}) to enter the dendrite of the post-synaptic neuron, resulting in a reduction in membrane potential (Figure 1.9.b) If the post-synaptic neuron accumulates a sufficient quantity of positive charges from all connected neurons through its dendrites (inputs), it produces spikes that propagated along its axiom (output) subsequent neurons in the network. A neuron naturally returns to its resting potential if it is not subjected to incoming spikes. After spiking, the neuron is locked to its resting potential for a given period of time (refractory period). The evolution of the neuron membrane potential is synthesized by the *leaky integrate and fire* (LIF) model [11, 84] illustrated in Figure 1.9.c, which can be expressed as :

$$C\frac{\mathrm{d}V(t)}{\mathrm{d}t} = I(t) - \frac{V(t)}{R} \tag{1.41}$$

where C is the cell membrane capacity, V the voltage across the membrane, R the membrane resistance and I the input current. This equation is for the evolution of the membrane potential below the threshold voltage where the spike is produced. After that, a refractory period is generally added.

Although the neuron is the core of the processing part in all topologies of neural networks, synapses carry the memory function in their synaptic *weight*. These changes in synaptic weight are believed to be a key mechanism in memory formation and learning new information. It allows the brain to adapt and rewire its neural networks in response to experiences and stimuli. From a biological point of view, synaptic weight can change through a process known as synaptic plasticity. Long-term potentiation (LTP) increases the connection between two neurons by enhancing neurotransmitter release and dendritic receptor sensitivity. In contrast, long-term depression (LTD) occurs when a presynaptic neuron is consistently active, but the postsynaptic neuron is only weakly stimulated, leading to degradation of dendritic receptors, fewer neurotransmitters, and therefore weak synaptic connection [85, 87]. The Hebbian theory [86] that attempts to formulate the potentiation and depression mechanism of synapses in a neural network can be summarized as "*those (neurons) who fire together, wire together*" and "*those who (neurons) fire out of sync, lose their link*". According to this rule, *spike-timing-dependent plasticity* (STDP) uses the relative time between presynaptic

and postsynaptic neurons to mediate the strength of the synaptic connection [88, 89]. When the presynaptic neuron fires before the postsynaptic neuron ($\Delta T > 0$), it leads to an increase in synaptic weight due to this causal relationship. On the contrary, if the post-synaptic neuron fires before the pre-synaptic neuron ($\Delta T < 0$), indicating an anti-causal sequence, it results in a decrease in synaptic weight. The variation of synaptic weight (in%) is represented by the curve in Figure 1.9.d as a function of the time delay between spikes, observed experimentally in [85, 86].

1.3.3 Working principle of spiking neural networks

In SNNs, neurons are organized into layers and each layer is connected via synapses to the next layer. If each and every neuron of layer *i* is connected to all neurons in layer *i+1*, the network is called *fully connected*. This is the most common topology of neural networks. Propagation of information in SNNs is performed through spikes. The neuron stores the signals coming from its inputs and fires if all conditions have been met according to the LIF model. The STDP learning rule described above adapts the weight of the synapses. As this learning mechanism depends only on the pre- and post-synaptic neurons, it is called a "local" learning rule and often comes along with an unsupervised learning approach. On the contrary, a more classical learning uses a back-propagation of the error with respect to the correct answer to update the synaptic weight. This approach is non-local and often needs supervision to validate or annihilate the prediction of the NN. Another advantage of spiking neuronal networks is the extraction of time-dependent information from the data as temporal coding is intrinsically used in SNN [90]. However, most of the tests to evaluate NN performances are based on static entries (MNIST), not especially devoted to SNN application where they are expected to perform better than former ANN as underlined in Bouvier *et. al.* [91]. The binary nature of the SNN also simplifies the realization of the hardware NN imposing a constant (binary) output voltage or current. In addition to that, the sparsity of the SNNs, which is related to the fraction of neurons that are active at any given time, is also a non-negligible advantage when considering the energy efficiency of the neural network. As neurons are only active during the spiking time, low power consumption is expected for this type of NN. However, a direct comparison in energy efficiency is still an open question in the neuromorphic computing community because it strongly depends on the hardware on which the network is mapped and on the task to be solved [91]. Recent work [92] highlights some benefits of the SNN in terms of energy efficiency compared to the ANN.

1.3.4 Hardware implementation of spiking neural networks

CMOS-based technology for SNNs

It is possible to identify four major neuromorphic accelerators that are designed to perform SNN simulations with a very extensive structure. These computing platforms contain many cores on-chip and multichip configurations, taking advantage of running many computations in parallel. They are often configurable in different ways and versatile for different tasks. The most famous large-scale accelerators are SpiNNaker [14], TrueNorth [12], Neurogrid [15] and Loihi [13]. They are expected to show high throughput and scalable architecture. A summary of their characteristic is shown in table 1.1.

Despite the demonstrated performances of all those CMOS-based approaches, the learning is done either off-chip (TrueNorth, SpiNNaker, Neurogrid) or using STDP without back-propagation of the error. In particular, those platforms do not take advantage of the SNN potential for treating spatio-temporal data. More intensive comparisons can be found in the literature [16, 72, 73, 90, 91, 93].

Processor	SpiNNaker [14]	Neurogrid [15]	TrueNorth [12]	Loihi [13]
Implementation	Digital	Analog	Digital	Digital
Technology	130 nm	180 nm	28 nm	14 nm
Weight resolution	8b-32b	13b	1b-4b	1b-64b
Online learning	Yes	No	No	Yes
Neurons per cores	1000	65 000	256	1024
Cores per chip	16	1	4096	128
Energy/synaptic event (pJ)	27 000	941	26	15

Table 1.1: Comparison of four large scale hardware SNNs, adapted from [93]

Spintronic solutions for synapses

Synapses play the role of memory in all the different topologies of neural networks. Although multilevel synaptic weights are interesting for neural networks in general, more basic *binary* synapses, with only two resistance levels, have already demonstrated their efficiency in neural networks [94–97]. STT-MRAM technology already provides this binary synaptic weight and some architectures have emerged to use it as stochastic memristive synapses [98] in emulated spiking neural networks. The integration of spintronic-based devices and especially DW-driven dynamics for synaptic and neuronal functionalities was already initiated in 2012 by M. Sharad *et al.* [99]. Further investigations finally propose a spin-torque memristor based on DW propagation in p-MTJ [18] to emulate multi-level synapses (Fig. 1.10.a.b.c). Depending on the position of the DW in the free layer, the devices show different resistance levels. More recently, a concept based on in-plane MTJs with variation in the relative angle between the free layer (FL) and the reference layer (RL) also demonstrates continuous variation in resistance in response to successive electrical pulses [17, 100] (Fig. 1.10.d.e). Similar results were achieved in the free layer with granular structure in p-MTJ [101].

The possibility of using the crossbar architecture with MTJ is a strong advantage to realize matrix-vector multiplication of synaptic weight from one neuron layer to the next [98, 102, 103].

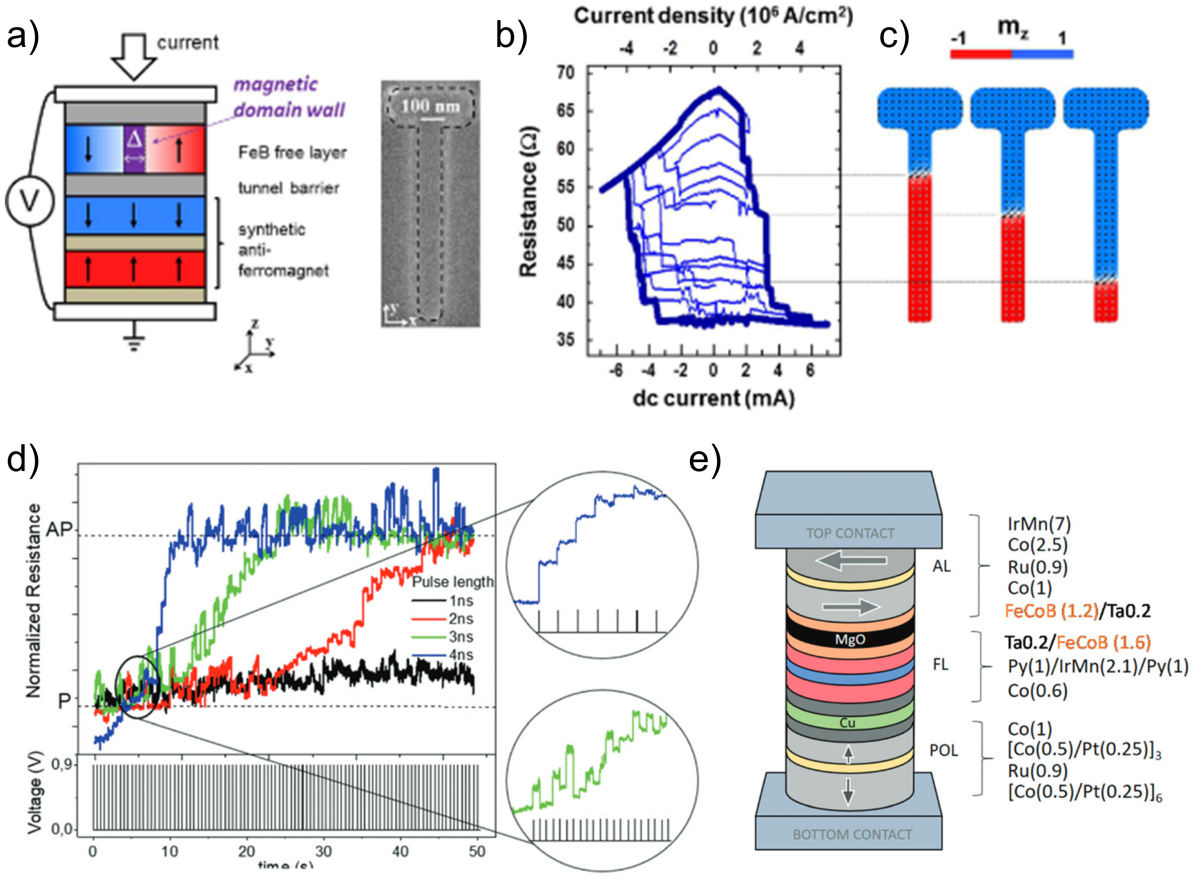

Figure 1.10: (a) Schematic of the MgO based magnetic tunnel junction with the DW in the FeB free layer (left) and Scanning electron microscope image of the sample (right). (b) Resistance as a function of the vertically injected DC current measured in an external field H_z = 85 Oe. (c) Micromagnetic simulations of the DW propagating in a magnetic track of 100 nm width. (a-c) Illustrations extracted from S. Lequeux *et al.*[18]. (d) Resistance variation due to a 0.9 V pulse train with varying pulse durations and a 1 s delay between two consecutive pulses. (e) Schematic of the memristive device for the demonstration in (d). (d-e) Illustrations extracted from Mansueto *et al.* [17]

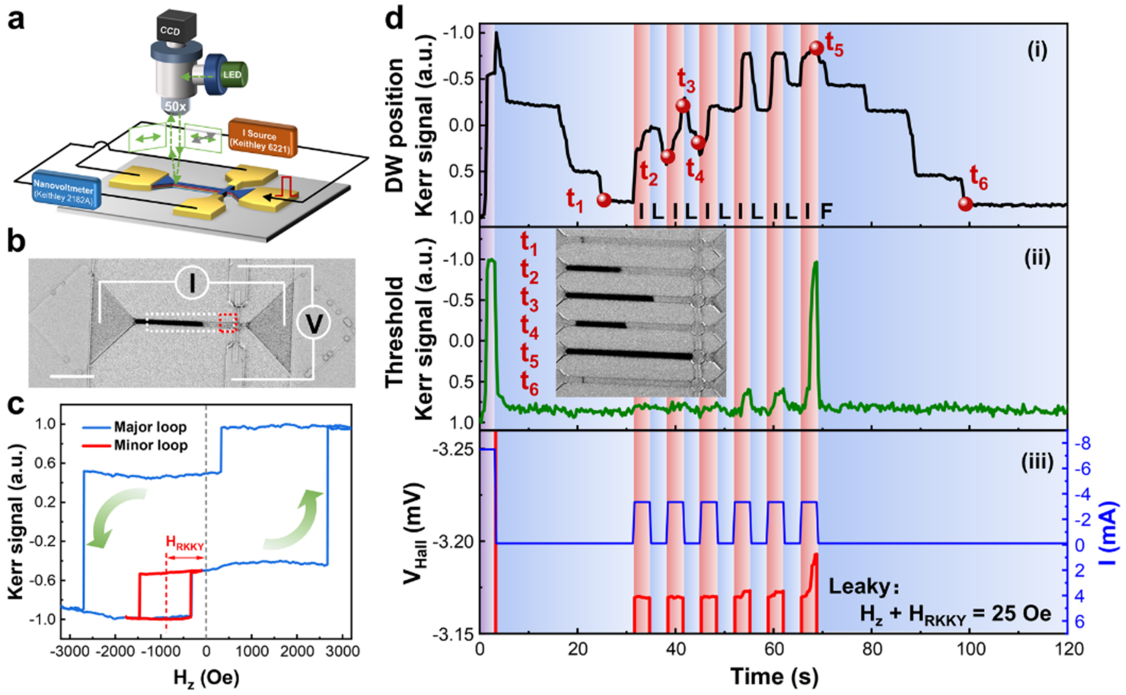

Figure 1.11: (a) Schematic of p-MOKE setup for in-situ magneto-electrical transport probing. (b) Kerr image with the white dashed box indicating the domain-wall (DW) stripe and the Kerr signal in (d.ii), red dashed box refers to the threshold region and the corresponding Kerr signal in (d.ii). The scale bar is 20 μm. (c) Major K-H loop of the device. H_{RKKY} refers to the effective field of the RKKY interaction and is equal to 885 Oe. (d) Dynamic DW motion emulated LIF processes under an applied field that partially compensates H_{RKKY} with an effective net field of $\approx$25 Oe. Dynamic DW motion processes are recorded at different stages as depicted in (d.i), the reversal characteristics of the threshold region in (d.ii), and the anomalous Hall voltage under associated applied current pulses in (d.iii). Illustrations are extracted from [104].

Spintronic solutions for spiking neurons

Concerning the spintronics-based approach to mimic the functionality of the spiking neurons, only a few researches have proposed hardware solutions to date. D. Wang *et al.* [104] studied the use of DW propagation on a magnetic track to emulate the integration of input spikes. In particular, they demonstrate leaky integrate-and-fire (LIF) function without the need of external reset (see Fig. 1.11). The solution proposed in the paper is appealing despite the relatively large dimension of the device, which is not easily scalable, and the use of an external magnetic field. A. Sengupta *et al.* [105, 106] emulates a stochastic spiking neurons with a spin-orbit torque (SOT) MTJ promising for implementation in cross-bar architecture and also explore the use of SOT-MTJs for short-term and long-term stochastic synapse [107] with STDP learning rule. These simulations studies based on spintronics devices paves the ground for more experimental demonstrations. Another modeling study by D.R. Rodrigues *et al.* [108] explores a new concept of spiking neurons based on MTJ without a resetting procedure and capable of emulating the bio-realistic spiking behavior analogous to the Hodgkin-Huxley model of the neuron. However, this simulation work relies on slight temperature variation (+/- 1 °C) which seems complicated to physically control in a fabricated device.

1.4 Literature review on dual free layer structure

A dual free layer structure is composed of two ferromagnetic material separated by a spacer which can be either a insulating material in case of MTJ, or, a non-magnetic metallic material for a spin-valve structure. The relatively low stability of the FM layers on both sides of the spacer makes them switchable by STT. This section highlights some interesting studies related to the dynamics in dual free layer systems. Despite the different targeted applications behind these studies, they rely on dynamics similar to the one demonstrated in this thesis.

1.4.1 Modeling perpendicular and in-plane dual free layer MTJ

The pioneer study by Matsumoto *et al.* [22] on the dual free layer magnetic tunnel junction (DFL-MTJ) predicted this windmill dynamic in simulation. From this paper, micromagnetic and macrospin simulations show the windmill dynamic in various structures of DFL-MTJ: in-plane DFL-MTJ, out-of-plane DFL-MTJ, and in-plane DFL-MTJ with SAF. In all the structures, it seems that it is possible to excite the windmill dynamic state with more chaotic behavior obtained in the in-plane structure. The spike-like dynamic is achieved mainly with the perpendicular configuration, whereas the in-plane structure shows more precessing motion before the spiking event. The values used in the Matsumoto paper are quite far from the value we expect to find in an MTJ. In fact, the saturation magnetization used is 200 kA/m, whereas the FeCoB layer in p-MTJ shows values closer to 1250 kA/m. As will be described in the next section, high saturation magnetization makes the windmill motion more difficult to generate. Also, something important to mention is the formation of the windmill dynamics in both polarities at the same absolute value of the current density.

1.4.2 Experimental evidences of windmill dynamics

R. Choi *et al.* [109] demonstrate the windmill dynamics in the MHz range in the spin-valve structure. Although the spin-valve configuration is interesting, it does not provide a very high magnetoresistance ratio (GMR 4%) and resistance value. The spin-valve structure is composed of [Co(0.3nm)/Pd(0.7nm)]x2,[Co(0.15nm)/Ni(0.6nm)]x2, Co(0.3nm), Cu(4nm),[Co(0.15nm)/Ni(0.6nm)]x2, [Co(0.3nm)/Pd(0.7nm)]. The authors could only experience oscillations in one polarity of the current, claiming a very asymmetric spin-torque efficiency depending on the direction of the current. The spin torque efficiency is higher in the layer that received the electrons after the spacer compared to the one from which the electrons become spin polarized. The current density applied in this type of device is around $2.10^8 A/cm^2$ to generate windmill dynamics.

L. Thomas *et al.* [110] showed oscillations in the MHz range on a conventional STT-MRAM device (Fig. 1.14.a). Electrical characterization of this type of device at high voltage bias shows interesting oscillation behavior, as illustrated in Fig. 1.14.b. In this short abstract [110], the authors raise the importance of the coupling between the hard layer and the reference layer of the SAF which seems to play a role in the dynamic. If the coupling is too weak, only the RL of the SAF switches while the hard layer is fixed. On the other hand, if the coupling is strong, all the SAF is reversed during the windmill dynamic.

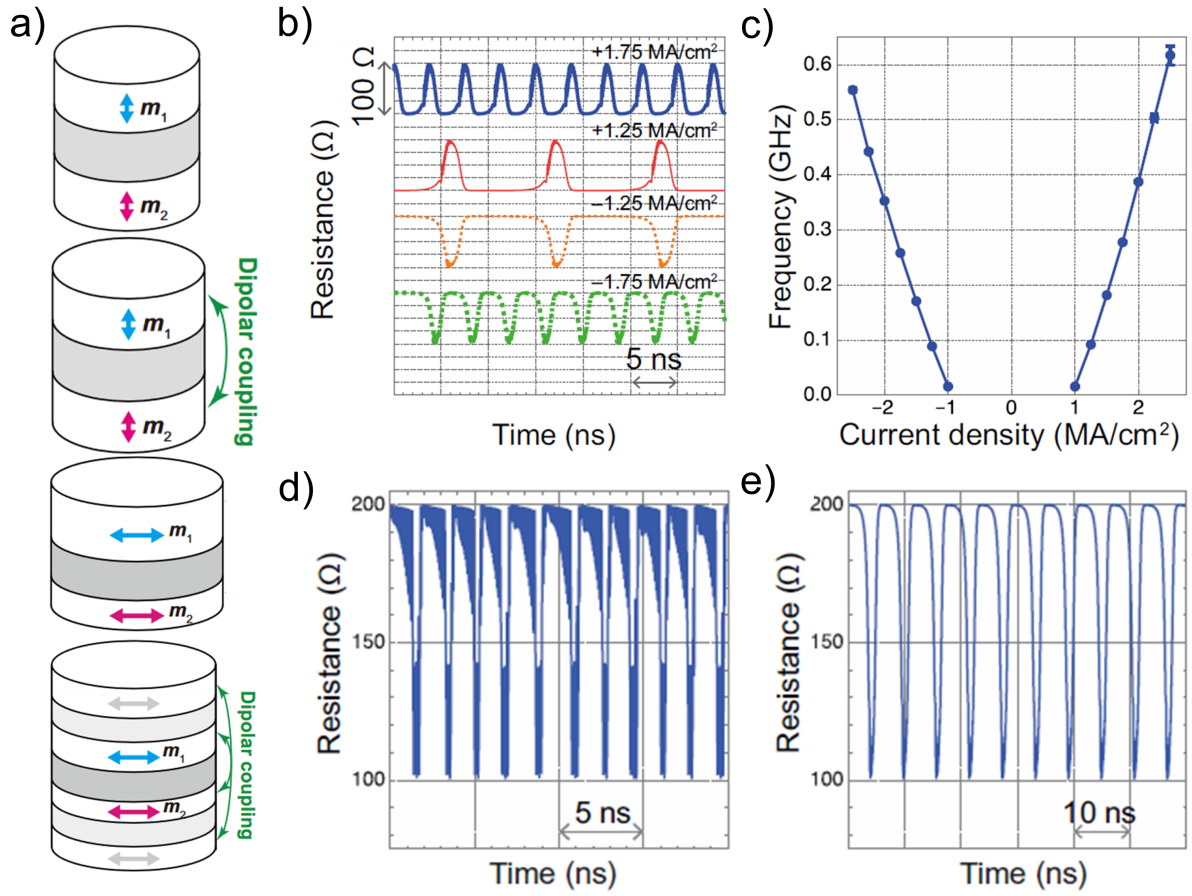

Figure 1.12: (a) Dual free-layer p-MTJ and in-plane MTJ used for the simulation studies. (b) Simulated time traces and the corresponding windmill frequency (c) as a function of the applied current density. Simulated time traces with in-plane (d) and out-of-plane (e) MTJ showing windmill dynamics in both cases with sharper switches for the out-of-plane configuration. (b-e) Figures extracted from R. Matsumoto *et al.* [22].

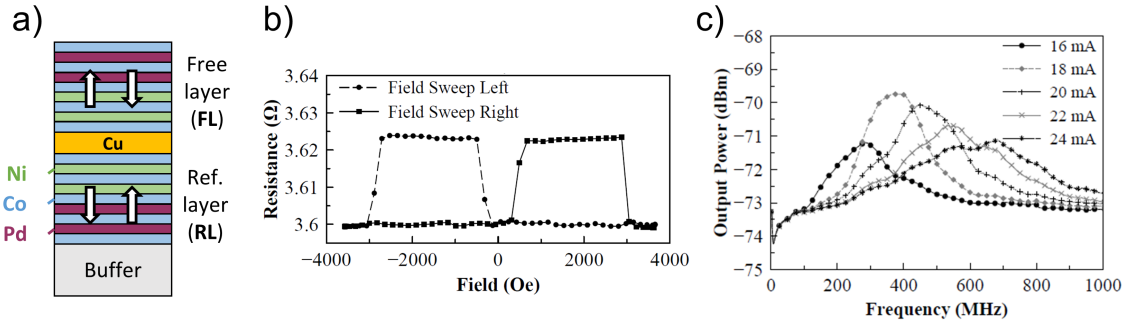

Figure 1.13: (a) Spin-valve structure made of multilayers of Pd / Co and Ni / Co used by R. Choi *et al.* [109] to demonstrate windmill dynamics. (b) Resistance versus field loop of a 120 nm circular nanopillar and (c) output power of the device for various currents below 1.1 kOe of applied magnetic field, extracted from R. Choi *et al.* [109].

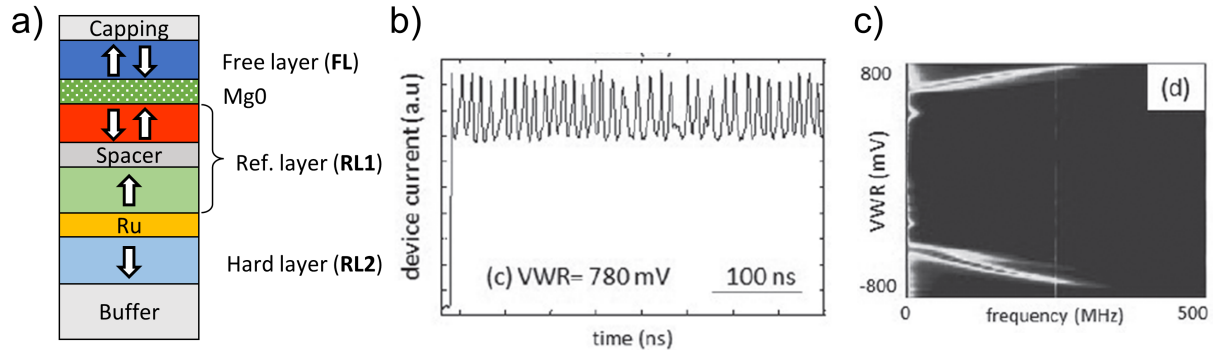

Figure 1.14: (a) P-MTJ with SAF used in L. Thomas *et al.* [110] to show perpetual switching of FL and RL1 layer. Figures extracted from the paper: (b) Time-resolved measurement of the dynamic under 780 mV of voltage bias and (c) spectrum of the signal acquired for different values of voltage bias. (b-c) are illustrations extracted from L. Thomas *et al.* [110].

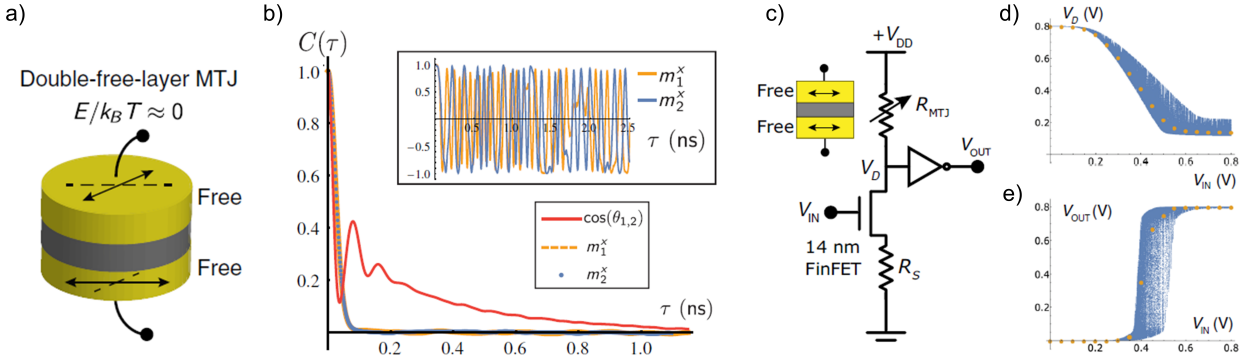

Figure 1.15: (a) Double-free-layer structure where the magnetization of the free layers fluctuates in the plane in the presence of thermal noise. (b) The normalized auto-correlation of m^x for both layers and $\cos(\theta_{1,2})$ are shown for 2R = 10 nm as an example.(c) The double free-layer MTJ in a 1T-1MTJ circuit, where a $R_S = 5k\Omega$ resistance is used to shift the overall characteristics. (d) The drain voltage is measured while the input is swept from 0 V to 0.8V over 0.5 μs. Illustrations are extracted from K. Camsari *et al.* [111].

1.4.3 Dual free layer MTJ for stochastic computing

K. Camsari *et al.* [111] investigated the double free-layer structure with in-plane magnetization as a building block for stochastic computing. As the two free layers are unstable at room temperature without any external excitation (field or voltage), the switching regime is systematically dominated by thermal energy. The rate at which the two layers decorrelated from each other is shown in Fig. 1.15.b) using the auto-correlation function of the cosine angle (i.e., MTJ resistance) of the signal. As we can see, the auto-correlation falls close to 0 within 1 ns, meaning that the resistance of the MTJ at time *t+1* ns cannot be predicted knowing the resistance at time *t*. If one were to get a sampling every 1 ns in the device, we would obtain an excellent randomness. However, many intermediate resistances appear in the signal, and a binarization step would be necessary in hardware development. Furthermore, a ratio of 50% between the P and AP states is not easily achievable in a nanopillar device without external compensation. In the case of in-plane configurations, the dipolar field between the layers favors their antiparallel alignment.

Chapter 2

Experimental techniques

Contents

2.1 Introduction

From material growth to electrical characterization of the MTJ pillars, this chapter presents the techniques needed to understand the magnetic and electrical properties at the thin-film and device levels. Thin-film characterization techniques, such as magneto-optical Kerr effect, vibration sample magnetometer, and ferromagnetic resonance setup, are detailed for characterization at sheet film sample. Then, the nanofabrication process flow summarizes the important steps in turning those wafers into nanodevices. Finally, the quasi-static and time-resolved measurement setups provide access to the electrical current transport properties of the MTJ pillars.

2.2 Magnetic stack deposition

The magnetic thin films developed, studied, and presented in this thesis were deposited by Stephane Auffret with a DC magnetron sputtering technique at Spintec. This specific physical vapor deposition method relies on the induction of a plasma from heavy and inert materials such as Ar (Ar). After stabilizing a high vacuum inside the chamber, typically ranging from 10^{-6} to 10^{-9} mbar, a controlled pressure system allows the introduction of gas around 10^{-3} mbar. The inert material ionizes with the applied high voltage (in the kV range) between the cathode behind the target and the anode grounded to the chamber. Positive heavy charges (Ar+) are drawn towards the cathode and subsequently collide with the target material, causing its particles to be expelled into the vacuum and deposited on the substrate. A distinguishing feature of this technique is the application of a magnetic field within the chamber, which confines electrons to a relatively small area near the target. This enables the creation of a denser plasma, leading to an increased deposition rate. Furthermore, the quality of the deposited films is enhanced because the magnetic field prevents interference between the electrons and both the substrate and target particles during the deposition process.

The deposition machine contains a load-lock chamber, in which the 25 wafers can be loaded at once, a main chamber for material deposition, and a treatment chamber for oxidation and etching. It is important to note that because of the separation between the targets in the main chamber, simultaneous co-sputtering of two materials is not possible. Consequently, the deposition of different materials must be performed sequentially, one target at a time. To obtain an MgO layer, we first deposited a metal layer of Mg in the main chamber before the wafer was exposed to oxygen in the treatment chamber. Precise control of the oxidation state is achieved by regulation of the oxygen pressure and exposure time within the treatment chamber. Additionally, for the deposition of a uniform thin film on a 4-inch wafer, the rotating sample holder is placed directly beneath the target. However, it is important to note that despite the effort to achieve uniformity, there is still a slight non-uniformity of 10% to 15% at the edges of the wafer. In contrast, to deposit a wedge of material thickness along a particular direction of the wafer, a different approach is used. The sample is deliberately displaced off-axis and the rotation is stopped. Using this technique, we can reach a ratio of 2 between the maximum and minimum thicknesses on the wedge.

2.3 Thin film characterization

2.3.1 Magneto-optical Kerr effect

The magneto-optical Kerr effect magnetometer (MOKE) was used to characterize magnetic materials at the thin-film level. This tool offers the advantage of rapidly mapping large wafers (4 inches). Using wedges, as described in the preceding section 2.2, it becomes particularly helpful to understand the influence of material thickness on magnetic properties. The MOKE setup, illustrated in Fig. 2.2, involves a laser beam initially polarized in the p direction, which upon reflection from the sample acquires an s-polarization component. The analyzer filters out the s component and the p component is measured with the detector. The intensity shift between the incident and reflected laser beams reveals alterations in the magnetization direction and/or amplitude. According to Maxwell's equations [23], light is an electromagnetic wave that can be fully described by its frequency and time-dependent electric field **E**. The latter can be decomposed into two modal amplitudes ε_s and ε_p along their modal vector polarizations $\overrightarrow{s}$ and $\overrightarrow{p}$ that are orthogonal to each other:

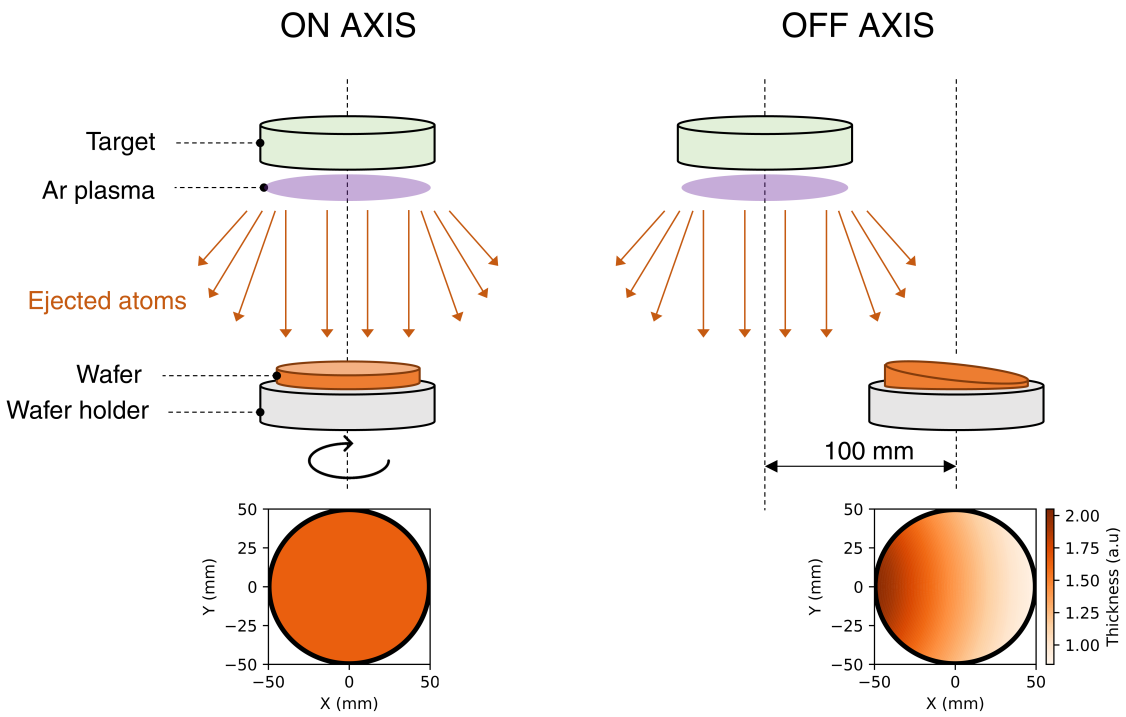

Figure 2.1: DC Magnetron sputtering technique with ON axis (left) and OFF axis (right) deposition setting. By using OFF-axis deposition, a gradient of thickness appears along one wedge of the sample. By rotating the sample about 90°, a second gradient of thickness can be obtained in the cross direction.

$$E_\omega = \varepsilon_s . \overrightarrow{s} + \varepsilon_p . \overrightarrow{p} \tag{2.1}$$

The time evolution of the electric field completely characterizes the polarization of light, also referred as *ellipticity* due to the shape of the electric field trajectory. The azimuth (denoted as θ in Fig. 2.2.b) refers to the rotation angle between the principal axis of the polarization ellipse and the s direction, while the ellipticity (ε in Fig. 2.2.b) refers to the relationship between the minor (b) and major (a) axes of the polarization ellipse ($\tan\varepsilon = b/a$).

When a laser beam interacts with a magnetized sample, the azimuth and ellipticity change according to the reflection coefficients synthesized in the reflection matrix Eq.2.3. In case of a polar Kerr effect (magnetization along the normal of the sample and in the scattering plane), r_{sp} and r_{ps} are identical. The analyzer projects the reflected signal in the p direction to filter out the s component. Finally, the signal acquired by the detector provides the Kerr rotation θ (i.e., the real part of the MOKE signal Φ_p). Given that the magnetization of the sample along z is proportional to the Kerr rotation, hysteresis loops can be obtained by sweeping the field during the measurement.

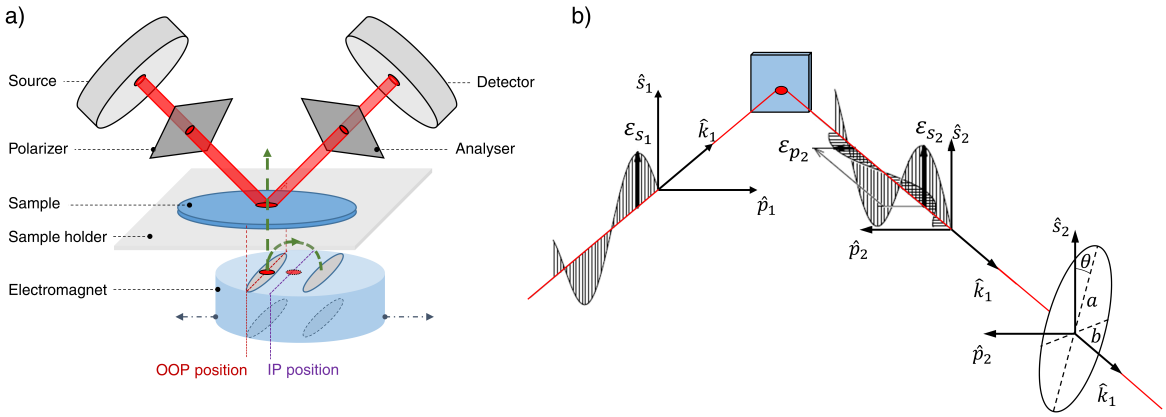

Figure 2.2: (a) NanoMOKE measurement set-up and (b) schematic of the Magneto-optical Kerr effect where the incident light is *s*-polarized and acquires a *p*-polarization component when hitting the sample.

$$\begin{bmatrix} \varepsilon_{s,2} \\ \varepsilon_{p,2} \end{bmatrix} = \begin{bmatrix} r_{ss} & r_{sp} \\ r_{ps} & r_{pp} \end{bmatrix} \begin{bmatrix} \varepsilon_{s,1} \\ \varepsilon_{p,1} \end{bmatrix} \tag{2.2}$$

$$\Phi_p = \frac{\varepsilon_{s,2}}{\varepsilon_{p,2}} = \frac{r_{sp}}{r_{pp}} = \theta + i\varepsilon \tag{2.3}$$

From the curves obtained by MOKE measurement, we can extract the thickness of the dead layer and the interfacial anisotropy assuming a constant M_s. The relation between the interface anisotropy K_i, the saturation magnetization M_s, the effective thickness t_{eff}, and the effective anisotropy energy density K_{eff} is defined by :

$$2.K_{\text{eff}}.t_{\text{eff}} = 2\ K_i - \mu_0.M_s^2.t_{\text{eff}} \tag{2.4}$$

The first step is to calculate the thickness of the dead layer t_{DL} from the evolution of the magnetization amplitude with respect to the total FM thickness. As the magnetic volume grows linearly with respect to the thickness of the FM in the region of 100 % of remanence, the dead layer is extrapolated from the intersection of this linear fit with the total FM thickness axis, as illustrated in Appendix 8.1. The effective thickness t_{eff} is recovered by subtracting the thickness of the dead layer from the nominal thickness of the layer. We note here that the amplitude of the MOKE signal is proportional to the saturation magnetization of the FM layer but does not allow for a direct measurement of it.

The second step is to calculate the effective anisotropy energy density K_{eff}. For ferromagnetic materials, the anisotropy energy E_{anis} is defined by the area under the M-H curve (see Fig. 2.3.a). The energy density K_{eff} is derived by dividing over the volume :

$$E_{anis} = \int H(M)\,\mathrm{d}M \tag{2.5}$$

$$K_{\text{eff}} = \frac{1}{V}\int H(M)\,\mathrm{d}M \tag{2.6}$$

The integration of the normalized Kerr signal gives directly the anisotropy field H_K :

$$H_K = \frac{2\ K_{\text{eff}}}{\mu_0 M_s} = \frac{K_{\text{eff}}}{V\ \mu_0 M_s} \int H(m)\,\mathrm{d}m \tag{2.7}$$

We can see that in a Stoner–Wohlfarth model (single-domain), the anisotropy field H_k (saturation in the hard-axis direction) coincides directly with the coercive field (easy-axis direction). The anisotropy energy is then simply obtained by multiplying the anisotropy field with the saturation magnetization. However, this is not the case when considering a full-sheet film with different grains. We must go through the area calculation to retrieve the anisotropy energy.

These normalized M-H curves can be reasonably fitted with an arctan function as shown in Fig. 2.3.a, and Hk can be expressed analytically from the fit:

$$M(H) = A.\tan^{-1}\left(\frac{H}{B}\right) \tag{2.8}$$

$$H_K = H_{sat}.\left(1 - A.\tan^{-1}\left(\frac{H_{sat}}{B}\right)\right) + \frac{1}{2}.B.A.\ln\left(\left(\frac{H_{sat}}{B}\right)^2 + 1\right) \tag{2.9}$$

where A is a dimensionless parameter, B is a fitting parameter in units of magnetic field, H the out of plane field and H_{sat} the saturation field.

Two different strategies are possible in the last step depending on whether the saturation magnetization is assumed known or must be extracted from the MOKE measurement. We consider it reasonable to take the value of M_s from VSM or SQUID measurements. In that case, the effective anisotropy energy density K_{eff} is derived by multiplying the anisotropy field H_K by $\frac{1}{2}\mu_0 Ms$ for different thicknesses of the FM. The evolution of this parameter is shown in Fig. 2.3.b as a function of the effective thickness where the intersection with the y axis is 2 K_i and the slope is $\mu_0 M_s^2$ according to Eq. 2.4.

2.3.2 Vibrating sample magnetometer

A vibrating sample magnetometer (VSM) is a versatile tool commonly used in research and industrial settings to characterize magnetic materials. The basic principle behind a VSM involves subjecting a sample to a vibrating motion while simultaneously applying a magnetic field to it. As the sample vibrates up and down, the alternating magnetic field creates an electric field in the pick-up coils which is proportional to the magnetization of the sample. First, the material to be analyzed is shaped into a 4x4 mm^2 sample, often in the form of a thin film or a solid block, depending on the nature of the material. The sample is mounted on a rod and placed in a vertical vibrating motion. The magnetic response of the sample under an external magnetic field is recorded by detecting the induced electromotive force (emf) in the pick-up coils. This measurement is based on Faraday's law of electromagnetic induction. The VSM provides valuable data about the magnetic properties of the material under investigation, such as saturation magnetization, magnetic hysteresis loops, and magnetic susceptibility.

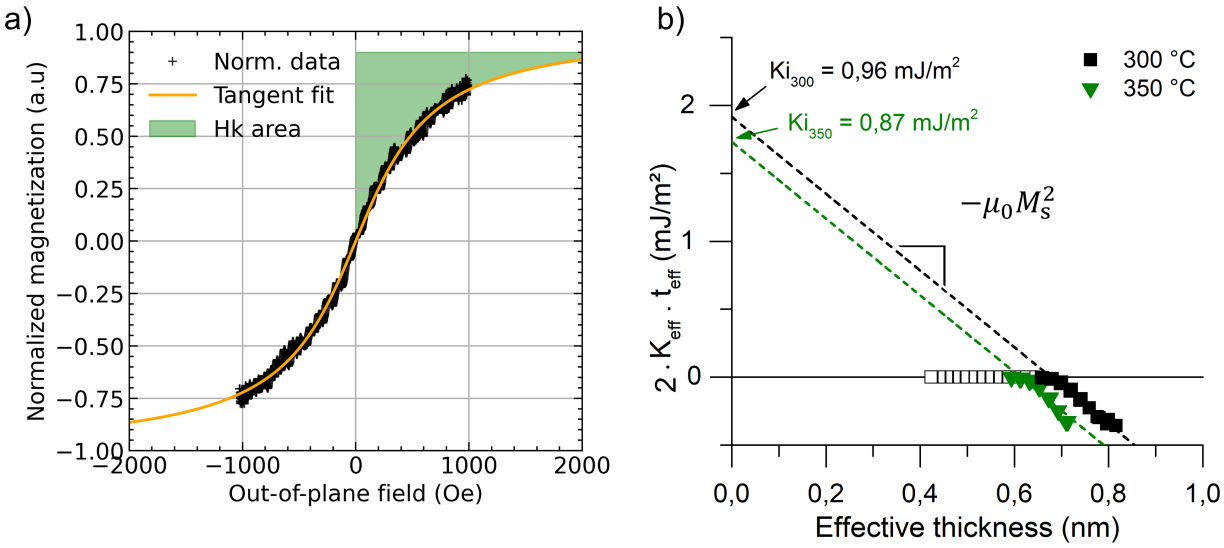

Figure 2.3: (a) Example of out-of-plane loop recording with MOKE in the in-plane magnetized region of MgO/FeCoB[17Å]/W system. The green area is fitted with the equation 2.8 to calculate the anisotropy field. (b) Evolution of the effective anisotropy with increasing thickness of FeCoB. The interception with the y vertical axis gives the interfacial anisotropy while the slope is representative of the saturation magnetization.

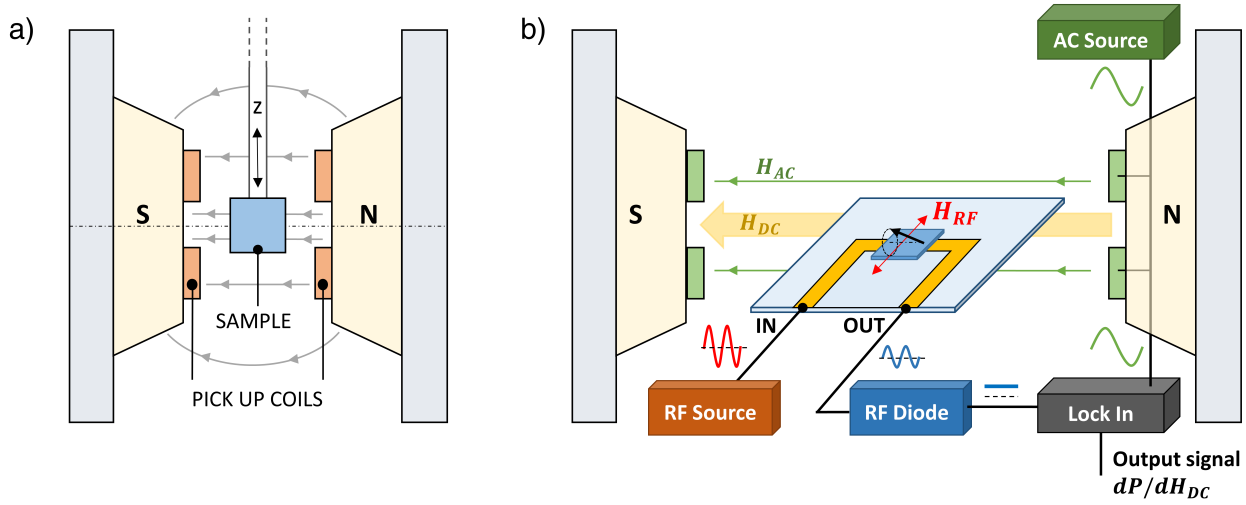

Figure 2.4: VSM (a) and FMR (b) measurement set-up

2.3.3 Ferromagnetic resonance

Ferromagnetic resonance (FMR) experiments are a common technique used to investigate the magnetic properties of ferromagnetic materials. Ferromagnetic materials have spontaneous magnetization, where the atomic magnetic moments align parallel to each other, resulting in macroscopic magnetization. When subjected to an external magnetic field, these magnetic moments experience precession around the field direction. At a specific resonance frequency, known as the FMR frequency, the precession of the magnetic moments reaches maximum amplitude. The typical experimental setup of FMR consists of a sample of ferromagnetic material, usually in the form of a thin film or a single crystal, placed within a uniform and static external magnetic field (see Fig.2.4.b). To induce resonance, an additional radio-frequency (RF) magnetic field is applied perpendicularly to a static field. When the frequency of the RF field matches the FMR frequency, the energy absorbed by the sample is maximized, leading to observable changes in the output RF signal. To enhance the sensitivity of the measurement, a small oscillatory external field is added on top of the large DC magnetic field. Using a lock-in system, the signal coming from the RF diode is derived with respect to the AC source that feeds the coils. The value of the external magnetic field that provides the best absorption of the input signal at a given frequency is noted H_{res}.

An example of an FMR curve is shown in Fig. 2.5.a. By varying the frequency of the input RF signal, one can plot the resonance frequency *vs* external field curve (see 2.5.b), which should behave according to the Kittel formula (Eq.2.10). From the fit, the anisotropy field or saturation magnetization can be extracted. Using the line width of the power absorption spectra, one can also obtain the Gilbert damping by equation 2.11.

$$f_{res} = \frac{\gamma}{2\pi}\mu_0\sqrt{(H_{res}+H_K)(H_{res}+H_K+M_s)} \tag{2.10}$$

$$\Delta H = \Delta H_0 + \frac{4\pi}{\gamma}\alpha f_{res} \tag{2.11}$$

2.4 Nanofabrication process

Once the stacks have been optimized at the sheet film level, nanofabrication can take place in the clean-room facility. Spintec has the opportunity to have access to a wide range of tools for etching and material deposition, as well as electron beam lithography and photolithography (laser, UV, deep-UV) and chemical benches for device development projects. Most of the steps inside the clean room are carried out by students themselves, acquiring significant experience in those technological steps. Furthermore, the fabrication process of MTJs described below involves numerous steps with a wide variety of tools. Only the stack deposition with the magnetron sputtering machine and the E-beam lithography steps are carried out by permanent staff at Spintec, Stephane Auffret, and Laurent Vila, respectively.

The main steps are briefly described in the following sections.

a. Sample annealing and hard-mask deposition. Before starting the fabrication process, the magnetic stack is deposited with DC magnetron sputtering on a 4 inch wafer and annealed for 10 min between 250 and 350 °C. The annealing step is crucial to crystallize the MgO barrier and FeCoB adjacent to it. The specific BCC crystal structure increases the tunnel magnetoresitance ratio by allowing mostly

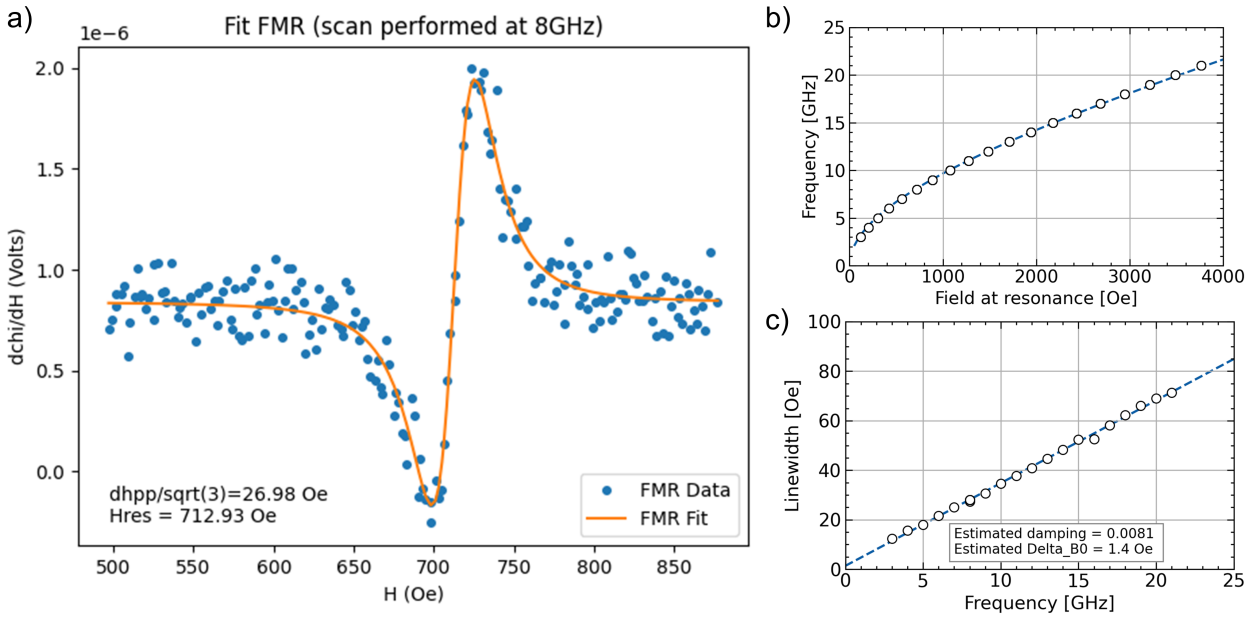

Figure 2.5: (a) Example of FMR measurement curve obtained at a frequency of 8 GHz. The field at resonance in this example is 713 Oe and the line width is 27 Oe. (b) Example of the relationship between the resonance frequency and the external in-plane applied field. (c) Linewidth of the acquired signal as function of the frequency for damping extraction

spin-polarized electron channel (Δ_1) to cross the MgO barrier. Once the sample is annealed, a thin layer (3 nm) of ruthenium (Ru) is deposited followed by 150 nm of tantalum (Ta) to form the hard mask of the ion beam etching (IBE) step.

b. E-beam lithography. Electron-beam (E-beam) lithography is employed to define circular structures with a small diameter, down to 50 nm. A layer of poly(methyl methacrylate) (PMMA) polymer is spin coated on the wafer, followed by 300 seconds of baking at 180°C. Subsequently, the PMMA layer was exposed using E-beam lithography, as shown in Fig. 2.6.b. The development step with a mixture of methyl isobutyl ketone (MIBK) and isopropanol (IPA) in a 1:3 ratio removes the resin that has been stricken by the E-beam.

c. Cr-deposition. Chromium (Cr) is used to fill the holes defined by e-beam lithography. A deposition rate of 0.1 nm/s is maintained during 200 s using quartz crystal microbalance (QCM) in the physical vapor deposition (PVD) process.

d. Lift-off process. During the lift-off process, PMMA is removed with acetone, and Cr remains only on top of the Ta hard mask as nanosize dots defined during the e-beam lithography.

e. RIE of the hardmask. The Ta hard mask is chemically etched during the reactive ion etching (RIE) step. The high selectivity of the Ta etch rate over Cr results in Ta being removed everywhere except below Cr. Sulfur hexafluoride provides isotropic etching, while the passivator (CH_2F_2) protects the walls of the pillar to be over-etched. An optimized combination of SF_6 and CH_2F_2 allows for a vertical and anisotropic etching direction. To control the etching time, an interferometry system measures the interference created by shining the sample with a laser beam. The intensity captured by the photodetector

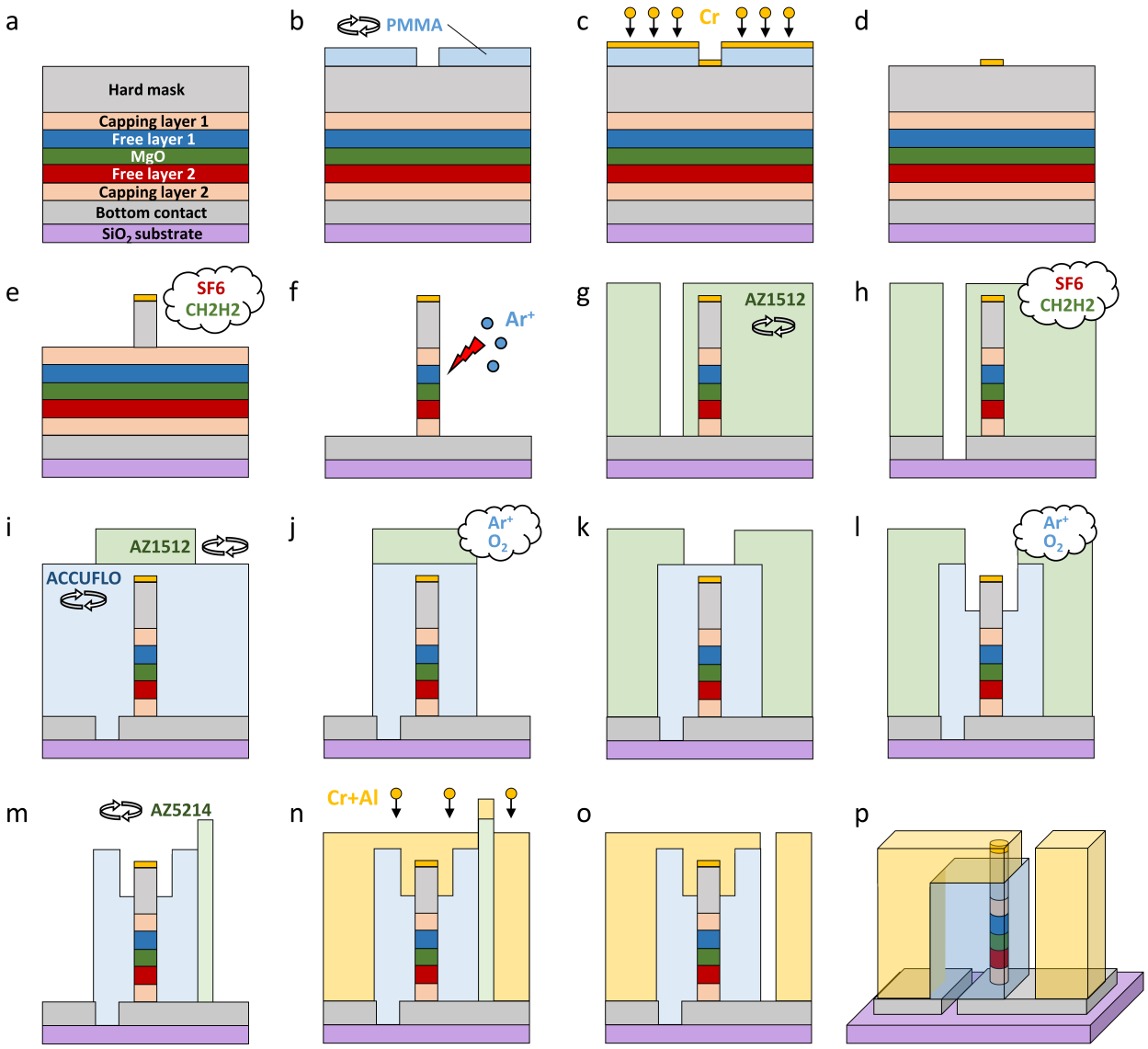

Figure 2.6: (a) Sample depostion, annealing and hard-mask deposition. (b) PMMA spin-coating, E-beam lithography and development. (c) Cr-deposition. (d) Lift-off process. (e) Reactive ion etching (RIE) of the hardmask. (f) Ion beam etching (IBE) of the magnetic stack. (g) Bottom electrode lithography. (h) Bottom electrode etching. (i) Deposition of Accuflo and lithography to define the etching area. (j) RIE of the insulating layer. (k) Lithography for Accuflo thinning. (l) Accuflo thinning with RIE. (m) Lithography to define top electrical contact. (n) Sputtering of Cr (20 nm) and Al (150 nm). (o) Lift-off to separate the top and bottom contact. (p) 3D schematic of the patterned nano-pillar at the end of the fabrication process.

changes as the interference pattern of the reflected signal becomes constructive or destructive. The first derivative of the signal showed a peak when the hard mask was etched. The optimal end point is shown to be 3 seconds after the peak. Deviations from this optimal endpoint can lead to an under- or over-etched pillar. Underetching will result in local masking during the IBE process and short circuits after bottom contact definition, while overetching might cause the fall of the pillar and, consequently, open circuit at the electrical testing.

f. IBE of the magnetic stack. Directly after hard mask etching, the magnetic stack is patterned using IBE, which presents the advantage of being highly anisotropic. The ion beam is oriented at 35° with respect to the normal of the pillar. By doing so, a good trade-off is made between re-deposition, which might create conductive sidewalls, and vertical enough to prevent large pillar diameter with tapered shape. Once the layers before the bottom metallic contact layer are completely removed, a last etching at a grazing angle (80°) ensures that the wall of the pillar is clean of re-deposition.

g. Bottom electrode lithography. To define the metallic contact, a UV photolithography exposed the part of the wafer where the Ta buffer would be etched in the next step. Beforehand, an AZ1512HS resin was spin coated and baked at 120 ° C for 90 seconds. After mask alignment and exposure to UV light, the AZ developer removes the region exposed to UV light.

h. Bottom electrode etching. RIE performs the etching of the buffer layer and creates contact pads for further device characterization.

i. Deposition and lithography of the insulating layer. Polymer encapsulation (ACCUFLO) is deposited to separate the lower and upper contact pads. On top of this layer, a UV lithography step removes the resist on the pads so as to be able to proceed to the metallization of the contact (last step).

j. Insulating layer etching. The ACCUFLO is etched down to the pad by RIE. During this step, and with the use of a profilometer, the etching speed of the ACCUFLO is calculated as well as the amount of ACCUFLO needed to be thinned down in the next step.

k-l. Insulating layer thinning. Another photolithography step is needed prior to the thinning of the ACCUFLO to define a window centered on the pillar. The ACCUFLO is thinned to expose the pillar, and its remaining thickness should cover up to half of the hard mask layer to achieve electrical contact.

m-o. Top contact definition. The last photolithography step is different from the previous one because the AZ resist is exposed twice, making it a negative resist. The first exposure to the AZ is done with a mask followed by a backing step. The entire sample is exposed during a second exposure in *flood* mode to reverse the resist. After development of the resist, 10 nm Cr and 300 nm Al are deposited with PVD tools to complete both the top and bottom contact. Finally, the last lift-off step removed the metallic part throughout the sample except in the top and bottom contact area.

2.5 Magneto-electric characterization techniques of patterned devices

2.5.1 Quasi-static measurement

The wafer yield is assessed using an automated probe station after fabrication. The probe station allows for rapid mapping of the electrical and magnetic properties of thousands of MTJ devices present in the sample. The wafer yield is determined by removing devices that show short or open circuits due to potential fabrication defects. This step is crucial in identifying issues related to specific critical stages during the fabrication process. Short-circuit devices may arise from excessive etching of the polymer window prior to top electrode deposition. However, open-circuit devices can result from loss of pillars during the patterning process or insufficient etching of the polymer window before contacting the top electrode. On the pillars showing reasonable resistance values, the magnetoresistance response is measured as a function of a perpendicular magnetic field, which can reach 300 mT. Using a source meter coupled to a digital multimeter (DMM), the resistance of the MTJ is read while simultaneously sweeping the magnetic field (see Fig 2.7.a). The synchronization between the resistance measurement and the applied magnetic field is achieved using a wave generator that triggers both the DMM and the power supply of the electromagnet. Voltage pulses can be applied through the pulse generator connected to the MTJ via the RF channel of a bias-T. The application of pulses is particularly relevant to investigate reversal by spin-transfer torque. The properties extracted from the quasi-static measurement and their voltage dependence are summarized hereafter :-

- The resistance of the device, and consequently the RA product assuming the pillar diameter
- The tunnel magnetoresistance ratio (TMR)
- The coercive field of the soft FM layers
- The offset field
- The STT efficiency
- The critical switching voltage with 100 ns of pulse width
- The yield of the sample.

Furthermore, temperature control of the sample from 20 to 100 ° C is available at one of the probe stations. Examining the effect of the temperature on all of the parameters mentioned above is possible with this method.

Finally, the magnetic properties can be extracted for different wafer positions and device sizes. It becomes possible to establish correlations between various device characteristics, such as material thicknesses or nominal diameter, and their corresponding electrical and magnetic properties. Although this type of measurement provides valuable information, the time-resolved magnetization dynamic cannot be recorded.

2.5.2 Time-resolved measurement

The time-resolved measurement is based on a *transmission mode* electrical testing in which the signal acquired in the oscilloscope is proportional to the current passing through the MTJ device. To be able to measure the junction in transmission mode, the contact is different from the "DC" set-up. In fact, in this

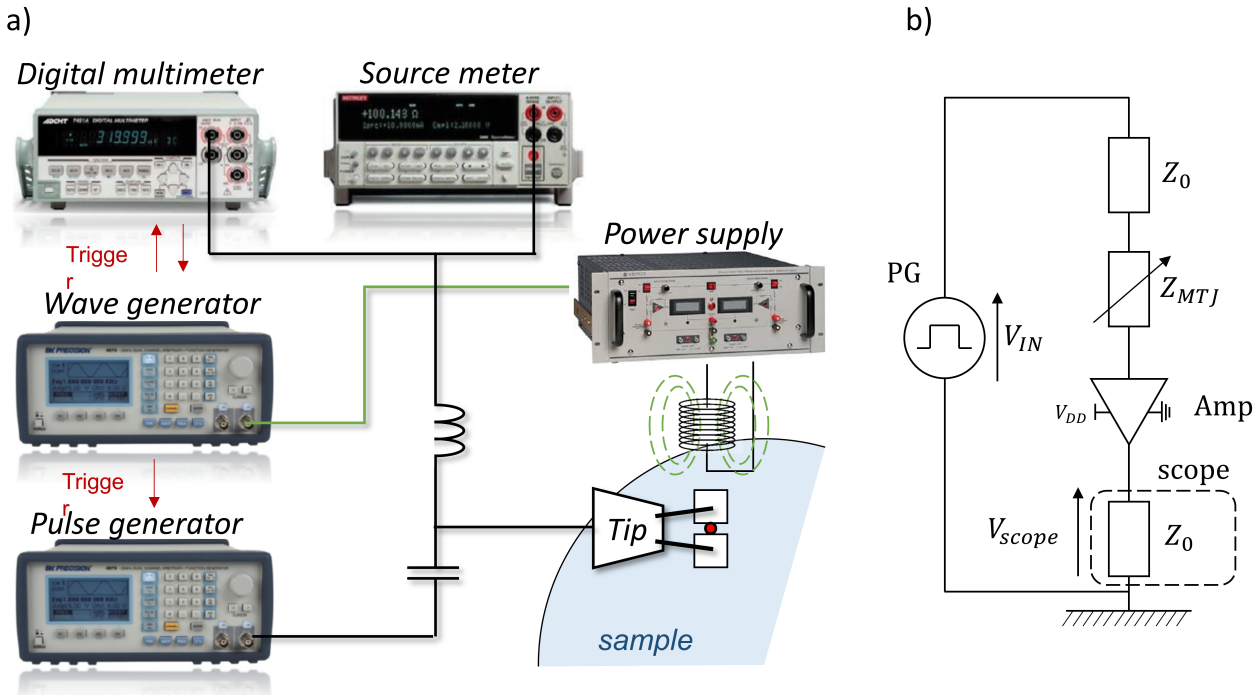

Figure 2.7: a) Schematic of the quasi-static measurement set-up. b) Electrical circuit of the time-resolved measurement

case, a G-S-S-G tip is used to acquire the signal through the junction. From a pulse generator, two output signals can be generated and combined using a splitter with 50% loss of signal. Due to the induction mismatch between the impedance of the circuit ($Z_0 = 50\ \Omega$) and that of the MTJ ($k\Omega$), the electrical pulse is reflected when reaching the MTJ. An additional voltage contribution from this reflection doubles the voltage applied. The electrical scheme of the transmission setup is shown in Figure 2.7.b. On the other side of the junction, the signal was amplified $5\times$ before recording in the oscilloscope. The large bandwidth (DC to 350 MHz) of the amplifier allows us to work with very long pulses down and can capture signal variation down to 3 ns. Additionally, the setup allows one to apply an external perpendicular magnetic field to the sample while being measured.

To calculate the resistance of MTJ over time, the following formula is used, V_{IN} is the input voltage of the pulse generator, V_{scope} is the voltage acquired by the scope, and C is a coupling factor taking into account the losses in the splitter at the output of the pulse generator (PG):

$$R_{MTJ} = \left(2\, C\, Z_0\, Gain_{amp} \frac{V_{scope}}{V_{IN}}\right) - 2\, Z_0 \tag{2.12}$$

Chapter 3

Modeling dual free layer MTJ for spiking neuron

Contents

3.1 Introduction

This chapter is dedicated to a description of the concept of dual free-layer MTJ in terms of structure and expected dynamics. The requirements in terms of material parameters to achieve this dynamical state are determined by energy calculations and macrospin simulations.

Previous work [22, 110] showed that a dual free-layer MTJ can be subjected to a windmill dynamic under constant voltage bias. This dynamic is due to the successive reversal of the two ferromagnetic layers by the spin-transfer torque (STT) effect. The free layer with higher stability will be named the *hard layer* and called HL, while the other layer will be named the *soft layer* and called SL. In Fig. 3.1.b, the evolution of magnetization over time for both layers shows the perpetual switching sequence expected in the dual free layer MTJ. Due to the contrast in resistance given by the TMR, the short AP states, ② and ④, of the MTJ can be attributed to the spikes. On the other hand, the longer P states, ① and ③, between the spikes determine the incubation time. The entire windmill period (two P states and two AP states) defines the frequency of the windmill. As there are two spikes within a windmill period, the spiking frequency is twice the windmill frequency.

To understand how material parameters are expected to play a role in the shape of the spike and the frequency of the spiking, the energy landscape is first calculated to extract the different energy barriers in the system. From the simple case of an uncoupled dual-free-layer system (without dipolar interaction), the complexity gradually increases with the addition of a dipolar field between the layers and the additional effect of an external magnetic field. Associated to STT switching models from the literature, the expected spike shape and spiking frequency can be derived as a function of current density, applied magnetic field, and material parameters. However, the hypothesis on which these models rely should be carefully checked. This point is addressed in the last part of this chapter.

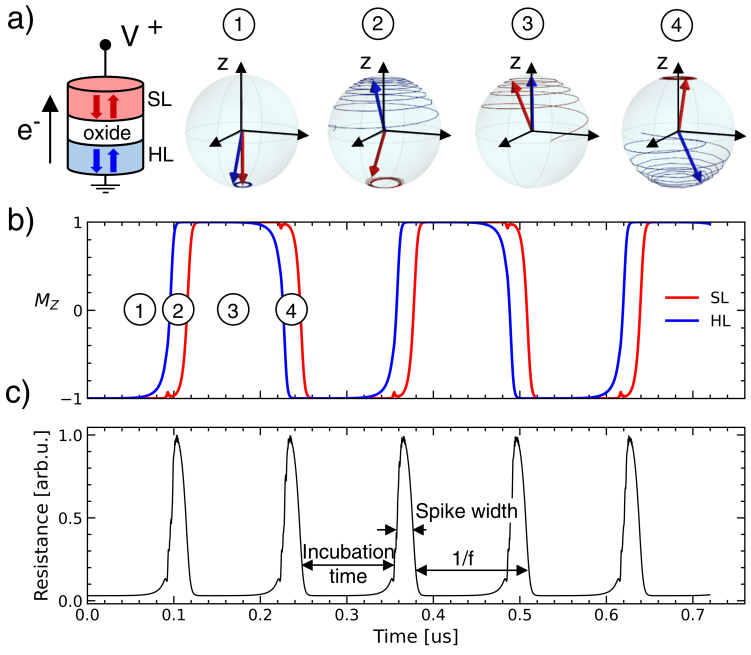

Figure 3.1: a) Schematic view of dual-free layer p-MTJ and 3D macrospin configurations corresponding to several stages of the windmill dynamics. Simulated time traces of b) the projection of the magnetization along z axis and c) the resulting normalized resistance under a bias voltage

3.2 Numerical investigations of dual free layer MTJ

3.2.1 Macrospin model for energy calculation

Considering that the magnetization is uniform in the ferromagnetic layer (FM), a macrospin representation is used to model each layer and calculate the energy terms of the coupled system. Fig. 3.2 shows the trilayers FeCoB/MgO/FeCoB considered in the macrospin model and the angles we use to locate the magnetization in the system of axes (x,y,z). The MgO thickness is assumed to be 1.1 nm, and the FeCoB top and bottom thicknesses are considered constant at 1.1 nm.

The first term accounted into the total energy of the system is the anisotropy energy, which depends on the interfacial anisotropy K_i. As a consequence of the thin layer geometry of the FM, the demagnetizing energy tends to bring the magnetization into the plane. This energy strongly depends on saturation magnetization M_s and demagnetizing factor. Together with the first anisotropy energy, they are called the *effective* anisotropy energy (Eq. 3.2). By convention, the hard layer (HL in blue) refers to the layer with a higher effective anisotropy, and the soft layer (SL in red) refers to the one with a lower effective anisotropy. The next contribution comes from the dipolar coupling between the FM layers, which mainly affects the small magnetized volume (see Eq. 3.4). In p-MTJ, the dipolar interaction favors mainly the parallel state, whereas in in-plane MTJ, the AP state is stabilized by the dipolar field. In the case of an applied external magnetic field, the Zeeman energy is taken into account in the total energy and is proportional to the applied field (Eq. 3.6). Considering the same saturation magnetization M_s for the soft and hard layer, the total energy of the system and the individual terms can be expressed as

- $E_{total}(\theta_{HL},\theta_{SL}) = E_{anis}(\theta_{HL}) + E_{anis}(\theta_{SL}) + E_{dipolar}(\theta_{HL},\theta_{SL}) + E_{ext}(\theta_{HL},\theta_{ext}) + E_{ext}(\theta_{SL},\theta_{ext})$ (3.1)

- $E_{anis}(\theta_{HL,SL}) = K_{\text{eff,HL,SL}}\left(1-\cos^2(\theta_{HL,SL})\right)V_{HL,SL}$ (3.2)

  where: $K_{\text{eff,HL,SL}} = \left(\dfrac{K_i}{t_{HL,SL}} - \dfrac{1}{2}\mu_0 M_s^2(N_z - N_x)\right)$ (3.3)

- $E_{dipolar}(\theta_{HL},\theta_{SL}) = \mu_0 M_s\left(|H_x|\sin(\theta_{HL})\sin(\theta_{SL}) + |H_z|\cos(\theta_{HL})\cos(\theta_{SL})\right)V_{HL,SL}$ (3.4)

  where $H_x = N_{dip,x}M_s$, and $H_z = N_{dip,z}M_s$ (3.5)

- $E_{ext}(\theta_{HL,SL},\theta_{ext}) = -\mu_0 M_s\, H_{ext}\cos\left(\theta_{HL,SL} - \theta_{ext}\right)V_{HL,SL}$ (3.6)

The parameters used in the macrospin model are summarized in Table 3.1.

The interactions taken into account for the first part of the study are the effective anisotropy of both layers. The effect of the dipolar interaction will be tackled in a second step.

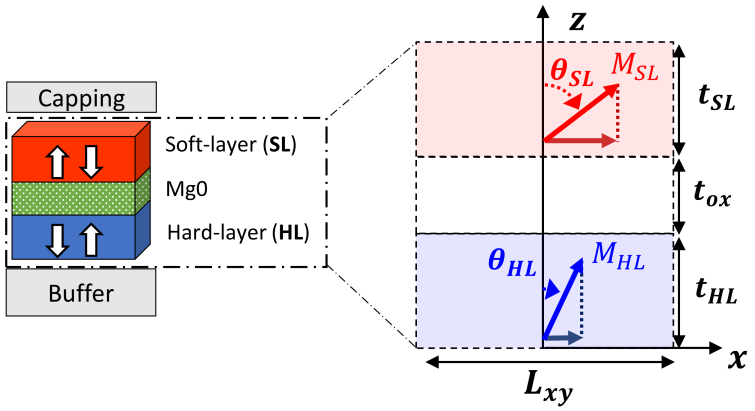

Figure 3.2: Schematic of the two macrospins representing the hard-layer and soft-layer separated by the oxide barrier.

Parameters	Symbol	Value	Unit
Saturation magnetization	M_s	10^6	A/m
Interfacial anisotropy of HL	$K_{i,HL}$	0.70	mJ/m2
Interfacial anisotropy of SL	$K_{i,SL}$	0.66	mJ/m2
Lateral dimension	L_{xy}	35	nm
Layer thickness	$t_{HL,SL}$	1.1	nm
Damping	α	0.01	-
TMR	TMR	100	%
Resistance area product	RA	10	$\Omega.um^2$
Demagnetizing factor $\perp$ to the plane	N_z	0.916036	-
Demagnetizing factor $\parallel$ to the plane	N_x	0.041982	-
Dipolar component $\perp$ to the plane	$N_{dip,z}$	-0.03985	-
Dipolar component $\parallel$ to the plane	$N_{dip,x}$	0.01993	-

Table 3.1: Parameters of the macrospin model

3.2.2 Dual free-layer MTJ without dipolar interaction

Energy barrier calculation

In a first approximation, the calculation of the energy landscape for this uncoupled system considering only the anisotropy of the layer and the demagnetization resulting from the shape of the pillar. Fig. 3.3.a illustrates the energy landscape calculated as a function of the angle between the magnetization of each layer and the out-of-plane direction. The four out-of-plane configurations involved in windmill dynamics are located at the corners of the 2D color map in Fig. 3.3.b. Transitioning from one configuration to the next requires overcoming the energy barrier between the two states. The energy barrier and the thermal stability of the layer i ($\forall\, i \in [HL, SL]$) can be expressed by :

$$E_{b,i} = K_{\text{eff},i}\, V = \frac{H_{K,i}\, \mu_0 M_s\, V}{2} \tag{3.7}$$

$$\Delta_i = \frac{E_{b,i}}{k_B T} \tag{3.8}$$

$$\tag{3.9}$$

The energy barrier related to the switching of the hard layer (Δ_{HL}) is clearly higher than the one of the soft layer (Δ_{SL}) as shown in Fig. 3.3.c. Due to non-negligible thermal excitation at room temperature, the process of magnetization reversal is inherently subject to stochasticity. The Néel-Arrhenius law quantifies the likelihood of magnetization reversal over time, accounting for a specific thermal stability factor. From this model, the median lifetime is derived by taking the probability of 50% switching.

$$P(t) = 1 - \exp\left(\frac{t}{\tau_0}\exp\left(-\Delta_i\right)\right) \tag{3.10}$$

$$\tau_i = \tau_0 \exp\left(\Delta_i\right) \tag{3.11}$$

$$\tag{3.12}$$

Regardless of the switching sequence (clockwise (+) or anticlockwise (−) in Fig. 3.3.b.c), the highest energy barrier to overcome in the dynamic sequence of the windmill remains constant and is represented by Δ_1. This energy will be termed the "activation energy". The positive (negative) polarity of the switching sequence relates to the sequence in which the reversal of the hard (soft) layer induces an antiparallel (AP) state configuration, while the reversal of the soft (hard) layer leads to a parallel (P) state configuration. The transition from one configuration to another can occur primarily through three mechanisms: thermal activation, with the application of an external magnetic field, or with spin-polarized current. Switching via STT is discussed in the following two sections.

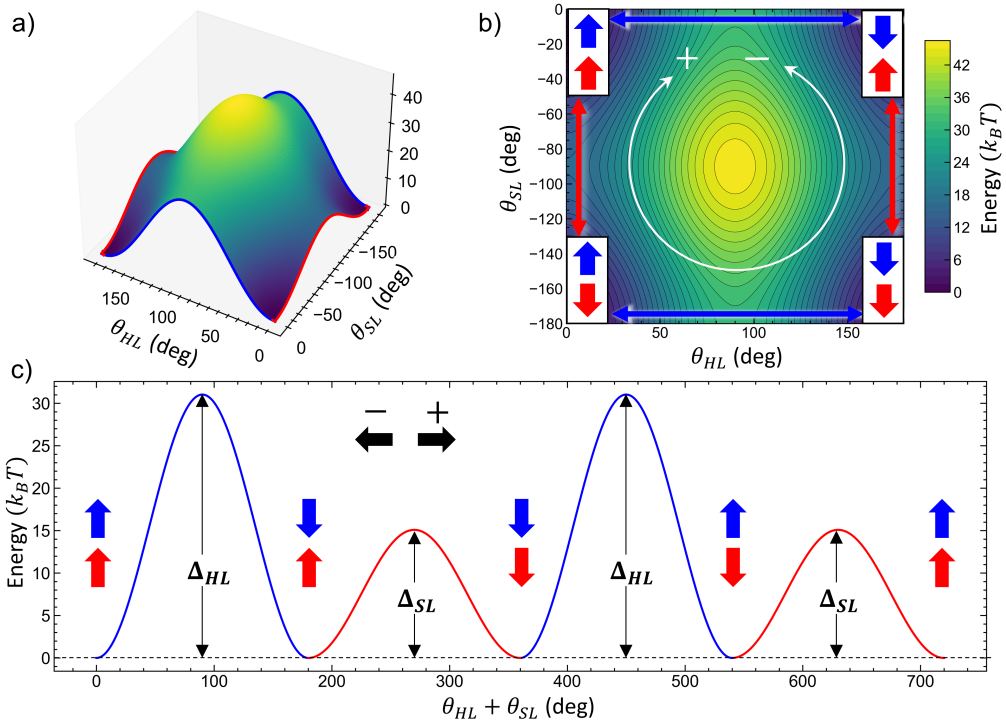

Figure 3.3: (a) Energy landscape of the dual free layer system without dipolar coupling as function of θ_{HL} (θ_{SL}), angle between the magnetizations of M_{HL} (M_{SL}) and the normal of the plane. (b) Same as (a) in a 2d colormap representation. The white arrow highlights the two possible polarities of the switching sequence. (c) Energy taken by the system across the different stages of the windmill dynamic. Positive polarity of the switching sequence is assumed when the hard-layer switches first from P to AP state, and vice versa for the positive polarity.

Spin-transfer torque induced switching

As outlined in section 1.2.5, the spin-transfer torque effect introduces an extra component in the Landau-Lifshitz-Gilbert-Slonczewski (LLG-S) equation. Although an analytical expression for dynamics may not be directly attainable, it remains feasible, using a zero-temperature approximation, to compute the critical current density J_{c0} required to initiate the switching of a ferromagnetic layer (FM) characterized by an anisotropy field H_K, damping coefficient α and e the electron charge.

$$J_{c0} = 2\frac{|e|\alpha}{\hbar\eta}\mu_0 M_s.t.H_K \tag{3.13}$$

$$\tag{3.14}$$

Two different regimes coexist to determine the switching probability as a function of the current density and the material parameters of the MTJ. The thermally activated regime is defined when the applied current density is significantly lower than the critical current density ($J_{\text{app}} < J_{c0}$). On the contrary, the precessional regime is valid for a much higher current density ($J_{\text{app}} \gg J_{c0}$) where the stochastic characteristic time exceeds the switching time. Several attempts have been made to formulate a single expression for the switching probability across the entire range of applied current densities, and this remains a challenge. So far, only phenomenological models have been proposed, which are briefly discussed in Section 1.2.5. Among them, the Yang model gives a relatively simple expression of the switching time valid for all the current density values :

$$\tau = \frac{k.\Delta.B + A.\exp\left((1-k).\Delta.\left(1-\frac{J}{J_{c0}}\right)\right)}{\ln\left(1+\exp\left(-k.\Delta.\left(1-\frac{J}{J_{c0}}\right)\right)\right)} \tag{3.15}$$

$$A = -\tau_0.\ln(1-P) \tag{3.16}$$

$$B = \frac{1}{2}.\tau_D.\ln\left(-\frac{4.\Delta}{\ln(P)}\right) \tag{3.17}$$

$$\tau_D = \frac{1}{\alpha\gamma\mu_0 H_K} \tag{3.18}$$

This unified model gives the switching probability as a function of the applied current density for given material parameters. As shown in Fig. 3.4.a, the unified model fits the Néel-Brown model and Sun's model in the low and high current density, respectively. In Fig. 3.4.b, the cumulative distribution of switching in the thermally assisted regime exhibits a broad profile, distinctly contrasting with the much narrower distribution observed in the precessional regime.

Based on this model, the behavior of the windmill dynamic can be extrapolated for given thermal stability values of the soft and hard layers. As an example, the median switching times of HL and SL are shown in Fig. 3.5.a.d for $\Delta_{SL} = 16.5$ and $\Delta_{HL} = 29$ for positive and negative current polarity. The time traces in Fig. 3.5.b.e are generated by randomly selecting the switching times from the lifetime distribution of the P and AP lifetimes provided by the unified Yang expression. In positive (negative) current polarity, the transition from AP to P corresponds to the SL (HL) reversal, whereas the transition from P to AP indicates the HL

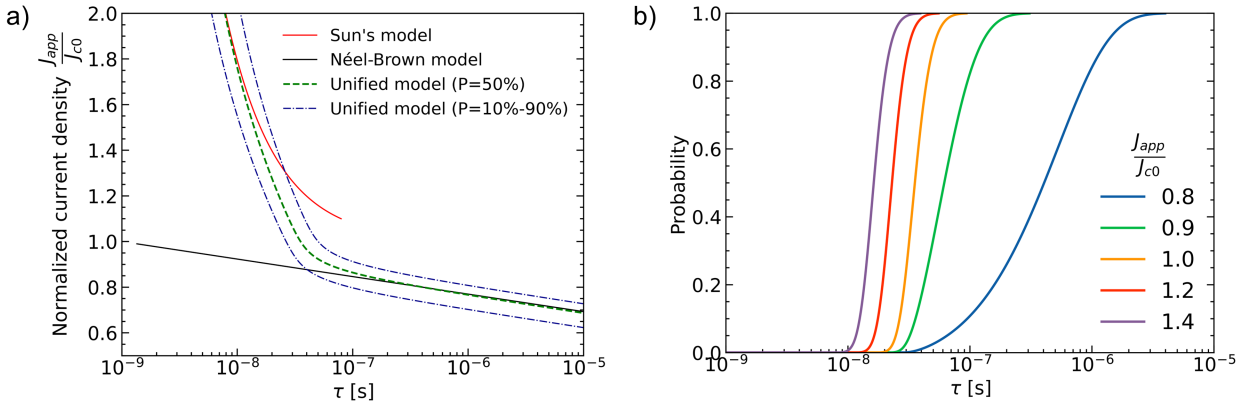

Figure 3.4: a) Switching delay as function of the applied current density normalized by J_{c0}. b) Cumulative distribution function for different value of applied current density using the unified model in a)

(SL) reversal. Since the SL switches faster under a given applied voltage, the P states dominate the signal in positive polarity (Fig. 3.5.b.c), while symmetrically the AP states take over in the negative polarity (Fig. 3.5.e.f). As a consequence, the time traces demonstrate sharp spikes in high resistance for positive current polarity and sharp spikes in low resistance for negative polarity. As the energy landscape remains unchanged with current polarity, as reported in Fig. 3.3.c, the proportions of the P and AP states and their lifetime distribution are precisely opposite when reversing the current polarity. In this model, the shape of the spikes is entirely determined by the relative anisotropy of the HL compared to that of the SL. Generally, when the two values of effective anisotropy are closer, the signal exhibits greater symmetry. The shape of the spikes will be discussed later in Section 3.2.5.

To conclude, the uncoupled macrospin model, which relies on the switching probability of Yang's model, predicts that the windmill dynamic is expected to occur in both polarities of current. Furthermore, the spike signal is symmetric, with a high resistance spike in positive polarity and a low resistance spike in negative polarity. However, the dipolar interaction has not been included in the energy calculation and might affect the windmill dynamic. The next section addresses this point in detail.

3.2.3 Dual free-layer MTJ with dipolar interaction and external magnetic field

Energy barrier calculation

Including a dipolar interaction between layers alters the energy landscape, resulting in the configuration shown in Fig. 3.6.a. In this landscape, parallel states achieve the lowest energy level, whereas antiparallel configurations exhibit an energy of 30 k_BT. Moreover, the dipolar field introduces an asymmetry in the two possible switching sequences. Specifically, the positive polarity of the switching sequence involves energy costs Δ^+_{HL} and Δ^+_{SL}, while the negative polarity leads to energy costs Δ^-_{SL} and Δ^-_{HL}. The total energy required for the four reversals remains consistent across both polarities. However, it is allocated differently among the barriers: $\Delta^+_{HL} > \Delta^-_{HL} > \Delta^-_{SL} > \Delta^+_{SL}$. Considering that the AP state is a metastable state, the critical power needed to initiate the windmill dynamic is thus dependent on the polarity. The activation energy must overcome the biggest of the two energy barriers for each polarity ($E^{\pm}_{activation} > max\left(\Delta^{\pm}_{HL}, \Delta^{\pm}_{SL}\right)$). In the case presented in Fig. 3.6.a, $E^+_{activation} = \Delta^+_{HL}$ and $E^-_{activation} = \Delta^-_{HL} < \Delta^+_{HL}$, it is clear that the most energy efficient

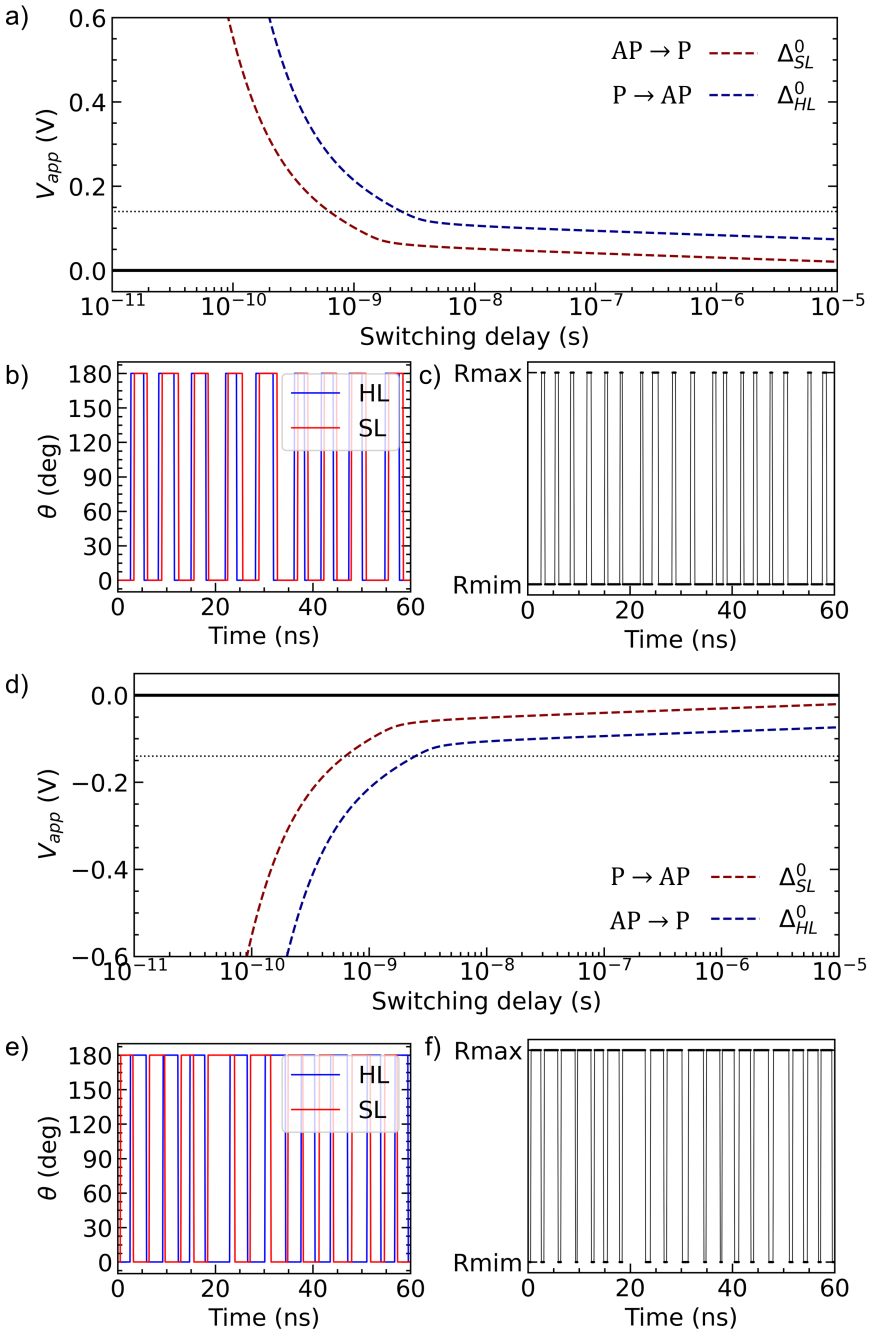

Figure 3.5: Median switching delay as function of the applied bias across the MTJ for positive (a) and negative (d) polarity without dipolar interaction. The associated time traces of the magnetization switches (b-e) reconstructed from the probability distribution of the Yang's equation 3.15. (c) and (f) : Resistance of the devices through time deduced from the AP and P configuration of the MTJ. Positive polarity (c) shows spikes in high resistance whereas negative polarity (f) makes the MTJ spikes in low resistance state.

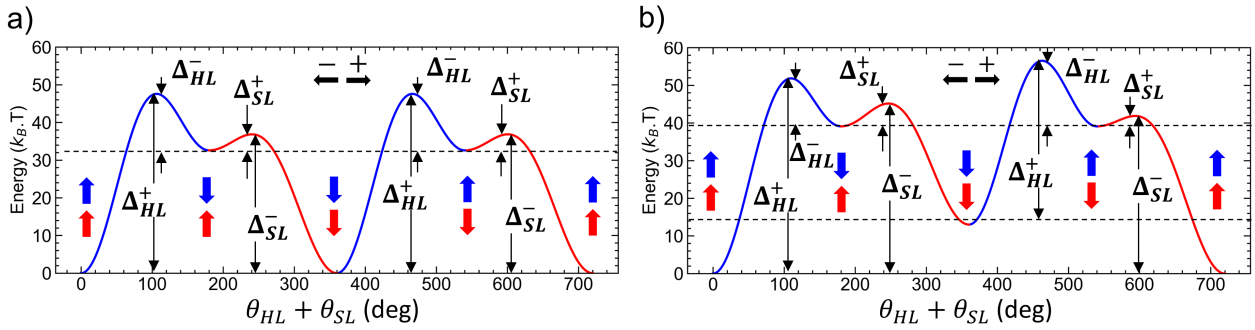

Figure 3.6: Energy taken by the system across the different stages of the windmill dynamic in case of a dipolar interaction between the layers (a) and with an external magnetic field applied (b). In (b), 4 thermal stability factors can be defined for each polarity of switching sequence.

polarity is the negative one. At this stage, the two parallel states are indistinguishable in terms of the energy barrier, as is the case for the two antiparallel states.

The final interaction capable of altering the equilibrium among the four potential states is an external magnetic field. Configurations aligned with the external field will be favored, while those in the opposite direction will acquire more energy. An illustration of how a 100 Oe magnetic field can perturb the energy landscape is presented in Fig. 3.6.b. Within the two parallel configurations, the $\downarrow\downarrow$ state exhibits the highest energy value because both layers are oriented oppositely to the applied magnetic field (along the +z direction). The discrepancy between the two parallel states causes all the possible states to be disentangled in terms of energy barrier, leading to four different lifetimes for each polarity of the switching sequence.

Spin-transfer torque induced switching

The addition of dipolar interaction into our model introduces a polarity-dependent variation of the thermal stability of each layer, as shown in Fig. 3.6.a. Consequently, the medians of the switching delay (dark blue and dark red curves) shift towards faster or slower switching, depending on whether the dipolar field aids or hinders the transition.

For example, in positive polarity (Fig. 3.7.a), Δ^+_{HL} is higher than its equivalent without dipolar field Δ^0_{HL} while Δ^+_{SL} is lower than Δ^0_{SL}. Consequently, the signal is even more asymmetric, with very sharp spikes and long incubation times between them (Fig. 3.7.b.c). Surprisingly, the negative polarity shows similar time traces (Fig. 3.7.e.f). This is explained by the lower effective thermal stability of the HL compared to the SL in this polarity (i.e. $\Delta^-_{HL} < \Delta^-_{SL}$). Inversion in the thermal stability of the hard and soft layers causes the signal to populate the P state more compared to the AP state. However, with more asymmetry between the effective anisotropy of HL and SL, the signal exhibits low-resistance spikes in the negative polarity, similar to the case without dipolar interaction (Fig. 3.5.f).

External magnetic field induced switching

To manipulate the magnetization direction, it is also common to use an external magnetic field, where the magnetization tends to align along the field due to the Zeeman effect. In a zero-temperature approximation, the external magnetic field has to overcome the effective anisotropy field to be able to switch the magnetization from one out-of-plane equilibrium position to the other. When the MTJ is subject to spin polarized

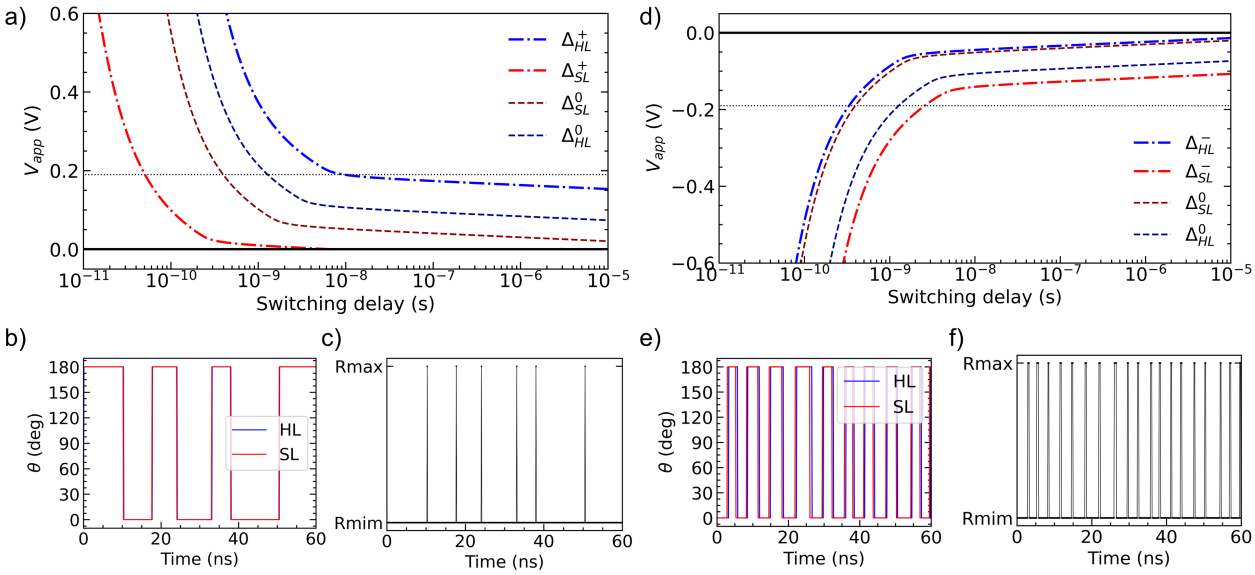

Figure 3.7: Median switching delay as function of the applied bias across the MTJ for positive (a) and negative (d) polarity. Dark-blue and dark-red lines provide the expected curves for the ideal case without dipolar interaction, completely symmetric with respect to the polarity of the voltage. The associated time traces (b) and (e) of the magnetization switches reconstructed from the probability distribution of the Yang's equation 3.15. (c) and (f) : Resistance of the devices though time deduced from the AP and P configuration of the MTJ. Positive and negative polarity shows spikes in high resistance.

current and external magnetic field, the impact of the external field can be seen as a modification of the thermal stability factor similarly to the effect of the spin-transfer torque in the thermal stability barrier :

$$\Delta_i = \Delta_{i_0} * \left(1 - \frac{\pm H_{app}}{H_{K,i}}\right)^2 \text{ where } \Delta_{i_0} \in [\Delta_{SL}, \Delta_{HL}] \tag{3.19}$$

As the windmill sequence involves switching of the magnetization from down to up and up to down z-directions, the field direction has to be reversed to complete one single windmill sequence. Even with a change in the magnetic field direction, the windmill sequence will be possible only in the negative polarity because the soft layer always switches first from the P state to the AP state. It is not convenient for applications to drive the windmill dynamic with magnetic field, as it creates more complexity in the fabrication of a field line on top of each device. It is much more convenient for embedded technology to use the STT effect of a spin-polarized current to switch the magnetization direction. The effect of the external magnetic field on the windmill dynamic will be discussed in Section 3.2.5 related to the spike shape.

3.2.4 Regulation of the mean spiking frequency

The overall behavior of the dual-free-layer MTJ can be seen as spiking neurons characterized by a spiking response to an excitation input signal. Under constant excitation, the neuron fires at a given frequency. In order to be effectively employed in neural networks, the evolution of the frequency with respect to the input must display non-linear behavior, as detailed in Section 1.3. Because the magnetization reversal in MTJ is driven by a probabilistic process, the spiking frequency can only be represented through an average. This

mean spiking frequency is determined by the mean lifetimes associated with the windmill dynamic. The windmill period is defined by the complete loop over all magnetic configurations ($\uparrow\uparrow - \uparrow\downarrow - \downarrow\downarrow - \downarrow\uparrow$) that contains two P states and two AP states. The spiking period is instead half the windmill period because two spikes occur within a single windmill period. The spiking frequency is then defined by :

$$\overline{f} = \frac{2}{\overline{\tau_{\uparrow\uparrow}} + \overline{\tau_{\uparrow\downarrow}} + \overline{\tau_{\downarrow\downarrow}} + \overline{\tau_{\downarrow\uparrow}} + 4.\overline{\tau_{trans}}} \tag{3.20}$$

where τ_{trans} denotes the transition time between states. In the absence of any external magnetic field, the two P states are indistinguishable as well as the two AP states (i.e. $(\tau_{\uparrow\uparrow}, \tau_{\downarrow\downarrow}) \rightarrow \tau_P$, $(\tau_{\uparrow\downarrow}, \tau_{\downarrow\uparrow}) \rightarrow \tau_{AP}$). and the frequency is expressed as :

$$\overline{f} = \frac{1}{\overline{\tau_{AP}} + \overline{\tau_P} + \overline{\tau_{AP\rightarrow P}} + \overline{\tau_{P\rightarrow AP}}} \tag{3.21}$$

The individual lifetimes of τ_{AP} and τ_P in this context are defined using the unified expression detailed in Equation 3.15. In most cases, the transition times between the AP and P states ($\tau_{AP\rightarrow P}$ and $\tau_{P\rightarrow AP}$) are expected to be insignificantly small compared to the lifetimes of the P and AP states. In fact, the transition time, which spans from 10% to 90% of the resistance signal, is relatively small compared to the total switching time (i.e., mainly the incubation time is representative of the total switching time). This phenomenon primarily stems from the maximal torque exerted by the STT term, which occurs at a relative angle of 90 degrees between the two magnetizations. However, when the switching time approaches the nanosecond time scale, the transition time might affect the overall spiking frequency in larger proportion.

The next two sections investigate the influence of the current density and the material parameters on the mean spiking frequency of a dual free-layer MTJ.

Current density

The spiking frequency is inherently influenced by the current density because the spin-transfer torque reduces the switching delays of all the transitions involved in the windmill dynamics. In the thermally assisted regime, it is expected that the spiking frequency will exhibit a notable variation, attributed to the exponential dependence of the applied voltage on the mean lifetime within this regime. Furthermore, even a slight difference in stability between the HL and SL layers could lead to a significant difference in the mean lifetimes of the P and AP states. Following the example of Fig. 3.5.a, where the thermal stability factors of HL and SL are, respectively, 29 and 16.5 k_B T, the relationship of the two lifetimes associated with the states AP and P is of the order of 5 decades ($\frac{\tau_{HL}}{\tau_{SL}} = \exp(\Delta_{HL} - \Delta_{SL}) = 10^{5.4}$) for a ratio less than 2 between the stability of SL and HL. So, for a high asymmetry between the thermal stability of HL and SL, the spiking frequency can be approximated by the inverse of the mean switching time of HL ($\overline{f} = 1/\tau_{HL}$), which causes the spiking frequency to vary exponentially with the current density:

$$\overline{f} = \frac{1}{\tau_0} exp\left[-\Delta_{HL}\left(1 - \frac{J}{J_{c0,HL}}\right)\right] \tag{3.22}$$

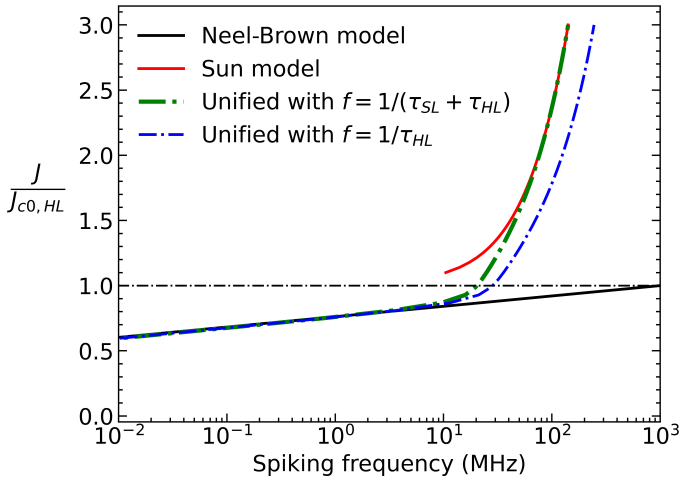

Figure 3.8: Spiking frequency as function of the normalized current density for Néel-Brown model with $f = 1/\tau_{HL}$ approximation, Sun model with $f = 1/(\tau_{HL} + \tau_{SL})$, and for the unified expression with $f = 1/(\tau_{HL} + \tau_{SL})$ and $f = 1/\tau_{HL}$ approximation.

In the precessional switching regime, the drastic change in switching time with respect to the applied current density reduces to a 1/J dependency ($\tau \propto 1/J$). Consequently, for small asymmetry between the SL and HL thermal stability, the approximation based on the negligible SL reversal time compared to that for HL might no longer be true. In the precessional regime, which is described by Sun model, the frequency as function of the current density would be :

$$\overline{f} = \frac{1}{\overline{\tau_{HL}} + \overline{\tau_{SL}}} = \frac{(J - J_{c0,HL})(J - J_{c0,SL})}{B_{HL}\, J_{c0,HL}(J - J_{c0,SL}) + B_{SL}\, J_{c0,SL}(J - J_{c0,HL})} \tag{3.23}$$

$$\text{with : } \overline{f} \underset{\frac{\tau_{SL}}{\tau_{HL}} \to 0}{\longrightarrow} \frac{1}{B_{HL}} \frac{J - J_{c0,HL}}{J_{c0,HL}} \tag{3.24}$$

To unify both the thermally assisted and the precessional regimes and obtain an approximation of the spiking frequency in the intermediate regime, Yang's expression (Eq. 3.15) can be used. In the intermediate regime, the frequency is expected to still be dominated by the HL reversal, so the approximations made for the thermally activated mechanism apply in that case ($\langle f \rangle \approx 1/\tau_{HL}$). The frequency as a function of the normalized current density is illustrated in Fig. 3.8 for the Néel-Brown model with the approximation of Eq. 3.22, the Sun model (Eq. 3.23) and Yang's model.

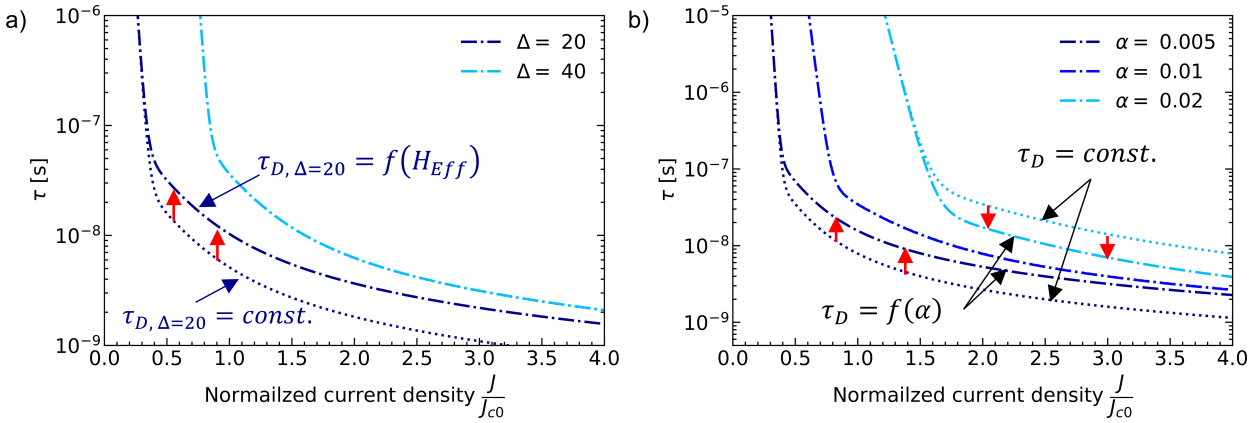

Figure 3.9: Switching delay as function a normalized current density for different effective anisotropy (a) and different damping value (b). The dependency of the effective anisotropy and damping on the attempt time τ_D increases the effective switching time in the precessional regime.

Material parameters

In addition to increasing the current density to achieve higher spiking frequencies, another alternative worth investigating is the effect of material parameters on the critical current density. The critical current density is expressed as :

$$J_{c0} = 2\frac{|e|\alpha}{\hbar\eta}\mu_0 M_s\, t\, H_{\mathrm{K}} \tag{3.25}$$

$$\text{with : } H_{\mathrm{K}} = \frac{2K_{\mathrm{eff}}}{\mu_0 Ms} = \left(\frac{2K_i}{t} - M_s\,(Nz - Nx)\right) \tag{3.26}$$

Increasing the spin polarization factor η offers a direct advantage in reducing the critical switching current and increasing the spiking frequency without any drawbacks. This factor would be determined by the quality of the FeCoB/MgO/FeCoB trilayer. Alternatively, one may consider decreasing the effective anisotropy field H_{K} or reducing the damping α. However, it is crucial to be cautious, as these parameters also impact the attempt time frequency in the unified model, as reported in [65]:

$$\frac{1}{\tau_D} = \alpha\gamma\mu_0 H_{\mathrm{K}} \tag{3.27}$$

A reduction in the attempt time frequency would result in a shift of the onset of the precessional regime towards longer switching times. To validate the proposition that decreasing the damping and effective anisotropy is advantageous for the overall switching time, Fig. 3.9.a.b shows their impacts on the switching time. Although the impact is significant in the precessional switching regime (highlighted by the red arrows), the low effective anisotropy curves ($\Delta = 20$) and the low damping curves ($\alpha = 0.005$) remain below the one with high effective anisotropy and high damping, respectively. In conclusion, it is favorable to decrease the effective anisotropy and the damping to obtain a higher spiking frequency at a given applied current density.

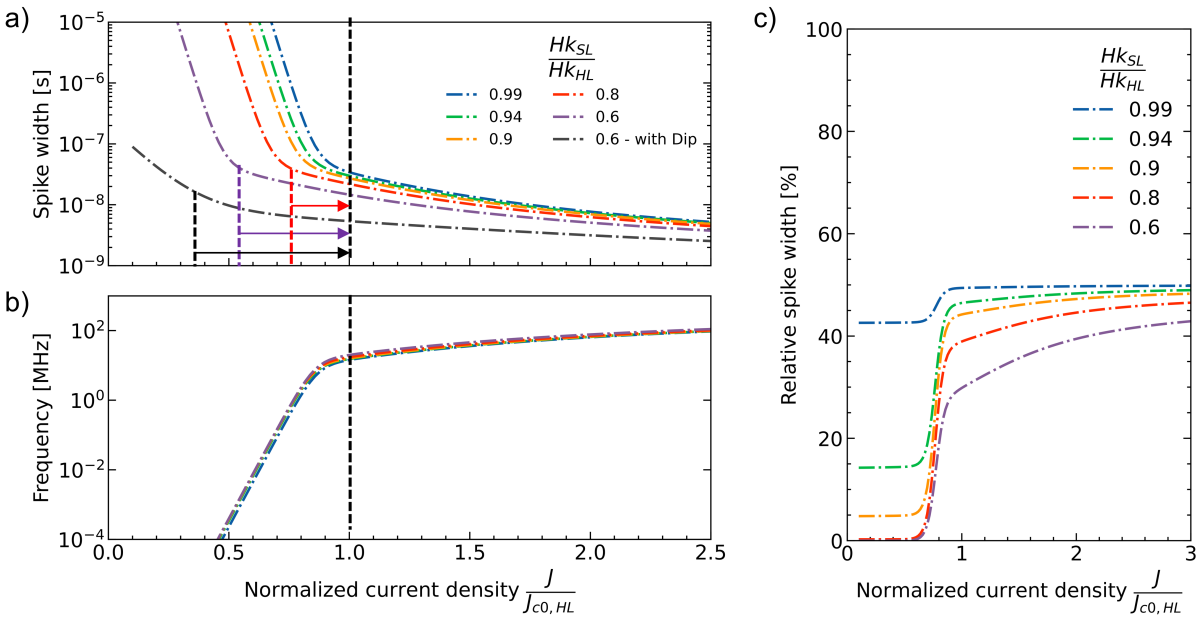

Figure 3.10: Spike width (a), spiking frequency (b) and relative spike width (c) as function of the normalized current density for different ratio of effective anisotropy between the HL and SL.

3.2.5 Spike shape design

The spiking signal is characterized by the width of the spikes and the incubation time between them (see Fig. 3.1). In this section, the spike width is shown to be controllable via different means: by adjusting the relative effective anisotropy between the SL and the HL in the presence of dipolar interaction or by applying an external magnetic field. From an application point of view, it might be interesting to provide a fairly regular spike width over a wide range of spike frequency if these spikes are designed to drive other synaptic devices [98].

Relative effective anisotropy

To control the shape of the spike, the first option consists of tuning the relative stability of the hard and soft layers. More asymmetry between layers is expected to lead to sharper spikes (SL lifetime) and longer incubation times (HL lifetime). The mean spike width is given by the SL lifetime in positive polarity and the HL lifetime in negative polarity. Fig. 3.10.a shows the evolution of the spike width for different asymmetry in terms of the effective field for positive current polarity. For high asymmetry between layers, the intermediate regime of HL reversal (around $J/J_{c0,HL} = 1$) gives a large plateau where the spike width varies only from 30 to 10 ns, while the incubation time exponentially drops from 10 us to 100 ns, corresponding to a change in the spiking frequency from 0.1 to 10 MHz. It is observed that the spike shape has little effect on the overall spiking frequency, as demonstrated in Fig. 3.10.b and as expected.

The dipolar field also affects the spike width with respect to the incubation time, promoting the parallel alignment even more. As a consequence, in the positive current polarity, the asymmetry between the incubation time and the spike width will be even more pronounced. This effect is illustrated in Fig. 3.10.a for $H_{K,SL}/H_{K,HL} = 0.6$ with and without dipolar interaction. The plateau with constant spike width increases with dipolar interaction in positive polarity.

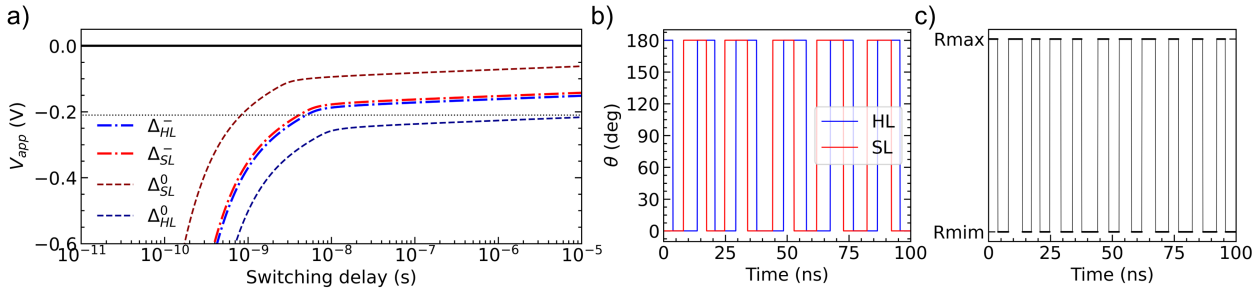

Figure 3.11: Median switching time as function of the applied bias across the MTJ for similar effective stability between the HL and SL. The associated time traces of the magnetization switches (b) and resistance (c) reconstructed from the probability distribution of the Yang's equation 3.15.

When the current polarity is reversed, the dipolar interaction and STT between the layers act in the opposite direction. As a result, the energy barrier from AP to P and the P to AP transition are relatively similar (see the distribution of energy barriers in Fig. 3.6.a). This negative current polarity can exhibit a more evenly balanced signal between the P and AP states. If the relative anisotropy of the layer is fine-tuned with respect to the dipolar field, it is possible to obtain a signal with a 50/50 distribution between the P and AP states, as represented in Fig. 3.11. This unbiased type of signal can be interesting for implementation of a true random number generator (TRNG) in the thermally activated regime.

External magnetic field

Finally, the spiking signal is expected to change with the application of an external magnetic field in the perpendicular direction. As reported in Fig. 3.6.b, all transitions from one configuration to the other show a unique energy barrier, which also depends on the current polarity. In total, different energy barriers (four for each current polarity) are expected to be observable in the time traces as distinguishable lifetimes, noted $\tau_{SL,HL}$. Note that the first and second indexes of the lifetimes τ refer to the SL and HL orientations, so $\tau_{\uparrow\downarrow}$ refers to the configuration where the SL points up and the HL points down. The four positive polarity energy barriers associated with their lifetime $\tau_{SL,HL}$ are expressed as follows :

$$\Delta^{+}_{HL,\uparrow} = \Delta_{HL,0}.(1 - \frac{-H_{dip} - H_{app}}{H_{K,HL}}) \rightarrow \tau_{\uparrow\uparrow} \tag{3.28}$$

$$\Delta^{+}_{HL,\downarrow} = \Delta_{HL,0}.(1 - \frac{-H_{dip} + H_{app}}{H_{K,HL}}) \rightarrow \tau_{\downarrow\downarrow} \tag{3.29}$$

$$\Delta^{+}_{SL,\uparrow} = \Delta_{SL,0}.(1 - \frac{H_{dip} - H_{app}}{H_{K,SL}}) \rightarrow \tau_{\uparrow\downarrow} \tag{3.30}$$

$$\Delta^{+}_{SL,\downarrow} = \Delta_{SL,0}.(1 - \frac{H_{dip} + H_{app}}{H_{K,SL}}) \rightarrow \tau_{\downarrow\uparrow} \tag{3.31}$$

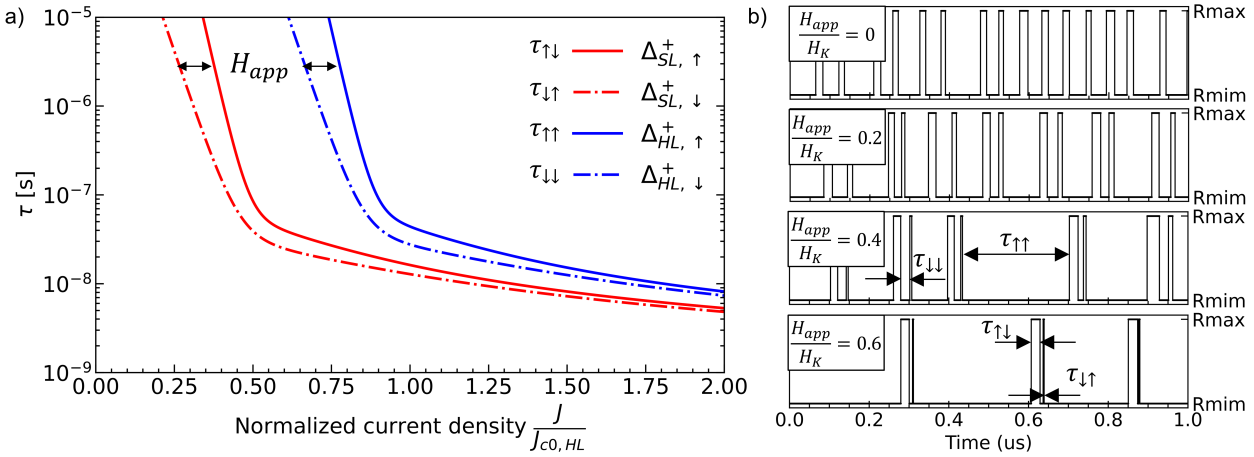

Figure 3.12: a) Median switching time of the different transition involved in the windmill dynamic in presence of an external magnetic field. The two configurations corresponding to the AP and P states shows different lifetimes, and the shift increases with stronger applied magnetic field. b) Example of time traces extracted from the unified model for different ratio of $\frac{H_{ext}}{H_K}$. The asymmetry between the two lifetimes involved in each state (P and AP) increases with the intensity of the external magnetic field applied.

Similarly, it is possible to define the other 4 energy barriers in the negative polarity as :

$$\Delta^-_{HL,\uparrow} = \Delta_{HL,0}.(1 - \frac{H_{dip} + H_{app}}{H_{K,HL}}) \rightarrow \tau_{\downarrow\uparrow} \tag{3.32}$$

$$\Delta^-_{HL,\downarrow} = \Delta_{HL,0}.(1 - \frac{H_{dip} - H_{app}}{H_{K,HL}}) \rightarrow \tau_{\uparrow\downarrow} \tag{3.33}$$

$$\Delta^-_{SL,\uparrow} = \Delta_{SL,0}.(1 - \frac{-H_{dip} - H_{app}}{H_{K,SL}}) \rightarrow \tau_{\uparrow\uparrow} \tag{3.34}$$

$$\Delta^-_{SL,\downarrow} = \Delta_{SL,0}.(1 - \frac{-H_{dip} + H_{app}}{H_{K,SL}}) \rightarrow \tau_{\downarrow\downarrow} \tag{3.35}$$

Fig. 3.12.a illustrates the expected switching delay between the four configurations when applying a positive current. The two parallel configurations ($\tau_{\uparrow\uparrow}$ and $\tau_{\downarrow\downarrow}$) present a higher lifetime compared to the antiparallel configurations, due to the help of the current polarity and the dipolar field. The shift between the two AP and two P states is attributed to the external magnetic field. In the reconstructed time traces of Fig. 3.12.b, the increase in the magnetic field amplitude makes the asymmetry clearly visible. Using an external magnetic field is the only way to identify with certainty the magnetic configuration as a function of time from resistance time traces. Without any external magnetic field, the two AP and P states are completely inseparable.

3.2.6 Energy efficiency

The energy efficiency is at the core of every new architecture trying to compete with CMOS based computing technology. In particular, it was previously shown that the main contribution in Spiking neural networks based on SRAM for data retention was that the consumption came mainly from synaptic weight storage compared to the computing part. As it is too early to envision the global working principle of the SNN

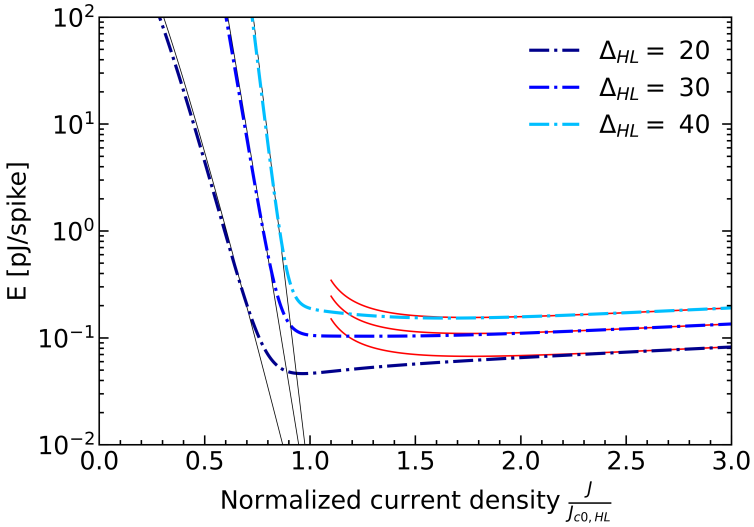

Figure 3.13: a) Energy per spike as a function of the normalized current density for different values of the thermal stability factor. The most efficient switching region is shown to be in the intermediate switching regime.

compatible with the dual free-layer MTJ at this stage, the energy efficiency will be evaluated through an average of the energy needed to produce one single spike. The energy per spike can be calculated as follows:

$$E_{/spike} = RA_P \, J^2 \, A \, \frac{1}{f} \tag{3.36}$$

The evolution of the energy per spike in the thermally assisted and precessional regime is shown in Fig. 3.13. The energy per spike is minimal in the intermediate regime, where it drops exponentially from the thermally assisted regime before increasing slightly in the precessional regime. The value plotted in Fig. 3.13 considers the same approximations as those made in the frequency calculation in Section 3.2.4. The resistance is considered constant and equal to RA_P ($RA_P = 9\ \Omega.\mu m^2$) in the calculation of the energy per spike. However, if the signal mainly populates the AP state, the assumed RA value should be RA_{AP}. Reducing the RA product and the diameter of the device drastically reduces the power consumption of the device according to the equation 3.36.

It is crucial to note that the Yang expression, the Néel-Brown model, and the Sun model rely on several assumptions which may not necessarily hold in our scenario. Furthermore, the layers are expected to switch one by one, which means that θ_{SL} (θ_{HL}) is constant at 0 or 180 degrees during the HL (SL) switching. In the next section, the validity of these assumptions is investigated through macrospin simulations.

3.3 Macrospin simulation

3.3.1 Coupled LLG-S equations for macrospin simulations

The two macrospins used for the simulation are based on the same geometry as the energy calculation in the previous section. However, the hypotheses underlying the macropsin simulations are less restrictive than the STT switching model presented earlier. Specifically, they are not limited to high-energy barriers or any assumptions derived from the reference layer orientation. The simulation results in this section are obtained by solving, step by step, the two coupled LLG-S equation [43, 57] (Eq. 3.37) representing the magnetization HL and SL :

$$\frac{\partial \mathbf{m_i}}{\partial t} = -\frac{\gamma_0}{(1+\alpha_i^2)}\Big(\mathbf{m_i} \times \mathbf{H_{eff_i}} + \alpha \mathbf{m_i} \times (\mathbf{m_i} \times \mathbf{H_{eff_i}})\Big),\ for\ i \in [\text{SL,HL}] \tag{3.37}$$

$$\text{with : } \mathbf{H_{eff_i}} = \mathbf{H_{demag,i}} + \mathbf{H_{anis,i}} + \mathbf{H_{ext,i}} + \mathbf{H_{ST,ij}} + \mathbf{H_{dip,ij}} + \mathbf{H_{th,i}} \tag{3.38}$$

The effective field $\mathbf{H_{eff_i}}$ of the magnetic layer $i \in$ [SL, HL] takes into account the following contributions:

- Anisotropy field : $\mathbf{H_{anis,i}} = \dfrac{2K_u}{\mu_0 M_s}(\mathbf{m} \cdot \mathbf{u_k})\mathbf{u_k}$ with $\mathbf{u_k} = (0,0,1)$
- Dipolar field : $\mathbf{H_{dip,ij}} = -\dfrac{M_s}{Vol_i}\Big(\mathbf{N_{dip_i}} \cdot \mathbf{m_j}\Big)$
- Demagnetizing field : $\mathbf{H_{demag,i}} = -\mathbf{N_i} \cdot M_s \cdot \mathbf{m_i}$
- Spin torque : $\mathbf{H_{ST,ij}} = \dfrac{\hbar}{-2e}\dfrac{\eta}{\mu_0 M_s\, t_i}\dfrac{V}{R_p\, S}(\mathbf{m_i} \times \mathbf{m_j})$; with $\eta = \dfrac{\sqrt{TMR(TMR+2)}}{2(TMR+1)}$
- Thermal field : $\mathbf{H_{th,i}} = \Gamma_i(t)\sqrt{\dfrac{2\ \alpha_i\ k_B\ T}{\gamma_0\ \mu_0 M_s\ Vol_i\ \delta t}}$
- External magnetic field : $\mathbf{H_{ext,i}}$

3.3.2 Validity of the STT switching model

In this section, the investigation focuses on assessing the validity of the extended Yang's model using macrospin simulation with dipolar interaction. In particular, the hypothesis concerning the strict sequential switching of the layer is important to validate.

Fig. 3.14.a.b once again illustrates the energy landscape of the system without and with the dipolar field for macrospin model. The critical voltage for a median switching time of 100 ns is calculated from the unified macrospin model in Fig. 3.14.c as a function of the thermal stability factor for different intensity of the dipolar interaction. For example, a HL with an energy barrier of 29 $k_B.T$ without dipolar interaction has a critical switching voltage of about 0.11 V. Taking into account the stray field from the SL, noted as H_{dip}, the ratio $H_{dip}/H_{K,HL}$ is equal to 0.28. The HL critical voltage is pushed to 0.18 V in the positive current polarity, while it is reduced to 0.04 in the negative one. The same calculations are done for the SL and both, $V^{\pm}_{100,HL}$ and $V^{\pm}_{100,SL}$, are reported in 3.14.a.b for both current polarities. These values are then compared with the macrospin simulations. The temporal evolution of the SL and HL magnetization derived

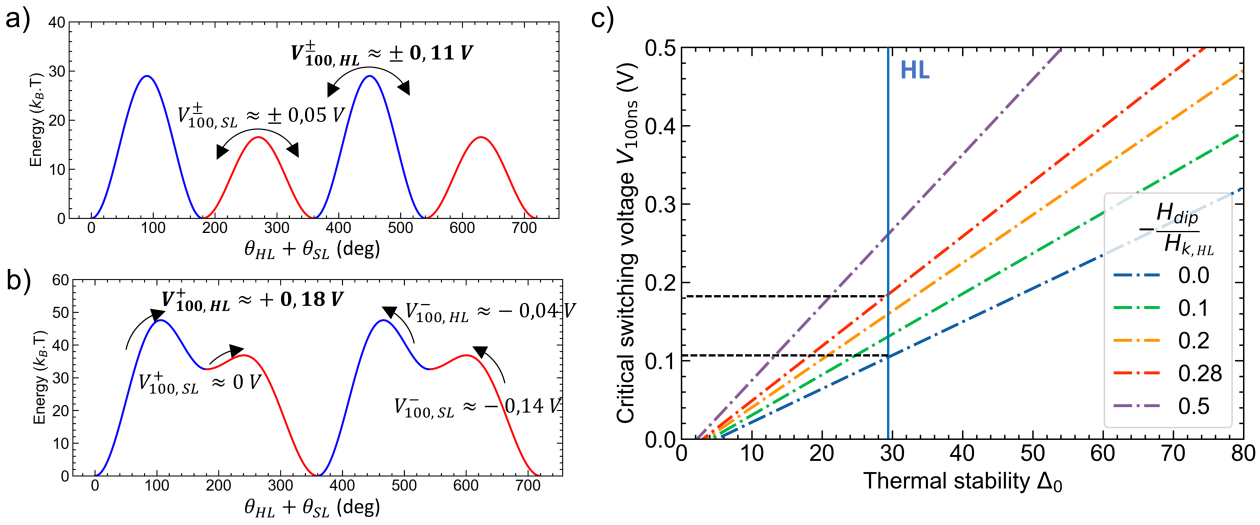

Figure 3.14: Energy barriers of the system without (a) and with (b) dipolar interaction. c) Critical switching voltage at 100 ns for different value of the thermal stability factor and dipolar field contribution. The critical switching voltage associated to a energy barrier of 29 $k_B.T$ is predicted to be around 0.11 V without dipolar interaction and 0.18 V with dipolar interaction respectively.

from macrospin simulations is depicted in 3.15.a.b. In the absence of a dipolar field, the windmill dynamics starts at approximately $\pm$ 0.12 volts. This behavior aligns with the predicted thermally activated switching of the HL, which occurs at approximately $\pm$ 0.11 volts (as seen in Fig. 3.15.a.c).

However, when accounting for the dipolar field interaction between the layers, the critical switching current at 100 nanoseconds deviates from the anticipated value according to the analytical model, particularly in the positive polarity. Furthermore, a clear manifestation of non-coherent switching is observed in positive polarity (Fig. 3.15.b). These discrepancies from the model can be attributed to the invalidation of the assumption regarding the out-of-plane (OOP) orientation of the SL during the HL switching process. Indeed, the soft layer appears to start to switch before the HL has fully regained its OOP orientation. This degeneracy arises from the partial synchronization between the soft and hard layers during the transition from a parallel (P) to antiparallel (AP) configuration. Singularities also appear even in the absence of the dipolar field. Partial synchronization can be observed in positive polarity during HL reversal, although this effect has less impact on windmill dynamics compared to the case with dipolar interaction.

As synchronization is detrimental to the windmill dynamic, the factors that cause synchronization are analysed in the next section and some ways to mitigate it are explored. This study is based on both analytical approaches and numerical calculations using macrospin simulations.

3.3.3 Synchronization of the SL and HL in the positive polarity

The initial step involves defining the term "synchronized" within the context of the two-free-layer system. To simplify the approach, the 2D space problem (θ, ϕ) is reduced to a 1D space assuming that both layers rely always on the (x,z) plane ($\phi_{SL} = \phi_{HL}$) of Fig. 3.16. This plane is convenient because the mutual contributions of the STT and the damping result in forces within this plane and vary only θ, while the precession around the effective field is confined in the perpendicular direction. The positions of HL and SL are then totally determined by θ_{HL} and θ_{SL} respectively. The precession frequency (around z) is calculated directly from the

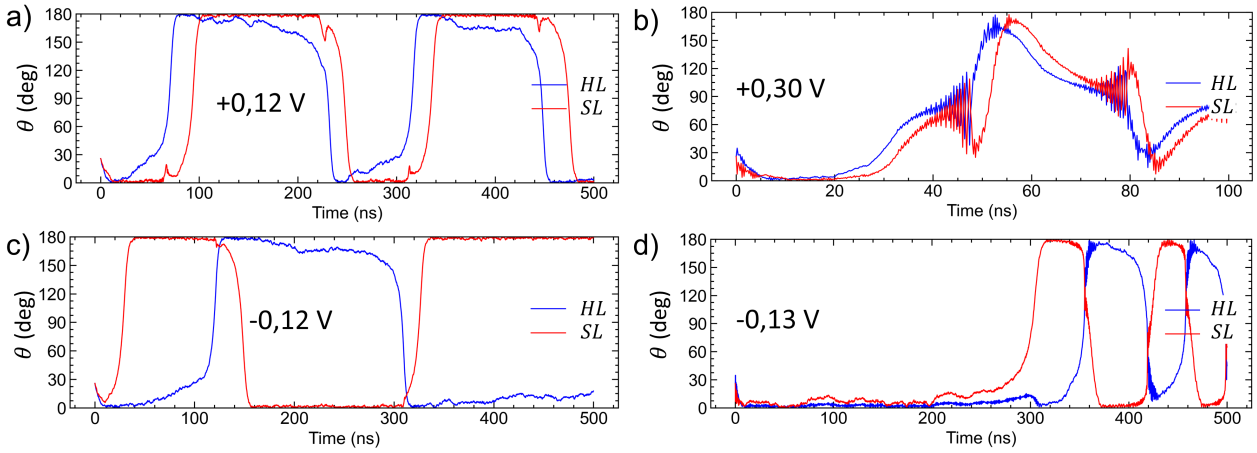

Figure 3.15: Macrospin simulations corresponding to the energy landscape of Fig. 3.14.a.b for positive (a-b) and negative (c-d) voltage bias. In case of (b) the dipolar field disturbs significantly the windmill dynamics due to partial synchronization of the SL and HL.

LLG-S equation for different configurations of the SL and HL. A configuration is referred to as "in-plane synchronized" when both layers exhibit the same precession frequency, ensuring that $\frac{\partial \phi_{SL}}{\partial t} = \frac{\partial \phi_{HL}}{\partial t}$ (see Fig. 3.16.c). However, the values of $\dot{\theta_{HL}}$ and $\dot{\theta_{SL}}$ may differ. When synchronization occurs, the frequency shift between the two magnetizations becomes zero. By this simple approach, the frequency shift between the hard and soft layers is calculated and plotted in Fig. 3.17 for different values of (θ_{HL},θ_{SL}).

In the absence of a dipolar field, the frequency shift near (θ_{HL},θ_{SL}) equal to (0,0) is very large, so that the 2 layers do not synchronize easily (Fig. 3.17.a). It is only when θ_{HL} approaches 60 degrees that the frequency shift crosses 0, meaning that the precession frequency is the same for both layers. Note that this crossing will always occur in this polarity of switching because HL has a higher anisotropy field than SL, making its precession frequency starting at a higher value compared to SL. When going in-plane, the HL precession frequency drops to 0 and passes through the SL precession frequency systematically. The lock-in range between the two layers is expected to be centered around the 0 frequency shift, highlighted by a white line in Fig. 3.17. The locking range for a small value of θ_{SL} is around 60°. It correlates with the observations of the macrospin simulation in 3.15.a where the SL magnetization presents a kink during the HL reversal, exactly in these 50-60 °.

In the presence of a dipolar field (Fig. 3.17.b), the 0 frequency shift curve starts more progressively from (θ_{HL}, θ_{SL}) equal to (0,0). As the hard layer starts to switch (that is, θ_{HL} increases), the path suggested by the in-plane synchronization makes the soft layer immediately follow the hard layer (i.e., θ_{SL} also increases). This synchronization is only possible if the SL is reactive to the HL dynamics as this 0 frequency shift curve only shows the quasi-equilibrium solution. As the STT prefactor of the SL (affecting $\dot{\theta_{SL}}$) is expected to be more important than the one of the HL (affecting $\dot{\theta_{HL}}$), this condition must be respected.

According to the macrospin simulations in Fig. 3.15.b, the in-plane synchronization appears to occur. During the initial phase of the reversal, the dipolar field helps to synchronize by promoting parallel alignment of the layers. However, beyond a critical angle, the antiparallel alignment of the layers is preferred by the dipolar field. In that particular region, the STT push back the SL out of plane, which again fall into a preferred synchronized state. This competition between the dipolar field and the STT, depending on the angle of the layers, creates an oscillation visible in the magnetization versus time near 90 °. Eventually, this decoupling

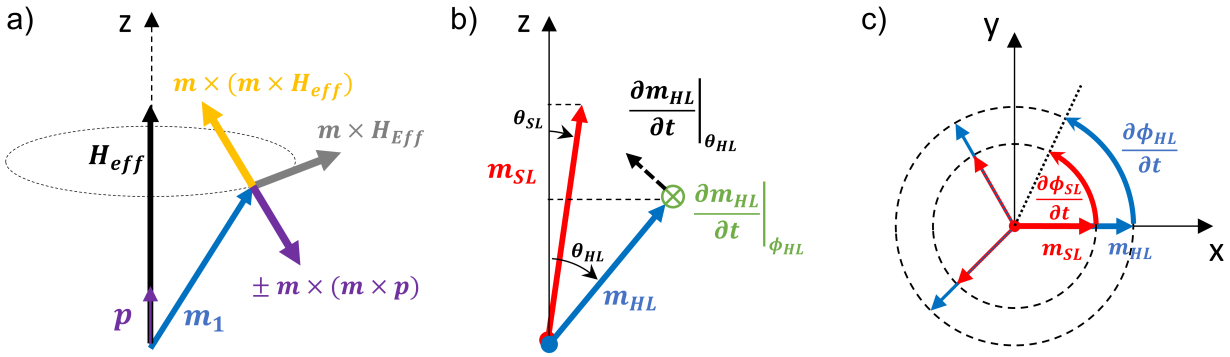

Figure 3.16: (a) 3D representation of the forces acting on a magnetization considering LLG-S equation. b) Introduction of θ_{SL} and θ_{HL} to locate the HL and SL with respect to the perpendicular z-direction. In this polar coordinate, the precession term is fully described by the ϕ component while the damping and STT term and damping term acts on the θ component. c) In-plane synchronization between HL and SL where both layer exhibit same precessional frequency and the SL remains in the plane form by the z-axis and the HL direction (m_{HL} vector).

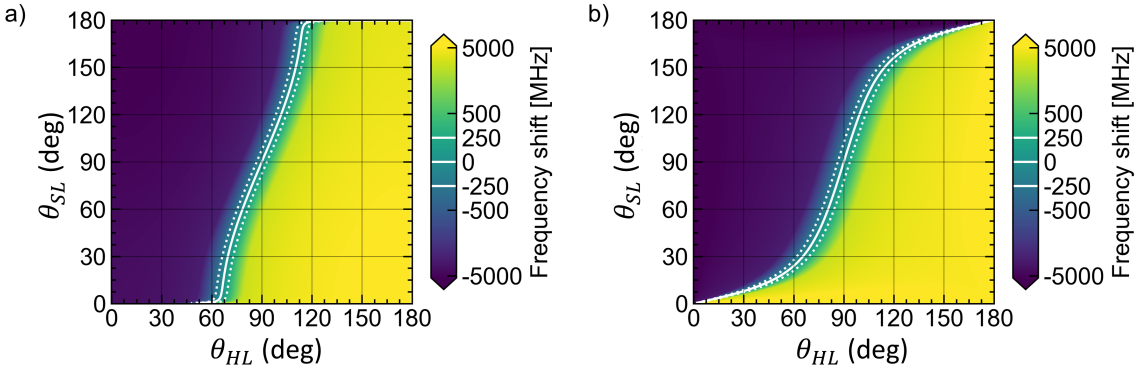

Figure 3.17: Frequency shift between the hard and the soft layer without dipolar (a) and with dipolar interaction (b). The in-plane synchronized state is represented by the white line and the dotted lines refer to +/- 250 MHz of frequency shift between the layers.

leads to a complete switch of the SL and HL layers.

Determining the exact locking range between the hard and soft layer is a challenge. However, previous studies on STNO showed that this calculation is possible through the expression of c-variable LLG-S [59, 112]. The empiric demonstration here can serve as a starting point for a more detailed study on the synchronization of this singular dual free-layer structure. However, from this analysis, the dipolar field has been identified to be the cause of major synchronizations between the SL and the HL in positive polarity. To significantly reduce this impact on the windmill dynamic, two different approaches are proposed in the next section.

The first approach consists of reducing the impact of the dipolar field with respect to the effective anisotropy field of both layers. Fig. 3.18.a shows the 0-frequency change between HL and SL and the effect of a different ratio of $H_{dip}/H_{K,HL}$, while the ratio $H_{K,SL}/H_{K,HL}$ remains constant at 0.4. Reducing the ratio of $H_{dip}/H_{K,HL}$ delays the critical angle for which the SL starts to deviate from 0 degrees (out-of-plane position). The limit case $H_{dip}/H_{K,HL} \rightarrow 0$ overlaps the case without dipolar interaction where the frequency shift is so large from θ_{HL} equal to 0 to 60 °that the two layers are not synchronized and θ_{SL} stays close

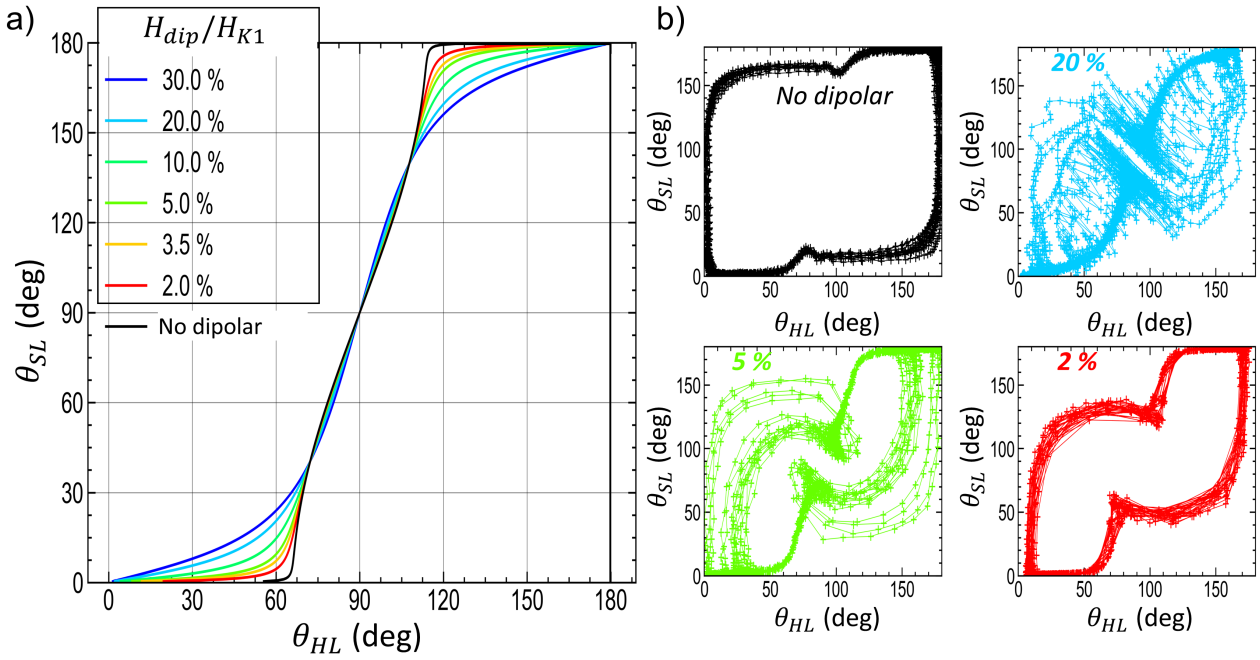

Figure 3.18: (a) IP-synchronized trajectory between HL and SL and respective (b) macrospin model trajectories for different ratio of $H_{dip}/H_{K,HL}$. Increasing the effective anisotropy of both layers make the trajectories approaching the one without any dipolar field. Note that the coupling only through spin-torque is not enough to make the 2 layers IP-synchronized up to 90-90 position (black trajectory).

to 0 degrees. Note that Fig. 3.18.a considers only positive θ values that only simulate the more "parallel" orientation between the layer (i.e. positive x hemisphere). The macrospin simulation associated with some values of $H_{dip}/H_{K,HL}$ is represented in 3.18.b and qualitatively follows the calculated synchronized curves in Fig. 3.18.a in the range [0°, 80°]. The main difference is close to the (90,90) configuration around which the system oscillates. As the magnetization approaches the orientation in the plane ($\theta = 90$), the dipolar field favors the AP alignment between the two layers. The AP configuration would correspond to a negative value of θ_{SL} in which there is no sign of possible synchronization between the layers. It is why the linear part of the curve where $\theta_{HL} \in [80°, 110°]$ in Fig. 3.18.a does not overlap the macrospin simulation in Fig. 3.18.b.

In conclusion, it is only when the influence of the dipolar field is significantly diminished relative to the anisotropy field (by approximately 2%) that the system begins to exhibit behavior closer to a non-dipolar case. The cost associated with the increase of the anisotropy field raises the critical switching current for the same pillar geometry.

The second approach to modify partial synchronization involves altering the ratio of effective anisotropies between HL and SL, with a fixed value of $H_{dip}/H_{K,SL} = 0.5$. This adjustment results in an increase in the frequency shift while keeping the dipolar field constant relative to the effective anisotropy of the soft layer. As illustrated in Fig. 3.19, the onset of SL switching is progressively delayed as the asymmetry between $H_{K,HL}$ and $H_{K,SL}$ increases. The signal transitions from a highly synchronized state, represented by the blue trajectory with $H_{K,SL}/H_{K,HL} = 40\%$, to a state of nearly uncoupled switching at $H_{K,SL}/H_{K,HL} = 5\%$ (shown by the yellow trajectory). This observation suggests that a higher degree of asymmetry between the layers in terms of effective anisotropy enhances the likelihood of avoiding partial synchronization of the signal.

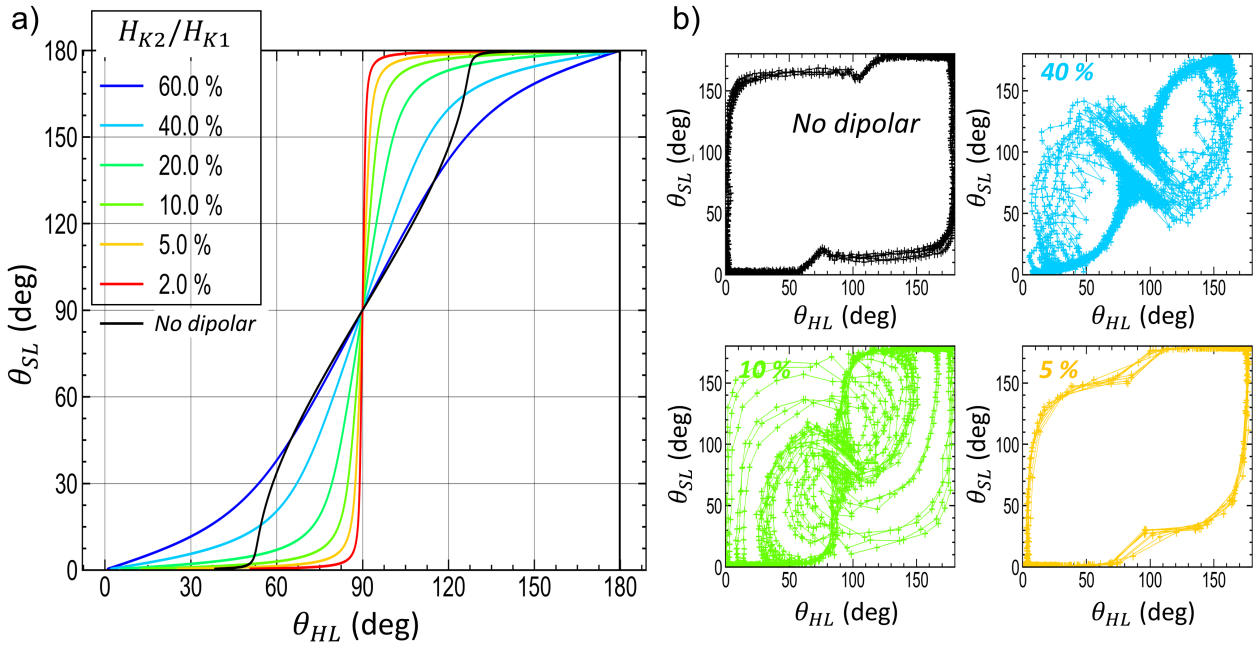

Figure 3.19: (a) in-plane-synchronized trajectory between HL and SL and respective (b) macrospin model trajectories for different ratio of $H_{K,SL}/H_{K,HL}$. By increasing the asymmetry between the two layers, the trajectory (yellow) recovers the one without dipolar interaction.

3.4 Towards realization of dual free layer MTJ

The first design (Fig. 3.20.b) emerging from the numerical analysis is composed of a simple p-MTJ structure. The asymmetry in the effective anisotropy between the hard layer and the soft layer should be quite high. It is expected that the dipolar field between the layers impacts the behavior quite significantly, particularly in one of the two current polarities. The second design (Fig. 3.20.c) mitigates the effect of the dipolar field by adding a soft SAF layer to the SL and the HL. The intended effect is to cancel out the dipolar field from both free layers. The two concepts are depicted in Fig. 3.20.b.c compared to a MRAM structure. The first design is appealing because of its simplicity of fabrication by removing the SAF structure.

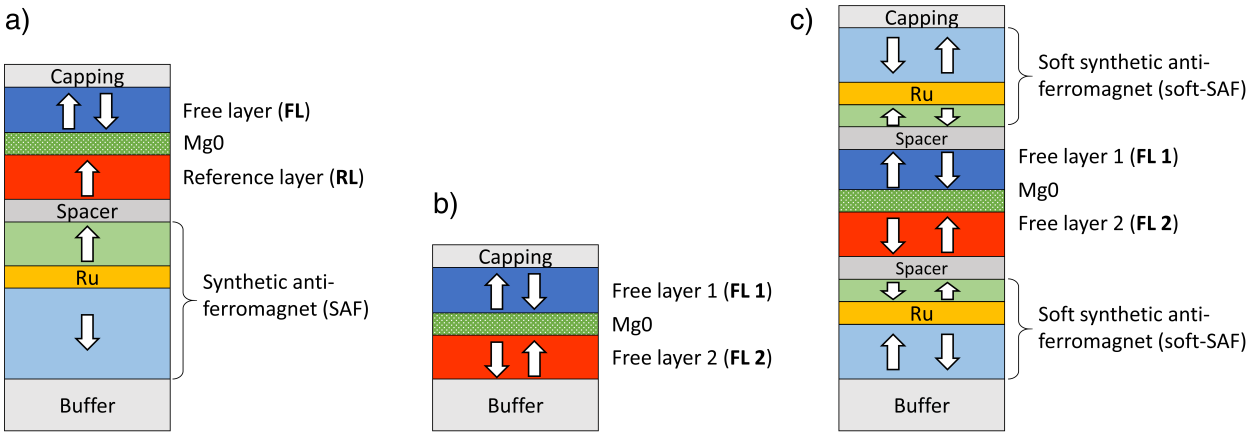

Figure 3.20: Schematic representation of (a) a MRAM structure with synthetic anti-ferromagnet, (b) a dual free layer MTJ, (c) a dual free-layer with double soft-SAF.

3.5 Conclusion

The analytical and numerical approach of the dynamics in dual free-layer MTJ yields some important conclusions on the expected behavior of the device with respect to the material parameters and external excitations. The main key points highlighted in this chapter are summarized below.

- The STT switching model available in the literature predicts that the windmill motion is achievable in positive and negative current polarity. However, the dipolar field between the layers in a dual free-layer structure is significantly impacting the windmill dynamics, making the spike signal asymmetric between positive and negative polarity. In general, positive polarity shows a spike in the high-resistance state, whereas negative polarity exhibits a short spike in the high-resistance state.

- The spiking frequency is mainly influenced by the HL reversal in the thermally assisted regime. It becomes important to also take into account the SL reversal in the intermediate and precessional regime. Decreasing the effective anisotropy of the HL and the damping shows a significant increase of the frequency in the thermally assisted regime, while the effect is attenuated in the precessional regime as a result of the decrease of the attempt frequency.

- The spike shape can be controlled either by material engineering or by an external magnetic field. Increasing the relative asymmetry between the HL and SL in terms of anisotropy enhances the spiking frequency at which the spiking time remains similar. The application of a perpendicular magnetic field affects the windmill dynamics, but should not prevent it from happening. In particular, two consecutive spikes are expected to have different spike widths when applying an external field.

- The minimal energy consumption per spike was identified to be in the intermediate switching regime. For example, an hard layer with $\Delta = 30$ is expected to show around 0.1 pJ / spike under the optimized condition.

- The conclusions envisioned from the existing STT model are based on strong assumptions, which are validated in memory-oriented devices with high retention and a single free layer. It was then needed to perform macrospin simulations to confirm the windmill dynamics in multiple cases. The simulations show good agreement with the STT switching model in the negative polarity; however, they diverge significantly in the positive polarity when considering a dipolar interaction. This dipolar field has been shown to be detrimental to the windmill dynamics. Solutions were proposed to overcome this issue, in particular by increasing the relative effective anisotropy between the SL and the HL.

The conclusions of the numerical analysis drive the conception of MTJ towards 2 different designs. The first one has a simple dual-free layer structure, and the second one has a double soft-SAF structure to reduce the impact of the dipolar field. In the next chapter, optimization of the material parameters at the sheet-film level is conducted with NanoMOKE, VSM, and FMR measurements.

Chapter 4

Material developments for dual free layer MTJ

Contents

4.1 Introduction

In the previous chapter, we discussed the essential characteristics of magnetic layers required to create windmill dynamics in structures with perpendicular magnetic anisotropy. In this current chapter, the concepts of dual-free-layer MTJ and double soft-SAF MTJ is optimized from a material point of view. In particular, the characterization of FeCoB/MgO interfaces to extract interface anisotropies will constitute a significant part of this chapter. Over several years, Spintec has developed magnetic tunnel junctions through numerous projects involving many PhD students and postdocs. Consequently, my work on stack development relies on the continuous knowledge accumulated during this time. The first part of this chapter aims to provide a brief summary of the fundamental knowledge crucial for MTJ stack development.

4.2 General stack design of MTJ at Spintec

Among the previous works at Spintec, the common knowledge concerning the development of the FeCoB/MgO/FeCoB trilayer is fundamental to the concept we want to develop in this thesis. In addition, studies related to the optimization of capping layers and the annealing procedure are extremely relevant to obtain functional MTJs. These three points are briefly summarized in this section.

4.2.1 FeCoB/MgO/FeCoB trilayer

First, the trilayer FeCoB/MgO/FeCoB is the heart of all MTJs because of the potential high TMR value provided by the crystallization of the MgO and FeCo layers. Coherent tunneling through the Δ_1 symmetry of the *s-p-d* orbitals is possible, increasing the filtering effect of the MgO barrier. However, the TMR values are very sensitive to defects in the MgO barrier. Commercialized MRAM devices demonstrate TMR values over 200% (Samsung [113], Intel [114]). However, we are not expecting to reach a TMR value as high mainly because the deposition tool does not reach ultrahigh vacuum conditions, uses natural oxidation conditions instead of RF-sputtering techniques, and is not dedicated to the development of MTJ only, making cross-contamination by other elements possible. The deposition tool employed has yielded a maximum TMR of up to 120% .

The FeCoB material brings high spin polarization of the electrons at the Fermi level necessary to provide the maximum angular momentum deposited in the other FeCoB layer by the spin-transfer torque effect. FeCoB composition is fixed at 72%, 8%, 20% for the Fe, Co and B elements, respectively. FeCoB thickness below 1 nm affects the TMR value because the spin polarization of the electrons starts to drop. Moreover, the crystalline quality of the FeCo layer increases with its thickness [115]. Then, it is preferred to target a thicker FeCoB value with respect to these two criteria.

The RA product of the stack is also an important parameter when characterizing the MTJ structure. It can be tuned by using different oxidation conditions of the MgO barrier, which depend on the oxidation time, the oxygen pressure, and the Mg thicknesses. As natural oxidation is used in our case, the Mg element is deposited in two steps. A first Mg layer is deposited on top of the FeCoB (bottom electrode), and oxygen is introduced inside the chamber, making the first Mg layer over-oxidized. Then, a second layer of Mg covers this over-oxidized MgO and pumps out excess oxygen in the first layer. Previous studies at Spintec lead to an optimal value for the second Mg thickness at 5 Å. The first Mg thickness can be optimized for different purposes and is usually around 7.5-8.0 Å.

It is also important to note that the two interfaces of FeCoB/MgO and MgO/FeCoB do not reach the same maximal value of anisotropy, and that this maximum is obtained for different values of the FeCoB layer. Higher anisotropies are obtained when the MgO layer is grown on top of FeCoB (bottom electrode side) compared to FeCoB on top of MgO (top electrode side). This phenomenon has its origin in the interface roughness of the deposition, which increases with the number and thickness of the deposited layers. On the top electrode side, the roughness is expected to be higher than that on the bottom electrode side.

4.2.2 Capping layers and texture breaker

Capping layers that cover the FeCoB layers play a crucial role in attracting the boron (B) element, allowing crystallization of the FeCo/MgO/FeCo trilayer. The FeCoB layer during the deposition of the MTJ stack remains amorphous in the presence of the B element. During the annealing procedure, the B element is trapped

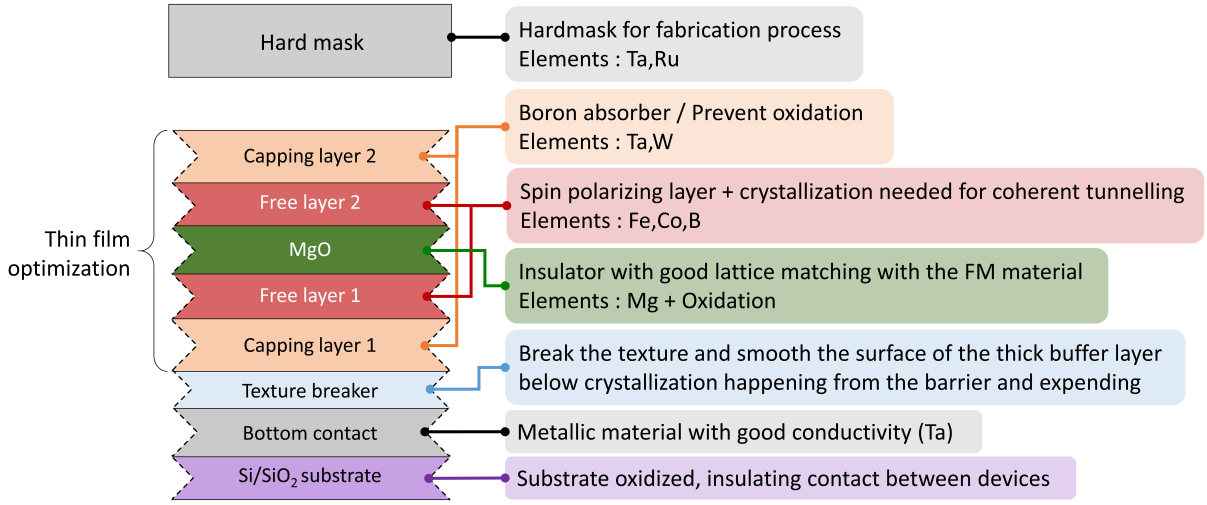

Figure 4.1: Schematic representation of a dual free layer stack

in the capping layer, making crystallization of the MgO barrier and the FeCo layer possible. Typically, the materials used for those layers are Ta or W, with increasing interest given to W because of its tolerance to higher annealing temperatures and the fact that it shows slightly higher interfacial anisotropy. This particular feature has been analyzed at Spintec by J. Chatterjee et al. [116] and Daniel S. Hazen [117]. The reason why W capping achieves better performance is attributed to the fact that Fe tends to migrate away from the MgO interface due to its higher affinity for Ta (FeTa : -3468 meV / atom) than for the W atom (FeW : -554 meV/atom) [118]. A lower amount of Fe near the MgO barrier results in a lower interfacial anisotropy.

4.2.3 Annealing condition

Annealing of the stack after deposition is required to obtain a high TMR and an interfacial perpendicular anisotropy. Three main considerations must be taken into account when defining the annealing process. The main purpose of the annealing step is to improve the crystallinity of the bcc (100) MgO phase and propagate it to the FeCo layer, while the capping layer captures the B atoms [119] [120]. The quality of the crystallization tends to increase with annealing temperature as the atoms acquire more energy to migrate, and the number of defects reduces. However, the annealing temperature is limited by the migration of the non-magnetic element of the capping layer. In fact, if the temperature is too high or maintained for too long, the material in the capping layer also starts to diffuse into the barrier, as shown in [41][121]. Consequently, the TMR and the interfacial anisotropy will drop. Finally, the stack should be resistant to a certain thermal budget equivalent to annealing at 400 °C for 30 min to meet the CMOS back end of line (BEOL) annealing requirements [122]. These three main factors set the boundaries for the optimal annealing procedure. The Spintec annealing procedure relies on a fast increase in temperature to the desired set point followed by 10 min at a stable temperature to finish with a rather quick cooling of the chamber. The free parameter is the annealing temperature, which ranges from 250 to 450 °C. The annealing step takes place under a vacuum of $5.10^{-}6$ mbar.

4.3 Dual free-layer structure

The basic structure of the dual-free layer is shown in Fig. 4.1. From the simulation studies in Chapter 3, the anisotropy of the soft and hard layers has to be significantly different to avoid partial synchronization of the layers. As the bottom electrode shows a higher interfacial anisotropy, it will be preferred to grow the hard layer on this side. On the contrary, the soft layer will be designed on the top electrode side. Second, to increase the asymmetry between the hard and soft layers, Ta will be used as the capping layer for the SL, while W will be preferred for the HL. To be able to choose the thicknesses of the different materials in the full stack, several studies on half-MTJ are first needed to isolate the contribution from the top and bottom FeCoB. Kerr mapping on a NanoMOKE® setup allows for fast investigation of magnetic properties, such as coercive field and remanence, without the need to pattern devices and measure them electrically.

As the coercive field is dependent on experimental conditions (field sweep frequency for example), it does not constitute a direct measurement of the anisotropy field but it is expected that the former evolves similarly to the latter. In order to decouple the impact of the experimental conditions from the effective anisotropy, the interfacial anisotropies have been calculated from the Kerr measurement with the methods described in section 2.3.1. We must also expect that the coercive field obtained at thin film level differs from the final coercive field of the devices. Indeed, larger coercive fields are generally demonstrated on the devices because of the absence of defects within the smaller area of the device compared to the thin film measurement. The reduction of the demagnetisation field near the edges of the pillar also contributes to this increase of coercive field.

Beyond the calculation of the interfacial anisotropy with the Kerr measurement, the coercive field mapping gives already precious information to identify the suitable values of FeCoB and MgO thicknesses. The first step will focus on the bottom W/FeCoB/MgO subsystem, while the second step isolate the top MgO/FeCoB/Ta subsystem.

4.3.1 Bottom free layer design

Half-stack MTJ of substrate/W[2]/FeCoB[t1]/MgO[t2]/FeCoB[0.4]/W[2]/Pt[5] has been deposited and annealed at 300, 325, 350, 375 and 400°C to evaluate the evolution of interfacial anisotropy and dead layer thickness with annealing temperature. Fig. 4.2 presents the out-of-plane coercivity mapping of the MTJ half-stack for different annealing temperatures. In the as-deposited sample, the interfacial anisotropy is weak, whereas it becomes significant after the first annealing step at 300°C. Annealings at 325°C and 350°C give rise to a similar value of the coercive field, while a decrease in coercivity is observed after annealing at 375°C. The MOKE signal can be used to calculate the dead-layer thickness and interfacial anisotropy by assuming the saturation magnetization value of the FeCoB layer at 1.5 MA/m. In Fig. 4.3.a, the dead layer thickness (0.4 nm) is extracted by extrapolating the out-of-plane magnetized region with 100% of remanence after annealing at 350°C. The dead layer thickness increases as the annealing temperature rises due to intermixing at the FeCo / W interface (Fig. 4.3.b). The estimation of the interfacial anisotropy was carried out using the in-plane magnetized region of the wafer (i.e. for thicker FeCoB). The anisotropy field is calculated from the area under the curve in the case of in-plane magnetization. The evolution of this area with different thickness values is used to extract the interfacial anisotropy as described in 2.3.1. Figure 4.4 shows the evolution of the interfacial anisotropy with the annealing temperature considering a saturation magnetization of the $Fe_{72}Co_8B_{20}$ at 1.5 MA/m. The saturation magnetization is fixed at 1.5 MA/m according to other recent

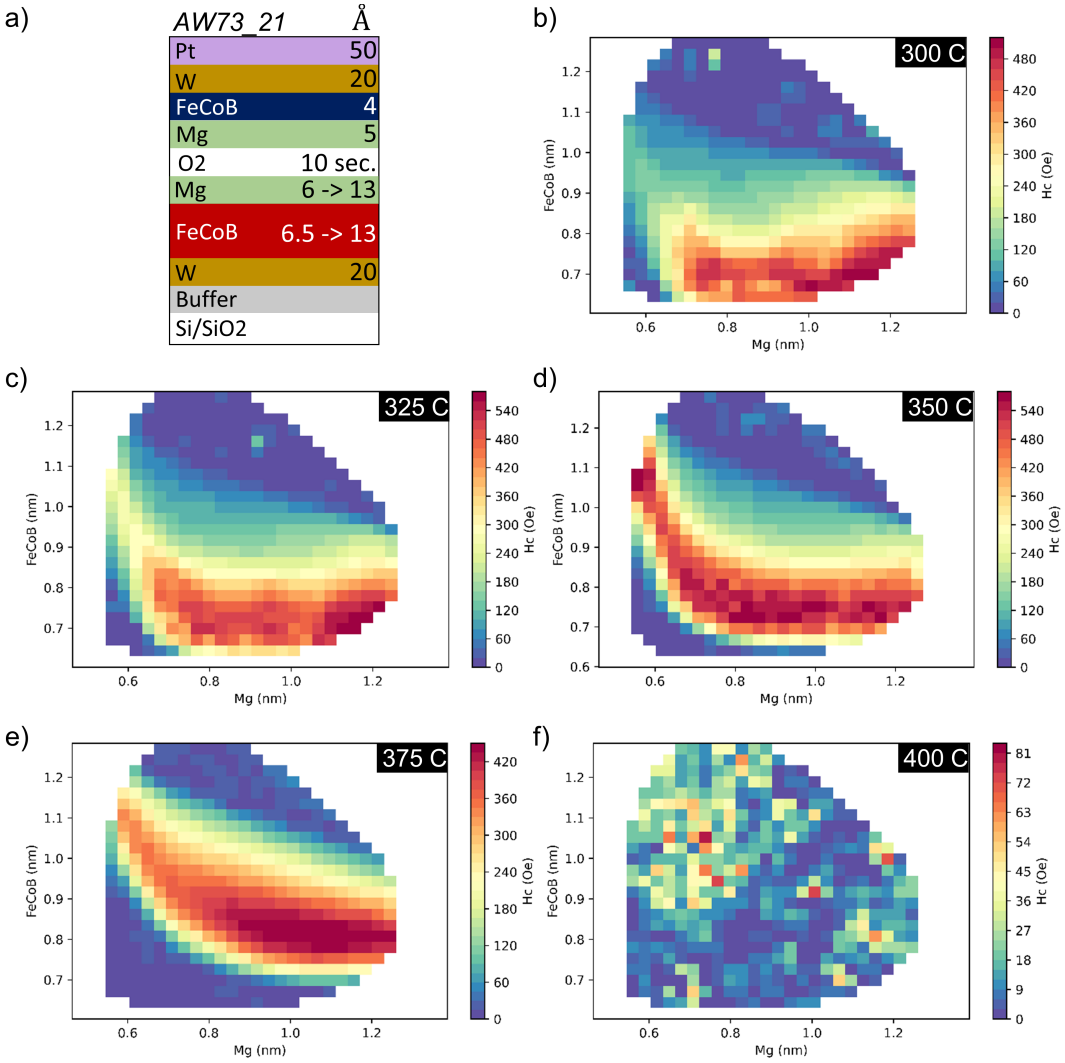

Figure 4.2: a) Half-MTJ structure composed of bottom W/FeCoB/MgO electrode with cross-wedges on FeCoB and bottom Mg layer. (b-f) Coercivity mapping at different annealing temperature of the half-MTJ structure (a).

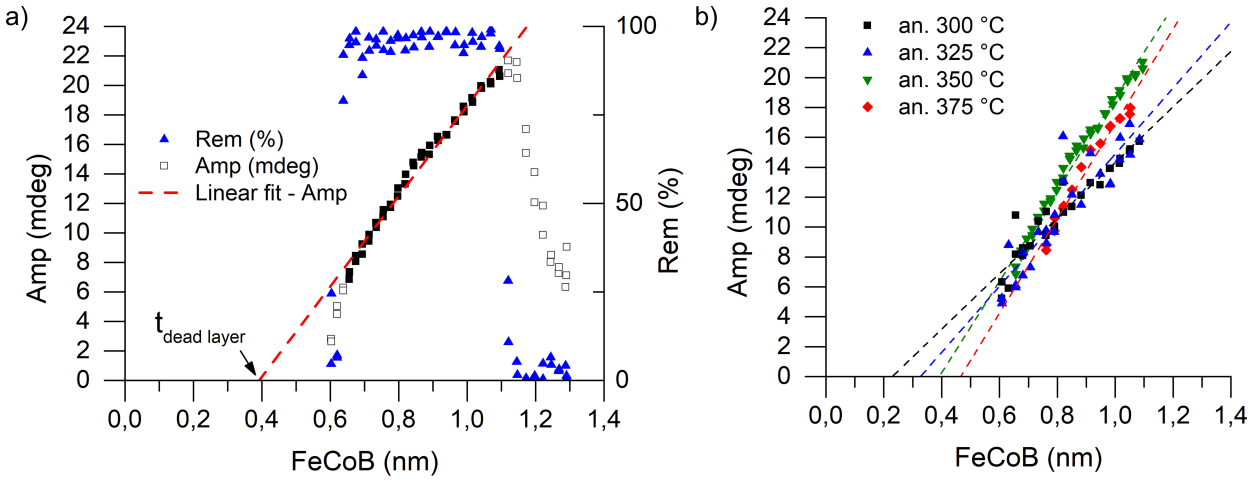

Figure 4.3: (a) Amplitude of the MOKE signal as function of the FeCoB thickness for a bottom Mg thickness of 8.5 Åafter annealing the sample at 350°C. The extrapolation to 0 amplitude of the linear fit in the 100% remanence region lead to the dead layer thickness of 0.4 nm. (b) Dead layer calculation for 300°C, 325°C, 350°C, 375°C of annealing temperature.

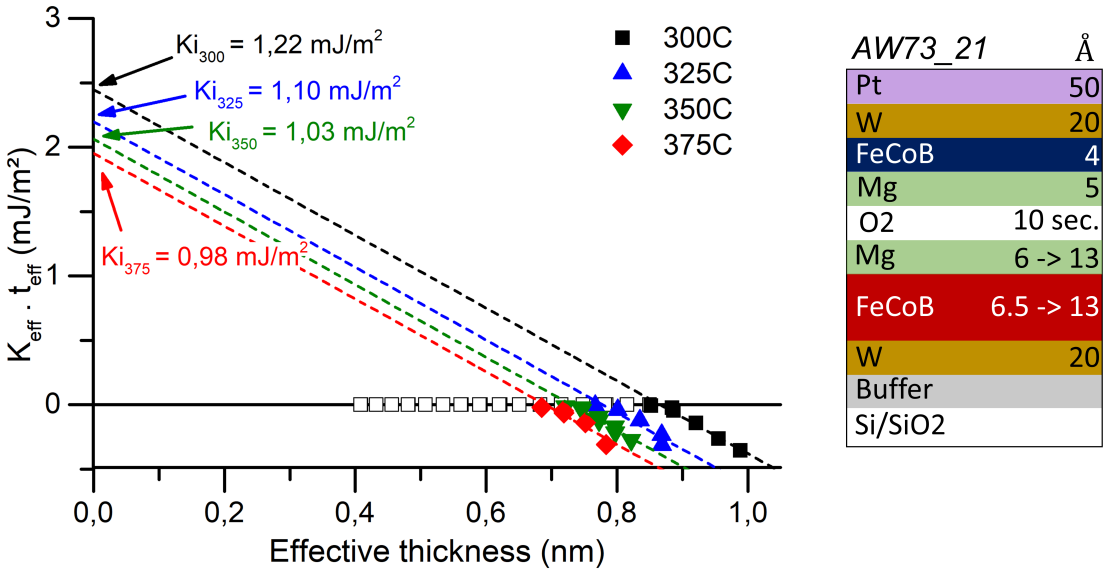

Figure 4.4: Extrapolation of the interfacial anisotropy from the effective anisotropy energy obtained with out-of-plane MOKE measurement of in-plane magnetized region. The interfacial anisotropy is maximal after the first annealing at 300°C and progressively drops with higher annealing temperature.

Year	From	Structure	Ann. Temp (C)	Ms (kA/m)	Ki (mJ/m²)	t_d (Å)
2015	L. Cuchet	MgO/FeCoBx/Ta1/Pt2	300	1240	1.1	6.0
2017	J. Chatterjee	Mg0(1.2)/FeCoB(t)/Ta1/Pt3	315	1216 ± 26	0.78 ± 0.02	5.5
2017	J. Chatterjee	Mg0(1.2)/FeCoB(t)/Ta1/Pt3	340	1262 ± 14	0.87 ± 0.03	5.6
2017	J. Chatterjee	Mg0(1.2)/FeCoB(t)/Ta1/Pt3	400	1252 ± 54	0.85 ± 0.025	6.1
2017	J. Chatterjee	Mg0(1.2)/FeCoB(t)/W2/Ta1/Pt3	340	1210 ± 26	1.02 ± 0.037	5.5
2017	J. Chatterjee	Mg0(1.2)/FeCoB(t)/W2/Ta1/Pt3	400	1368 ± 49	1.06 ± 0.028	6.25
2017	J. Chatterjee	Mg0(1.2)/FeCoB(t)/W2/Ta1/Pt3	425	1340 ± 50	1.05 ± 0.034	6.2
2017	J. Chatterjee	Mg0(1.2)/FeCoB(t)/W2/Ta1/Pt3	455	1375 ± 41	1.13 ± 0.038	6.5
2022	C. Fillion	Ta/FeCoB/TaOx	300	1480 ± 60	-	6.1 ± 0.3
2023	J. Urrestarazu	.../MgO/FeCoB/W	300	1630	-	5.1

Table 4.1: Summary of the magnetic properties of FeCoB deposited at Spintec since 2015. The values are extracted from [115, 123–125] Note that all the half-stacks in the table probe properties of the top electrode side.

measurements of this properties at Spintec carried out by C. Fillion [123] and J. Urrestarazu [124]. Previous values of saturation magnetization and interface anisotropy are summarized in table 4.1.

To compare this result with the Ta capping layer, we deposited the same stack, with Ta replacing the W. Assuming a constant M_s at 1.5 MA/m, the interfacial anisotropy measured for the Ta capping was 13% less ($Ki_{350}(\mathrm{Ta}) = 0.89$ mJ/m²) than the one obtained with W ($Ki_{350}(\mathrm{W}) = 1.03$ mJ/m²) after annealing the samples at 350 °for 10 minutes (Fig. 4.5). For this reason, it is more interesting to keep the W capping to promote higher interfacial anisotropy on the bottom electrode side. Furthermore, the dead layer is slightly thicker for Ta ($t_{DL}(\mathrm{Ta}) = 5.0$ Å) compared to W ($t_{DL}(\mathrm{W}) = 3.9$ Å) for the same annealing temperature (see Fig.8.1.a in Appendix 8.1).

The reason why the W capping demonstrates better interfacial anisotropy at MgO/FeCoB interface is still unclear. First hypothesis relies on the different crystallization state of the MgO. S.-E. Lee *et. al* [126] shows that in p-MTJ with Ta capping, the Ta atoms migrate significantly into the MgO barrier compared to the equivalent stack with W capping after annealing at 400 °C. It results in a degradation of the MgO crystalline structure in the case of Ta capping layer while the stack with W capping demonstrates an almost complete fcc(100) crystalline structure of the MgO. The authors also demonstrate higher solubility of the Fe and Co atoms in the Ta capping compared to the W capping. This hypothesis is also demonstrate by J. Chatterjee [115, 116] which shows less Fe element at the MgO/FeCoB interface with Ta capping with secondary-ion mass spectrometry (SIMS) measurement. For a perspective to this work, imaging the stacks through transmission electron microscopy (TEM) could be an interesting approach in order to confirm the effects of the capping element on the crystallinity of the MgO barrier. Nevertheless, the increase in the interfacial anisotropy with W is not drastic, so we could also use Ta as a capping layer for the bottom FeCoB layer.

4.3.2 Top free layer design

As we aim for a weaker interfacial anisotropy on the top side of the MgO barrier, a Ta layer of 20 Å serves as a capping layer on the top FeCoB free layer. A half-MTJ stack with magnetically dead FeCoB layer

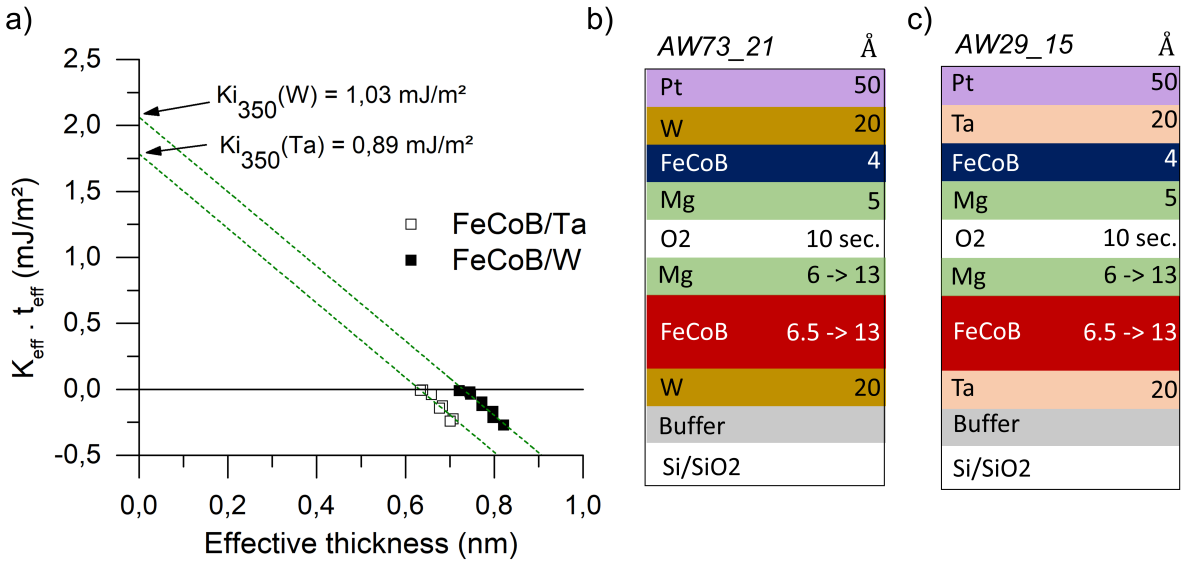

Figure 4.5: (a) Bottom interfacial anisotropy calculation from MOKE measurement in the case of (b) W and (c) Ta bottom cap layer.

in the bottom has been deposited to compare it with its equivalent bottom half-MTJ. From the coercivity mapping of the MOKE measurement, a significant difference can be observed as to whether the top or bottom of the MgO interface is used to induce PMA. The maximum coercive field obtained with the bottom Ta/FeCoB/MgO is twice that of the top MgO/FeCoB/Ta trilayer as shown in Fig. 4.6. To confirm that this change in coercivity is due to a decrease in the interfacial anisotropy, we must proceed to the extraction of the dead layer thickness and to the calculation of the interfacial anisotropy. The dead layer in the top FeCoB layer ($t_{DL}(\text{top}) = 7.7$ Å) is 50% thicker than the value found for the bottom FeCoB ($t_{DL}(\text{bottom}) = 0.5$ Å). This result is in agreement with previous results obtained from L. Cuchet at Spintec [125]. This might be due to the sputtering condition, where the Ta atoms, when deposited on top of the FeCoB layer, can damage the surface of FeCoB (Ta is heavier than the Fe and Co atoms), leading to more intermixing at the Ta/FeCoB interface.

In terms of interfacial anisotropy, it turns out that both sides of the MTJ show similar values: $Ki_{350}(\text{top}) = 0.87$ mJ/m² and $Ki_{350}(\text{bot}) = 0.89$ mJ/m². Calculating interfacial anisotropy, considering a constant M_s at 1.5 MA/m, results in $Ki_{300} = 0.96$ mJ/m² and $Ki_{350} = 0.87$ mJ/m² after annealing at 300 °C and 350 °C, respectively.

4.3.3 Soft layer with Ru/W capping

To further reduce the anisotropy of the soft layer, we investigated the case of an insertion of Ru between the FeCoB and the capping layer of the top electrode. In the case of Ru insertion, the B elements are expected to diffuse less into the W layer, reducing the crystallization of the FeCoB layer. The coercive field decreases significantly when the Ru insertion layer is added, as demonstrated in Fig.4.8. Despite the important reduction of the coercive field with Ru/W capping, the out-of-plane remanence of the magnetization remains close to 100 % from 1.2 to 1.4 nm of FeCoB. In the reference sample with W capping, the coercive field reaches 600 Oe at 1.15 nm of FeCoB while the remanence is maximal from 1 to 1.55 nm of FeCoB. The

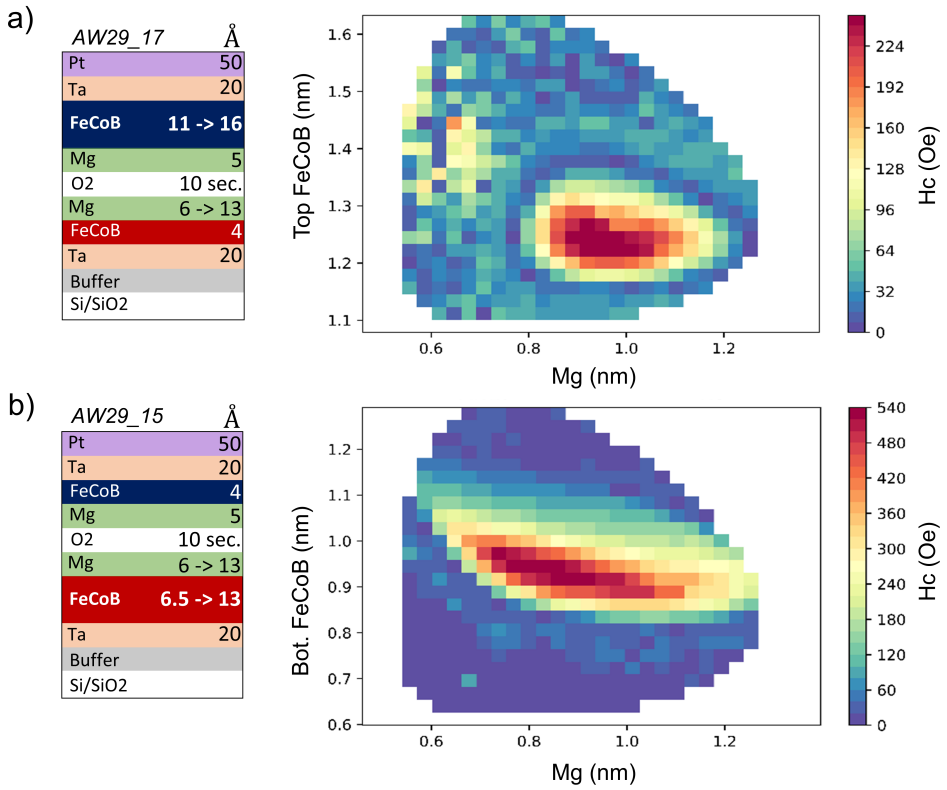

Figure 4.6: Coercive field mapping from MOKE measurement on half-MTJ stack composed of (a) only top MgO/FeCoB/Ta and (b) only bottom Ta/FeCoB/MgO.

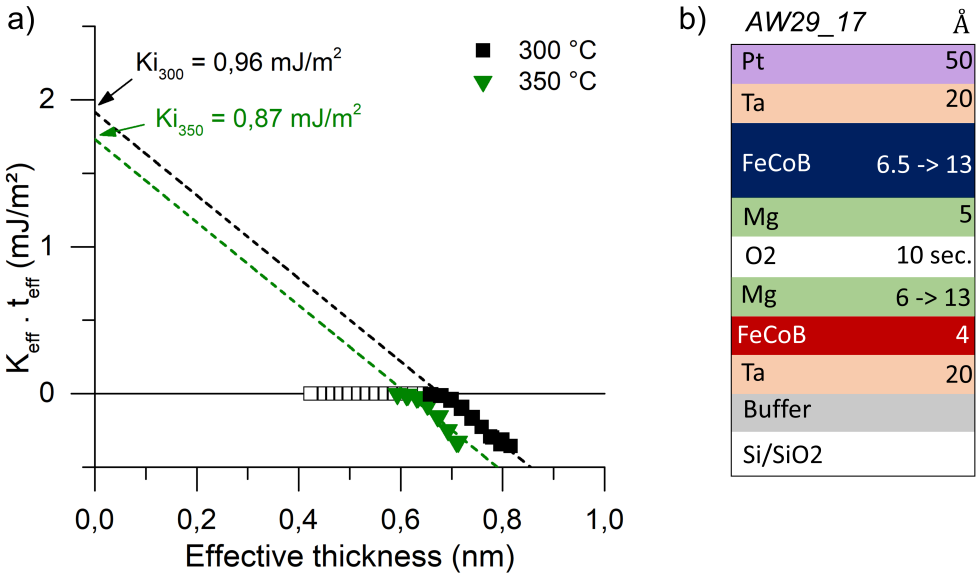

Figure 4.7: (a) Top interfacial anisotropy calculation from NanoMOKE measurement in the case of Ta capping layer. (b) The stack structure corresponding to the measurement in (a).

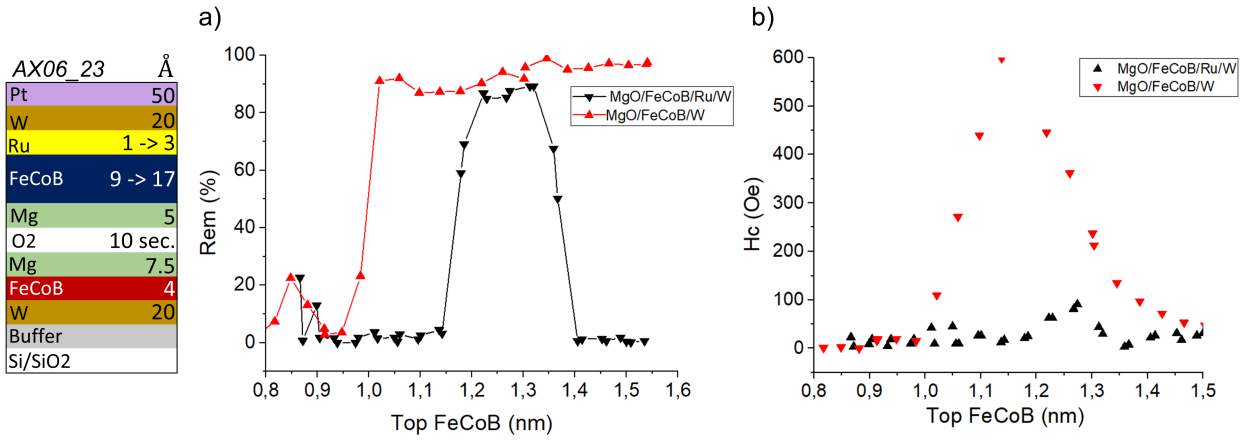

Figure 4.8: (a) Remanence and (b) coercive field as function of the FeCoB thickness for half-MTJ with Ru(1.8)/W(20) capping and W(20) capping respectively, after annealing at 300 °C.

use of Ru definitely matches the requirement in terms of low anisotropy, which we are looking for in our samples. However, because of some problems during the nanofabrication process, this sample did not show any exploitable results.

4.3.4 FMR measurement of W/FeCoB/MgO trilayer

Since the damping parameter is important in evaluating the critical switching voltage of the magnetization reversal in MTJ, ferromagnetic resonance measurements were carried on a sample composed of a substrate / W [2] / FeCoB [0.4] / MgO / FeCoB [t] / W [2] / Pt [5]. However, as the sensitivity of the measurement decreases for a lower volume of magnetic material, the absorption spectra in Figure 4.9.a could only be obtained for FeCoB thicknesses greater than 2.4 nm that belong to the in-plane magnetized region of the sample. The resonance field as a function of the RF frequency is plotted in Figure 4.9 for samples with FeCoB thicknesses of 2.4 to 3.0 nm For each FeCoB thickness, the fit of the experimental data with equation 4.1 gives an effective saturation magnetization that includes interfacial anisotropy, saturation magnetization, and the thickness of the dead layer (t_d) of FeCoB: $M_{s,eff} = M_s - \frac{2.K_i}{\mu_0(t-t_d)M_s}$. Since the dead layer thickness is extracted quite precisely from the MOKE measurement, Ki and Ms are the two fitting parameters in the expression of the effective saturation magnetization. We found a saturation magnetization for the top FeCoB of 1.49 $\pm$ 0.58 MA/m and the top interfacial anisotropy Ki at 1.23 $\pm$ 0.15 mJ/m² is consistent with the MOKE measurement. Finally, the damping is calculated from the linear fit of the linewidth variation ΔH with the microwave excitation frequency. The expression of the linewidth (ΔH) with respect to the resonance frequency (f_{res}) is given by Eq. 4.2 where ΔH_0 is the linewidth offset. The damping value varies from 0.007 to 0.011 as the thickness is reduced from 3.0 to 2.4 nm. The damping value of FeCoB is within the range of the value found in the literature [127] and similar trends of increasing damping with thinner FeCoB have been reported [128–130]. However, the reason why this damping increases significantly remains an open question. A possibility is that for a thin FM layer, energy dissipation at the interface with the non-magnetic Ta layer might lead to an increase in damping.

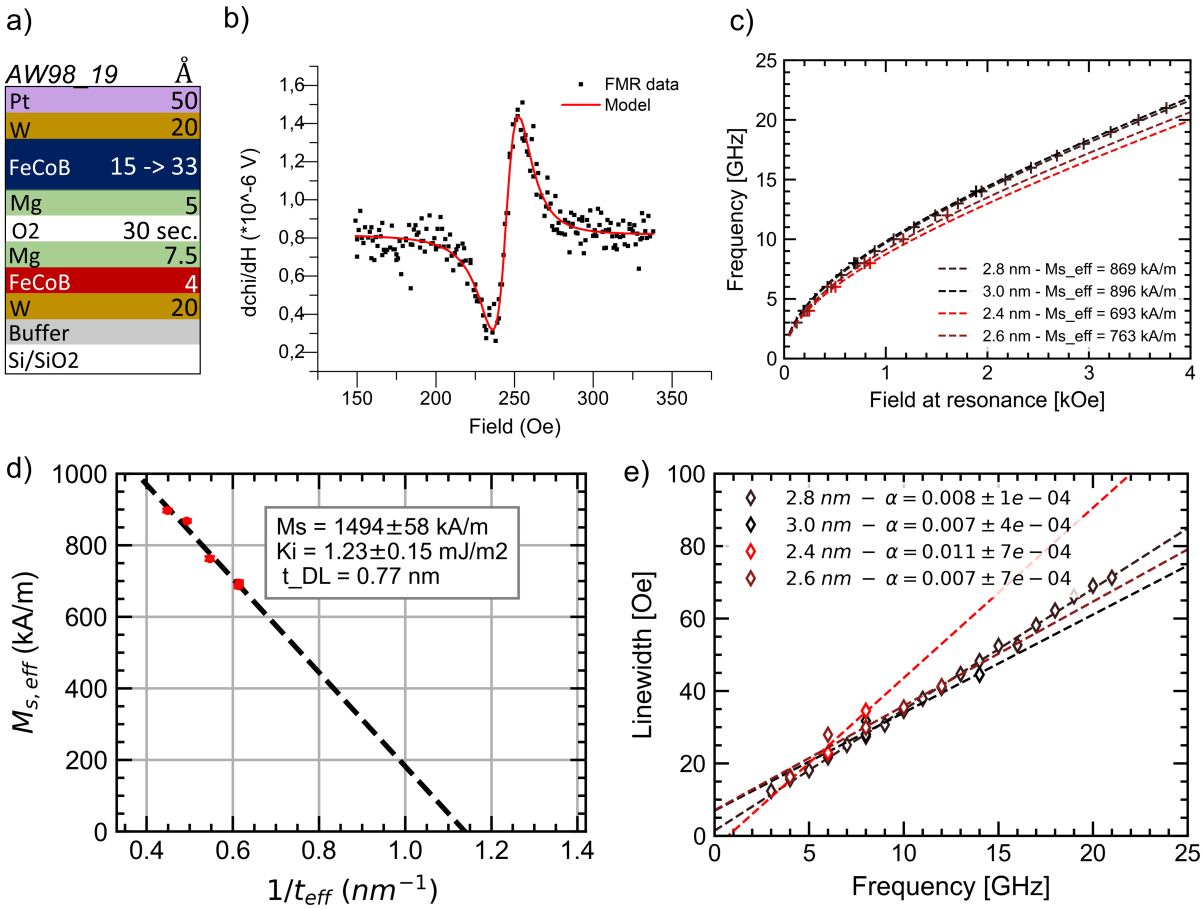

Figure 4.9: a) The stack structure used for FMR measurement with wedge of FeCoB thickness from 15 to 33 Å. b) Derivative of the power absorbed by the sample as function of the in-plane magnetic field. c) The field at resonance for different frequency of the RF signal for 2.4, 2.6, 2.8 and 3.0 nm of FeCoB. d) The effective saturation magnetization as function of the effective thickness (considering a dead-layer thickness of 0.77 nm). e) Linewidth as function of the external frequency and fitting with Eq.4.2 to extract the damping parameter as function of FeCoB thickness.

$$f_{res} = \frac{\gamma}{2\pi}\mu_0\sqrt{H_{ext}(H_{ext}+M_{s,eff})} \tag{4.1}$$

$$\Delta H = \Delta H_0 + \frac{4\pi}{\gamma}\alpha f_{res} \tag{4.2}$$

4.3.5 Full MTJ-stack for nanofabrication

The complete MTJ stack is presented in Fig. 4.10, including all material optimizations performed on half-MTJ stack samples. The Kerr mapping presents some relatively small coercivity (less than 300 Oe) at thin-film level promising for small critical current density. The total coercive field is maximal for bottom FeCoB around 0.65 nm and top FeCoB around 1.2 nm, which is consistent with the MOKE mapping in Fig. 4.2.b and Fig. 4.8.b. Similarly, the coercive field decreases with thicker top and bottom FeCoB. Despite

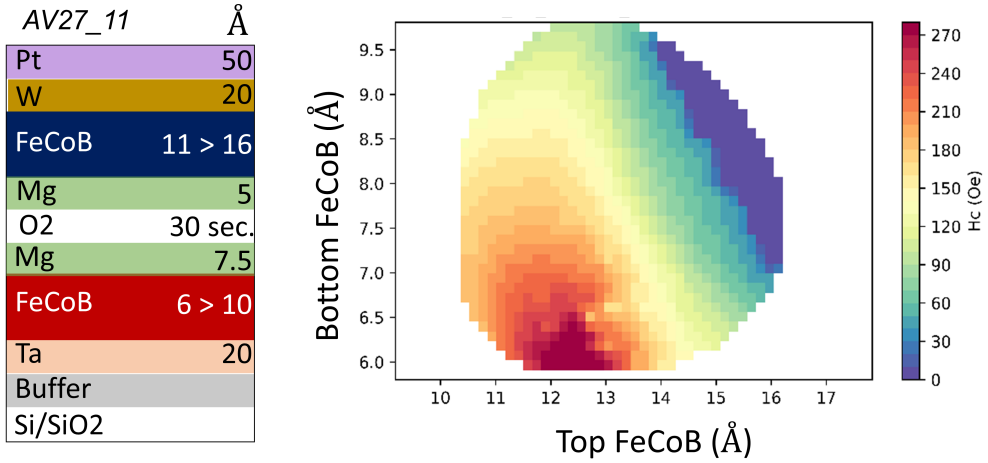

Figure 4.10: Full MTJ stack (left) for nano-fabrication process composed of two cross-wedges for the top and bottom FeCoB layer. MOKE mapping of the wafer demonstrating the influence of the effective anisotropy of both layer on the total coercive field, after been annealing at 300 °C.

the absence of dipolar coupling at full-sheet film level, the two free layers seem to be coupled because the hysteresis loop exhibits only a single jump.

4.4 Double Soft-SAF MTJ structure

The third part of this chapter aims to develop the concept of double soft-SAF MTJ in order to reduce the dipolar field on the two free layers. As mentioned in chapter 3, the dipolar field between the layers could affect the critical switching current and the dynamics of the FM layers in the P -> AP switching. The main challenge of this structure is very similar to the one encountered in an MRAM device, where a SAF is added to the side of the reference layer (RL) to reduce the stray field seen by the free layer (FL). A classical SAF structure in MRAM based on p-MTJ relies on [Pt/Co] multilayers with a Ru spacer to guarantee the antiferromagnetic coupling between the two parts of the SAF. Strong stability is observed in these SAFs due to repetition of the Pt / Co interfaces, which provide high interfacial anisotropy (around 1-2 mJ/m2 [131]). Similarly, this concept of SAF can be applied to our structure to reduce the impact of the dipolar field between the layers. Strong stability is not required in our concept, so that the multilayers of Pt/Co might be reduced to a simple Pt/Co bilayer. To compensate both ferromagnetic moments, each free layer should be compensated for by its own antiferromagnetic counterpart. The description of the concept of double soft-SAF is presented in Fig. 4.11 and the main challenges related to its development are listed below :

- The lower number of [Pt/Co] repetitions should guarantee a perpendicular magnetized Co in the top and bottom SAFs, whereas the total magnetic volume of Co should compensate for the FeCoB dipolar field.
- The AF coupling through RKKY in Ru should be optimized in top and bottom side of stack
- The AF coupling should maintain AF alignment of the two part of each SAF in the dynamic regime. This last point is accessible only with electrical measurements of patterned devices and simulation.

Optimization of the bottom and top soft SAF is needed to define which thicknesses of Pt and Co are required to obtain PMA in the SAF and which Ru thicknesses provide maximum antiferromagnetic coupling. This optimization is carried out separately for the bottom and the top soft-SAF in the next sections.

4.4.1 Bottom soft-SAF design

The stability of each soft-SAF is now given by several contributions: the perpendicular anisotropy of the Pt/Co bilayer and the one of the FeCoB/MgO, as well as the RKKY coupling through the Ru layer. First, a single Pt/Co bilayer was deposited with a wedge on the Co layer to investigate the PMA region at the interface of Pt/Co. In Fig. 4.12, the coercive field drops from 300 Oe to 150 Oe, while the Co thickness increases from 1.2 to 1.65 nm. Remanence is maximal in that region, which confirms that a sufficient amount of PMA is obtained with a single Pt/Co bilayer. The interesting weak effective anisotropy region with 100 % of remanence is located around 1.5 nm from Co. Although the saturation magnetization of Co is expected to increase slightly in Pt / Co compared to the bulk value of Co (1.4 MA/m [58]), it stays relatively close to FeCoB saturation magnetization (1.4-1.5 MA/m) and the magnetic compensation should arise at a similar thickness value for those two layers.

On the other side of the Ru layer, the FeCoB/W/Co system acts as a single FM layer. Insertion of Co is necessary to preserve the strong RKKY coupling observed in the Co / Ru / Co subsystem [132]. Fig. 4.13.b shows how the effective anisotropy changes with the thickness of FeCoB in the FeCoB / W / Co FM layer. The key point is to provide just enough overall effective anisotropy to maintain the perpendicular

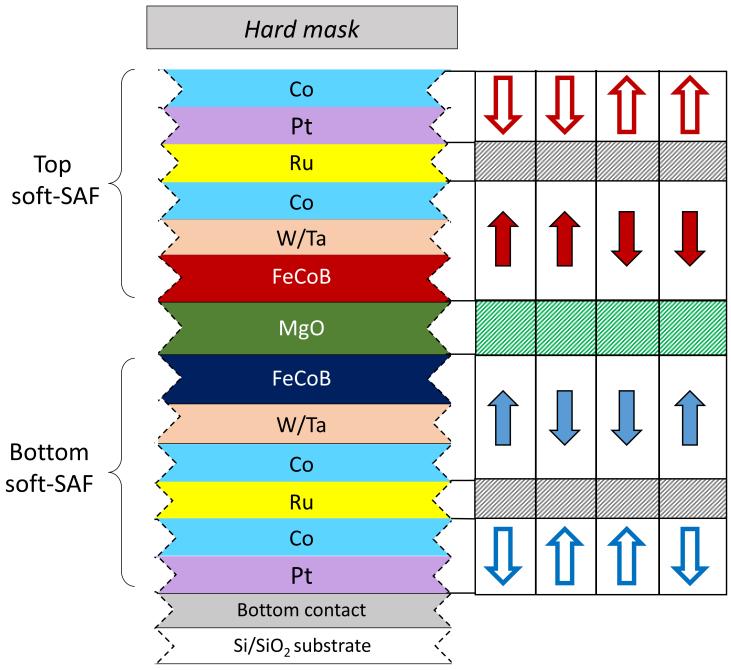

Figure 4.11: Concept of the double soft-SAF structure to reduce dipolar field screen on both free-layer. The four different configuration of the windmill dynamic is presented on the right. For every configuration, the bottom and top free layer are AF coupled their Pt/Co bilayer.

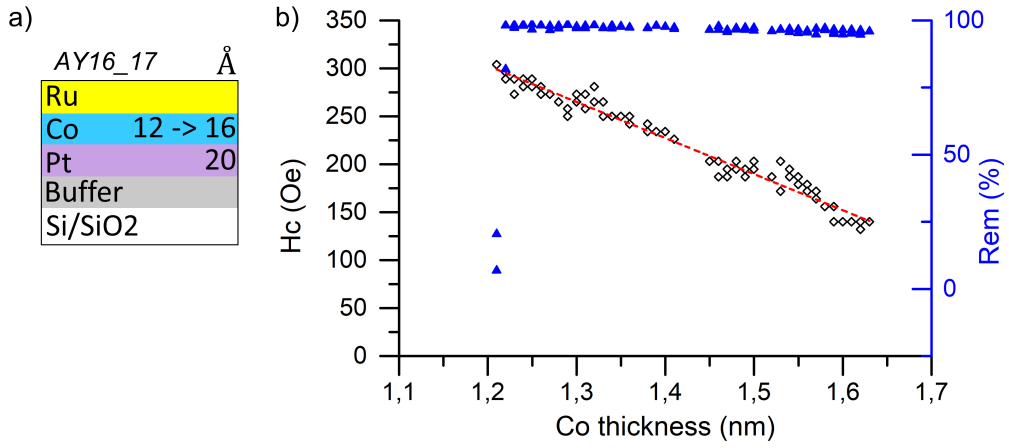

Figure 4.12: a) Sample with single wedge of Co deposited on top of Pt. b) Coercivity and remanence as function of the Co thickness

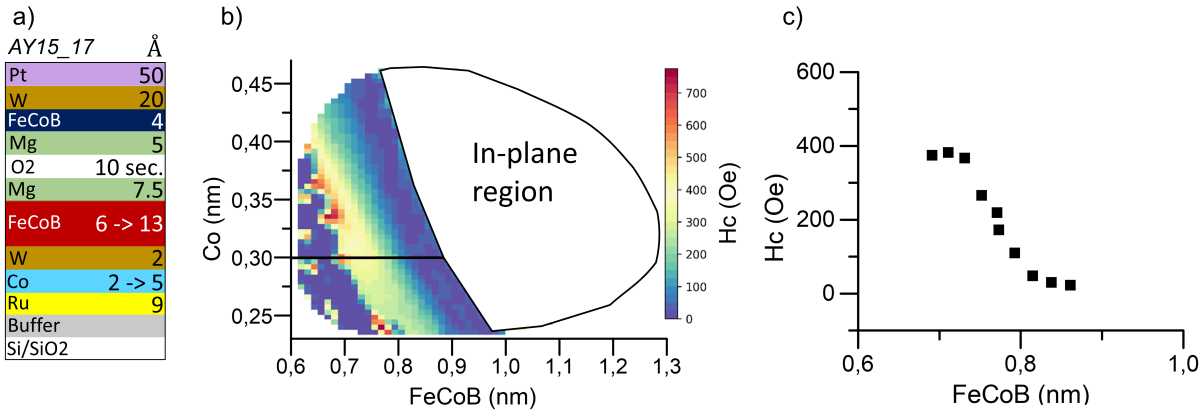

Figure 4.13: a) Stack structure used to verify the PMA region with FeCoB/W/Co magnetic layer, after annealing at 300 °C. b) The coercivity mapping as function of the Co thickness next to the Ru layer and of the FeCoB thickness. c) Coercivity as function of FeCoB thickness for a Co fixed at 0.3 nm showing the limit of the PMA region at 0.8 Å

configuration of the MTJ. To respect this criterion, the FeCoB thickness is chosen at 0.8 nm, while Co is typically 0.3 nm. Fig. 4.13.c shows the evolution of the coercive field as a function of the bottom FeCoB thickness for a Co thickness of 0.3 nm. The coercive field at 0.8 nm of FeCoB is just below 100 Oe, which seems a reasonable value to target weak stability for the FeCoB/W/Co trilayer.

The last step to optimize the bottom SAF is to make sure that the AF coupling takes place through the non-magnetic Ru layer. The second AF peak of Ru is known to appear around 0.8-0.9 nm [36], so stacks with wedges of Ru from 0.6 to 1.0 nm were deposited and annealed at 300 °C. To investigate the rkky coupling through Ru, we proceed to VSM measurement on a half-MTJ stack with a magnetically dead top layer for different values of Ru thickness. The results with 0.8 and 0.85 nm of Ru thickness showed two distinct coercive fields, which could be explained by the demonstration of two independent effective anisotropies of the top and bottom layers. The fact that the remanent magnetization is saturated out-of-plane proves that the AF coupling is evidently too weak to dominate the stability of each of the subsystems (FeCoB/W/Co and Pt/Co). This conclusion also applies to thicker Ru up to 1 nm and thinner Ru down to 0.7 nm. Until now, there has been no convincing explanation for why RKKY does not occur in this sample despite the similar Ru thickness range commonly used in similar MRAM stacks at Spintec [117]. The same approach was then carried out for the top FeCoB electrode to check whether AF through RKKY coupling was feasible on the other side of the MgO barrier.

4.4.2 Top soft-SAF design

The top-SAF design is also based on a Pt / Co bilayer to promote perpendicular anisotropy [35, 133] together with the use of a Ru spacer to promote AF coupling between the two parts of the SAF. The main difference between the bottom and top soft-SAF designs is the insertion of a platinum layer directly on top of the Ru spacer. The reason for depositing Ru/Pt/Co instead of Ru/Co/Pt is that the PMA was only present when Co was deposited on top of a Pt seed layer. Pt generally promotes the crystallographic orientation [111] necessary for PMA at the interface with Co. It has previously been shown [35, 134–137] that the perpendicular interfacial anisotropy of Pt/Co is strongly dependent on the crystallographic structure of Pt on which Co is grown. PMA is maximum for the crystallographic structure of Pt [111], which is obtained when Pt is the

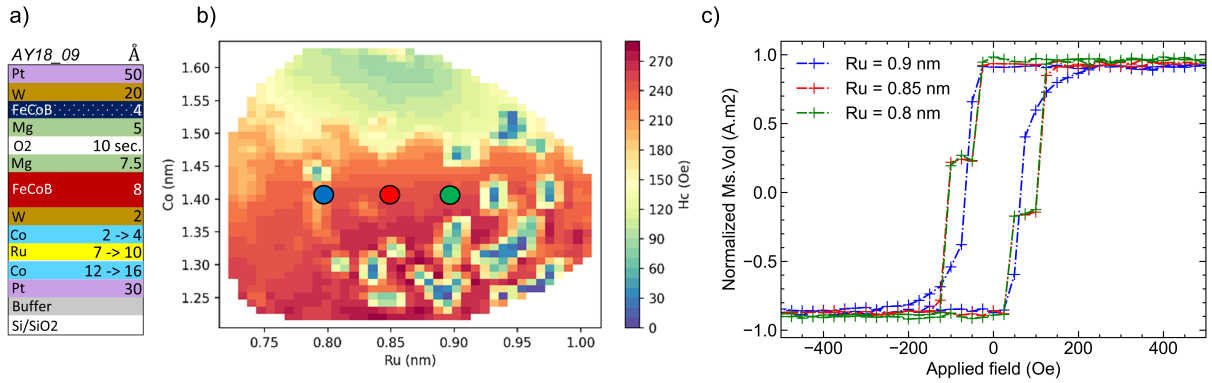

Figure 4.14: a) Stack structure deposited for evaluation of RKKY interaction on the bottom side with Pt/Co/Ru/Co/W/FeCoB. b) Coercive field mapping of the stack with perpendicular applied magnetic field. c) Zoom of out-of-plane VSM measurement loop taking at 0.8, 0.85 and 0.9 nm of Ru.

seed layer. However, the insertion of Pt between Ru and Co can shift and reduce the AF peak of the RKKY coupling through Ru, as demonstrated in [138].

First, the PMA of the Ru/Pt/Co subsystem grown on the top side of the MTJ should be confirmed before investigating the region of AF coupling through interlayer exchange coupling. Fig. 4.15.a shows that a single layer of 0.4 nm of Pt is sufficient to provide PMA to Co grown on top of it. To remain in the region of maximal remanence, the Co thickness should not be greater than 1.5 nm. As we want to preserve the RKKY coupling through Ru, we should minimize the Pt thickness, so that we picked 0.45 nm of Pt and around 1.5 nm for Co as a good combination for this part of the top SAF.

Investigating AF coupling through the Ru spacer in the top SAF subsystem is carried out using VSM measurements on a half-MTJ stack presented in Fig. 4.16.a. Cross-wedges of the top FeCoB from 0.9 to 1.4 nm and Ru from 0.7 to 1 nm are used to explore the multiple compositions for a soft-SAF. Fig. 4.16.b shows a large plateau of AF obtained with Ru of 0.76 nm. This plateau decreases with a slightly thicker Ru thickness. We can note how sensitive the RKKY coupling through Ru and Pt is to the thickness of the spacer.

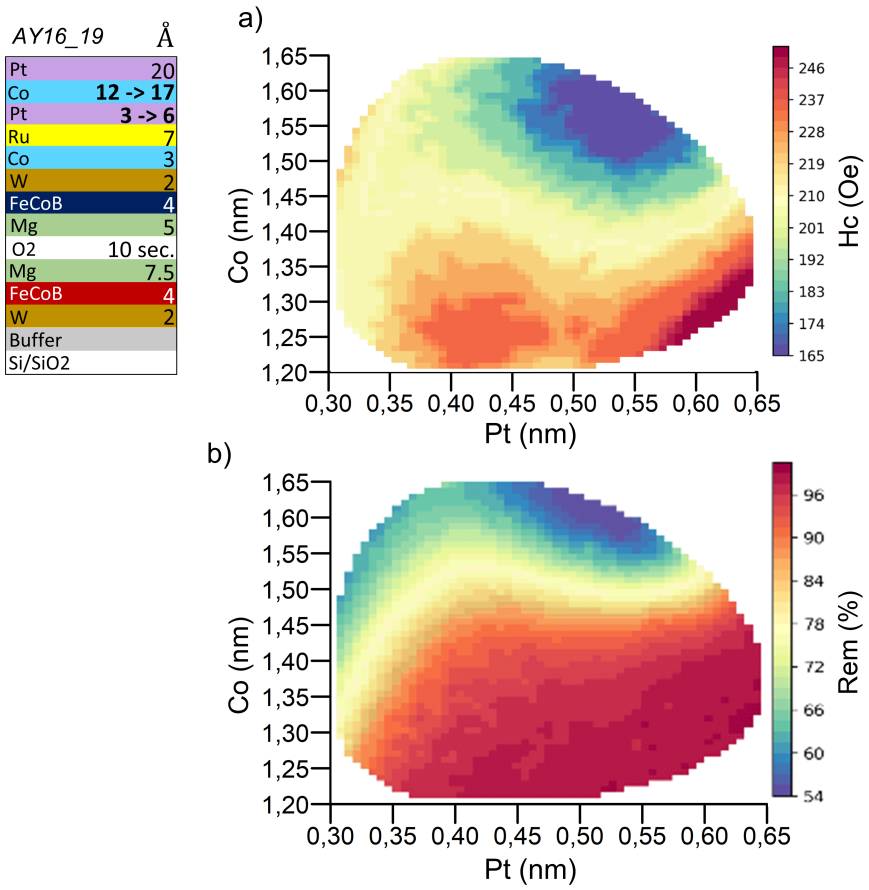

Figure 4.15: Coercivity mapping (a) and remanance mapping (b) of Pt/Co bilayer grown on the top side of the half-MTJ stack as function of Pt and Co thickness

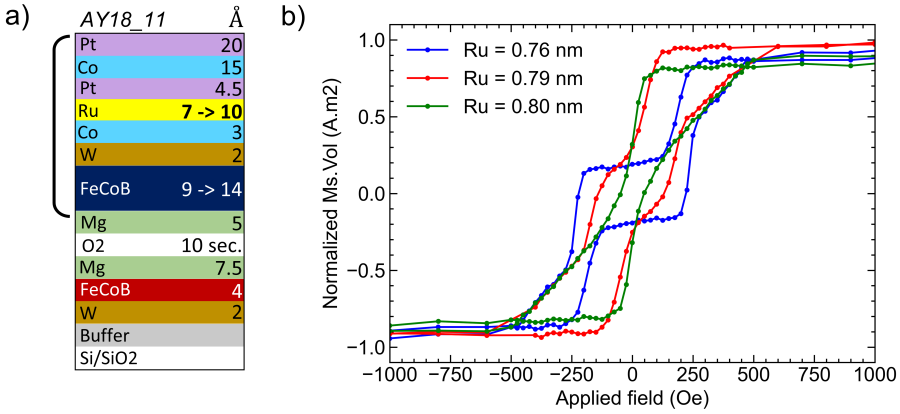

Figure 4.16: a) Stack structure deposited for evaluation of RKKY interaction on the top side of the MgO with FeCoB(t1)/W(2)/Co(3)/Ru(t2)/Pt(4.5)/Co(15)/Pt(20). b) Out-of-plane VSM measurement loop taking at 0.76, 0.79 and 0.8 nm of Ru.

4.5 Conclusion

This chapter developed two different concepts that are promising for generating windmill dynamics. Using MOKE measurements, we first optimized half-stack MTJ and extracted the interface anisotropy of MgO/FeCoB/Ta and MgO/FeCoB/W. In particular, we find that the interfacial anisotropy drops from 1.22 mJ/m2 to 0.98 mJ/m2 when increasing the annealing temperature from 300 °C to 375 °C. Similarly, the dead layer thickness degrades from 0.22 to 0.5 nm with higher annealing temperatures, proving that atoms from the W capping layer start to diffuse. We chose to use a W seed on the bottom side of the MTJ because it provides 13% more interface anisotropy compared to the use of Ta. The free layer MgO / FeCoB / Ta demonstrates a relatively low interface anisotropy of 0.96 mJ/m2 at 300 °C compared to the bottom interface anisotropy of 1.22 mJ/m2 obtained with W. Additionally, the dead-layer thicknesses on the top side of the stack are shown to be almost twice those on the bottom side. To enhance the asymmetry between the top and bottom effective anisotropy, the full stack for nanofabrication uses a cross-edge of the top and bottom FeCoB. The coercive field mapping of the complete stack exhibits horizontal and vertical variations of the coercive field according to the evolution of the coercive field of each layer.

In parallel to this first concept, a second solution based on double soft-SAF MTJ has been developed to anticipate the effect of the dipolar coupling between the two free-layers. The same approach that relied on the optimization of the half-MTJ led to successful results regarding the top side of the MTJ. The top soft-SAF composed of MgO/FeCoB/W(2)/Co(3)/Ru(7.6)/Pt(4.5)/Co(1.5)/Pt(20) demonstrates AF coupling at zero field. However, in the bottom part of the MTJ, AF coupling through the Ru spacer was not achieved. Further material development is needed to achieve AF coupling and realize a bottom soft-SAF electrode.

The next chapter will present the electrical results on the nanopatterned dual-free layer MTJ.

Chapter 5

Nanodevice characterization

Contents

5.1 Introduction

Once optimization at the film level is complete, the wafer is patterned in clean room facilities following the steps described in the chapter on experimental techniques 2. The successive UV lithography during the fabrication process allows us to electrically access the MTJ device through the top and bottom contact. The wafer is separated into different dies organized in a grid. Each die is identified by two letters, the first for the row (y-axis) and the second for the column (x-axis). This organization of the wafer in dies allows us to evaluate the influence of different thicknesses (through wedge depositions) on the electrical properties. In addition to these two parameters, different diameters of the pillars are defined by the E-beam mask for each die. The influence of the MTJ pillar size can be evaluated separately if the yield inside a single die is sufficiently high for different pillar sizes.

In this chapter, we correlate the expected behavior from analytical models and macrospin simulations with the electrical characterization of MTJ. From the quasistatic properties of the junctions, the investigation of the coercive field of the hard layer (HL) and the soft layer (SL) already highlights the different asymmetry between the two layers. The DC and pulse phase diagrams are then used to determine the critical voltage (or current density) of each layer. The ratio between the two critical voltages is shown to correlate with the ratio of the two coercive fields. The time-resolved measurement finally demonstrates the windmill dynamic in the MTJs under DC current. Analysis of the spike shape with respect to the thickness of both FeCoB layers and the presence of an external magnetic field overlaps some expected behaviors from the modeling chapter 3.

The composition of the MTJ was optimized in the sheet film to investigate the impact of the relative stability of the hard and soft layers. A cross-wedge of 90 °defines a variation in the thickness of the top FeCoB soft layer from 1.1 to 1.6 nm and of the bottom FeCoB hard layer from 0.65 to 0.95 nm, as shown in Figure 5.1. The TMR value of each junction on the wafer is extracted from the resistance versus field loops to be plotted as a function of the two FeCoB thickness wedges 5.1.b. The maximum TMR obtained is about 45 %, probably due to a low FeCoB thickness of the hard layer. Indeed, the spin polarization of the electrons is not complete for too thin FeCoB layer (below 1.0 nm), as reported in [125] (p.89). The TMR seems to be significantly higher in the edges of the wafer than in the central part. As will be explained in the next section, this low TMR value is due to the reversal at a similar field of both HL and SL. Automatic measurement of the entire wafer shows a yield of around 70 % of working devices over the 20 000 testing devices.

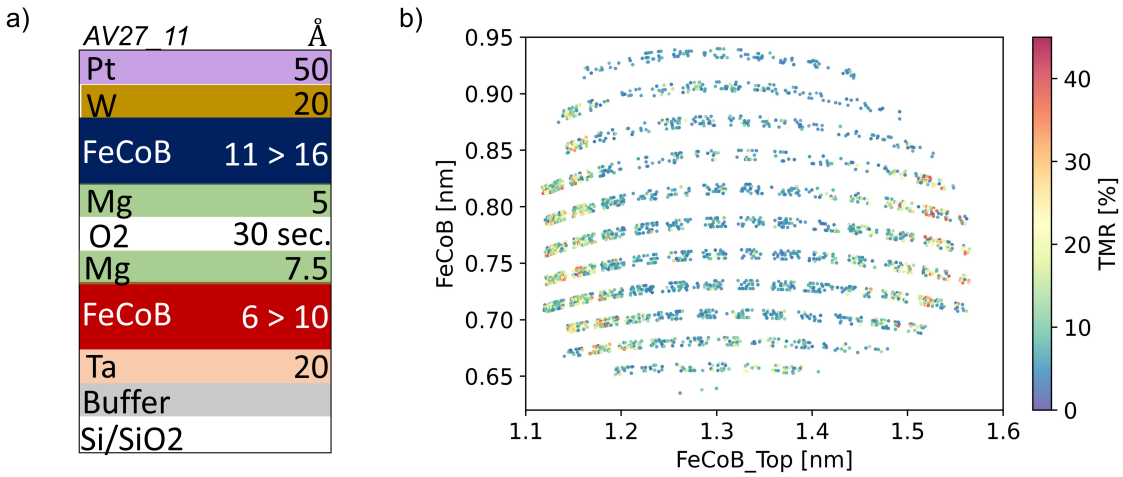

Figure 5.1: a) Stack composition of the fabricated sample. b) TMR mapping as function of the FeCoB at the top (x-axis) and at the bottom (y-axis) side of the MgO barrier

5.2 Static properties

5.2.1 Coercive field of hard and soft layer

The coercive field of each layer is expected to be a good indicator of the thermal stability. To evaluate the coercive field of the two layers, 15 resistance versus field loops are measured under a DC bias voltage of 20 mV. An example of major and minor R-H loops are shown in Fig.5.2.a and Fig.5.2.b respectively for a MTJ of nominal diameter 150 nm with bottom FeCoB thickness of 0.73 nm and top FeCoB of 1.15 nm. The soft layer coercivity is 445 Oe while the offset field is 750 Oe. To estimate the HL coercive field, the stray field from the SL is expected to decrease by 1/3 as the volume of the SL is 1/3 less than the volume of the HL. Then, the HL coercivity is expected to be around 2400 Oe. As the switching field of the soft and hard layer are often similar, extracting only the inner loop is not feasible over the whole wafer. The extracted coercive fields of the HL and SL represent both the effect of the dipolar and anisopotropy fields. The following discussion is then based on the effective coercive field of the soft and hard layer considering that the main variations in coercive fields are expected to come from the changes in anisotropy fields. In Fig. 5.2.a-c, the average resistance of the 15 R-H loops are plotted for three devices along the top FeCoB thickness wedge located by the star symbol in the wafer (Fig. 5.2.d.e). Figure 5.3.d.e shows the evolution of the coercivity of SL and HL throughout the wafer, independently of the pillar size.

On the left-hand side of the wafer, the coercive field of the SL is much smaller than that of the HL. As the thickness of the top FeCoB increases, the SL gains stability to reach a pic around 1.25 nm, as shown in 5.3.g. The coercivity of the top layer decreases again for a top FeCoB thicker than 1.4 nm. These observations are consistent with the results at the sheet film level, where the maximum coercive field obtained for the soft layer is around 1.25 nm with the MOKE measurement (5.3.i). The evolution of the HL coercivity is also visible across the y direction of the wafer, where the coercivity first increases up to 0.75 nm and decreases back from 0.75 to 1 nm (Fig. 5.3.f). The same behavior is also visible at the film level, as attested by the MOKE measurement in Fig. 5.3.h.

From this first quasi-static measurement across the wafer, different regions of the wafer can be attributed to different asymmetry in terms of effective anisotropy through the coercive field measurement. On the left-

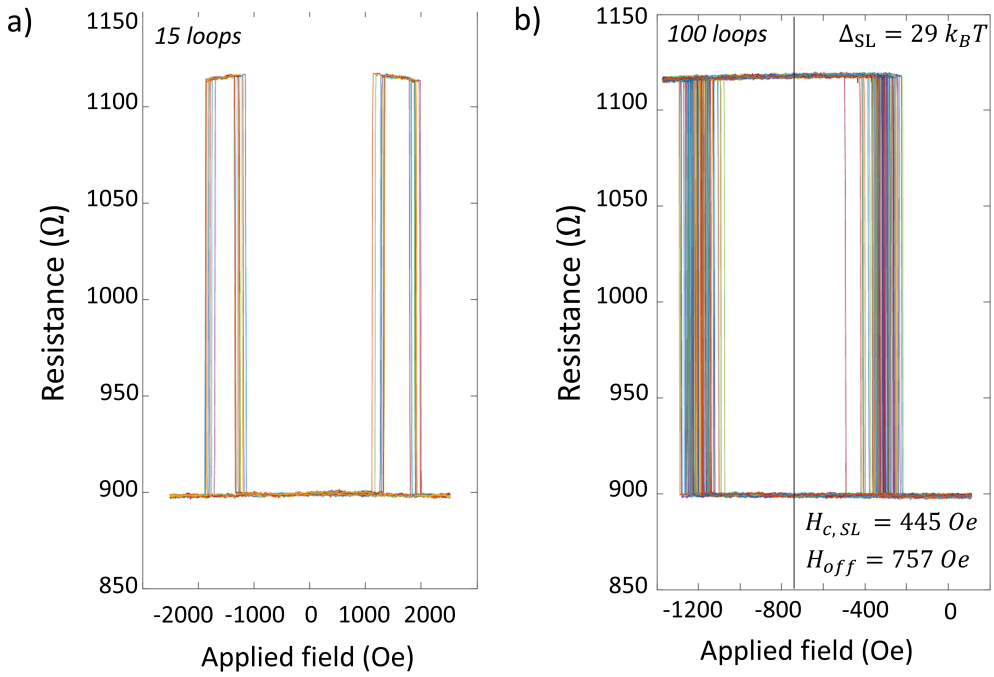

Figure 5.2: a) Example of major resistance versus external field loops recorded at 20 mV for a MTJ with 150 nm of pillar diameter, 0.73 nm of bottom FeCoB and 1.15 nm of top FeCoB. b) 100 minor loops measured on the same device showing 445 Oe of offset field and 445 Oe of coercive field for the SL.

hand side of the wafer (thin-top FeCoB), the asymmetry is large, whereas on the middle and right sides of the wafer, the asymmetry is reduced. This asymmetry factor is quantified by the coercive field ratio between the two layers in figure 5.4. At approximately 1.05 nm of top FeCoB layer, the ratio of the coercive field is about 50%, while it reaches 100% towards the thicker top FeCoB. Above 1.5 nm, it seems that the asymmetry increases again with a ratio of 0.8.

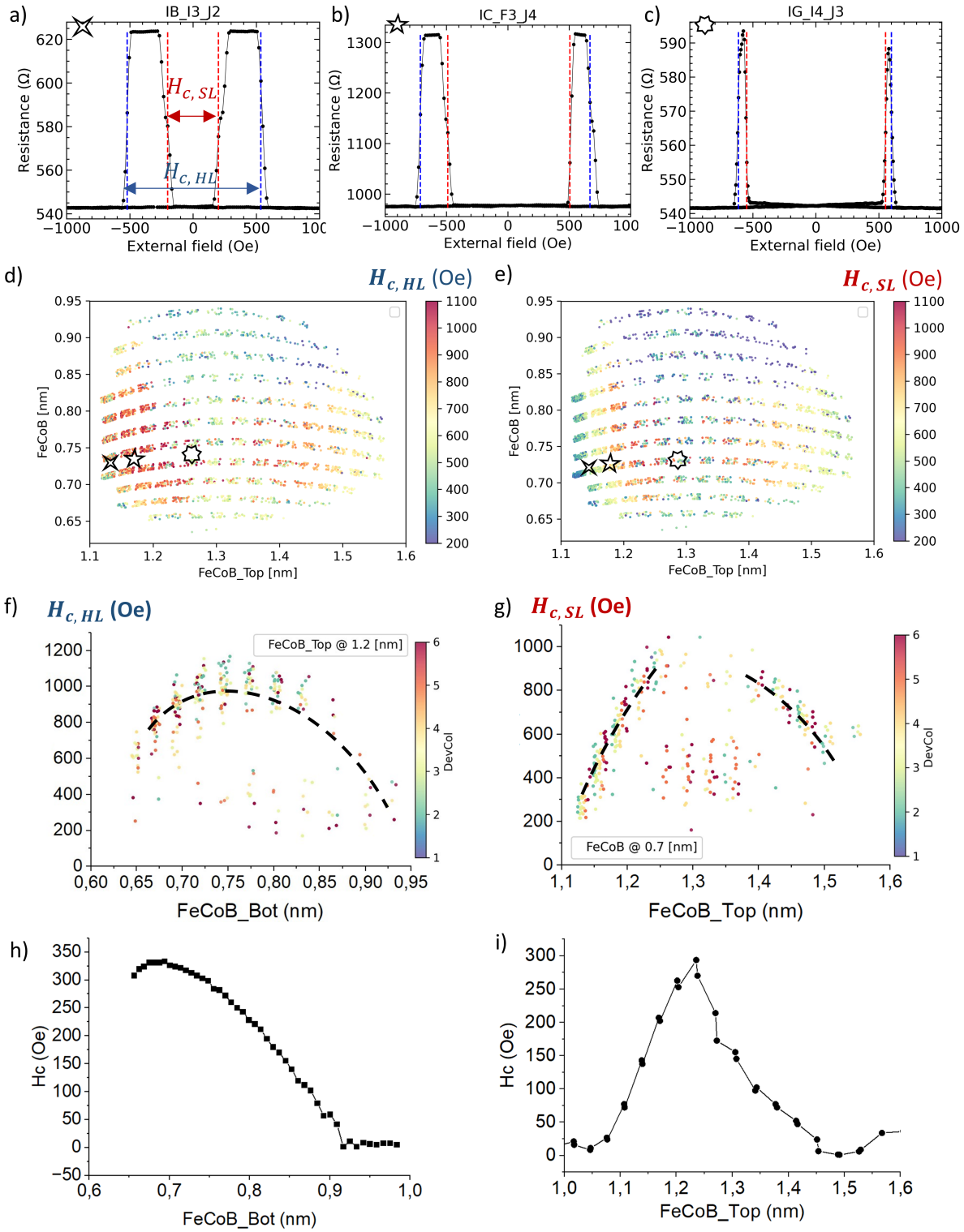

Figure 5.3: a-c) Examples of resistance versus external field loop recorded at 20 mV for different position on the wafer denoted by the star symbols in the coercivity map of the bottom hard-layer (d) and top soft layer (e) as function of the FeCoB thicknesses. Coercive field of the hard (f) and soft (g) layer as function of the top (bottom) FeCoB thickness considering a fixed bottom (top) FeCoB. h) and i) are the coercive field of the bottom and top FeCoB layer respectively, at sheet film level.

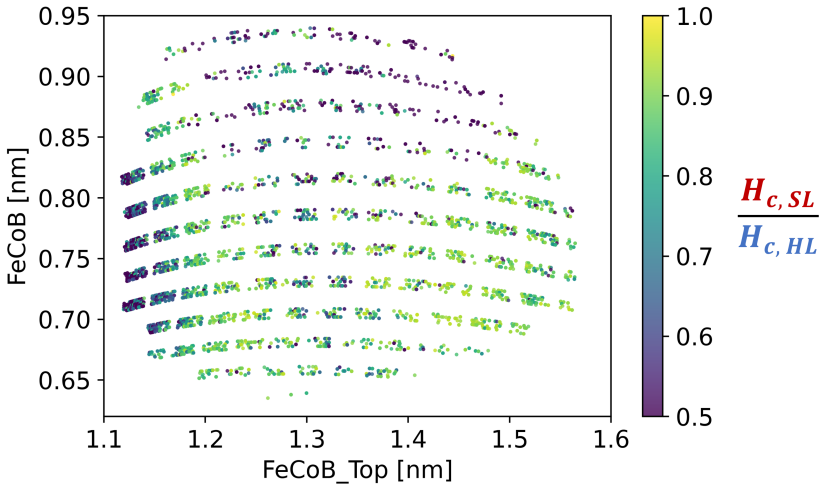

Figure 5.4: Ratio between the coercive field of the soft and hard layer as function of the position on the wafer. The left hand-side of the wafer shows much more asymmetry in term of coercive field compared to the middle and right hand-side of the wafer.

5.2.2 Phase diagram characterization

To evaluate the impact of the spin-transfer torque on the coercive field of both layers, the DC phase diagram compiles multiple R-H loops at different DC biases. To achieve higher voltages, a pulse phase diagram can be used, where the resistance is recorded after a 100 ns input pulse for each field point. This technique allows for slightly higher voltages by stressing the barrier less in comparison to a DC input current. In the DC and pulse diagrams, the resistance appears in the color code (blue: low resistance, red: high resistance) after normalization between 0 and 1. DC and pulse phase diagrams are shown, respectively, in Figures 5.5.a-c and 5.5.d-f for three junctions taken at different positions on the wafer.

The first junction (Fig. 5.5.a and 5.5.d) is located on the left-hand side of the wafer where at low bias voltage the two coercive fields are distinguishable. The increase of the bias voltage reduces the coercive field in the negative polarity for both SL and HL due to the STT effect and the heating effect. In this current polarity, the electrons flow from the SL to the HL, so that the STT effect favors the SL to achieve an AP configuration with respect to the HL. Consequently, the SL coercive field is reduced. The outer branches (HL coercive field) react similarly because the STT pushes the HL to be in the P state with respect to the SL. Thus, the coercive field of the HL is also reduced by the negative polarity of the current.

In the positive polarity, the STT effect stabilizes the SL in a parallel configuration. The coercivity of the SL is then supposed to increase with a high positive voltage. However, Joule heating has the opposite effect on the stability of the layer. In the DC phase diagram, the heating contribution results in the coercive field decreasing as the square of the applied current. Using the pulse phase diagram, it is possible to decouple the contribution of the STT effect from the heating effect for a reasonable value of the applied voltage, while the DC phase diagrams always show a mix of both contributions. In the pulse phase diagram (Fig. 5.5.d), the STT effect is visible starting at 0.4 V in positive polarity, which causes the SL coercive field to increase and the HL coercive field to decrease.

A thicker top FeCoB increases the coercive field of the SL as shown in figure 5.3.g. The second phase diagrams (5.5.b and 5.5.e) are located in this thicker region, where both SL and HL exhibit very similar

coercive field values. Most junctions with comparable thicknesses show potential windmill dynamics in both current polarities. Some junctions on the right-hand side of the wafer show phase diagrams similar to Fig 5.5.c and 5.5.f. where the positive polarity of the current seems to demonstrate a lower critical voltage compared to the negative polarity.

When the switching field of the SL and HL is fitted on the DC phase diagram, the critical voltages, observed, respectively, $V_{c,SL}$ and $V_{c,HL}$ can be extracted (Fig. 5.5g). Second-order polynomial functions are used to fit the switching fields with respect to voltage bias, in which the linear behavior is attributed to the STT effect and the quadratic behavior to the Joule heating [139, 140]. The calculation of the critical voltage of the SL is shown in Figure 5.5.h. For weak SL (left side of the wafer), the critical voltage achieves 0.2 V for some junctions, while on the right side of the wafer the critical voltage is double. On the contrary, the HL critical voltage remains quite constant over the wafer. In terms of the critical voltage ratio between HL and SL, the conclusions are very similar to the results obtained with the coercive field of figure 5.3. In fact, the higher asymmetry in the critical voltage in Figure 5.5.i is identified in the region where the coercive fields are very different from each other.

Finally, reversing the HL in the positive polarity from a P to an AP configuration requires more energy than in the negative polarity from AP to P. This is visible in the phase diagram in figure 5.5.a where the critical voltage of the HL falls within 0.45 V in the negative polarity and does not even appear in the positive polarity at 0.5 V. According to the macrospin simulation in chapter 3, it clearly demonstrates the influence of the dipolar field, which favors the parallel alignment of the layers and breaks the symmetry between the positive and negative critical voltages of each layer. The energy landscape in that case (5.5.a) is then well described by the figure 3.6.a where Δ_{HL}^{+} is larger than Δ_{SL}^{-} and Δ_{HL}^{-}. However, a critical look at this asymmetry in voltage polarity can also be justified by a polarity-dependent spin-torque efficiency or a polarity-dependent heating effect [139, 141]. Furthermore, it is important to note that the quasi-static measurement is based on averaging the junction resistance over a long period of time inside which short spikes in the AP state will have a very limited impact compared to the long P-state lifetime.

In conclusion, quasi-static measurements of the DC and pulse diagrams showed promising results with time-resolved measurement. The wedge of FeCoB on the top layer is especially useful for varying the relative effective anisotropy between the SL and HL. The critical voltage of both layers correlates with their coercive field value. Interpretation of the phase diagrams seems to confirm some expected behaviors of the macrospin simulation. In particular, it is possible to infer that the left-hand side of the wafer is prone to show long AP states and sharp spikes in P states in negative polarity because of the large asymmetry between the SL and HL in terms of effective anisotropy. The situation may differ when the two layers show similar coercivity. The time-resolved signal is expected to be more balanced between the P- and AP-states because of the comparable stability of the layers. These scenarios now need to be confirmed by time-resolved measurements to access the shape of the spikes.

5.3 Time-resolved characterization of dual free layer MTJs

5.3.1 Spiking signal characterization method

Using a time-resolved measurement setup (see Section 2.5.2 of Chapter2), the resistance of the MTJ is recorded over time for different values of applied voltage and applied magnetic field. An example of a time trace recorded by the oscilloscope during the application of a 500 μs electrical pulse on an MTJ showing

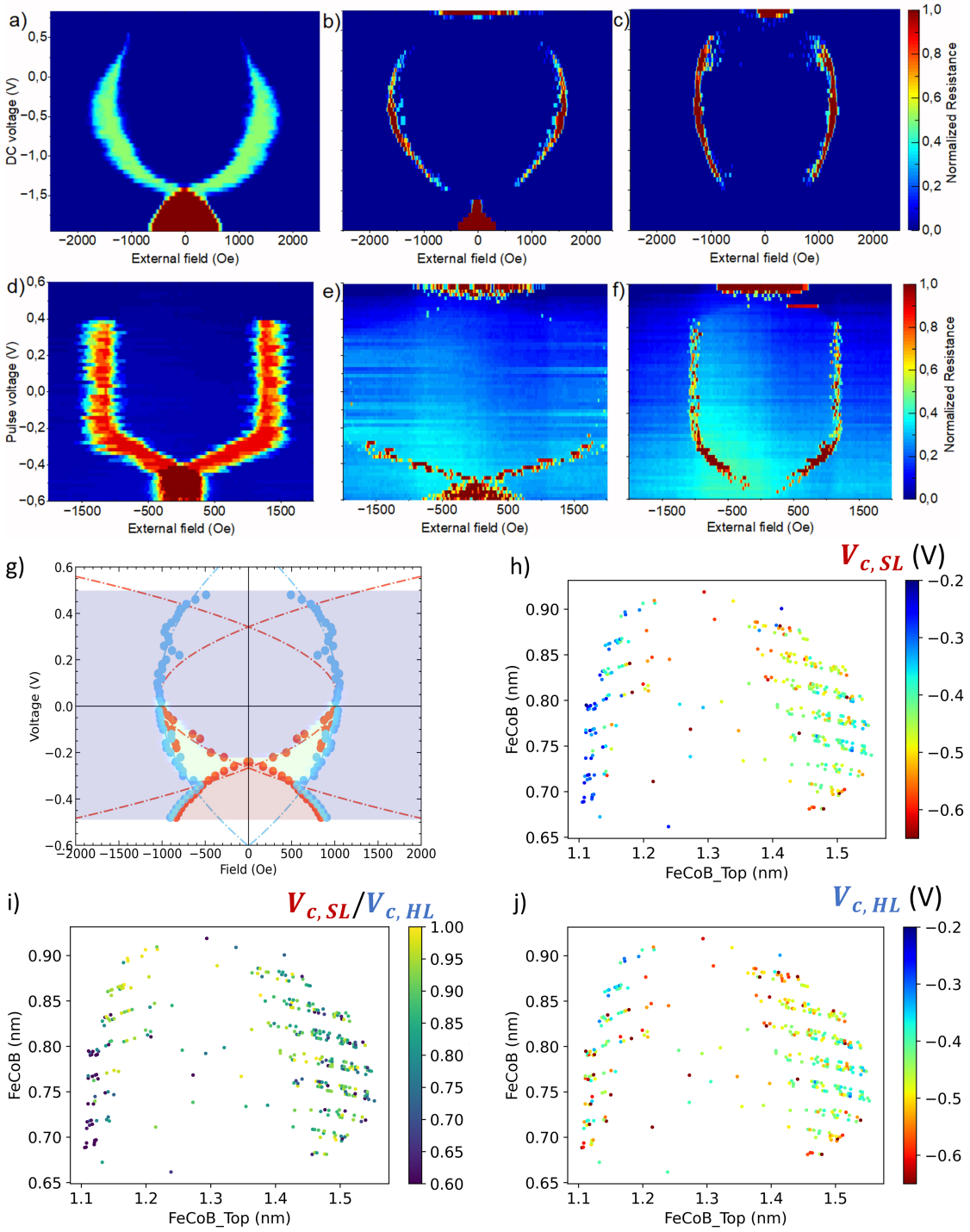

Figure 5.5: (a,d) Phase diagrams of a junction on the left hand-side of the wafer where the two coercive fields are significantly different with possible windmill dynamic in the negative polarity. (b,e) Phase diagrams of a junction in the middle of the wafer where the two coercive fields are identical and both current polarities could show the windmill dynamic. (c,f) Phase diagrams of a junction on the right-hand side of the wafer where the two coercive fields are close to each other with possible windmill dynamics in positive polarity. Top row (a-c) are DC phase diagrams, and the bottom row (d-f) pulse phase diagrams. g) Extraction of the critical voltage for the hard (blue) and soft (red) layer. h) and j) Critical voltages of the soft and hard layers plotted as function of the top and bottom FeCoB layers. i) The ratio of both critical voltages to be compared with the ratio of the coercive field in Figure 5.4.a).

a spiking dynamic is plotted in Figure 5.6.a. The signal detected by the oscilloscope is proportional to the current across the MTJ. To distinguish P from the AP state, two different thresholds are needed. The formula to calculate the resistance of the MTJ is presented in the section Methods 2.5.2.

The different states of the MTJ (AP, P and transitions) are identified with two thresholds, $V_{thrs,AP}$ and $V_{thrs,P}$ as shown in Figure 5.6.b-e. The values of these thresholds are highly dependent on the measurement setup bandwidth and the noise level of the circuit. Electric noise is particularly visible in the P states in the time traces 5.6.c. $V_{thrs,P}$ and $V_{thrs,AP}$ should obviously dominate this noise level. Secondly, the use of two thresholds avoids an incomplete switching to be counted by taking into account a reversals only if the time trace crosses both threshold levels. For example, a switch from P to AP state counts only if the time trace crosses $V_{thrs,P}$ then $V_{thrs,AP}$. This feature is particularly useful for discriminating backswitching behavior. The use of two thresholds allows binarization of the signal, which is necessary to investigate the stability of the layers with respect to the macrospin models developed in Chapter 3. Finally, the two-threshold system makes possible statistics on the transition time between the P- to AP-state and AP- to P-state. The following threshold values were shown to be a good compromise for our setup : $V_{thrs,AP} = 0.4(Vmax - Vmin)$ and $V_{thrs,AP} = 0.6(Vmax - Vmin)$.

The median lifetimes of the state P and AP are then calculated from the cumulative distribution function (CDF) of the lifetimes (Fig. 5.6.g.). The median switching times for each layer and each polarity are accordingly noted τ_{bot}^{+}, τ_{bot}^{-} for the bottom layer and τ_{top}^{+}, τ_{top}^{-} for the top layer. The effective stability values ($\Delta_i^{\pm}$ for i $\in [bot, top]$) and the critical voltage of each layer ($V_{c0,i}^{\pm}$) can be independently fitted in the positive and negative current polarity according to their median switching time ($\tau_i^{\pm}$) with the unified equation:

$$\tau_i^{\pm} = \frac{k.\Delta_i^{\pm}.B + A.\exp\left((1-k).\Delta_i^{\pm}.\left(1-\frac{V}{V_{c0,i}^{\pm}}\right)\right)}{\ln\left(1+\exp\left(-k.\Delta_i^{\pm}.\left(1-\frac{V}{V_{c0,i}^{\pm}}\right)\right)\right)} \tag{5.1}$$

$$A = -\tau_0.\ln(1-P) \tag{5.2}$$

$$B = \frac{1}{2}.\tau_D.\ln\left(-\frac{4.\Delta_i^{\pm}}{\ln(P)}\right) \tag{5.3}$$

$$\tag{5.4}$$

An example of an experimental median switching time fitted with this model is shown in figure 5.6.e. In the Eq. 5.1, the effective thermal stability includes the thermal stability of the layer alone and the dipolar field interaction with the other layer. The relationship between the two thermal stabilities is expressed as follows :

$$\Delta_{top}^{\pm} = \Delta_{top}^{0}\left(1 \mp \frac{H_{dip,bot\to top}}{H_{K,top}}\right)^2 = \Delta_{top}^{0}\left(1 \mp h_{r,top}\right)^2 \tag{5.5}$$

$$\Delta_{bot}^{\pm} = \Delta_{bot}^{0}\left(1 \pm \frac{H_{dip,top\to bot}}{H_{K,bot}}\right)^2 = \Delta_{bot}^{0}\left(1 \mp h_{r,bot}\right)^2 \tag{5.6}$$

If measurement data exists in both polarity of current, the fitting condition uses a common thermal

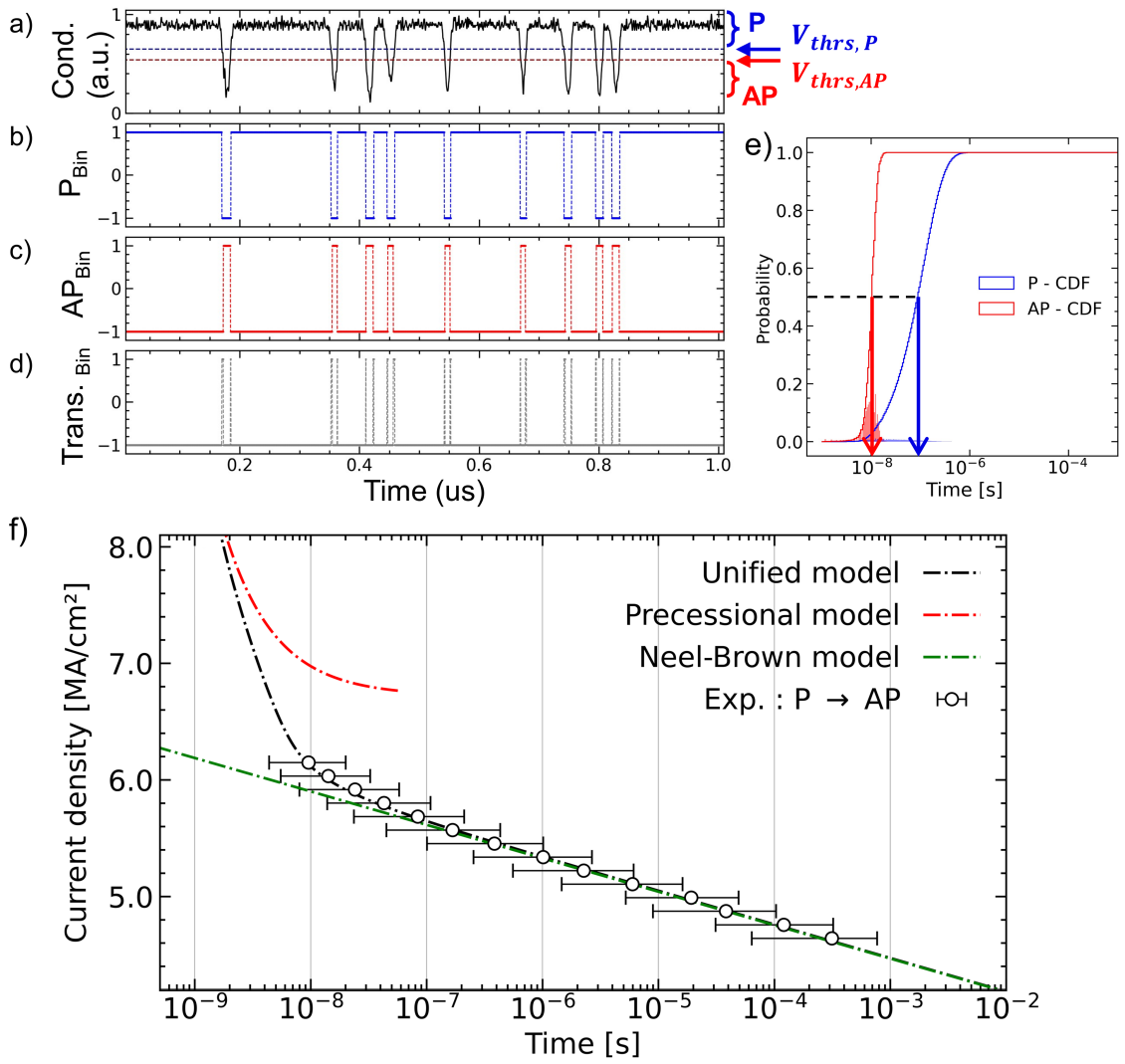

Figure 5.6: a) Example of time trace recorded at -530 mV with the time-resolved measurement set-up. b-d) Binarization for the time trace into P state (d), AP state (e) and transition between those states (f) defined by the threshold voltages $V_{thres,P}$ and $V_{thres,AP}$. e) Extraction of the median lifetime of the P and AP state according to the cumulative distribution curves. The binarization procedure is repeated for different voltages (or current densities) and plotted in (f) with fitting of the data with the unified model.

stability factor (Δ_i^0) and a critical voltage ($V_{c0,i}$) in the unified equation, and the fitting parameters become Δ_i^0 and $h_{r,i}$ for each layer.

The thermal stability of the top and bottom layers is then used to draw the expected energy landscape, considering that the macrospin model applies in our case. Before applying this analysis to all the junctions on the wafer, we investigated in detail three different cases of MTJs corresponding to different locations in the wafer.

1. The first example treats the case of a MTJ with large asymmetry in the thermal stability between the top and bottom layer. This type of junction has previously been identified by coercive field measurements to figure on the left-hand side of the wafer, where the top FeCoB is thin (1.15 nm).

2. The second case investigates an MTJ with similar thermal stability between the top and bottom layers. These types of MTJ are located in the middle of the wafer with a top FeCoB around 1.35 nm.

3. Finally, the last case shows some time traces with a large P to AP transition time, which could be a sign of synchronization between the layers.

5.3.2 Case 1 : High asymmetry in effective thermal stability

In this first scenario, the investigated junction is located in the region with a thin top FeCoB (1.15 nm) and a bottom FeCoB thickness of 0.7 nm. As shown in the quasi-static characteristic of the wafer, this region exhibits a large difference in the coercive field between the two magnetic layers as well as an important shift in the critical switching voltages. The time traces of this junction in positive and negative current polarity are shown in figure 5.7.a.b.

From the time traces, we can notice a significant difference between the positive and negative polarity. In positive polarity, the MTJ is somehow trapped in the P state. In the negative polarity, the time traces are mainly populated by the AP state, and sharp spikes are observed in the P state with frequency of spikes increasing with voltage bias. Calculating the median switching time for both layers is only possible in the negative polarity and is plotted in Figure 5.7.c.

From the fit of these median switching times with the unified model, it is possible to retrieve the effective thermal stability factor of each layer (Δ_{Bot}^- and Δ_{Top}^-) and the effective critical switching voltages ($V_{c0,Bot}^-$ and $V_{c0,Top}^-$). The equivalent energy landscape in a macrospin view is shown in Figure 5.7.d along with a table containing the parameters extracted from the fit. The result is that the ratio between the effective stability factor of both layers is almost of 2. As only the negative polarity contains usable information, extraction of the equivalent positive effective thermal stability and dipolar field energy $\Delta_{Dipolar}$ is not possible.

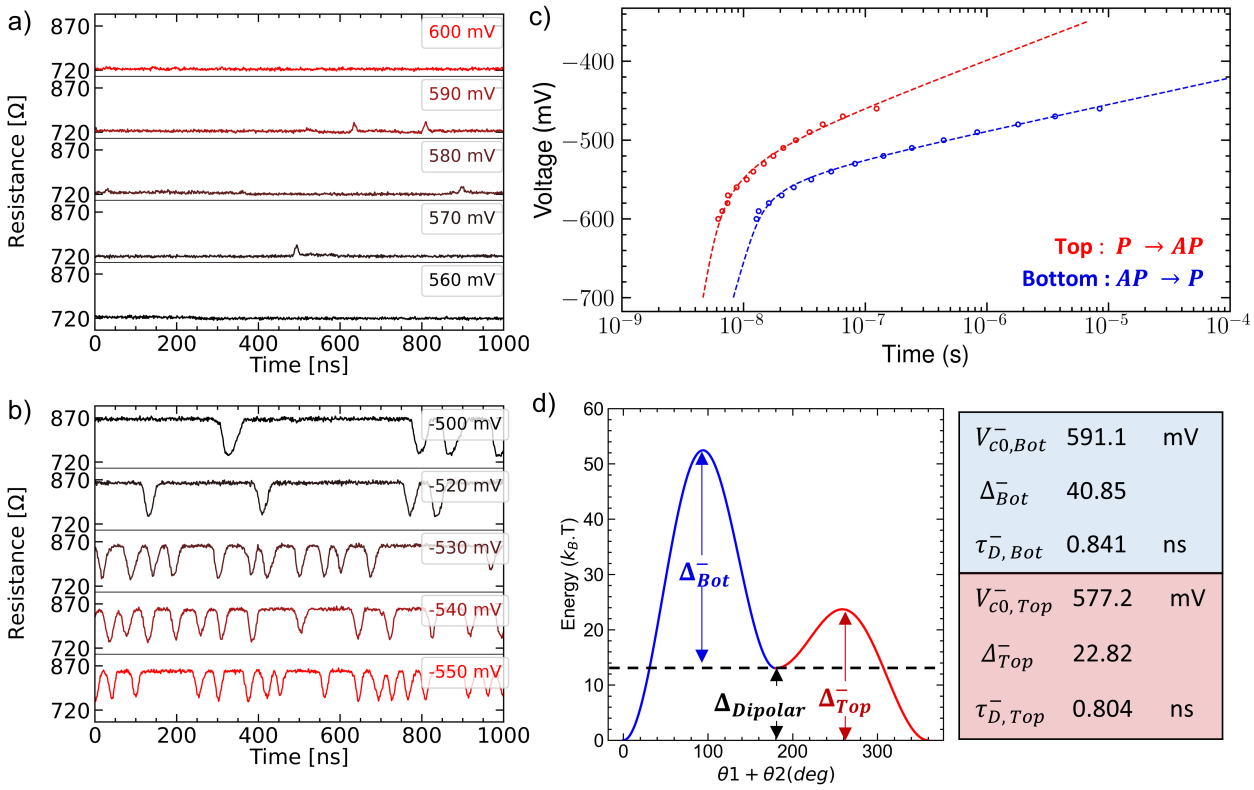

Figure 5.7: (a) and (b) are time traces recorded with the time-resolved measurement set-up in the positive and negative current polarity respectively. (c) compiles the median switching time for P to AP switching (top FeCoB layer) and AP to P switching (bottom FeCoB layer) as function of the voltage applied. Fitting of the equations (dashed line) are done with the unified model of Eq 5.1. (d) represents the energy barriers involved in the windmill dynamics in the negative polarity of current along with a table of the fitted parameters.

5.3.3 Case 2 : Low asymmetry in thermal stability

In this second case, a junction with a thicker top layer of FeCoB (1.3 nm) is studied. It is anticipated, based on quasi-static measurements, that the layers will be more evenly balanced in terms of stability, as they both exhibited the same coercive field. The time traces in both polarities of current are plotted in figure 5.8.a.b. The major difference from the case is the onset of the windmill dynamics in both current polarities. Also, the more stable state is the P state in both polarities, which certainly means a high dipolar field interaction between the layers. As both polarities present valuable information, the fitting method takes common parameters in positive and negative current polarities. Each effective thermal stability is replaced by the thermal stability $\Delta_{0,Top}$ ($\Delta_{0,Bot}$) associated with an additional parameter, noted $h_{r,Top}$ ($h_{r,Bot}$), which refers to the ratio of the dipolar field to the anisotropy field. The relation between the effective thermal stability, the thermal stability and the h_r ratio is given by Eq. 5.5 and Eq. 5.6.

The extraction of relevant parameters from the fit of the median switching time is gathered in the figure 5.8.e along with a representation of the energy landscape taken by the system in a macrospin view. In that case, the dipolar energy is obtained using the effective stabilities in the positive and negative polarity for each layer:

$$\Delta_{Dip,\,Top} = \Delta^{-}_{Top} - \Delta^{+}_{Top} \tag{5.7}$$

$$\Delta_{Dip,\,Bot} = \Delta^{+}_{Bot} - \Delta^{-}_{Bot} \tag{5.8}$$

The result of the dipolar energy calculated from the bottom and top layers is equal in this case ($\Delta_{Dip,\,Top} = \Delta_{Dip,\,Bot} = 23.6$). It indicates that the assumptions made in the macrospin model apply in this case. In particular, the hypothesis that relies on strict sequential switching of the layers and non-synchronization between them seems valid. It can be noted that the positive voltage polarity shows sharper (better) spikes compared to the negative polarity. Despite the similar thermal stability of the top layer ($\Delta^0_{Top} = 31$) and the bottom layer ($\Delta^0_{Bot} = 37$), a high asymmetry between the two effective thermal stabilities results from the dipolar coupling between the layers. In the positive current polarity, the difference between the two effective thermal stabilities is greater than in the negative polarity: $\Delta^{+}_{Bot} - \Delta^{+}_{Top} = 29.4 > \Delta^{-}_{Top} - \Delta^{-}_{Bot} = 17.8$. This higher asymmetry in the positive current polarity maintains a thermally assisted regime for the incubation between spikes, whereas the sharp spikes are driven by the intermediate and processional regimes. As a result, the spiking frequency evolves exponentially within a wide range of voltages (from 450 to 550 mV), while the spike width is relatively constant. The singular case is well described by the macrospin model in Chapter 3 and Fig. 3.10.

In conclusion, a low asymmetry in the thermal stability factors between the layer ($\Delta^0_{Top}, \Delta^0_{Bot}$) allows generating spikes in both current polarities. The asymmetry needed to create sharp spikes with long incubation time between them is provided by the dipolar field. The prediction from the macrospin simulation is in good agreement with the experimental time traces.

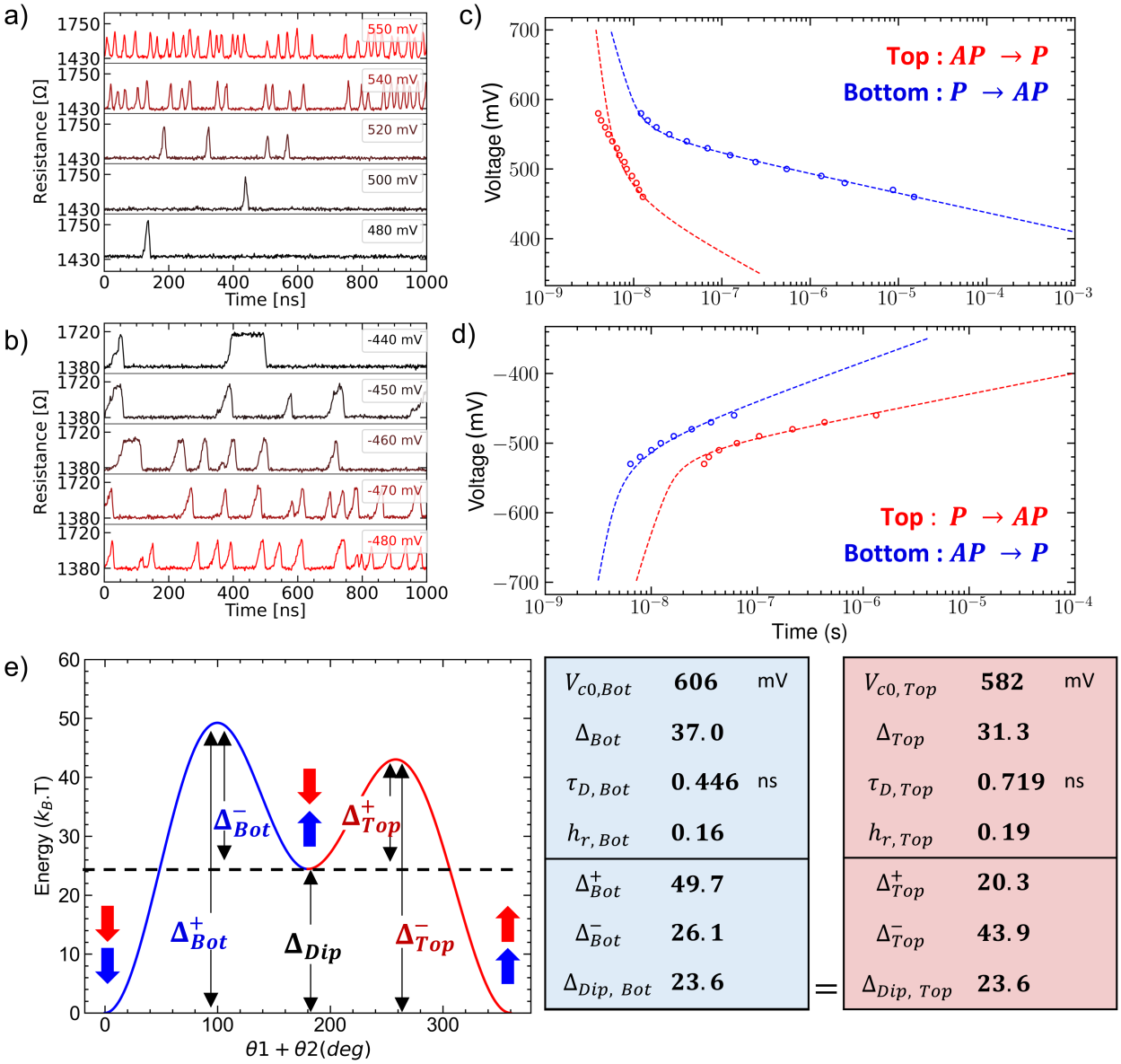

Figure 5.8: (a) and (b) are time traces recorded with the time-resolved measurement set-up in the positive and negative current polarity respectively. (c) and (d) Median switching time for P to AP switching (top FeCoB layer) and AP to P switching (bottom FeCoB layer) as function of the voltage applied in the positive and negative current polarity, respectively. The fitting of the equations (dashed line) is done with the unified model of Eq 5.1 with a common set of parameters for the two blue curves (bottom FeCoB) and a common set of parameters for the two red curves (top FeCoB). (e) represents the energy landscape in both polarities involved in windmill dynamics in a macrospin approach.

5.3.4 Case 3 : Low asymmetry in effective thermal stability

In the two previous examples, the asymmetry in terms of the P and AP lifetimes was significant, which arises from the different effective thermal stability between SL and HL. This third case investigates two MTJs with quite symmetric time traces between the P and AP lifetimes. This example focuses on the MTJ in the thick-top FeCoB area (1.4-1.45 nm). The time traces in the negative current polarity are plotted in Figure 5.9.a. The first thing to note, common to all time traces, is the long switching time from the P state to the AP state, while the switching time from the AP state to the P state remains sharp, as was in the two previous cases. This delay in the transition between P to AP switching appears in many devices where the lifetimes of the P and AP states are close to each other (see the Appendix 8.2). Similar P and AP lifetimes in the thermally assisted regime are expected to result in similar values of effective thermal stability. However, the values extracted by fitting the median switching time are significantly different: $\Delta^{-}_{Bot} = 22 < \Delta^{-}_{Top} = 42$. The experimental results are markedly different from what the macrospin model predicted. The fitting parameters are certainly far from the real value. It is more likely that the effective thermal stability of the bottom and top layers are very close to each other in that case. The reason for these long transition times from the P state to the AP state can be found in the macrospin simulations in the case of a relatively small asymmetry in the stability of the layer. Synchronization between the two magnetic layers appears to be the source of long transitions between the P- and AP-state. The effect of the partial synchronization between the layers on the median switching time is a global overestimation of the P lifetimes. In the end, the only reliable lifetime is the AP lifetime to evaluate the median switching time. The median lifetime of P is expected to show a similar value.

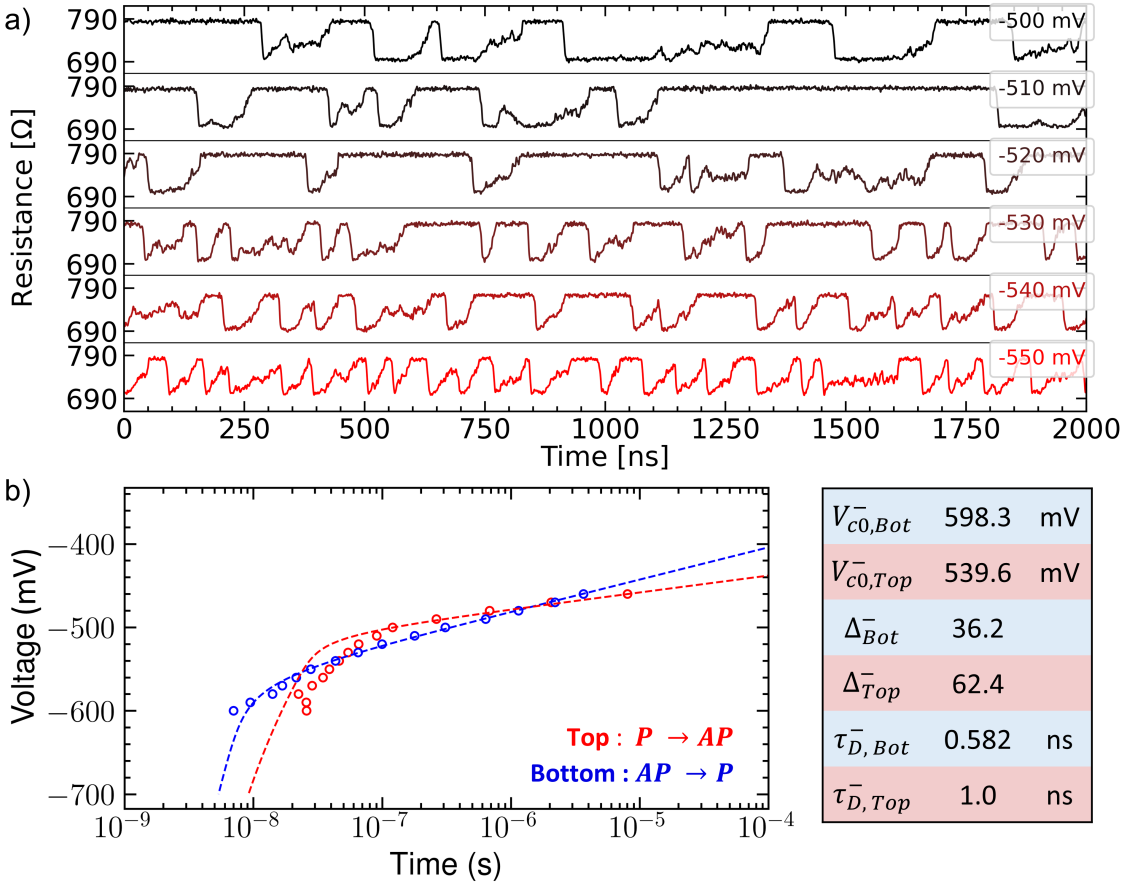

Figure 5.9: (a) plots several time traces recorded with the time-resolved measurement set-up in the negative current polarity. (b) compiles the median switching time for P to AP switching (top FeCoB layer) and AP to P switching (bottom FeCoB layer) as function of the voltage applied. Fitting of the equations (dashed line) are done with the unified model of Eq 5.1.

5.3.5 Effective thermal stability factor of top and bottom FeCoB

The case studies investigated in the previous section are necessary to understand under which conditions the windmill dynamics is created. However, more statistics are necessary because the nano-fabrication process inherently leads to deviations from the nominal diameter of the pillar and can also induce defects during the IBE step. As the thicknesses of the top and bottom FeCoBs vary across the wafer, it will be interesting to see whether the assertions of the three case studies are verified at the wafer level. This section will be dedicated to the analysis of the results extracted from time-resolved measurements on the full wafer. This large-scale dynamical characterization is also correlated with the quasi-static measurements of the MTJs with respect to top and bottom FeCoB thicknesses.

Under some assumptions on the homogeneous magnetization dynamics of the magnetic layer, the macrospin model predicts a spiking signal for a wide range of thermal stability values. In particular, we have seen in the modeling chapter that the spike shape can be tuned by the relative effective anisotropy (or stability) between the two magnetic layers. As mentioned in the second case study, there are two effective thermal stabilities for each current polarity. Fig. 5.10.a-d summarizes the four stabilities as a function of the two FeCoB wedges. Each data point represents one MTJ tested in positive (a-b) and negative (c-d) polarity from 450 to 600 mV. Junctions with enough data in both current polarities were analyzed by the common fitting approach described in section 5.3.1. An example of a common fitting approach applied on a full die is presented in appendix 8.3. As mentioned above, this method allows us to extract the thermal stability of the layer alone (Δ_i^0) along with the ratio of the dipolar field to the anisotropy field ($h_{r,i}$). To obtain the effective thermal stability ($\Delta_{top}^{\pm}$, $\Delta_{bot}^{\pm}$), we simply use Eq.5.5 and Eq.5.6. Instead, for a single-polarity analysis, only the effective thermal stabilities can be derived from the fit of Eq. 5.1, without any possible extraction of the dipolar field. These effective stabilities are supposed to refer to the energy barriers between each configuration. Fig.5.10.e. draws the expected energy landscape from a macrospin model point of view and the notation used to interpret the data. The analysis is conducted separately for the top and bottom layers in the following sections.

Top FeCoB layer

The negative polarity of the current shows very interesting results, in which the effective thermal stability of the top layer (Δ_{Top}^{-}) changes according to the thickness of the top FeCoB. For thin layer of FeCoB, the stability of the top layer falls below 20 k_BT, while it increases to 60 k_BT for thicker FeCoB. This effective thermal stability is a consequence of the effect of the anisotropy field and the dipolar field. To differentiate both contributions, the thermal stability of the top layer alone (Δ_{Top}^{0}) and the ratio between the effective field and the anisotropy field are plotted in Figure 5.11.a-b for a constant thickness of the bottom FeCoB (0.7 nm). Despite the important dispersion of the results, the variation of the top FeCoB thickness seems to affect mainly the stability of the top layer while the ratio $h_{r,\,Top}$ remains quite constant along the wedge. Therefore, it is most probable that the variation in the effective thermal stability of the top layer is provided by modifying the effective anisotropy field. The increase in stability of the top layer is in good agreement with the evolution of the SL coercive field described previously in Fig. 5.3.

Positive current polarity shows only a small value for the effective thermal stability factor of the top layer ($\Delta_{Top}^{+} < 20$). In fact, the dipolar field accelerates the switching time of the top layer from the AP state to the P state, resulting in a weaker effective stability. Additionally, we can observe the same increase in stability from a thinner to a thicker top FeCoB layer as in the negative polarity. We notice that the left-hand side of

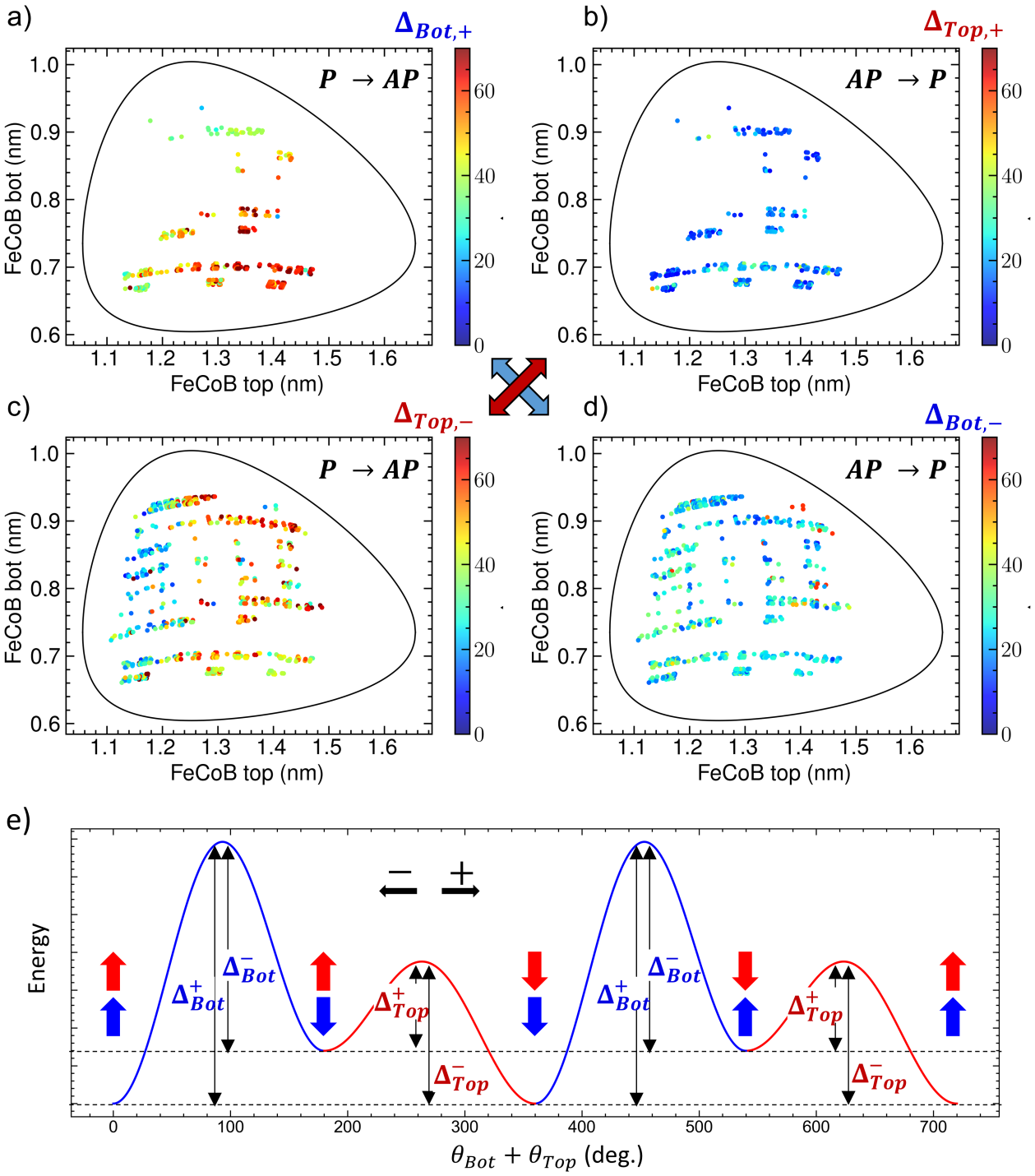

Figure 5.10: Effective stability factor for the top (b,c) and bottom (a,d) FeCoB layer for positive (a,b) and negative (c,d) current polarity as function of FeCoB top and bottom thickness. (e) Schematic representation of the energy barriers involved in the spiking dynamics in a macrospin representation

the wafer does not show any results on the positive polarity. The reasons for this are the same as those given in the first example: the effective thermal stability factor of the bottom layer is too large to be switched at reasonable voltages; or the thermal stability of the top layer is too small, resulting in a lifetime that cannot be detected due to the bandwidth limit of the circuit.

Bottom FeCoB layer

The stability of the bottom layer exhibits a behavior completely different from that of the top layer. First, the effective thermal stability of the bottom layer in negative polarity (Δ^{-}_{Bot}) decreases slightly as the top FeCoB thickness increases. For a constant thickness of the bottom FeCoB, there is no evident reason, in terms of the anisotropy field, for the stability of the bottom layer to be reduced. Similarly to the case of the top FeCoB layer, the thermal stability of the layer alone (Δ^{0}_{Bot}) and the field factor $h_{r,\,Bot}$ are represented in Fig. 5.11.c.d as a function of the top FeCoB thickness and for a constant value of the bottom FeCoB (0.7 nm). We can clearly identify that the variation in the effective thermal stability of the bottom electrode layer (Δ^{-}_{Bot}) in negative polarity is due to an increase in the dipolar coupling. Indeed, the larger volume of a thick top FeCoB layer will generate a larger magnetic stray field than a thinner layer. This opposite evolution of the effective top and bottom stability with this wedge consequently reverses the spiking signal. Spikes are observed in the P state for thin top FeCoB and in the AP state for thick top FeCoB as confirmed by the time traces of the first two examples.

In positive current polarity, the bottom effective stability (Δ^{+}_{Bot}) remains quite large due to the fact that the dipolar field stabilizes the parallel state of the bottom layer. However, the effective stability decreases slightly over 0.8 nm of FeCoB thickness. Again, the dissociation between the effective anisotropy and the effect of the dipolar field is shown in Fig. 5.11.e.f. As expected from the coercive field mapping at the sheet film and patterned level (Fig. 5.3.f.h), the effective thermal stability in both polarities is reduced due to the decrease in the anisotropy field with a thicker FeCoB layer.

Relative effective stabilities of top and bottom FeCoB layer

The effective thermal stability of each layer can be compared for a given current polarity in order to anticipate the output signal characteristic. By convention, we define the following ratio for each polarity of current which can vary form -1 to +1 :

$$r^{\pm}_{\Delta} = \frac{\Delta^{\pm}_{Bot} - \Delta^{\pm}_{Top}}{\Delta^{\pm}_{Bot} + \Delta^{\pm}_{Top}} \tag{5.9}$$

In the positive current polarity, a ratio (r^{+}_{Δ}) greater than zero indicates that the output signal shows incubation time in the P state and spikes in the AP state. This relationship is reversed if this ratio is smaller than 1. In the negative polarity, the opposite effect is observed, which means that a ratio (r^{-}_{Δ}) greater than zero indicates spikes in the P state and incubation time in the AP state. The ratio in the negative polarity case (r^{-}_{Δ}) is shown in Fig. 5.12 mapped on the wafer (a) and across the top FeCoB wedge (b). It is quite clear that the ratio drops from a positive value below 1.2 nm of the top FeCoB to a highly negative value for thicker FeCoB. The average inversion point is found to be around 1.2 nm of the top FeCoB. The first case study specifically shows an example of a MTJ with thin-top FeCoB where the signal spikes in the P state, while the second case study presents the expected behavior for a thicker top FeCoB layer with spikes in the AP states.

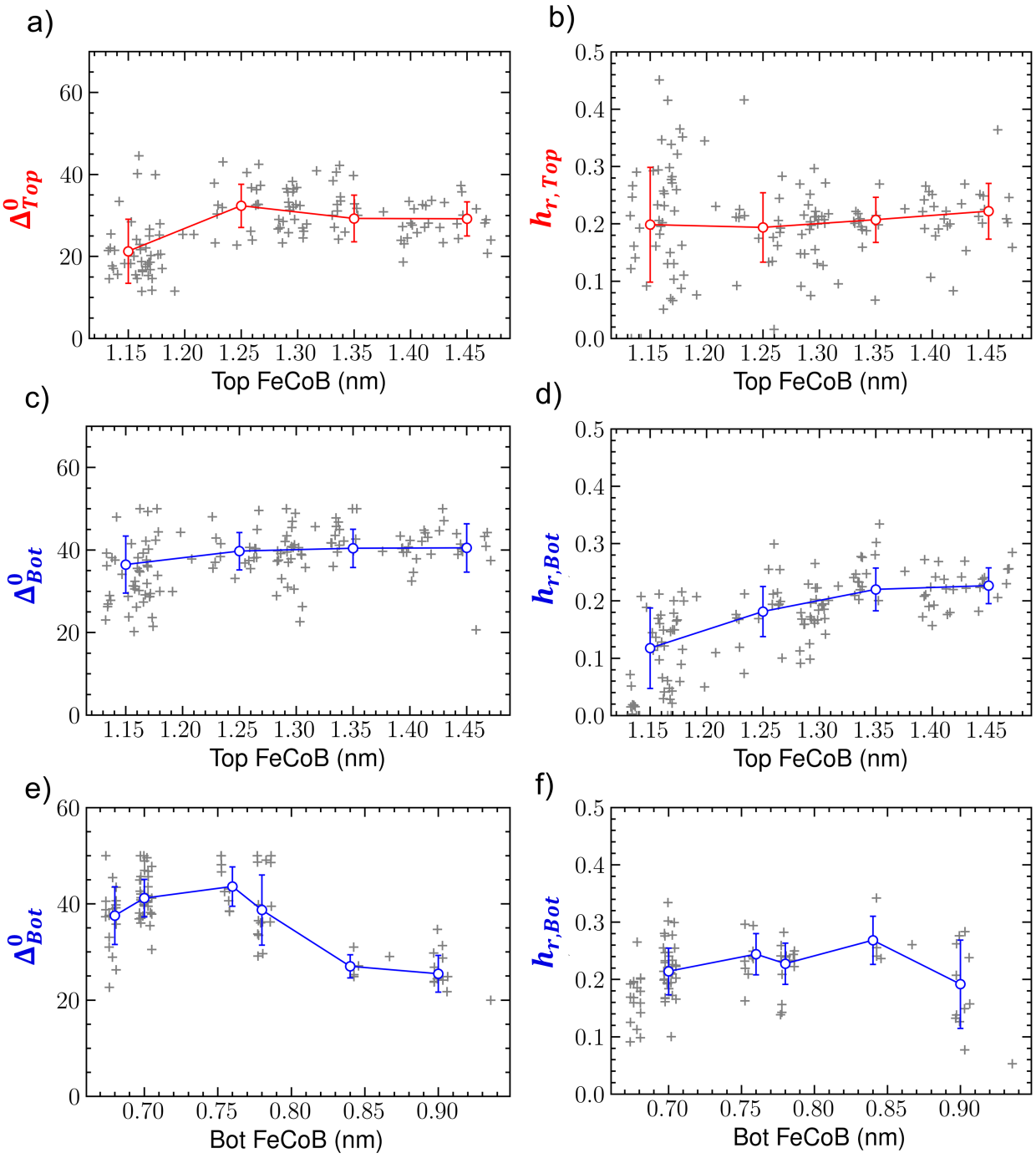

Figure 5.11: Thermal stability (a) and ratio of the dipolar field over the anisotropy field (b) of the top layer as function of the top FeCoB thickness, extracted from common fitting of both current polarity. (c) and (d) refers to the same value of (a) and (b) respectively calculated for the bottom FeCoB layer. (e) and (f) shows the thermal stability and ratio of the dipolar field over the anisotropy field of the bottom layer as function of the bottom FeCoB thickness

One might maintain a cautious approach when fitting the data with the unified model presented in Eq. 5.1. Particularly in the case where only an intermediate regime or only a thermally assisted regime is recorded in a single current polarity (decoupled fitting). Extraction of the critical switching voltage and effective stability of the layer is not straightforward. To overcome this issue, we can directly use the median switching time of the bottom and top layers. This strategy avoids going through fittings of the model to extract critical parameters that need a lot of data points to be estimated correctly. Thus, a second ratio, observed $r_{\tau}^{\pm}$, refers directly to the median switching time of the top and bottom layer in the raw time traces. The main drawback is that this ratio depends on the voltage amplitude (V). It is defined as :

$$r_{\tau}^{\pm}(V) = \frac{<\tau_{Bot}^{\pm}(V)> - <\tau_{Top}^{\pm}(V)>}{<\tau_{Bot}^{\pm}(V)> + <\tau_{Top}^{\pm}(V)>} \tag{5.10}$$

Similarly to the ratio using the effective thermal stability factor (Eq. 5.9), a positive value of r_{τ}^{-} indicates the predominance of an AP state over a P state. Inversely, if the same ratio is largely negative, the signal exhibits a long P lifetime compared to the AP lifetime. The evolution of this ratio in negative polarity is plotted in Fig.5.12.c.d. for voltage bias at 500 mV. Starting with a positive value for the thin top FeCoB layer, this ratio shows an inversion of the sign around 1.3 nm and stays negative for thicker top FeCoB. This observation is comparable to the conclusion based on the thermal stability factors. However, for a very thin FeCoB layer, it seems that the fittings fail to predict the important asymmetry between the P and AP states of the signal. This is because in that region only the negative polarity can be recorded by the measurement setup because of the reason already presented in the first example. From the precessional regime only, the thermal stability factor is much more difficult to estimate accurately. In positive current polarity, the asymmetry in the acquired signal is more pronounced. In fact, the stability ratios and lifetimes at 500 mV, shown in Fig. 5.13.a.b, remain mainly above 0.5. From a neuron-like oriented perspective, the interesting region to build spiking neurons would certainly be an MTJ junction with an important asymmetry between the effective top and bottom stability. As introduced in the simulation chapter, the wide range of voltages for which the incubation time varies significantly while keeping the spike shape quite constant might be relevant for this type of neuronal application. These regions have been identified with positive polarity for reasonable bottom FeCoB thickness and with negative polarity for thin top FeCoB.

In conclusion, in this section, we present evidence that the unified model presented in Chapter 3 applied to the time-resolved measurements of patterned devices. In particular, the energy landscape reconstructed from the experimental data accurately describes the windmill dynamics in terms of current polarity and spike shapes. A very asymmetric signal appears in the negative current polarity for thin top FeCoB with long incubation between spikes in the P state and sharp spikes in the AP state. In the same polarity, the thicker FeCoB layer indicates a weak effective asymmetry between the P and AP lifetimes despite being a promising region of the wafer from the stability ratio calculation. The dipolar interaction definitely affects the spiking signal by varying the effective thermal stability factor of each layer. MTJs showing the majority of P states in both current polarities demonstrates the presence of a dipolar field coupling between the top and bottom layers. However, what remains less evident to show is the synchronization of the top and bottom layers when the effective thermal stabilities are close to each other. This specific point will be addressed in the next section.

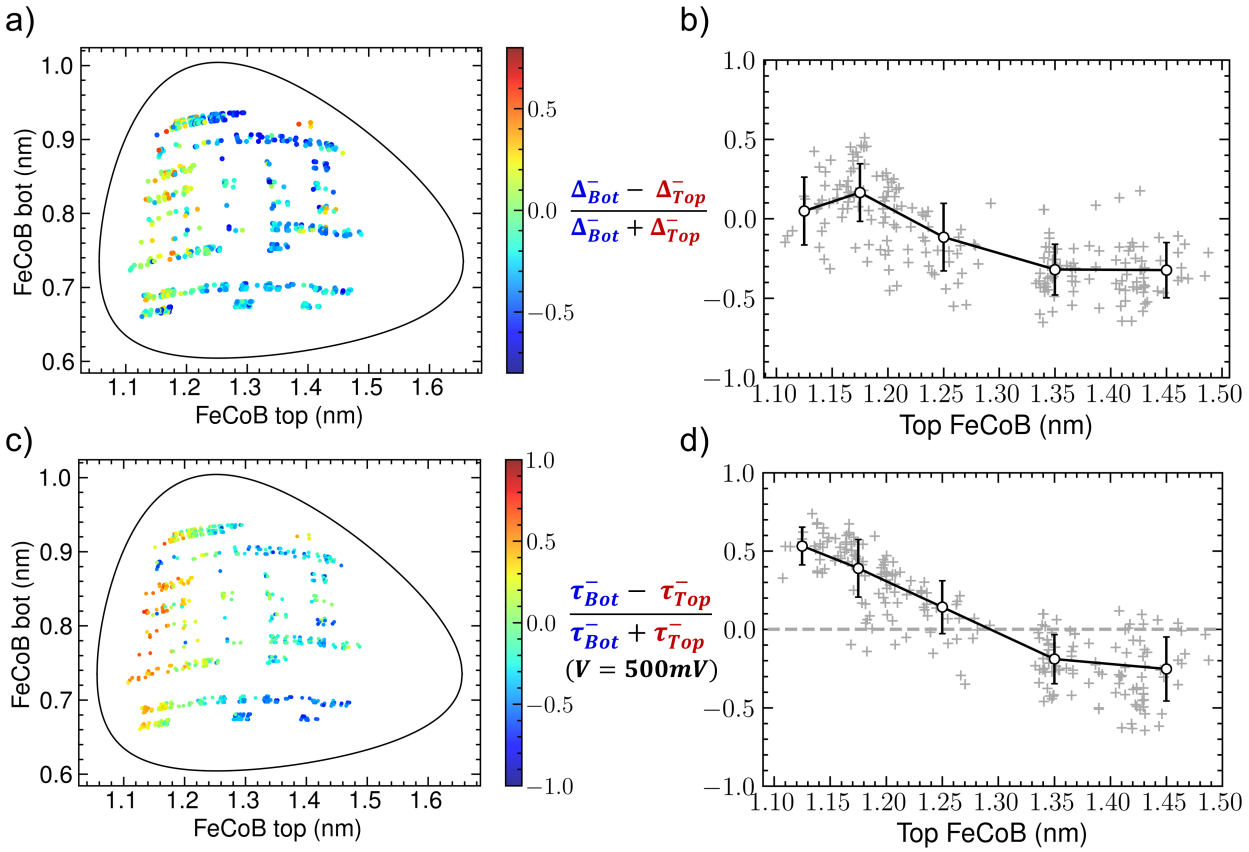

Figure 5.12: Relative stability of the top layer compared to the bottom one mapped over the wafer (a) and across the wedge of the top FeCoB (b) for bottom FeCoB between 0.7 and 0.85 nm. Relative median switching time at 500 mV between the top layer and the bottom one mapped over the wafer (c) and across the wedge of the top FeCoB (d) for bottom FeCoB between 0.7 and 0.85 nm.

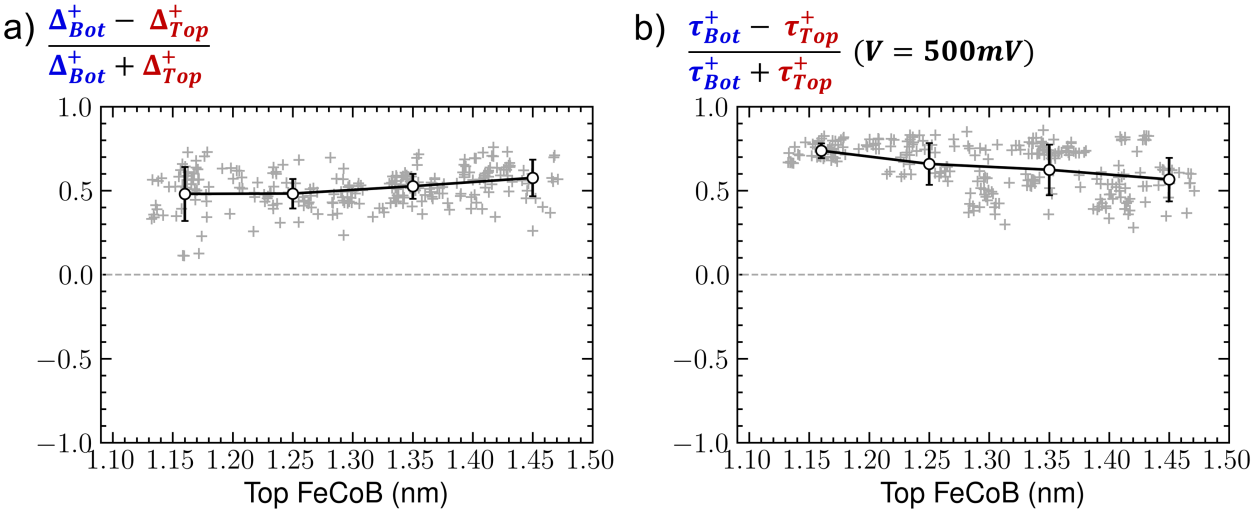

Figure 5.13: Relative stability (a) and relative switching lifetime at 500 mV (b) between the top and bottom layer across the wedge of the top FeCoB thickness for the positive current polarity.

5.3.6 Impact of the dipolar coupling on the spike shapes

The macrospin simulations showed that in the case of a significant dipolar field interaction between the two layers, the motion created deviates from the expected windmill dynamics. At the origin of this deviation, a synchronization between the two layers was observed in the simulated time traces. This synchronization appears primarily in the switching of the hard layer from the P state to the AP state. It has been identified that the synchronization seems to increase with lower asymmetry between the effective anisotropy of the SL and the HL; and with higher dipolar field with respect to the anisotropy field of the SL and HL. The first case corresponds to MTJs with a ratio of r_τ^- (or r_Δ^-) slightly negative and those with a ratio of r_τ^+ (or r_Δ^+) slightly positive. In contrast, the impact of the dipolar field is expected to be lower for large values of r_τ^+ and r_τ^-.

Because the magnetization direction is not directly accessible through resistance measurement of the MTJs, the most representative measurable element is certainly the transition time between the P and AP states. Macrospin simulations suggest that the transition time should increase because of the partial synchronization between the layers. Fig. 5.14 shows the ratio between the transition time from the P state to the AP state ($\tau^-_{P\to AP}$) and the transition time from the AP state to the P state ($\tau^-_{AP\to P}$). The mapping of the wafer highlights that most of the long transitions from P to AP occur in the thicker region of the top FeCoB and are more than three times longer than the one from the AP to the P state. This region exhibits a small negative value of the ratio r_τ^- (or r_Δ^-). In Fig. 5.14.b, the peak of the long transition from the P state to the AP state that occurs between 0 and -0.4 indicates a correlation between the transition time and the relative effective stability of the layer. In the positive polarity, the transition between the P-to-AP state remains reasonably stable (less than twice the AP-to-P transition time). This is expected from the fact that the positive polarity exhibits a higher asymmetry between the top and bottom effective stability.

In conclusion, the relative stability of the layer seems to have an impact on the transition time from the P-to-AP state. From macrospin simulations, these longer transitions originate from a partial synchronization of both layers. However, we point out here that those types of analysis based on time-resolved measurements are insufficient to confirm with certainty that a synchronization actually occurs in the system. Another cause that possibly significantly delays the switching time is the onset of a domain wall for device diameters larger than 50 nm. As most of our junctions have diameters larger than this dimension, the reversal through nucleation and propagation of a domain wall cannot be excluded. Further micromagnetic simulations on this topic might answer this question.

5.3.7 Impact of the external magnetic field : Case study

In this section, we focus on the analysis of a single MTJ to demonstrate the impact of the external magnetic field on the spike shapes. The MTJ under study has a diameter of 90 nm with $FeCoB_{top}$ = 1.35 nm and $FeCoB_{bot}$ = 0.75 nm. The approach to relate the critical parameters of each layer of the MTJ with the measured time traces is based on the fit of the cumulative distribution function (CDF) of Yang's expression as a function of the applied voltage and magnetic field. The fitting methods differs from the one used up to now because it takes into account the full distribution and not only the median switching time. The thermal stability factor, the critical current density (or critical voltage), the anisotropy field of the layer, and the attempt times in each regime (τ_D and τ_0) are the main fitting parameters of the unified expression. The critical current density is calculated from the critical switching voltage and the resistance-area product (RA) of the wafer ($V_{c0} = RA\ J_{c0}$). The CDF of the switching time from the P state to the AP state for different values of applied voltage are shown in Figure 5.15.b and the median switching time is reported in 5.15.a. It is

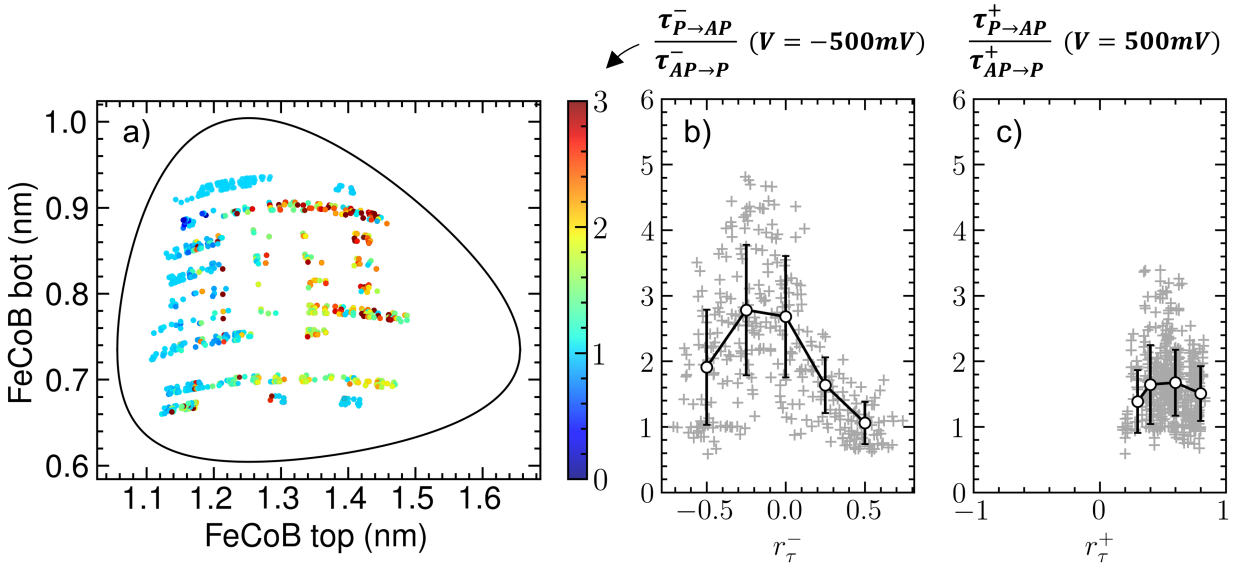

Figure 5.14: (a) Ratio between the transition time from the P to the AP state and the transition time from the AP state to the P state mapped over the wafer. This ratio is represented as function of the ratio of the lifetime between the P and AP state (r^-_τ) and (r^+_τ) for negative (b) and positive (c) current polarity respectively.

noticed that the fit quality degrades as the switching time is reduced to around 10 ns. This shift is attributed to the limited bandwidth of the set-up, which goes from DC to 350MHz. The switching times below 3 ns are then more difficult to identify, which makes the distribution of the switching time distorted. The energy barrier extracted from the fit is equal to 46 k_BT and the critical current density J_{c0} is 6.71 MA/m² (V_{c0} = 578 mV). The characteristic time related to the precessional regime (τ_D) is equal to 270 ps and the one in the thermal regime (τ_0) is 100 ps.

To access the dipolar field and anisotropy field, a perpendicular external magnetic field is applied to the MTJ while recording the time traces at different voltages. The effect on the CDF is shown in Figure 5.15.c. The external field affects the shape of the CDF since it brakes the symmetry between the two P states (↓↓, ↑↑) and the two AP states (↓↑, ↑↓), leading to four different characteristic times : $\tau_{\downarrow\downarrow}, \tau_{\downarrow\uparrow}, \tau_{\uparrow\uparrow}, \tau_{\uparrow\downarrow}$. Note that the first and second arrows in the notation ↑↓ refer to the SL and HL, respectively. At a given current density and for a positive applied magnetic field (+z), $\tau_{\downarrow\downarrow}$ and $\tau_{\downarrow\uparrow}$ times decrease because the field polarity helps magnetization reversals from ↓ to ↑ configurations due to the Zeeman energy. The $\tau_{\uparrow\uparrow}$ and $\tau_{\uparrow\downarrow}$ times increase because the positive applied field hinders the magnetization to switch from ↑ to ↓ orientation. The energy landscape in the case of a dual free layer MTJ subjected to an external magnetic field is presented in chapter 3 in Fig.3.6.b.

The consequences of the external applied field on the acquired signal are shown in the inset of Fig. 5.15.c where a long P state (↑↑) is followed by a shorter P state (↓↓). The asymmetries between the two P states and the two AP states increase with the field amplitude. The plateau at 50% of probability in Fig. 5.15.c confirms that there is the same number of short and long P states. This is an additional evidence that the windmill dynamics drives the spiking response of the device. The fit over the CDF with applied magnetic field allows us to extract the dipolar field (12.2 mT) and anisotropy field (147 mT).

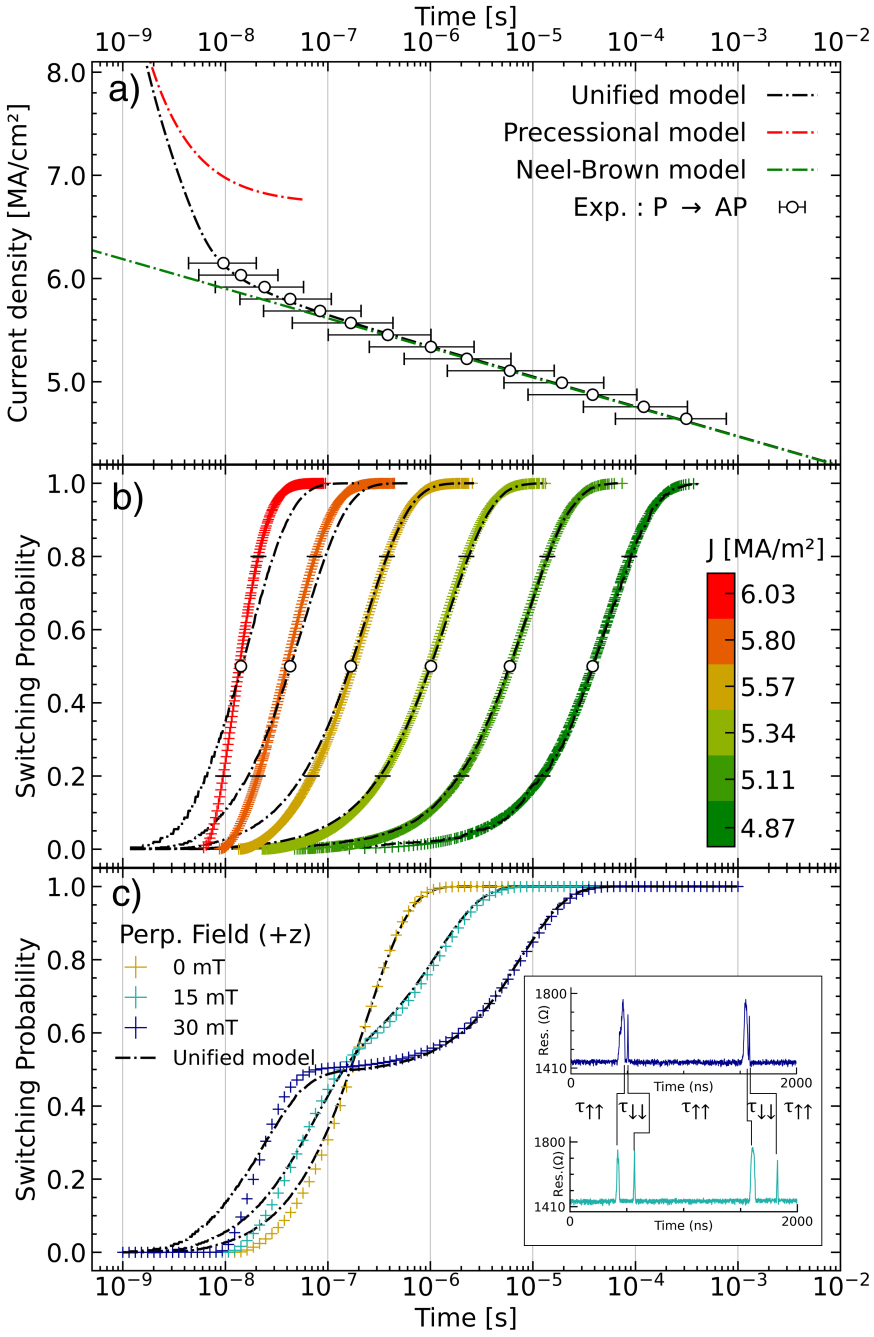

Figure 5.15: a) Median switching time of P→AP switching and b) the corresponding CDF for different injected current density at Happ = 0 mT. (c) CDF of the P→AP switching under 5.5 MA/m² of current density with 0, 15 and 30 mT of external magnetic field. Inset of (c) shows time traces of the resistance at 15 and 30 mT of applied magnetic field.

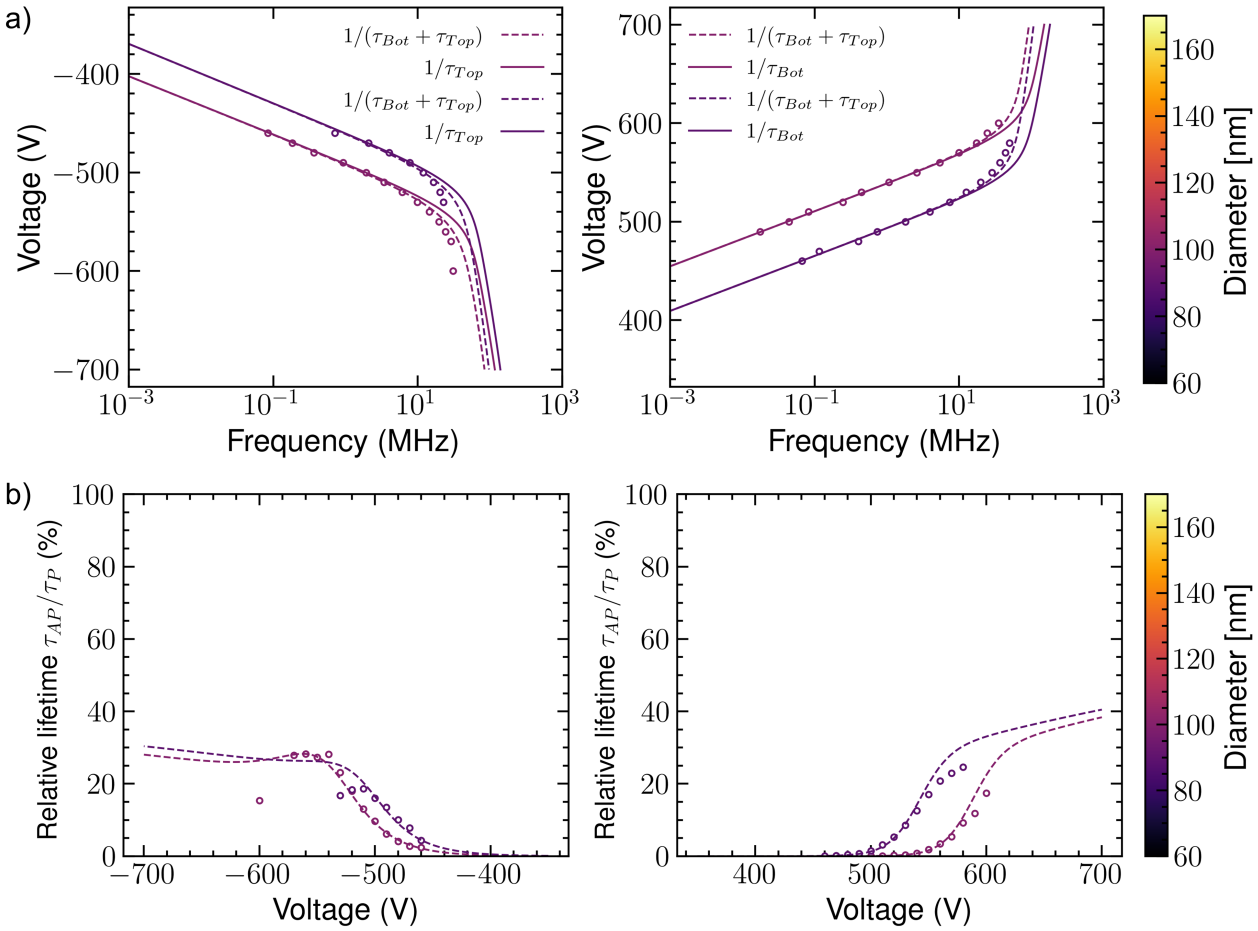

Figure 5.16: (a) Spiking frequency for positive (left) and negative (right) current polarity considering a calculation based only on the HL (full line) and the case with both HL and SL (dashed line). (b) Relative lifetime between P and AP state in the same two devices in (a) for positive and negative current polarity.

5.3.8 Spiking frequency and energy consumption

This last section on the analysis of real-time traces is dedicated to the spiking frequency together with the energy consumption of spikes. This section comes last in the analysis because the spiking frequency can be seen as a consequence of the switching times discussed in the previous sections. As a reminder, we can define two types of frequency in our system. The first is called the windmill frequency calculated from the full windmill period in terms of magnetic configuration. It is then composed of two P states, two AP states, and the four transitions between those states. A second frequency can be defined as the spiking frequency, which in a first approach is twice the windmill frequency. The spiking frequency is the one that is easily accessible by real-time resistance measurements and is mathematically expressed as a function of the mean lifetimes :

$$\overline{f} = \frac{1}{\overline{\tau_P} + \overline{\tau_{AP}} + \overline{\tau_{P\to AP}} + \overline{\tau_{AP\to P}}} \tag{5.11}$$

We note here the use of the *average* value of the switching time distribution, noted $\overline{\tau}$, compared to the median value previously introduced, noted $< \tau >$. From the macrospin model, the frequency is expected to evolve exponentially in the thermally assisted regime and become inversely proportional in the precessional regime as a function of the voltage applied (see Fig.3.8 in the modeling chapter 3). Furthermore, the dominance of the incubation time over the width of the spike is expected to lead to a good approximation of the average spike frequency as $1/\tau_{incubation}$. The evolution of the spiking frequency for two MTJs with the top FeCoB at 1.35 nm and the bottom FeCoB at 0.7 are shown in Figure 5.16.a in negative (left) and positive (right) current polarity. The spiking frequency reacts accordingly to the prediction of the macrospin model. It is worth to note that modeling the spiking frequency considering only the incubation time fits the experimental data accurately up to the intermediate regime. A desirable functionality towards SNN application might be to keep the spike width constant while varying significantly the spiking frequency. The very fast change in spiking frequency is achieved in the thermally assisted regime, while the spike width is mainly controlled by the effective anisotropy ratio between the top and bottom systems, as demonstrated in the macrospin modeling chapter (3.10.c).

The relative lifetime between the spike width and the incubation time calculated as $(\tau_{AP}/(\tau_P + \tau_{AP}) \times 100)$ is shown in Fig. 5.16.b as a function of the applied voltage for the two MTJs. As anticipated by the macrospin model, the relative lifetime is close to zero in the thermally assisted switching regime of the hard layer, while it increases significantly in the intermediate switching regime. The two criteria that provide a good candidate for a spiking neuron are simultaneously investigated by looking at the relative lifetime as a function of the normalized applied voltage. Normalization of the voltage is calculated by dividing the applied voltage by the critical voltage of the hard layer. The critical voltage chosen in this case is equal to the voltage for which the hard layer has a median switching time of 100 ns, denoted $V_{c,100ns}$.

To ensure a highly asymmetric output signal, the relative lifetime should remain as far as possible from 50% throughout the range of the thermally activated and intermediate switching regimes. The use of a common marker ($V_{c,100ns}$) that delimits the thermally activated and processional regime allows the devices to be compared considering different asymmetry in the effective thermal stability of the top and bottom layers. Fig.5.17 synthesizes the evolution of the relative lifetime for different dies across a top FeCoB wedge and for fixed bottom layer thickness (0.9 nm). This FeCoB wedge has previously been identified as a parameter that affects the relative effective stability of the layers in the negative current polarity (Fig. 5.13). We report the value of r_Δ^- for each die, which is a marker of asymmetry between the effective stability of the top and bottom electrodes.

The first graph (Fig. 5.17.a) presents the case of high positive asymmetry between layers ($r_\Delta^- = 0.3$). For this case, the relative lifetime is above 90% at the critical switching voltage, which is relevant for spiking neuron-like behavior. However, as we increase the thickness of the top FeCoB layer, the asymmetry in terms of effective thermal stability decreases ($r_\Delta^- \approx 0$) and the relative lifetime increases significantly even in the thermally activated regime (Fig. 5.17.c). These types of device are not suitable for spiking neurons. Finally, for the negative ratio (Fig. 5.17.e), the relative lifetime factor recovers a better asymmetry in the thermally activated regime. However, the intermediate regime already shows quite a high value (around 40% at $V_{c,100ns}$).

Finally, the frequency as a function of the applied voltage is shown for a similar junction composition with diameter ranging from 80 to 160 nm in Fig. 5.18. The larger diameter of the pillar generally has a significantly higher critical voltage, as shown in the left panel. However, the effective thermal stability, evaluated

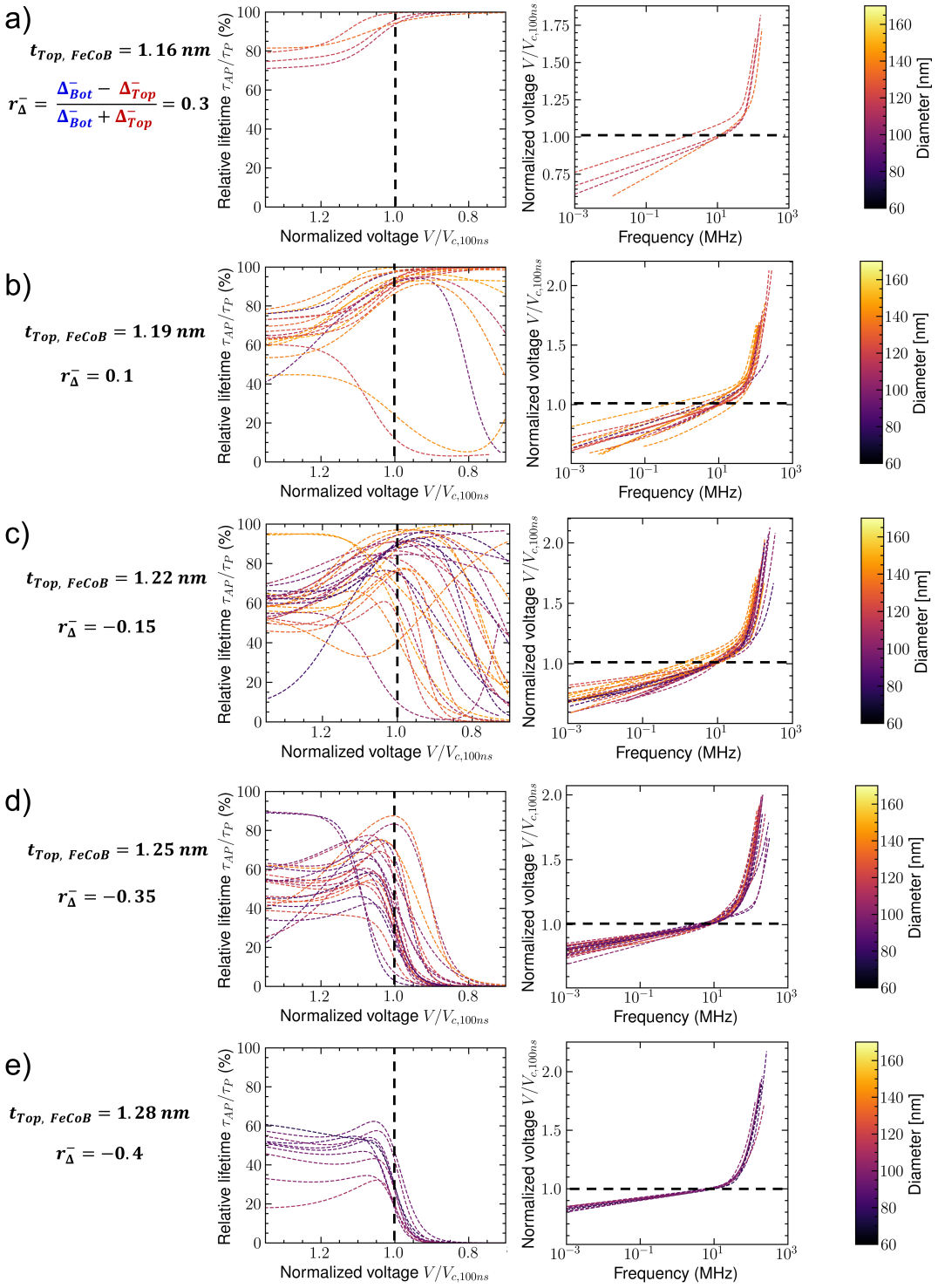

Figure 5.17: Relative lifetime between the P and AP state (left) and spiking frequency (right) as function of the normalized voltage for different dies on the wafer across the top FeCoB thickness wedge : a) $FeCoB_{Top}$ = 1.16 nm, b) $FeCoB_{Top}$ = 1.19 nm, c) $FeCoB_{Top}$ = 1.22 nm, d) $FeCoB_{Top}$ = 1.25 nm, e) $FeCoB_{Top}$ = 1.28 nm.

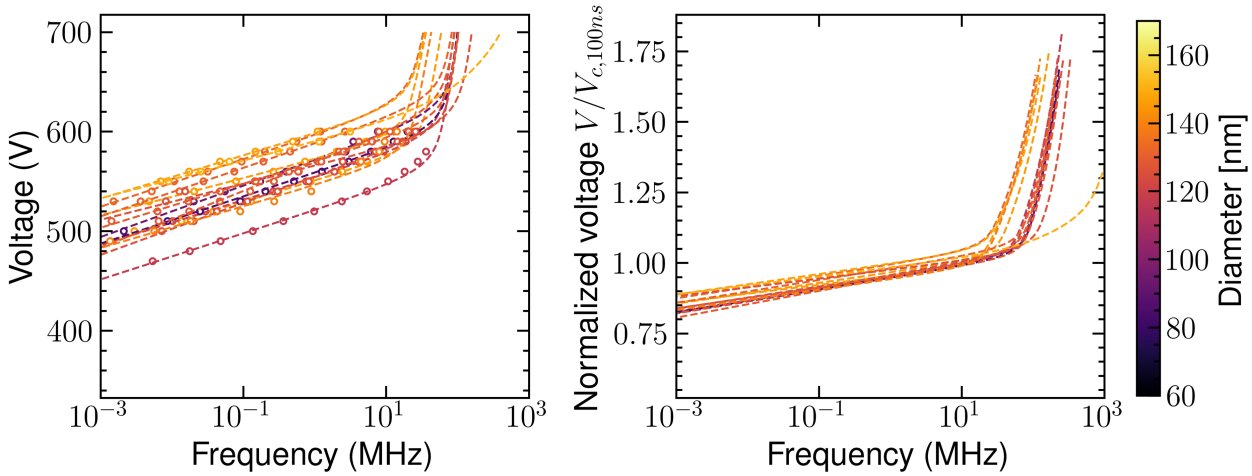

Figure 5.18: Spiking frequency as function of the applied voltage (a) and normalized voltage (b) for multiple MTJs of diameter from 80 to 160 nm located in the same die (same FeCoB thicknesses).

by the slope in the thermally activated regime, remains relatively constant for all pillar sizes, as demonstrated by the right panel, where the frequency is plotted as a function of the normalized voltage. Horizontal slopes result in greater thermal stability. From a macrospin model point of view, the thermal stability and the critical voltage should increase with respect to the diameter of the pillar due to the larger volume. However, in our case, only an increase in the critical voltage seems to occur, while the thermal stability remains, in general, quite constant. This discrepancy might have its origin in the different switching mechanisms involved in the case of a large diameter pillar. Indeed, the uniform magnetization reversal considered for low-diameter pillars might change toward domain-wall-like reversal as the pillar size increases. In particular, the thermal stability is expected to reach a plateau when the size is increased because of the limited amount of energy needed to nucleate a domain wall.

In order to evaluate the energy consumption of our device we calculated the dissipation power as $P = V^2/R_p$ and the energy per spike as $E_{\text{spike}} = P/f$ where f is the spiking frequency. The most energy efficient devices are the one with smallest lateral dimension as shown in Fig. 5.19. This dependency with voltage is attributed to the fact that we observed similar critical voltage for small and large device (V constant) while the device resistance increases as d^2 with the pillar diameter. It results that for small device, the dissipated power is reduced compared to larger diameter pillar. In term of energy per spike, we found that a pillar of around 80 nm powered by 0.15 mW and spiking at 50 MHz consumes around 3 pJ/spike. In comparison to the synaptic operation in hardware SNN in table 1.1 (from tens to thousand pJ/synaptic operation), our device consumption is quite low. Compared to a LIF neuron based on DW propagation proposed by [104] with 0.5 pJ/spike, our solution seems to be lightly less energy efficient. However, we can note that the main limitation on the energy efficiency of SNN generally comes from synaptic operations as they consume more than 90% of the total energy as highlighted in [92].

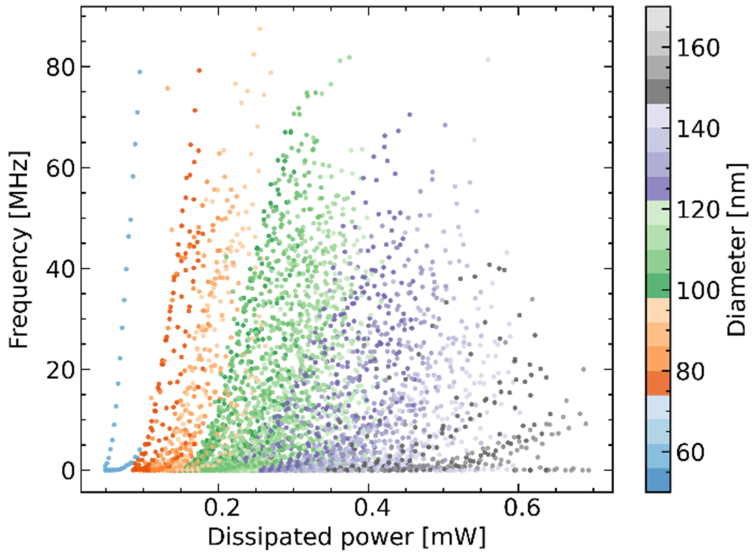

Figure 5.19: Power consumption of dual free layer MTJ as function of the spiking frequency and pillar diameter.

5.4 Conclusion

This chapter on the electrical characterizations of the nano-patterned devices demonstrate the existence of windmill dynamics in dual free layer MTJs of various pillar sizes. The range of thicknesses of the top and bottom FeCoB was used to change the asymmetry in the effective thermal stability of each layer. In quasi-static measurements, this asymmetry was identified as a relative change in the coercive field and critical switching voltage of both layers. Although similar behaviors were observed at the sheet-film level, it is difficult to determine which of the two coercive fields measured with a resistance versus field loop corresponds to the top and bottom FeCoB layers. It is only by using the time-resolved measurement setup that the assumptions were definitely confirmed.

In addition to that, the time-resolved measurements correlated the quasi-static properties of the MTJs. The evolution of the effective thermal stability correlated with the evolution of the coercive field measurement. MTJs with highly asymmetric effective stability between the HL and the SL are prone to show a much better spiking signal than MTJs, where both layers exhibit similar effective stabilities. The model presented in chapter 3 appears to be effective in predicting the primary characteristics of the spiking signal. However, a deviation from this model is particularly observed when both layers show similar thermal stability. This case has been attributed in the macrospin simulations to the synchronization of the top and bottom layers.

Furthermore, the behavior of the MTJs under an applied magnetic field can also be explained by the extension of the unified model. It shows notably that the windmill dynamics is resilient to an external magnetic field that can be generated by the closest neighbors in a very dense array of MTJs. To limit the effect of the dipolar field on windmill dynamics, several structures based on the double soft SAF structure have been proposed in the material development chapter 4. It would be of interest to fabricate more samples with this type of structure to validate the hypothesis that the dipolar coupling is at the origin of the partial synchronization observed in our system.

Chapter 6

Perspectives towards hardware computing platform for SNNs

Contents

In this last chapter, we propose some perspectives on how to use dual-free layer MTJ for spiking neurons applications. The path to achieving complete hardware SNNs based on spintronic devices is still long and involves more steps that are not addressed in this thesis. In particular, the integration of the spiking device with neighboring synapses remains a challenge and depends on the coding strategy (rate-coding, latency coding) of the network. The next two sections explore two ways to use the spiking device developed in this thesis. The first strategy is to use the MTJ as it is in the input neuron layer to feed neural networks with spike trains. The second approach is to emulate the integration of the input signal of a neuron with a capacitor to get closer to a leaky integrate-and-fire (LIF). Finally, the last part of this chapter discusses the challenges of implementing local learning rules such as spike-timing dependent plasticity (STDP) compatible with MRAM-based synapses.

6.1 Dual free layer MTJ as input neuron

The SNN are generally organized as layers of neurons with connection through synapses from one layer to the other. Inside the network, the information is encoded as spikes propagated by the neurons. The data treated by a spiking neural network can be very different from one application to the other (image, sound, text, etc.). We need an intermediate step to transform those data into usable inputs for the NN. There are two main types of coding strategy for SNN. The first transforms the input data into trains of spikes at a given frequency, which refers to the rate-coding approach (see Fig. 6.1.a). The second type uses the delay time from the first spike to encode the information and is known as "latency coding". With our dual free layer MTJ, we propose to map the inputs with respect to the rate-coding approach.

The dual-free-layer MTJ can be used during this intermediate step necessary to feed the network with spike trains. We take the example of a pattern recognition task to proceed in a black and white image. The image contains n black and white pixels coded on a gray scale from 0 (black) to 1 (white). To treat this image, the first layer of our SNN has the same number of inputs as the number of pixels on the image. We propose using a dual free-layer MTJ for each input pixel. On the MTJ a voltage proportional to the intensity of the pixel is applied. As demonstrated in this thesis, the output spiking rate evolves exponentially (in the thermally activated regime) as a function of the input voltage (see Fig. 6.1.b). The spike stream created for each input then propagates to the next layer of neurons. The wide range of spiking frequency reached in the thermally assisted regime allows to encode precisely the input data. However, as the switching process is stochastic in the thermal assisted switching regime, the time scale can significantly increase for low frequency and a large number of input levels.

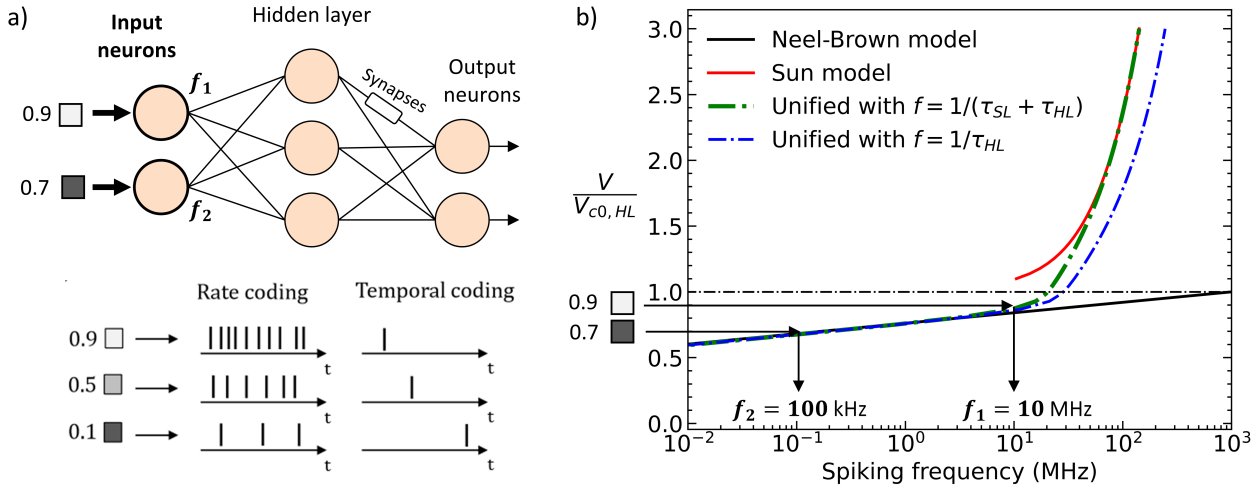

Figure 6.1: a) Schematic of a spiking neural network where input neurons transform the raw data into spikes trains (rate coding) or single spike (temporal coding) (b) Relation between the input voltage and the spiking frequency of the dual free layer system from the macrospin model defined in chapter 3.

6.2 Leaky integrate-and-fire (LIF) model with dual-free layer MTJ

The leaky integrate-and-fire (LIF) model is one of the simplest models used extensively in the development of the SNN algorithm. The model is presented in Chapter 1, we report here the evolution of the membrane potential $V(t)$ as a function of the cell membrane capacity C, the resistance of the membrane R and the input current I:

$$C\frac{\mathrm{d}V(t)}{\mathrm{d}t} = I(t) - \frac{V(t)}{R} \tag{6.1}$$

$$V(t) = 0 \text{ if } V(t) \geq V_T \tag{6.2}$$

It is quite straightforward to see an analogy between the biological model of Eq.6.1 and the equivalent parallel RC circuit in electricity (see Fig. 6.2.e) where the capacitor plays the role of an integrator with leaky functionality. However, the reset function of Eq.6.2 is more difficult to achieve with basic electronic components. In this section, we focus only on Eq.6.1.

To visualize the effect of successive input current pulses into our MTJ with a capacitor in parallel (C = 3 nF, R = 1000 Ω), we calculate the voltage across the MTJ by integrating the LIF equation over time. In this example, the input current pulses contains 10 pulses of 200 ns with 50 ns in between and with an amplitude of 1 mA. The voltage across the MTJ is expected to increase during pulses with respect to the RC time constant of the circuit and to decrease when no pulse is applied, as shown in Fig.6.2.b. To acquire the output signal, we use a scope with 50 Ω impedance placed in series with respect to the MTJ. As a consequence, the expected signal (in Fig.6.2.c) differs from the voltage across the MTJ. Fig. 6.2.d presents an example of an experimental time trace recorded with the scope on a dual free layer MTJ. As we expect, after several input pulses below the critical voltage of the hard layer, the charges accumulated in the capacitor eventually bring the capacitor voltage above the threshold voltage after the 4^{th} pulse. Spikes from the dual free layer MTJ are recorded in the 5^{th} and 6^{th} input pulses.

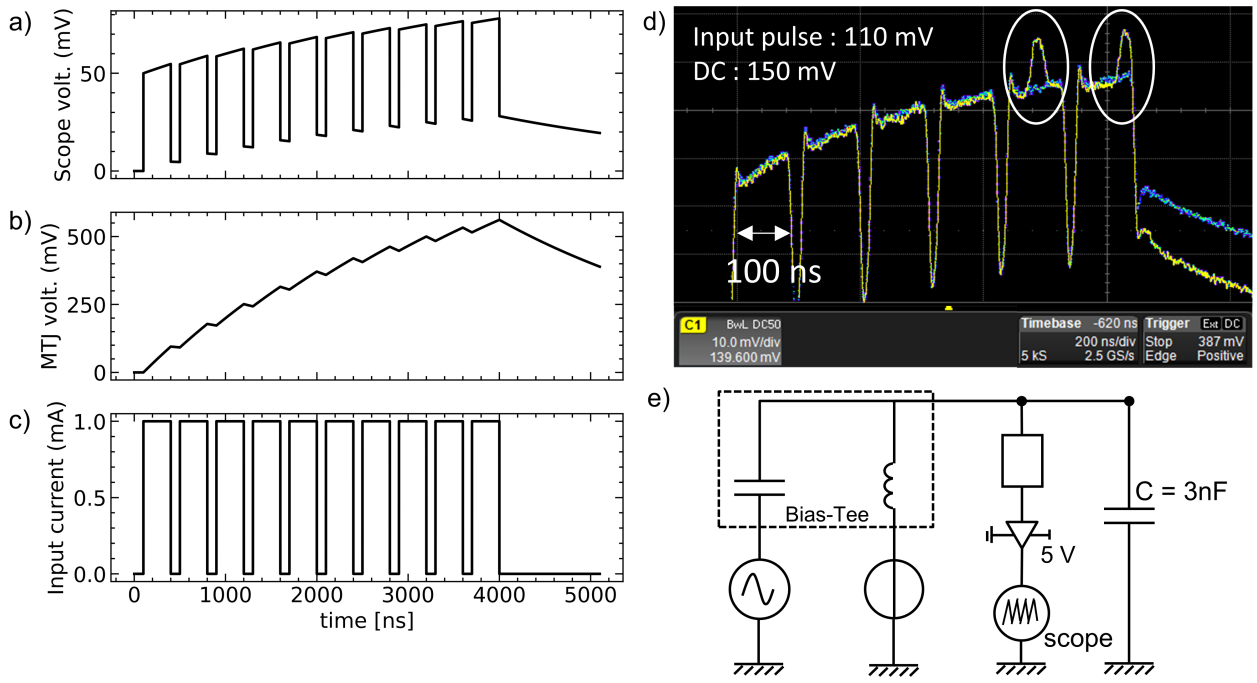

Figure 6.2: (a) Expected output voltage recorded by the scope in serie with the MTJ, with (b) the voltage across the MTJ when subjected to input current pulses of (c). In (d), the experimental time traces recorded with the scope with input DC current of 150 mV and 6 input pulses of 110 mV. In (e), the scheme of the electrical circuit to acquire the time trace in (d).

6.3 Hardware STDP learning rule with MTJs

Finally, we want to mention in this last part some experimental evidence of how a MRAM device can be used as a synapse with implementation of a STDP learning mechanism. Previous simulation work [105] predicted the great potential of implementing local learning rule with SOT-driven MTJ. We propose in this section to explore the use of a MTJ with a stable reference layer coupled to a SAF. This experimental demonstration rely on a MTJ device fabricated by Aurélien Masseboeuf at Spintec.

All types of neural networks must be trained to be efficient in solving useful tasks where training means updating the synaptic weight of the neural network. This training step can be done "on-chip" or "off-chip". The training phase is the most demanding phase in terms of time, complexity, and energy consumption compared with the inference phase. The algorithm to perform the training phase relies mainly on supervised learning with back-propagation of the errors through the networks, which can be particularly heavy for large NN. These methods are very robust to minimize the error in the output of the ANN. However, it requires access to all the synaptic weights of the hardware NN. As training generally needs to be done only once for a specific task, it can be computed on a different platform (for example, in a powerful data center) and then uploaded to the hardware SNN.

On the contrary, the local learning rules (such as STDP) propose to use only the information from neighboring synapses and neurons to update the synaptic weight. The main drawback of this "local" learning is that it might not minimize the global error of the neural network. This is why some combinations of back-propagation and local learning rules appeared in the literature recently to overcome this issue [142]. In this example, we focus on the STDP learning rule applied to binary synapse emulated by a MRAM device.

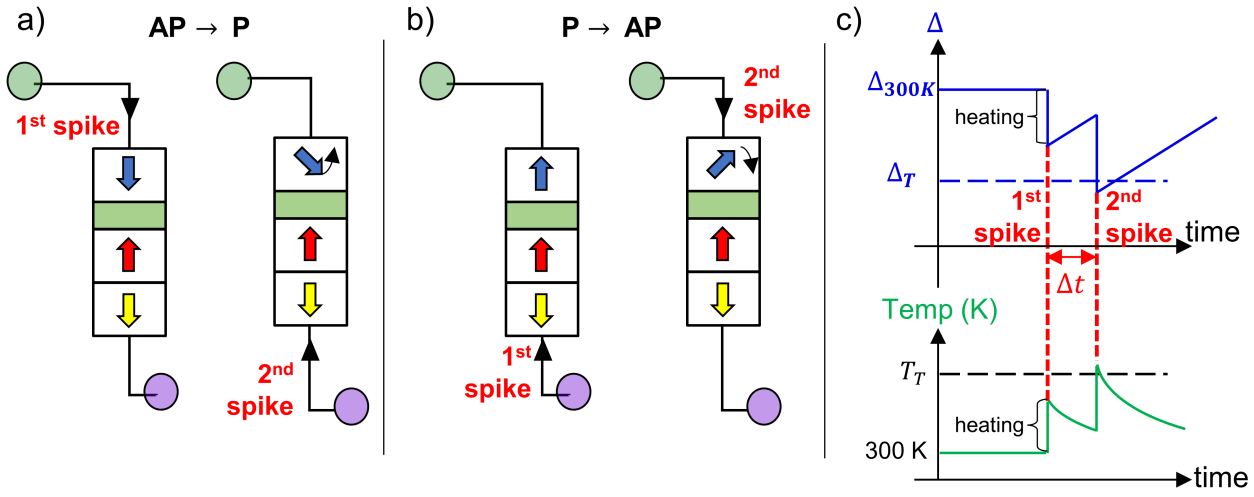

Figure 6.3: (a) and (b) illustrate the STDP principle with MRAM device with the causal (potentiation, AP to P switching) and the anti-causal (depression, P to AP switching) case respectively. (c) is a schematic of the thermal stability factor of the MTJ and the device temperature when two successive pulses are applied with a delay time of Δt. After the first input spike and delay Δt, the thermal stability is reduced from Δ_2 while the device temperature is increased to T_2.

The STDP learning rule allows one to modify the weight of a synapse depending on the relative delay time between a pre- and a post-synaptic spike. If the pre-synaptic neuron spike before the post-synaptic neuron, the causality forces the synaptic weight to increase (stronger link between the neurons). In contrast, synaptic weight decreases when the post-synaptic neuron fires before the pre-synaptic neuron.

The basic principle is to use the first spike to heat the junction, which lowers the energy barrier ($\Delta = \frac{E_b}{k_B T}$), and the second spike would be able to switch the junction if it appears close to the first spike. In case of causality (pre-neuron spikes before post-neuron), the junction switches from low (AP) to high (P) conductance. In the opposite situation, the MTJ switches from high conductance to low conductance. The probability of switching increases with the reduction of the delay between the spikes due to less cooling time. A schematic of the evolution of the thermal stability factor and the MTJ temperature is drawn in Fig. 6.3.c. The spike width and the spike amplitude should be optimized in order to guarantee a sufficient heating effect without switching the MTJ with a single pulse. An example of the impact of the delay time between the spikes and the switching amplitude to reverse the MTJ is shown in Fig. 6.4.a. The figure compiles the critical switching lines between P and AP states as a function of the voltage pulse amplitude and applied magnetic field. The relevant region is close to the 0 effective field. The inner black curve represents the extreme case of 2 consecutive spikes of 20 ns pulse with 0 delay time, while the outer black curve denotes the opposite extreme of infinitely long delay between 2 spikes of 20 ns. In between the black curve lie the cases of various delay times between 2 and 500 ns. The critical voltage varies from -220 mV to 170 mV for infinit and zero delay times, respectively. It proves that the elevation in the device temperature can be used to mimic STDP learning with a probabilistic update of the synaptic weight as function of the delay time. Fig. 6.3.b shows a superposition of 10,000 time traces recorded by the scope in series with the MTJ with a 50 Ω impedance. Two consecutive input pulses of 190 mV with 25 ns pulse duration and 5 ns of delay are applied to the MTJ. Some switches already occur from P state to AP state during the first pulse. After the second pulse, the time traces switched from P state to AP state.

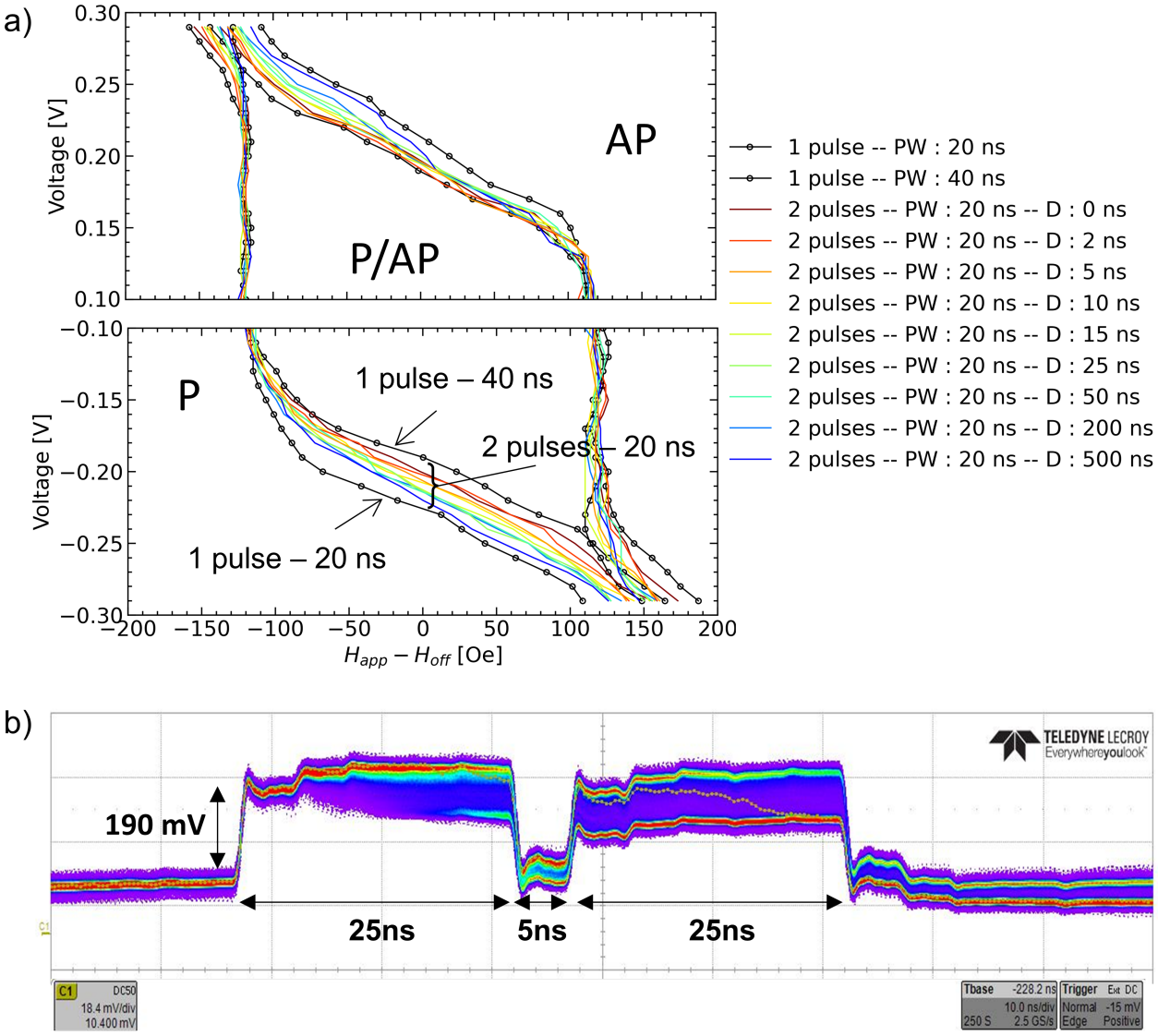

Figure 6.4: (a) Critical lines of P to AP and AP to P switching for different applied magnetic field and applied voltage. (b) shows time-resolved measurement of a MTJ subjected to two consecutive pulses of 190 mV with pulse width of 25 ns.

Chapter 7

Conclusion

This thesis falls within the context of the need to develop building blocks for hardware SNNs to solve complex tasks more efficiently, based on spatio-temporal data, for example. The potential of using spintronic-based devices for multilevel synaptic weight has been studied in the past with successful results [17]. Therefore, the aim of this thesis was to focus on the neuronal functionality in SNN using the same sprintronic-based approach [98]. From the modeling of the system to the fabrication and characterization of the nanopatterned MTJs, this thesis gives a complete study on the spiking dynamics obtained by the dual free layer magnetic tunnel junction (DFL-MTJ) system.

In chapter 3, we identified the key criteria according to the macrospin model and simulations to generate spiking dynamics. This numerical approach highlights the importance of the relative stability of the soft and hard layers in the spike shapes and the spiking frequency. The unified model adapted from the literature of STT switching model predicts the possibility of producing spikes in the high- or low-resistance state of the MTJ depending on the current polarity. The mean spiking frequency is shown to be highly non-linear in the thermally assisted switching regime because of the exponential evolution of the HL switching time. This non-linearity is a key feature in the majority of artificial neuron models. However, the dipolar field between the layers significantly affects the windmill dynamics, making the spiking signal asymmetric between positive and negative polarity. Additionally, both layers tend to synchronize when the HL switches from a parallel to an anti-parallel alignment. The consequence on the time traces is a degradation of the windmill dynamics and a longer switching time. The two different strategies presented to recover the spiking signal are based on the domination of the effective field of both layers on the dipolar field between them and the increase of the asymmetry between the effective field of each layer.

From this analysis, the chapter 4 presents the material development steps of the DFL-MTJ suitable for generating a spiking signal. The stacks deposited by the magnetron sputtering technique are annealed and analyzed by NanoMoke and VSM measurement to extract the interfacial anisotropy and saturation magnetization of the top and bottom FeCoB layers. The final wafer for nanofabrication is composed of two cross-wedges to vary the effective anisotropy ratio between the top and bottom FeCoB layers, which has been identified in the chapter 3 as a crucial parameter in the windmill dynamics. The control of MTJs for MRAM applications at the industry level is without a doubt a considerable advantage of this structure, which is BEOL compatible. In addition, the complexity added generally by the SAF element in the MRAM structure is absent in the case of a dual-free layer MTJ stack. It can be pointed out here that the fabrication process has been kept short in the thesis despite being a time-consuming task in the PhD. Instead, the shift

in focus was voluntary towards the concept description, the modeling, and the characterization at the wafer and device level. In my opinion, this was where the most important findings could be made for the scientific community.

Finally, a multiscale electrical characterization from the quasi-static to the dynamical properties extracted from the time-resolved setup confirms the existence of the windmill dynamics in our structure. It validates the workflow we adapted along this thesis to design a magnetic tunnel junction suitable for a spiking neuron application. MTJs with highly asymmetric effective stability between the HL and the SL are prone to show a much better spiking signal than MTJs where both layers exhibit similar stabilities. The unified model developed in the chapter 3 seems to be valid to anticipate the main characteristics of the spiking signal. However, a deviation from this model is particularly observed when both layers show similar thermal stability. This case has been attributed in the macrospin simulations to the synchronization of the top and bottom layers. Furthermore, the behavior of the MTJ under an applied magnetic field can also be explained by the extension of the unified model. It shows notably that the windmill dynamics is resilient to an external magnetic field that can be generated by the closest neighbors in a very dense array of MTJs. To limit the effect of the dipolar field on windmill dynamics, several structures based on a double soft-SAF structure have been proposed in the materials development chapter 4. It would be of interest to fabricate more samples with this type of structure to validate the hypothesis that the dipolar coupling is at the origin of the partial synchronization observed in our system.

In the last chapter, we provide some perspectives of application for the DFL-MTJ. The concept can be used to convert continuous input data into spikes trains and feed a SNN based on rate-coding. We also demonstrate that the LIF model can be emulated by coupling our DFL-MTJ with a capacitor in parallel. We finally propose to use MRAM device as a binary synapse with STDP learning rule based on first results obtained with time-resolved measurement.

Chapter 8

Appendix

8.1 Appendix 1

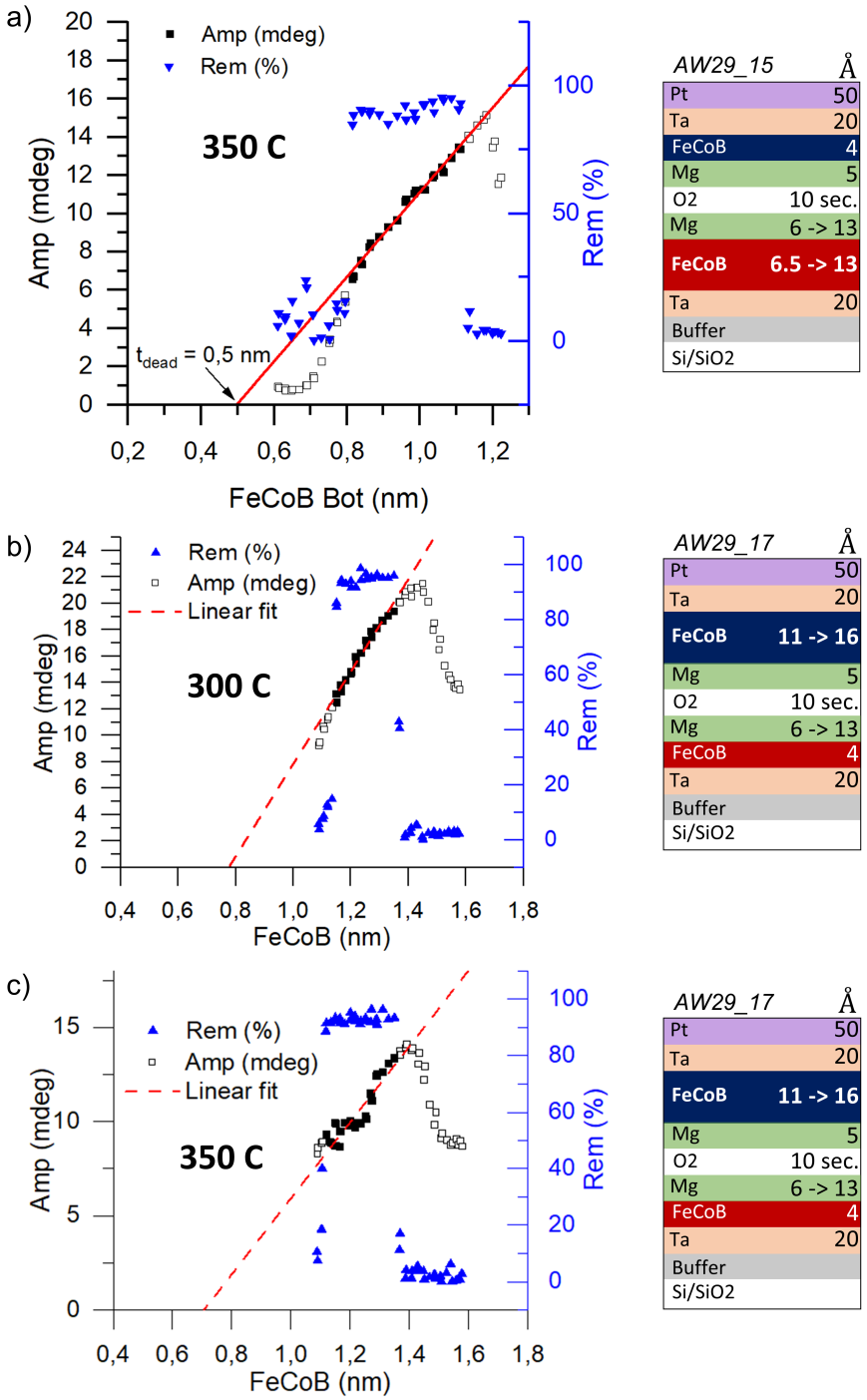

Figure 8.1: Dead-layer calculation from NanoMOKE measurement on half-MTJ stack with (a) bottom FeCoB layer and (b-c) top FeCoB layer. Samples used for (a) and (c) are annealed at 350 C and (b) is annealed at 300 C.

8.2 Appendix 2

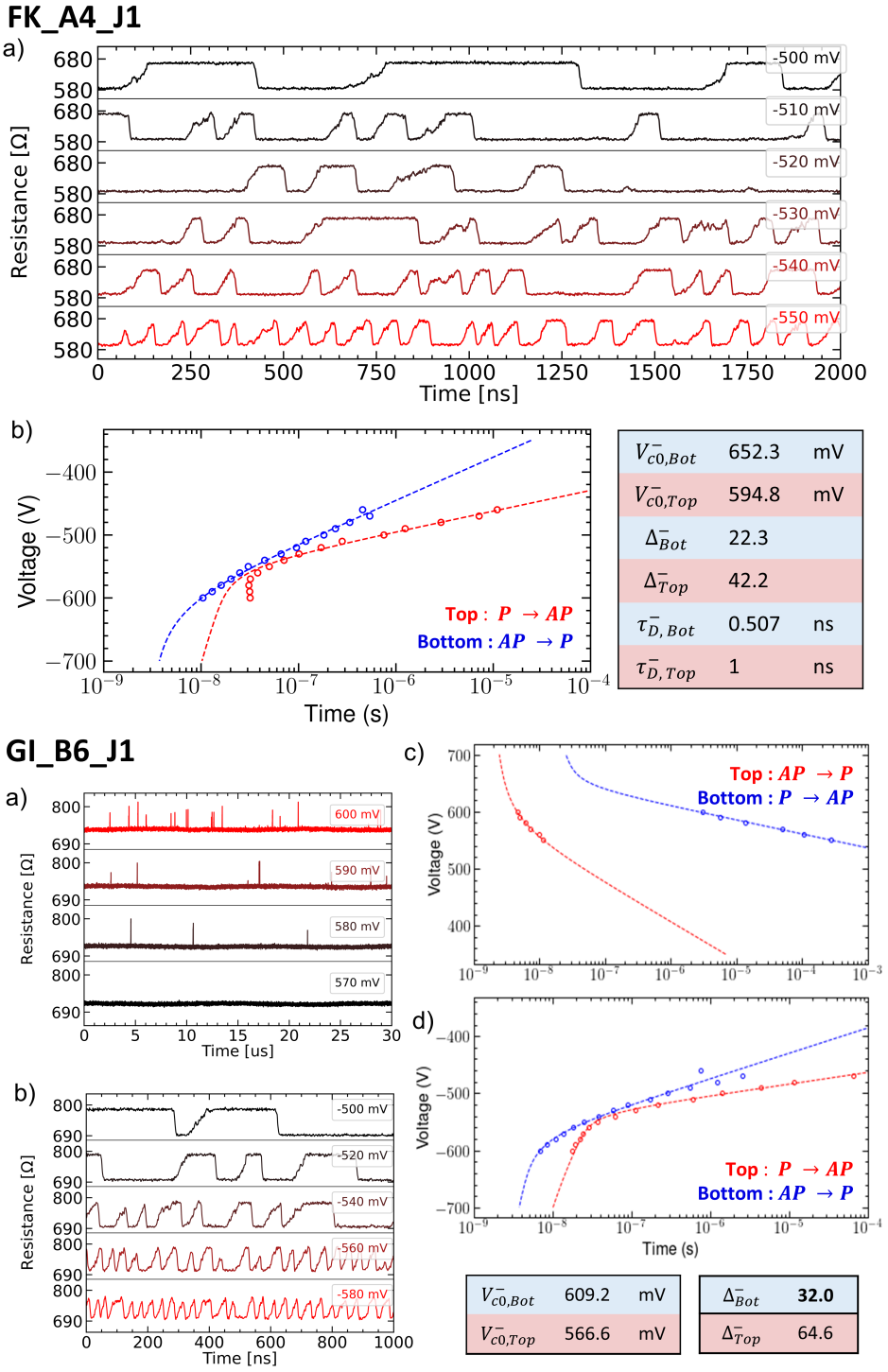

Figure 8.2: MTJ **#FK_A4_J1** : (a) time traces of a MTJ with similar lifetime between P and AP states. (b) Median switching time from P to AP and AP to P with the fitting from the unified equation. MTJ **#GI_B6_J1** : (a,b) plot the time traces at different applied voltage of a MTJ showing similar lifetime between the P and AP states in the negative polarity. We can clearly identified that in the time traces the transition time from P to AP is much longer than the one from AP to P. (c-d) are the Median switching time extracted from the time traces along with a table of the fitted parameters in the case of the negative current polarity.

8.3 Appendix 3

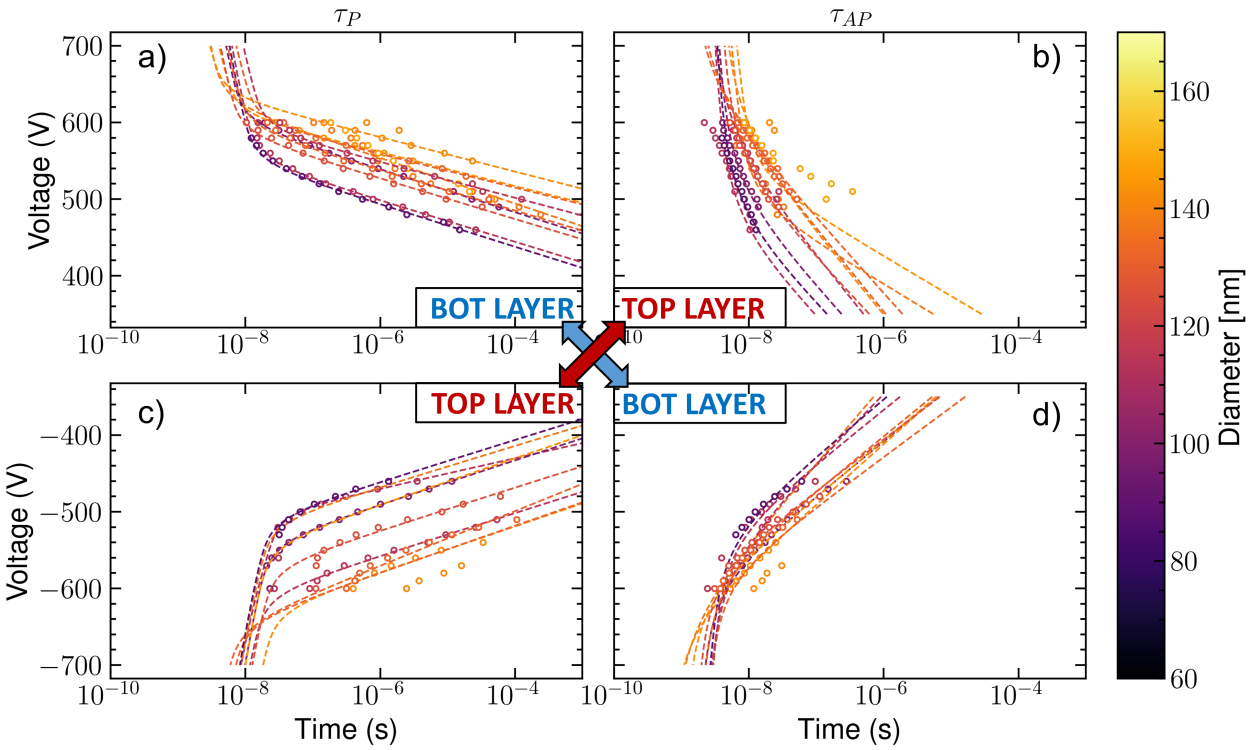

Figure 8.3: Median switching time as function of voltage for positive (a,b) and negative (c,d) current polarity for the top (b,c) and bottom (a,d) FeCoB layer. The dashed line refers to the fitting of the yang equation considering the same value of Δ_0, $V_{c,0}$ and $\pm h_r$ in both polarities for each bottom and top layer.

Bibliography

1. Moore, G. Cramming More Components Onto Integrated Circuits. *Proceedings of the IEEE* **86,** 82–85 (Jan. 1998).
2. Thompson, N., Greenewald, K., Lee, K. & Manso, G. F. *The Computational Limits of Deep Learning* en. in *Ninth Computing within Limits 2023* (LIMITS, June 2023).
3. Villarrubia, G., De Paz, J. F., Chamoso, P. & la Prieta, F. D. Artificial neural networks used in optimization problems. *Neurocomputing* **272,** 10–16 (Jan. 2018).
4. Krizhevsky, A. *Learning Multiple Layers of Features from Tiny Images* in (2009).
5. Girshick, R., Donahue, J., Darrell, T. & Malik, J. *Rich Feature Hierarchies for Accurate Object Detection and Semantic Segmentation* in *2014 IEEE Conference on Computer Vision and Pattern Recognition* (June 2014), 580–587.
6. Hinton, G. *et al.* Deep Neural Networks for Acoustic Modeling in Speech Recognition: The Shared Views of Four Research Groups. *IEEE Signal Processing Magazine* **29,** 82–97 (Nov. 2012).
7. Esteva, A. *et al.* Dermatologist-level classification of skin cancer with deep neural networks. en. *Nature* **542,** 115–118 (Feb. 2017).
8. Horowitz, M. *1.1 Computing's energy problem (and what we can do about it)* in *2014 IEEE International Solid-State Circuits Conference Digest of Technical Papers (ISSCC)* (Feb. 2014), 10–14.
9. Maass, W. Networks of spiking neurons: The third generation of neural network models. en. *Neural Networks* **10,** 1659–1671 (Dec. 1997).
10. Mead, C. Neuromorphic electronic systems. *Proceedings of the IEEE* **78,** 1629–1636 (Oct. 1990).
11. Lapicque, L. Recherches quantitatives sur l'excitation électrique des nerfs traitée comme une polarisation. *J. Physiol. Pathol. Gen.* **9,** 620–635 (1907).
12. Merolla, P. A. *et al.* A million spiking-neuron integrated circuit with a scalable communication network and interface. *Science* **345,** 668–673 (Aug. 2014).
13. Davies, M. *et al.* Loihi: A Neuromorphic Manycore Processor with On-Chip Learning. en. *IEEE Micro* **38,** 82–99 (Jan. 2018).
14. Furber, S. B., Galluppi, F., Temple, S. & Plana, L. A. The SpiNNaker Project. en. *Proceedings of the IEEE* **102,** 652–665 (May 2014).
15. Benjamin, B. V. *et al.* Neurogrid: A Mixed-Analog-Digital Multichip System for Large-Scale Neural Simulations. en. *Proceedings of the IEEE* **102,** 699–716 (May 2014).

16. Furber, S. Large-scale neuromorphic computing systems. en. *Journal of Neural Engineering* **13,** 051001 (Oct. 2016).

17. Mansueto, M. *et al.* Spintronic memristors for neuromorphic circuits based on the angular variation of tunnel magnetoresistance. en. *Nanoscale* **13,** 11488–11496 (July 2021).

18. Lequeux, S. *et al.* A magnetic synapse: multilevel spin-torque memristor with perpendicular anisotropy. en. *Scientific Reports* **6,** 31510 (Nov. 2016).

19. Romera, M. *et al.* Vowel recognition with four coupled spin-torque nano-oscillators. en. *Nature* **563,** 230–234 (Nov. 2018).

20. Romera, M. *et al.* Binding events through the mutual synchronization of spintronic nano-neurons. en. *Nature Communications* **13,** 883 (Feb. 2022).

21. Leroux, N. *et al.* Radio-Frequency Multiply-and-Accumulate Operations with Spintronic Synapses. en. *Physical Review Applied* **15,** 034067 (Mar. 2021).

22. Matsumoto, R., Lequeux, S., Imamura, H. & Grollier, J. Chaos and Relaxation Oscillations in Spin-Torque Windmill Spiking Oscillators. en. *Physical Review Applied* **11,** 044093 (Apr. 2019).

23. Maxwell, J. C. A Dynamical Theory of the Electromagnetic Field. *Philosophical Transactions of the Royal Society of London* **155,** 459–512 (1865).

24. in. *Selected Scientific Works of Hans Christian Ørsted* (eds Jackson, A. D. & Knudsen, O.) 417–420 (Princeton University Press, 1998). ISBN: 978-1-4008-6485-0.

25. Pauli, W. Über den Zusammenhang des Abschlusses der Elektronengruppen im Atom mit der Komplexstruktur der Spektren. de. *Zeitschrift für Physik* **31,** 765–783 (Feb. 1925).

26. Slater, J. C. Electronic Structure of Alloys. *Journal of Applied Physics* **8,** 385–390 (Apr. 2004).

27. Heisenberg, W. Mehrkörperproblem und Resonanz in der Quantenmechanik. de. *Zeitschrift für Physik* **38,** 411–426 (June 1926).

28. Dirac, P. A. M. & Fowler, R. H. On the theory of quantum mechanics. *Proceedings of the Royal Society of London. Series A, Containing Papers of a Mathematical and Physical Character* **112,** 661–677 (Jan. 1997).

29. Néel, L. Anisotropie magnétique superficielle et surstructures d'orientation. fr. *J. Phys. Radium* **15,** 225 (1954).

30. Monso, S. *et al.* Crossover from in-plane to perpendicular anisotropy in Pt/CoFe/AlOx sandwiches as a function of Al oxidation: A very accurate control of the oxidation of tunnel barriers. *Applied Physics Letters* **80,** 4157–4159 (May 2002).

31. Rodmacq, B., Auffret, S., Dieny, B., Monso, S. & Boyer, P. Crossovers from in-plane to perpendicular anisotropy in magnetic tunnel junctions as a function of the barrier degree of oxidation. *Journal of Applied Physics* **93,** 7513–7515 (May 2003).

32. Manchon, A. *et al.* X-ray analysis of oxygen-induced perpendicular magnetic anisotropy in Pt/Co/AlOx trilayers. *Journal of Magnetism and Magnetic Materials* **320,** 1889–1892 (July 2008).

33. Yang, H. X. *et al.* First-principles investigation of the very large perpendicular magnetic anisotropy at Fe | MgO and Co | MgO interfaces. en. *Physical Review B* **84,** 054401 (Aug. 2011).

34. Nakajima, N. *et al.* Perpendicular Magnetic Anisotropy Caused by Interfacial Hybridization via Enhanced Orbital Moment in Co / Pt Multilayers: Magnetic Circular X-Ray Dichroism Study. en. *Physical Review Letters* **81,** 5229–5232 (Dec. 1998).

35. Carcia, P. F., Meinhaldt, A. D. & Suna, A. Perpendicular magnetic anisotropy in Pd/Co thin film layered structures. *Applied Physics Letters* **47,** 178–180 (July 1985).

36. Parkin, S. S. P. & Mauri, D. Spin engineering: Direct determination of the Ruderman-Kittel-Kasuya-Yosida far-field range function in ruthenium. en. *Physical Review B* **44,** 7131–7134 (Oct. 1991).

37. Mott, N. Electrons in transition metals. *Advances in Physics* **13,** 325–422 (July 1964).

38. Julliere, M. Tunneling between ferromagnetic films. en. *Physics Letters A* **54,** 225–226 (Sept. 1975).

39. Moodera, J. S., Kinder, L. R., Wong, T. M. & Meservey, R. Large Magnetoresistance at Room Temperature in Ferromagnetic Thin Film Tunnel Junctions. *Physical Review Letters* **74,** 3273–3276 (Apr. 1995).

40. Miyazaki, T. & Tezuka, N. Giant magnetic tunneling effect in Fe/Al2O3/Fe junction. *Journal of Magnetism and Magnetic Materials* **139,** L231–L234 (Jan. 1995).

41. Ikeda, S. *et al.* Tunnel magnetoresistance of 604% at 300K by suppression of Ta diffusion in CoFeB-MgOCoFeB pseudo-spin-valves annealed at high temperature. *Applied Physics Letters* **93,** 082508 (Aug. 2008).

42. Butler, W. H. Tunneling magnetoresistance from a symmetry filtering effect. *Science and Technology of Advanced Materials* **9,** 014106 (Jan. 2008).

43. Slonczewski, J. Current-driven excitation of magnetic multilayers. en. *Journal of Magnetism and Magnetic Materials* **159,** L1–L7 (June 1996).

44. Berger, L. Emission of spin waves by a magnetic multilayer traversed by a current. en. *Physical Review B* **54,** 9353–9358 (Oct. 1996).

45. Tsoi, M. *et al.* Excitation of a Magnetic Multilayer by an Electric Current. en. *Physical Review Letters* **80,** 4281–4284 (May 1998).

46. Katine, J. A., Albert, F. J., Buhrman, R. A., Myers, E. B. & Ralph, D. C. Current-Driven Magnetization Reversal and Spin-Wave Excitations in Co / Cu / Co Pillars. en. *Physical Review Letters* **84,** 3149–3152 (Apr. 2000).

47. Huai, Y., Albert, F., Nguyen, P., Pakala, M. & Valet, T. Observation of spin-transfer switching in deep submicron-sized and low-resistance magnetic tunnel junctions. *Applied Physics Letters* **84,** 3118–3120 (Apr. 2004).

48. Diao, Z. *et al.* Spin transfer switching and spin polarization in magnetic tunnel junctions with MgO and AlOx barriers. *Applied Physics Letters* **87,** 232502 (Dec. 2005).

49. Kubota, H. *et al.* Evaluation of Spin-Transfer Switching in CoFeB/MgO/CoFeB Magnetic Tunnel Junctions. en. *Japanese Journal of Applied Physics* **44,** L1237 (Sept. 2005).

50. Hayakawa, J. *et al.* Current-Driven Magnetization Switching in CoFeB/MgO/CoFeB Magnetic Tunnel Junctions. en. *Japanese Journal of Applied Physics* **44,** L1267 (Sept. 2005).

51. Timopheev, A. A., Sousa, R., Chshiev, M., Buda-Prejbeanu, L. D. & Dieny, B. Respective influence of in-plane and out-of-plane spin-transfer torques in magnetization switching of perpendicular magnetic tunnel junctions. en. *Physical Review B* **92,** 104430 (Sept. 2015).

52. Bernert, K. *et al.* Phase diagrams of MgO magnetic tunnel junctions including the perpendicular spin-transfer torque in different geometries. en. *Physical Review B* **89,** 134415 (Apr. 2014).

53. Oh, S.-C. *et al.* Bias-voltage dependence of perpendicular spin-transfer torque in asymmetric MgO-based magnetic tunnel junctions. en. *Nature Physics* **5,** 898–902 (Dec. 2009).

54. Kubota, H. *et al.* Quantitative measurement of voltage dependence of spin-transfer torque in MgO-based magnetic tunnel junctions. en. *Nature Physics* **4,** 37–41 (Jan. 2008).

55. Li, Z. *et al.* Perpendicular Spin Torques in Magnetic Tunnel Junctions. *Physical Review Letters* **100,** 246602 (June 2008).

56. Gilbert, T. A phenomenological theory of damping in ferromagnetic materials. *IEEE Transactions on Magnetics* **40,** 3443–3449 (Nov. 2004).

57. Landau, L. & Lifshitz, E. en. in *Perspectives in Theoretical Physics* (ed Pitaevski, L. P.) 51–65 (Pergamon, Jan. 1992). ISBN: 978-0-08-036364-6.

58. Coey, J. M. D. *Magnetism and Magnetic Materials* en. ISBN: 978-1-139-48692-7 (Cambridge University Press, Mar. 2010).

59. Slavin, A. & Tiberkevich, V. Nonlinear Auto-Oscillator Theory of Microwave Generation by Spin-Polarized Current. *IEEE Transactions on Magnetics* **45,** 1875–1918 (Apr. 2009).

60. Brown, W. F. Thermal Fluctuations of a Single-Domain Particle. en. *Physical Review* **130,** 1677–1686 (June 1963).

61. Li, Z. & Zhang, S. Thermally assisted magnetization reversal in the presence of a spin-transfer torque. en. *Physical Review B* **69,** 134416 (Apr. 2004).

62. Koch, R. H., Katine, J. A. & Sun, J. Z. Time-Resolved Reversal of Spin-Transfer Switching in a Nanomagnet. en. *Physical Review Letters* **92,** 088302 (Feb. 2004).

63. Sun, J. Z. Spin-current interaction with a monodomain magnetic body: A model study. en. *Physical Review B* **62,** 570–578 (July 2000).

64. Sun, J. Z., Kuan, T. S., Katine, J. A. & Koch, R. H. *Spin angular momentum transfer in a current-perpendicular spin-valve nanomagnet* en. in (eds Razeghi, M. & Brown, G. J.) (July 2004), 445.

65. Tomita, H. *et al.* Unified understanding of both thermally assisted and precessional spin-transfer switching in perpendicularly magnetized giant magnetoresistive nanopillars. en. *Applied Physics Letters* **102,** 042409 (Jan. 2013).

66. Diao, Z. *et al.* Spin-transfer torque switching in magnetic tunnel junctions and spin-transfer torque random access memory. en. *Journal of Physics: Condensed Matter* **19,** 165209 (Apr. 2007).

67. Lim, H., Lee, S. & Shin, H. Unified Analytical Model for Switching Behavior of Magnetic Tunnel Junction. *IEEE Electron Device Letters* **35,** 193–195 (Feb. 2014).

68. Vincent, A. F. *et al.* Analytical Macrospin Modeling of the Stochastic Switching Time of Spin-Transfer Torque Devices. en. *IEEE Transactions on Electron Devices* **62,** 164–170 (Jan. 2015).

69. Yang, X., Zhang, Y., Zhang, Y. & Wang, P. A Universal Compact Model for Spin-Transfer Torque-Driven Magnetization Switching in Magnetic Tunnel Junction. en. *IEEE Transactions on Electron Devices* **69,** 6453–6458 (Nov. 2022).

70. Bedau, D. *et al.* Spin-transfer pulse switching: From the dynamic to the thermally activated regime. *Applied Physics Letters* **97,** 262502 (Dec. 2010).

71. Hosomi, M. *et al. A novel nonvolatile memory with spin torque transfer magnetization switching: spin-ram* in *IEEE InternationalElectron Devices Meeting, 2005. IEDM Technical Digest.* (Dec. 2005), 459–462.

72. LeCun, Y., Bengio, Y. & Hinton, G. Deep learning. en. *Nature* **521,** 436–444 (May 2015).

73. Tavanaei, A., Ghodrati, M., Kheradpisheh, S. R., Masquelier, T. & Maida, A. Deep learning in spiking neural networks. en. *Neural Networks* **111,** 47–63 (Mar. 2019).

74. Ramón y Cajal, S. & Ramón y Cajal, S. *Histologie du système nerveux de l'homme & des vertébrés* Ed. française rev. & mise à jour par l'auteur, tr. de l'espagnol par L. Azoulay. (Maloine, 1909).

75. Hodgkin, A. L. & Huxley, A. F. A quantitative description of membrane current and its application to conduction and excitation in nerve. en. *The Journal of Physiology* **117,** 500–544 (1952).

76. Mamaluy, D. & Gao, X. The fundamental downscaling limit of field effect transistors. *Applied Physics Letters* **106,** 193503 (May 2015).

77. Singh, G. *et al. A Review of Near-Memory Computing Architectures: Opportunities and Challenges* en. in *2018 21st Euromicro Conference on Digital System Design (DSD)* (IEEE, Aug. 2018), 608–617. ISBN: 978-1-5386-7377-5.

78. Corda, S. *et al. NMPO: Near-Memory Computing Profiling and Offloading* en. Tech. rep. arXiv:2106.15284 (arXiv, June 2021).

79. Münch, C., Bishnoi, R. & Tahoori, M. B. *Reliable in-memory neuromorphic computing using spintronics* en. in *Proceedings of the 24th Asia and South Pacific Design Automation Conference* (ACM, Jan. 2019), 230–236. ISBN: 978-1-4503-6007-4.

80. Sebastian, A., Le Gallo, M., Khaddam-Aljameh, R. & Eleftheriou, E. Memory devices and applications for in-memory computing. en. *Nature Nanotechnology* **15,** 529–544 (July 2020).

81. Zou, X., Xu, S., Chen, X., Yan, L. & Han, Y. Breaking the von Neumann bottleneck: architecture-level processing-in-memory technology. en. *Science China Information Sciences* **64,** 160404 (Apr. 2021).

82. Gerstner, W. & Kistler, W. M. *Spiking neuron models: single neurons, populations, plasticity* eng. ISBN: 978-0-511-07817-0 (Cambridge University Press, 2002).

83. Gerstner, W., Kistler, W. M., Naud, R. & Paninski, L. *Neuronal Dynamics: From Single Neurons to Networks and Models of Cognition* en. ISBN: 978-1-107-06083-8 (Cambridge University Press, July 2014).

84. Abbott, L. F. Lapicque's introduction of the integrate-and-fire model neuron (1907). *Brain Research Bulletin* **50,** 303–304 (Nov. 1999).

85. Bi, G. Q. & Poo, M. M. Synaptic modifications in cultured hippocampal neurons: dependence on spike timing, synaptic strength, and postsynaptic cell type. eng. *The Journal of Neuroscience: The Official Journal of the Society for Neuroscience* **18,** 10464–10472 (Dec. 1998).

86. Bi, G. & Poo, M. Synaptic modification by correlated activity: Hebb's postulate revisited. eng. *Annual Review of Neuroscience* **24,** 139–166 (2001).

87. Morris, R. G. M. D.O. Hebb: The Organization of Behavior, Wiley: New York; 1949. *Brain Research Bulletin* **50,** 437 (Nov. 1999).

88. Serrano-Gotarredona, T., Masquelier, T., Prodromakis, T., Indiveri, G. & Linares-Barranco, B. STDP and STDP variations with memristors for spiking neuromorphic learning systems. en. *Frontiers in Neuroscience* **7** (2013).

89. Iakymchuk, T., Rosado-Muñoz, A., Guerrero-Martínez, J. F., Bataller-Mompeán, M. & Francés-Víllora, J. V. Simplified spiking neural network architecture and STDP learning algorithm applied to image classification. en. *EURASIP Journal on Image and Video Processing* **2015,** 4 (Dec. 2015).

90. Ghosh-Dastidar, S. & Adeli, H. SPIKING NEURAL NETWORKS. en (2009).

91. Bouvier, M. *et al.* Spiking Neural Networks Hardware Implementations and Challenges: a Survey. *ACM Journal on Emerging Technologies in Computing Systems* **15,** 1–35 (Apr. 2019).

92. Dampfhoffer, M., Mesquida, T., Valentian, A. & Anghel, L. Are SNNs Really More Energy-Efficient Than ANNs? an In-Depth Hardware-Aware Study. *IEEE Transactions on Emerging Topics in Computational Intelligence* **7,** 731–741 (June 2023).

93. Nguyen, D.-A., Tran, X.-T. & Iacopi, F. A Review of Algorithms and Hardware Implementations for Spiking Neural Networks. en. *Journal of Low Power Electronics and Applications* **11,** 23 (June 2021).

94. Hubara, I., Courbariaux, M., Soudry, D., El-Yaniv, R. & Bengio, Y. Binarized Neural Networks. en.

95. Li, Y., Zhao, D. & Zeng, Y. BSNN: Towards faster and better conversion of artificial neural networks to spiking neural networks with bistable neurons. *Frontiers in Neuroscience* **16** (2022).

96. Lu, S. & Sengupta, A. Exploring the Connection Between Binary and Spiking Neural Networks. *Frontiers in Neuroscience* **14** (2020).

97. Zhuang, B., Shen, C., Tan, M., Liu, L. & Reid, I. *Structured Binary Neural Networks for Accurate Image Classification and Semantic Segmentation* in *2019 IEEE/CVF Conference on Computer Vision and Pattern Recognition (CVPR)* (June 2019), 413–422.

98. Vincent, A. F. *et al.* Spin-Transfer Torque Magnetic Memory as a Stochastic Memristive Synapse for Neuromorphic Systems. en. *IEEE Transactions on Biomedical Circuits and Systems* **9,** 166–174 (Apr. 2015).

99. Sharad, M., Augustine, C., Panagopoulos, G. & Roy, K. Spin-Based Neuron Model With Domain-Wall Magnets as Synapse. en. *IEEE Transactions on Nanotechnology* **11,** 843–853 (July 2012).

100. Mansueto, M. *et al.* Realizing an Isotropically Coercive Magnetic Layer for Memristive Applications by Analogy to Dry Friction. en. *Physical Review Applied* **12,** 044029 (Oct. 2019).

101. Mansueto, M. *Memristive magnetic memory for spintronic synapses* en. PhD thesis (Université Grenoble Alpes [2020-....], Dec. 2020).

102. Jung, S. *et al.* A crossbar array of magnetoresistive memory devices for in-memory computing. en. *Nature* **601,** 211–216 (Jan. 2022).

103. Palhares, J. H. Q. *et al.* A tunable and versatile 28 nm FD-SOI crossbar output circuit for low power analog SNN inference with eNVM synapses. *Solid-State Electronics* **209,** 108779 (Nov. 2023).

104. Wang, D. *et al.* Spintronic leaky-integrate-fire spiking neurons with self-reset and winner-takes-all for neuromorphic computing. en. *Nature Communications* **14,** 1068 (Feb. 2023).

105. Sengupta, A., Panda, P., Wijesinghe, P., Kim, Y. & Roy, K. Magnetic Tunnel Junction Mimics Stochastic Cortical Spiking Neurons. en. *Scientific Reports* **6,** 30039 (July 2016).

106. Yang, K. & Sengupta, A. Stochastic magnetoelectric neuron for temporal information encoding. en. *Applied Physics Letters* **116,** 043701 (Jan. 2020).

107. Srinivasan, G., Sengupta, A. & Roy, K. Magnetic Tunnel Junction Based Long-Term Short-Term Stochastic Synapse for a Spiking Neural Network with On-Chip STDP Learning. en. *Scientific Reports* **6,** 29545 (Sept. 2016).

108. Rodrigues, D. R. *et al.* Spintronic Hodgkin-Huxley-Analogue Neuron Implemented with a Single Magnetic Tunnel Junction. *Physical Review Applied* **19,** 064010 (June 2023).

109. Choi, R., Katine, J. A., Mangin, S. & Fullerton, E. E. Current-Induced Pinwheel Oscillations in Perpendicular Magnetic Anisotropy Spin Valve Nanopillars. en. *IEEE Transactions on Magnetics* **52,** 1–5 (Oct. 2016).

110. Thomas, L. *et al. Spin Transfer Torque driven dynamics of the synthetic antiferromagnetic reference layer of perpendicular MRAM devices* en. in *2017 IEEE International Magnetics Conference (INTERMAG)* (IEEE, Apr. 2017), 1–1. ISBN: 978-1-5386-1086-2.

111. Camsari, K. Y., Torunbalci, M. M., Borders, W. A., Ohno, H. & Fukami, S. Double-Free-Layer Magnetic Tunnel Junctions for Probabilistic Bits. en. *Physical Review Applied* **15,** 044049 (Apr. 2021).

112. Hem, J. Mécanismes de synchronisation dans les oscillateurs à transfert de spin. fr.

113. Song, Y. J. *et al. Demonstration of Highly Manufacturable STT-MRAM Embedded in 28nm Logic* in *2018 IEEE International Electron Devices Meeting (IEDM)* (Dec. 2018), 18.2.1–18.2.4.

114. Golonzka, O. *et al. MRAM as Embedded Non-Volatile Memory Solution for 22FFL FinFET Technology* in *2018 IEEE International Electron Devices Meeting (IEDM)* (Dec. 2018), 18.1.1–18.1.4.

115. Chatterjee, J. *Engineering of magnetic tunnel junction stacks for improved STT-MRAM performance and development of novel and cost-effective nano-patterning techniques* en. PhD thesis (Université Grenoble Alpes, Mar. 2018).

116. Chatterjee, J. *et al.* Enhanced annealing stability and perpendicular magnetic anisotropy in perpendicular magnetic tunnel junctions using W layer. en. *Applied Physics Letters* **110,** 202401 (May 2017).

117. Hazen, D. S. *Engineering and evaluation of double magnetic tunnel junctions with a switchable assistance layer for high performance spin transfer torque magnetic memory* en. PhD thesis (Université Grenoble Alpes [2020-....], June 2022).

118. Troparevsky, M. C., Morris, J. R., Kent, P. R. C., Lupini, A. R. & Stocks, G. M. Criteria for Predicting the Formation of Single-Phase High-Entropy Alloys. en. *Physical Review X* **5,** 011041 (Mar. 2015).

119. Yuasa, S., Suzuki, Y., Katayama, T. & Ando, K. Characterization of growth and crystallization processes in CoFeBMgOCoFeB magnetic tunnel junction structure by reflective high-energy electron diffraction. *Applied Physics Letters* **87,** 242503 (Dec. 2005).

120. Kozina, X. *et al.* A nondestructive analysis of the B diffusion in Ta–CoFeB–MgO–CoFeB–Ta magnetic tunnel junctions by hard x-ray photoemission. *Applied Physics Letters* **96,** 072105 (Feb. 2010).

121. Karthik, S. V. *et al.* Transmission electron microscopy investigation of CoFeB/MgO/CoFeB pseudospin valves annealed at different temperatures. *Journal of Applied Physics* **106,** 023920 (July 2009).

122. Kang, S. H. & Lee, K. Emerging materials and devices in spintronic integrated circuits for energy-smart mobile computing and connectivity. *Acta Materialia. The Diamond Jubilee Issue* **61,** 952–973 (Feb. 2013).

123. Fillion, C.-E. *Electric control of skyrmions for spintronic applications* en. PhD thesis (Université Grenoble Alpes [2020-....], Jan. 2023).

124. Urrestarazu Larrañaga, J. *et al. Electrical detection and nucleation of a magnetic skyrmion in a magnetic tunnel junction observed via operando magnetic microscopy* Sept. 2023.

125. Cuchet, L. *Magnetic and transport properties of single and double perpendicular magnetic tunnel junctions* fr. PhD thesis ().

126. Lee, S.-E., Shim, T.-H. & Park, J.-G. Perpendicular magnetic tunnel junction (p-MTJ) spin-valves designed with a top Co2Fe6B2 free layer and a nanoscale-thick tungsten bridging and capping layer. *NPG Asia Mater* **8,** e324–e324 (Nov. 2016).

127. Devolder, T. *et al.* Damping of CoxFe80xB20 ultrathin films with perpendicular magnetic anisotropy. en. *Applied Physics Letters* **102,** 022407 (Jan. 2013).

128. Ikeda, S. *et al.* A perpendicular-anisotropy CoFeB–MgO magnetic tunnel junction. en. *Nature Materials* **9,** 721–724 (Sept. 2010).

129. Enobio, E. C. I., Sato, H., Fukami, S., Matsukura, F. & Ohno, H. CoFeB Thickness Dependence of Damping Constants for Single and Double CoFeB-MgO Interface Structures. en. *IEEE Magnetics Letters* **6,** 1–3 (2015).

130. Okada, A. *et al.* Electric-field effects on magnetic anisotropy and damping constant in Ta/CoFeB/MgO investigated by ferromagnetic resonance. en. *Applied Physics Letters* **105,** 052415 (Aug. 2014).

131. Dieny, B. & Chshiev, M. Perpendicular magnetic anisotropy at transition metal/oxide interfaces and applications. *Reviews of Modern Physics* **89,** 025008 (June 2017).

132. Parkin, S. S. P., More, N. & Roche, K. P. Oscillations in exchange coupling and magnetoresistance in metallic superlattice structures: Co/Ru, Co/Cr, and Fe/Cr. *Physical Review Letters* **64,** 2304–2307 (May 1990).

133. Lin, C.-J. *et al.* Magnetic and structural properties of Co/Pt multilayers. *Journal of Magnetism and Magnetic Materials* **93,** 194–206 (1991).

134. Weller, D. *et al.* Interface and Volume Anisotropy of Mbe-Grown Co/Pt (111), (110) and (001) and Sputtered Co/Pt Multilayers. en. *MRS Online Proceedings Library* **313,** 791–797 (Dec. 1993).

135. Chatterjee, J. *et al.* Seed Layer Effect on the Magnetic Properties of Ultrathin Co/Pt Multilayers With Perpendicular Magnetic Anisotropy. *IEEE Transactions on Magnetics* **50,** 1–4 (Nov. 2014).

136. Johnson, M. T., Bloemen, P. J. H., Broeder, F. J. A. D. & Vries, J. J. D. Magnetic anisotropy in metallic multilayers. en. *Reports on Progress in Physics* **59,** 1409–1458 (Nov. 1996).

137. Carcia, P. F. Perpendicular magnetic anisotropy in Pd/Co and Pt/Co thin-film layered structures. *Journal of Applied Physics* **63,** 5066–5073 (May 1988).

138. Chatterjee, J. *et al.* Novel multifunctional RKKY coupling layer for ultrathin perpendicular synthetic antiferromagnet. en. *Scientific Reports* **8,** 11724 (Aug. 2018).

139. Strelkov, N. *et al.* Impact of Joule heating on the stability phase diagrams of perpendicular magnetic tunnel junctions. en. *Physical Review B* **98,** 214410 (Dec. 2018).

140. Mihajlović, G. *et al.* Origin of the Resistance-Area-Product Dependence of Spin-Transfer-Torque Switching in Perpendicular Magnetic Random-Access Memory Cells. en. *Physical Review Applied* **13,** 024004 (Feb. 2020).

141. Gapihan, E. *et al.* Heating asymmetry induced by tunneling current flow in magnetic tunnel junctions. en. *Applied Physics Letters* **100,** 202410 (May 2012).

142. Martin, E. *et al.* EqSpike: Spike-driven equilibrium propagation for neuromorphic implementations. en. *iScience* **24,** 102222 (Mar. 2021).